

**ISTANBUL TECHNICAL UNIVERSITY ★ GRADUATE SCHOOL OF SCIENCE**  
**ENGINEERING AND TECHNOLOGY**

**SHIP DRAG REDUCTION THROUGH AIR  
INJECTION TO BOUNDARY LAYER**

**Ph.D. THESIS**

**Serhan GÖKÇAY**

**Naval Architecture and Marine Engineering Department**

**Naval Architecture and Marine Engineering Programme**

**MAY 2012**



**ISTANBUL TECHNICAL UNIVERSITY ★ GRADUATE SCHOOL OF SCIENCE**  
**ENGINEERING AND TECHNOLOGY**

**SHIP DRAG REDUCTION THROUGH AIR  
INJECTION TO BOUNDARY LAYER**

**Ph.D. THESIS**

**Serhan GÖKÇAY**  
**(508062002)**

**Naval Architecture and Marine Engineering Department**

**Naval Architecture and Marine Engineering Programme**

**Thesis Advisor: Prof. Dr. Mustafa İNSEL**

**MAY 2012**



**İSTANBUL TEKNİK ÜNİVERSİTESİ ★ FEN BİLİMLERİ ENSTİTÜSÜ**

**SINIR TABAKA HAVA ENJEKSİYONU İLA GEMİ DİRENÇ DÜŞÜŞÜ**

**DOKTORA TEZİ**

**Serhan GÖKÇAY  
(508062002)**

**Gemi İnşaatı ve Gemi Makinaları Mühendisliği Anabilim Dalı**

**Gemi İnşaatı ve Gemi Makinaları Mühendisliği Programı**

**Tez Danışmanı: Prof. Dr. Mustafa İNSEL**

**MAYIS 2012**









*To my wife and son,*



## FOREWORD

I would like to express my gratitude for my thesis advisor Prof. Dr. Mustafa İnel, for suggesting the problem and for his guidance, encouragement and understanding throughout this investigation.

I would like to acknowledge the academics of Faculty of Naval Architecture and Ocean Engineering, specifically Assist. Prof. Şebnem Helvacıođlu, Assoc.Prof. İsmail Hakkı Helvacıođlu and Prof. Dr. Ömer Gören for their continuous encouragement.

I would like to thank Prof. Dr. Sander Çalışal for his comments to this work and valuable discussions.

I would like to thank Mr. Turhan Soyarslan for encouragement for the study, Ms. İnci Gündüz Baldođan and Mr. Şevki Bakırcı of Turk Loydu for enabling to conduct such a study during professional working life.

I would also like to acknowledge the Ata Nutku Ship Model Testing laboratory staff: Assoc.Prof. Emin Korkut, Seyfi Erim, Cemal Çelik for their help in the experimental part of the work. The assistance by Rafet Emek Kurt, Evrim Alözkan, Tolga Karacadal and Onur Özel during the initial tests is strongly appreciated.

My appreciation is extended to Dr. Gökhan Ergin of DANTEC Dynamics and Dr. Hayri Acar of ITU Trisonic Research Laboratory for their assistance on Constant Temperature Anemometry.

And finally special gratitude to my family; my wife Kübra Gökçay, my son Rüzgar Gökçay for their understanding of my long working hours in and outside home; my parents Nilgün and Cengiz Gökçay and my brother Gökhan Gökçay for their constant support in my whole life.

January 2012

Serhan GÖKÇAY



## TABLE OF CONTENTS

	<u>Page</u>
<b>FOREWORD</b> .....	<b>ix</b>
<b>TABLE OF CONTENTS</b> .....	<b>xi</b>
<b>ABBREVIATIONS</b> .....	<b>xiii</b>
<b>LIST OF TABLES</b> .....	<b>xv</b>
<b>LIST OF FIGURES</b> .....	<b>xvii</b>
<b>SUMMARY</b> .....	<b>xxi</b>
<b>ÖZET</b> .....	<b>xxv</b>
<b>1. INTRODUCTION</b> .....	<b>1</b>
<b>2. GENERAL REVIEW OF VISCOUS DRAG REDUCTION BY BOUNDARY LAYER MODIFICATION</b> .....	<b>11</b>
2.1 Introduction .....	11
2.2 Active Methods .....	12
2.2.1 Bubble Induced Drag Reuction.....	12
2.2.2 Air Film.....	20
2.2.3 Air Cavity.....	23
2.2.3.1 Experiments On Air Cavity.....	24
2.2.3.2 Numerical Computations On Air Cavity .....	28
2.2.4 Polymer Injection.....	32
2.3 Passive Methods .....	33
2.3.1 Compliant Coatings.....	33
2.3.2 Antifouling (Biofouling Control).....	34
2.4 Conclusions .....	35
<b>3. AIR LUBRICATION EXPERIMENTS ON FOUL-RELEASE COATED SURFACES</b> .....	<b>37</b>
3.1 Introduction .....	37
3.2 Motivation And Background.....	38
3.3 Experiments on vertical surfaces.....	39
3.3.1 Experimental Setup .....	39
3.3.2 Test Matrix .....	42
3.3.3 Results And Analysis .....	42
3.4 Experiments on horizontal surfaces(Tanker Model Flat of Bottom) .....	48
3.4.1 Flow Visualizations in Circulating Channel .....	49
3.4.1.1 Experimental Setup .....	49
3.4.1.2 Test Matrix .....	51
3.4.1.2 Results And Analysis .....	51
3.4.2 Experiments In Towing Tank .....	58
3.4.2.1 Total Resistance Measurements .....	58
3.4.2.2 Wave Pattern Resistance Measurements .....	59
3.4.2.3 Results And Analysis .....	61
3.5 Conclusions .....	65

<b>4. EXPERIMENTS ON BOUNDARY LAYER MODIFICATION BY SINGLE HOLE AIR INJECTION TO CROSS WATER FLOW .....</b>	<b>67</b>
4.1 Introduction .....	67
4.2 Experimental Facility .....	67
4.3 Experimental Setup .....	69
4.3.1 Air Injection System .....	73
4.3.1.1 Air Supply System.....	73
4.3.1.2 Air Flow Metering.....	74
4.4 Velocity Calibration of Circulating Channel.....	75
4.4.1 Instrumentation .....	75
4.4.1.1 Probe Traversing .....	75
4.4.1.2 Five Hole Pitot Tube .....	75
4.4.2 Circulating Channel Calibration Procedure .....	76
4.5 Measurements of velocity and volume of fraction profiles.....	78
4.5.1 Instrumentation .....	78
4.5.1.1 Principles of constant temperature anemometry .....	80
4.5.1.2 Single normal boundary layer probe .....	84
4.5.2 Probe Calibration Procedure .....	89
4.5.2.1 Calibration using specially designed facilities .....	89
4.5.2.2 In-situ calibration of the single normal boundary layer probe .....	91
4.5.3 Data Acquisition and Run Procedure (Test Matrix) .....	95
4.6 Local wall shear and wall void fraction measurements.....	96
4.6.1 Instrumentation .....	97
4.6.2 Probe Calibration Procedure .....	99
4.6.3 Data Acquisition and Run Procedure.....	102
4.6.4 Flow Visualization .....	103
4.6.5 Results and analysis of modified boundary layer measurements.....	105
4.6.5.1 Signal processing of acquired data from air injected flow .....	105
4.6.5.2 Developed software for processing the signal.....	108
Obtaining velocity charecteristics of continuous phase .....	108
Calculating local void fraction .....	109
Obtaining phase indicative function.....	110
Threshold Determination.....	112
4.6.5.3 Modification in boundary layer parameters .....	113
4.7 Summary and Conclusions .....	117
<b>5. CONCLUSIONS AND RECOMMENDATIONS .....</b>	<b>121</b>
<b>REFERENCES .....</b>	<b>127</b>
<b>APPENDICES .....</b>	<b>137</b>
APPENDIX A .....	138
APPENDIX B.....	169
<b>CURRICULUM VITAE .....</b>	<b>171</b>

## ABBREVIATIONS

<b>BL</b>	: Boundary Layer
<b>CO<sub>2</sub></b>	: Carbon Dioxide
<b>UN</b>	: United Nations
<b>IMO</b>	: International Maritime Organization
<b>CTA</b>	: Constant Temperature Anemometer
<b>BP</b>	: British Petroleum
<b>UNEP</b>	: United Nations Environment Programme
<b>IPCC</b>	: Intergovernmental Panel on Climate Change
<b>UNCTAD</b>	: United Nations Conference on Trade and Development
<b>IEA</b>	: International Energy Agency
<b>GHG</b>	: Green House Gasses
<b>ICAO</b>	: International Civil Aviation Organization
<b>UNFCCC</b>	: United Nations Framework Convention on Climate Change
<b>MARPOL</b>	: Marine Pollution Convention
<b>MEPC</b>	: Marine Environment Protection Committee
<b>SEMP</b>	: Ship Energy Management Plan
<b>EEDI</b>	: Energy Efficiency Design Index
<b>EEOI</b>	: Energy Efficiency Operational Index
<b>METS</b>	: Maritime Emissions Trading Scheme
<b>ICF</b>	: International Compensation Fund
<b>MBI</b>	: Market Based Instruments
<b>IACS</b>	: International Association of Classification Societies
<b>RANSE</b>	: Reynolds Averaged Navier-Stokes Solvers
<b>PELS</b>	: United Nations Framework Convention on Climate Change
<b>SMOOTH</b>	: Marine Pollution Convention
<b>TARGETS</b>	: Marine Pollution Convention
<b>ITU</b>	: Istanbul Technical University
<b>DNS</b>	: Direct Navier-Stokes Solver
<b>CFD</b>	: Computational Fluid Dynamics
<b>VOF</b>	: Volume of Fluid
<b>SPC</b>	: Self-Polishing Copolymers
<b>DC</b>	: Direct Current
<b>LDA</b>	: Laser Doppler Anemometer
<b>LDV</b>	: Laser Doppler Velocitymeter
<b>PIV</b>	: Particle Induced Velocitymeter
<b>RMS</b>	: Root mean Square
<b>PIF</b>	: Phase Indicative Function





## LIST OF TABLES

	<u>Page</u>
<b>Table 3.1</b> : Coding of test matrix for tanker model experiments .....	59
<b>Table 4.1</b> : Positions of the air injection fitting and measurement stations .....	71
<b>Table B.1</b> : Principle characteristics of the form M266B .....	169
<b>Table B.2</b> : Positions of data points from wall.....	170



## LIST OF FIGURES

	<u>Page</u>
<b>Figure 2.1</b> : Transition from bubble drag reduction to air-layer drag reduction (Elbing et al. 2008).....	22
<b>Figure 2.2</b> : Cavity formation on downstream of backward facing step.....	24
<b>Figure 2.3</b> : Escape of air from sidewalls and stern ramp (Gökçay et al. 2004).....	25
<b>Figure 2.4</b> : Comparison of viscous resistance coefficient (Ct-Cwp) for HC and AC forms. (Gökçay et. al 2004).....	27
<b>Figure 2.5</b> : Velocity streamlines of air phase combined with wall shear. ....	31
<b>Figure 3.1</b> : Experimental Setup (Composite Vertical Flat Plate). ....	41
<b>Figure 3.2</b> : Vertical flat plate test for $V=0.31$ m/s and $Q=0.5$ m <sup>3</sup> /h. ....	43
<b>Figure 3.3</b> : Vertical flat plate test for $V=0.31$ m/s and $Q=1.5$ m <sup>3</sup> /h.. ....	44
<b>Figure 3.4</b> : Vertical flat plate test for $V=1.75$ m/s and $Q=0.5$ m <sup>3</sup> /h. ....	44
<b>Figure 3.5</b> : Vertical flat plate test for $V=1.75$ m/s and $Q=1.5$ m <sup>3</sup> /h.. ....	45
<b>Figure 3.6</b> : Free surface waves created by the explosion of bubble coalescence ....	46
<b>Figure 3.7</b> : Comparison of frictional coefficients for vertical flat plate experiment. ....	47
<b>Figure 3.8</b> : Vertical flat plate experiment (air was injected from leading edge) ....	47
<b>Figure 3.9</b> : Vertical flat plate exp.: (a) 10 degrees of leeway. (b) 5 degrees of heel.....	48
<b>Figure 3.10</b> : Reference model and painted model. ....	49
<b>Figure 3.11</b> : Angle of air film edge. S5R1, $Fn=0.06$ , $Q=0.5$ m <sup>3</sup> /h. ....	52
<b>Figure 3.12</b> : Angle of air film edge. S5R2, $Fn=0.06$ , $Q=0.75$ m <sup>3</sup> /h. ....	53
<b>Figure 3.13</b> : Angle of air film edge. S5R3, $Fn=0.06$ , $Q=1.0$ m <sup>3</sup> /h.. ....	53
<b>Figure 3.14</b> : Angle of air film edge. S5R7, $Fn=0.158$ , $Q=0.5$ m <sup>3</sup> /h.. ....	53
<b>Figure 3.15</b> : Angle of air film edge. S5R16, $Fn=0.24$ , $Q=0.5$ m <sup>3</sup> /h.. ....	54
<b>Figure 3.16</b> : Advection velocity of the water-air interface estimated by HSC particle tracking method. ....	54
<b>Figure 3.17</b> : Multiple hole injection at high speed. ....	55
<b>Figure 3.18</b> : Multiple hole injection (a) transverse holes (b) longitudinal. ....	56
<b>Figure 3.19</b> : Air flow from porous media (a) low speed (b) high speed.....	56
<b>Figure 3.20</b> : Bubbles from the plastic porous media ....	57
<b>Figure 3.21</b> : Angle variation of air film edge with speed and air flow rate.....	58
<b>Figure 3.22</b> : Recorded wave cuts for model without air injection, $Fn=0.225$ . ....	60
<b>Figure 3.23</b> : Recorded wave cuts and wave cuts produced from wave pattern analysis for model without air injection, $Fn=0.225$ .....	61
<b>Figure 3.24</b> : Full Load Draught base model and single hole air lubrication comparison. ....	62
<b>Figure 3.25</b> : Full Load Draught base model and porous media air lubrication comparison. ....	62
<b>Figure 3.26</b> : Full Load Draught base model and air lubrication comparison .....	63
<b>Figure 3.27</b> : Half Load Draught base model and air lubrication comparison.....	63

<b>Figure 3.28:</b> Wave pattern resistance comparison between original and air lubricated forms.....	64
<b>Figure 3.29:</b> Wave pattern analysis at 1.0 m/s. ....	64
<b>Figure 3.30:</b> Wave pattern analysis plate at 1.44 m/s. ....	65
<b>Figure 4.1:</b> Schematic of the flat plate showing the air injection and measurement points.....	71
<b>Figure 4.2:</b> Probe types used in the experiments.....	86
<b>Figure 4.3:</b> Distance calibration of BL probe to the wall.....	88
<b>Figure 4.4:</b> BL probe calibrator.....	91
<b>Figure 4.5:</b> Calibration of the hot film probe by pithod tube .....	92
<b>Figure 4.6:</b> In-situ calibration (70mm out of the wall).....	93
<b>Figure 4.7:</b> Typical calibration plot with curve fitting.....	94
<b>Figure 4.8:</b> Flush mounted hot film probe calibrator .....	100
<b>Figure 4.9:</b> Typical calibration plot for flush mounted hot-film probe.....	102
<b>Figure 4.10:</b> Change in wall shear with free stream velocity .....	103
<b>Figure 4.11:</b> Typical boundary layer hot film probe signal in multiphase flow .....	106
<b>Figure 4.12:</b> Time series of voltage signal and the corresponding PIF.....	110
<b>Figure 4.13:</b> Time series of voltage signal and the corresponding PIF-alternative .....	111
<b>Figure 4.14:</b> The plot of threshold voltage analysis.....	112
<b>Figure 4.15:</b> Bottom view of air injection .....	114
<b>Figure A.1:</b> Use of fuel energy on board for a small cargo ship, head sea, Beaufort 6.....	138
<b>Figure A.2:</b> Body plan of M266.....	138
<b>Figure A.3:</b> Sketch of spherical 5-hole pitot tube probe.....	138
<b>Figure A.4:</b> Circulating water channel located at ITU.....	139
<b>Figure A.5:</b> Experimental setup .....	139
<b>Figure A.6:</b> Circulating channel calibration plot.....	140
<b>Figure A.7:</b> Positioning and measurement subsystems of traverse mechanism.....	140
<b>Figure A.8:</b> Effect of contamination on velocity drift .....	141
<b>Figure A.9:</b> Constant temprature anomometer measuring chain .....	141
<b>Figure A.10:</b> Characteristics of Fiber-Film Probe (Dantec 55R15) and Flush Mounted Hot-Film Probe (Dantec 55R46). ....	142
<b>Figure A.11:</b> Typical output file of voltage threshold analysis sub program.....	143
<b>Figure A.12:</b> Typical output file of the developed code .....	144
<b>Figure A.13:</b> Bottom view of p50 case with air injection of 1.4m <sup>3</sup> /h.....	145
<b>Figure A.14:</b> Bottom view of p50 case with air injection of 2.8m <sup>3</sup> /h.....	146
<b>Figure A.15:</b> Bottom view of p80 case with air injection of 1.4m <sup>3</sup> /h.....	147
<b>Figure A.16:</b> Bottom view of p80 case with air injection rate of 2.8m <sup>3</sup> /h.....	148
<b>Figure A.17:</b> Bottom view of p100 case with air injection of 1.4m <sup>3</sup> /h.....	149
<b>Figure A.18:</b> Bottom view of p100 case with air injection of 2.8m <sup>3</sup> /h.....	150
<b>Figure A.19:</b> Side view for p100 case for air flow rates: (a)1.4m <sup>3</sup> /h. (b)2.8m <sup>3</sup> /h. (c)5.6m <sup>3</sup> /h. (d)7m <sup>3</sup> /h.....	151
<b>Figure A.20:</b> Velocity, volume of fraction and turbulance intensity profiles for p50 case: (a)Station 1. (b)Station 2.....	152
<b>Figure A.21:</b> Velocity, volume of fraction and turbulance intensity profiles for p50 case: (a)Station 3. (b)Station 4.....	153
<b>Figure A.22:</b> Velocity, volume of fraction and turbulance intensity profiles for p50 case: (a)Station 5. (b)Station 6.....	154

<b>Figure A.23:</b> Velocity, volume of fraction and turbulence intensity profiles for p80 case: (a)Station 1. (b)Station 2 .....	155
<b>Figure A.24:</b> Velocity, volume of fraction and turbulence intensity profiles for p80 case: (a)Station 3. (b)Station 4 .....	156
<b>Figure A.25:</b> Velocity, volume of fraction and turbulence intensity profiles for p80 case: (a)Station 5. (b)Station 6 .....	157
<b>Figure A.26:</b> Velocity, volume of fraction and turbulence intensity profiles for p100 case: (a)Station 1. (b)Station 2 .....	158
<b>Figure A.27:</b> Velocity, volume of fraction and turbulence intensity profiles for p100 case: (a)Station 3. (b)Station 4 .....	159
<b>Figure A.28:</b> Velocity, volume of fraction and turbulence intensity profiles for p100 case: (a)Station 5. (b)Station 6 .....	160
<b>Figure A.29:</b> Flush mounted hot-film signals for p50, FM3 and $Q=0 \text{ m}^3/\text{h}$ .....	161
<b>Figure A.30:</b> Flush mounted hot-film signals for p50, FM1 and $Q=1.4 \text{ m}^3/\text{h}$ .....	161
<b>Figure A.31:</b> Flush mounted hot-film signals for p50, FM1 and $Q=1.4 \text{ m}^3/\text{h}$ (zoomed).....	162
<b>Figure A.32:</b> Flush mounted hot-film signals for p80, FM2 and $Q=1.4 \text{ m}^3/\text{h}$ (zoomed).....	162
<b>Figure A.33:</b> Wall shear stress measurements for p50 case. (a)FM1 position. (b)FM2 position.....	163
<b>Figure A.34:</b> Wall shear stress measurements for p50 case.(a)FM3 position. (b)FM4 position.....	164
<b>Figure A.35:</b> Wall shear stress measurements for p80 case. (a)FM1 position. (b)FM2 position.....	165
<b>Figure A.36:</b> Wall shear stress measurements for p80 case. (a)FM3 position. (b)FM4 position.....	166
<b>Figure A.37:</b> Wall shear stress measurements for p100 case. (a)FM1 position. (b)FM2 position.....	167
<b>Figure A.38:</b> Wall shear stress measurements for p100 case. (a)FM3 position. (b)FM4 position.....	168



## **SHIP DRAG REDUCTION THROUGH AIR INJECTION TO BOUNDARY LAYER**

### **SUMMARY**

Global warming is one of the main concerns for the world future and burning of fossil fuels is a primer contributor of manmade CO<sub>2</sub> emissions. Therefore, UN has set a target to reduce global warming resulting from imbalances to the greenhouse effect, which is 70% reduction in man-made CO<sub>2</sub> emissions by the year 2050, achieved through a mix of operational and logistical measures, application of existing and new technology.

For these reasons, numerous research attempts for reduction of marine emissions are searching for more widely use of renewable energy sources and much effort has been focused on the efficient use of the fossil fuels with the purpose of reduction in wasted energy and air pollution, hence lower particulation and reduced greenhouse gasses.

As a naval architectural point of view, the most interesting component of the consumed energy is the propulsion and engine related components. Obviously, energy losses from hull friction (viscous drag) and the wave generation are dominating components. There is much extensive research performed on the optimization of hull forms by streamlining the shape of the hull in order to reduce radiated waves and avoiding flow separation. Such improvements on wave resistance are reaching its limits; viscous component is to become the focal point for any further improvement. A number of techniques to reduce the viscous resistance have been proposed by boundary layer modification with the utilization of both active and passive methods.

Experiments on hull friction resistance reduction has shown that, air lubrication is one of the most profitable technique in boundary layer modification hence the frictional drag reduction. The underlying principle of air lubrication is to separate the surface of the hull from the water flow around the hull with a layer of air. Reduced wetted surface area is leading considerable amount of reduction in skin friction. Micro bubbles, air film or air cavity concepts are widely utilized techniques in order to achieve an effective lubrication.

The physical mechanisms for air cavity, micro bubbles, and air film are reviewed from the existing literature, both from theoretical reduction potential and practical application point of view. The experience has been extended by use of model test with vertical surfaces and horizontal surfaces with the application of air feeding mechanism through both orifices and porous media resulting in air film and micro bubble injection respectively. The experiments with the vertical surfaces have clearly demonstrated the gains from air lubrication on vertical surfaces are not possible with the current air lubrication techniques. However, air lubrication on horizontal surfaces has great potential of drag reduction by all three techniques. Micro bubbles and air film suffers from the air layer stability issues as air layer is pushed out of boundary layer through downstream.

Even though micro bubble concept is well investigated for both external and internal flow drag reduction, the practical problems in actual sea conditions have limited the use of the concept. Hence, this study has focused on air lubrication of a flat plate experiments for boundary layer modification by utilizing air jet, injected through a single hole to the cross water flow in a circulating water channel. Modified boundary layer measurements were compared with the undisturbed boundary layer characteristics in order to understand the influence of the air injection on boundary layer modification.

Profiles of liquid phase velocities, local air volume of fractions as well as turbulence intensities were extracted from the measurements of hot film boundary layer probe in six stations. Local wall shear measurements were also conducted through four measuring points by utilizing flush mounted hot film probes as well. Local wall shear measurements than matched with the boundary layer scan data in order to provide further understanding about the near wall modification. Techniques to analyze the CTA signal were developed which provide the reduction of the acquired voltage signal to velocity values by using power law calibration coefficients (linearization), the decomposition of the liquid phase velocity magnitudes with fluctuation levels (turbulence intensities) as well as the local air volume of fraction quantities.

The flow underneath the flat plate was observed through the windows located at sidewall as well as located at the bottom of the channel. Visualization data was obtained utilizing a camera so that acquired visual data was utilized for the interpretation of the velocity and void fraction profiles of the measurement stations located in modified boundary layer. Injected air separates into V shaped arm just behind the hole and it is for sure that the arms were created by the edge of air film. The angle of the V shape is directly proportional with airflow rate. In contrast, the angle is inversely proportional with free stream velocity.

For slower speeds and increasing airflow rates, while the angle is getting larger, the area between the V arms gets contact with only water and air is concentrated near the V arms and escapes from the hull sides. In case of moderate speeds and lower airflow rates, air bubbles are forming at larger distance and the area is mostly covered with air film. For faster speeds and increasing flow rates, while the angle is getting smaller, air is dispersing through the area between V shaped arms and generates air bubbles and the length of the arms are getting shorter.

The side view evaluation of the air injection shows that air jet is behaving like a flexible elliptical wedge and creates a cavity behind. The reattachment line visualized by the dispersed air bubbles can be seen clearly. For higher the air flow rates, steeper the air cavities are obtained. Air jet behaves like a point source and forms a compressible elliptical obstacle on the surface. Due to the fact that in the line and downstream of the point source, higher velocity field is occurring which probably creates a V shape air film arms. In order to understand the structure of the flow field behind the air jet, results of boundary layer velocity profiles with void fraction quantities and wall shear stress measurements were analyzed.

The drag reduction is strongly depended on near wall local air volume of fraction. Sudden decreases in void fractions with the increase in turbulent fluctuations lead increases in drag. For flow velocities which lead best local drag reductions can also lead highest drag increases due to dramatical change in the multiphase flow regime by increasing the air injected flow rates.

For lower speeds air modified velocity profiles of the liquid phase generally deviates from the reference profiles. Especially for higher air injection rates, the deviation increases. With increasing free stream velocity, the deviation reduces.



Unlike the air cavity, local drag reduction is strongly depended on air injection rates. Airflow rate increase will conclude both the increase in wall shear due to local void fraction decrease and probably form drag increases due to more disturbances in boundary layer.



## SINIR TABAKA HAVA ENJEKSİYONUYLA GEMİ DİRENÇ DÜŞÜŞÜ

### ÖZET

Kuşkusuz küresel ısınma, dünyanın geleceği açısından en büyük sorunlardan biri olarak görülmektedir ve bunun önemli bir nedeni olarak; fosil yakıtlarının yakılması, insan kaynaklı CO<sub>2</sub> emisyonlarından sorumlu tutulmaktadır. Bu nedenle Birleşmiş Milletler, bu emisyonların etkisinin azaltılması için önemli bir hedef koymuştur. Bu hedefe göre 2050 yılında insan kaynaklı CO<sub>2</sub> emisyonlarının %70 azaltılması hedeflenmiştir. Bu hedeflere erişmek için operasyonel, lojistik, mevcut ve yeni teknolojilerin uygulamasını içeren tedbirler önerilmiştir.

Bu nedenlerle denizcilik kaynaklı CO<sub>2</sub> emisyonlarının azaltılması için yenilenebilir enerji kaynaklarının kullanımının artırılması ve fosil yakıtlarının verimli kullanımı ile emisyonların azaltımı, hava kirliliğinin düşürülmesi ve dolaylı olarak sera gazı salınımının azaltılması üzerine çeşitli araştırmalar yapılmaktadır.

Gemi inşa mühendisliği açısından gemi sevki ve makinesi bileşenlerine harcanan enerji, en ilgi çekici alanı oluşturmaktadır. Burada teknenin sürtünme ve dalga direnç bileşenleri en baskın bileşen olarak ortaya çıkmaktadır. Tekne tarafından yayılan dalga enerjisinin azaltılması amacı ile akım hatlarına göre tekne form optimizasyonunun yapılması, üzerinde en fazla araştırma yapılan konulardan biridir. Bu nedenle dalga direnci üzerine yapılan form iyileştirmelerinde varılabilecek limitlere erişilmekte, daha fazla iyileştirmenin yapılacağı potansiyel alan olarak viskoz direnç bileşeninde yapılacak iyileştirmeler ön plana çıkmaktadır. Viskoz direnç bileşeninin azaltılması için çeşitli aktif veya pasif sınır tabaka modifikasyon metotları önerilmiştir.

Tekne sürtünme direnci azaltımı için yapılan deneyler, hava yağlamanın sınır tabaka değiştirme metotları arasında en etkili yöntem olabileceğini göstermiştir. Hava yağlamada temel prensip, tekne cidarını su akımından bir hava tabakası ile ayırarak azaltılmış ıslak satıhla sürtünme direnç düşüşünün sağlanmasıdır. Mikro kabarcık, hava filmi ve hava kavitesi kavramları efektif hava yağlamasına ulaşabilmek için yararlanılan tekniklerin başında gelir. Bu çalışma kapsamında hava kavitesi, mikro kabarcık ve hava filmi kavramları üzerine mevcut literatür, teorik direnç azaltımı potansiyeli ve pratik uygulamalar açısından incelenmiştir. Edinilen bilgi birikimi, düşey ve yatay düzlemler üzerinde tek delik ve geçirgen poroz yapıdaki levhalar üzerinden hava besleyerek, hava filmi ve mikro kabarcık yöntemleriyle yapılan deneyler ile genişletilmiştir. Bu kapsamda yapılan deneylerde öncelikle düz düşey levha üzerinde hava yağlaması uygulamaları pratikte karşılaşılabilecek farklı sürüklenme açıları ve meyil durumlarına göre denenmiştir. Hava yağlamanın etkinliğinin artırılması için model düz levha, özel geliştirilmiş silikon bazlı gemi boyasıyla kaplanmıştır. Düşey levha deneyleri sonucunda levhaya enjekte edilen hava, sephiyesi nedeniyle kısa bir mesafe sonra su yüzeyine çıkmış ve etkin bir hava yağlaması sağlayamamıştır. Bu bulgu da düşey düzlemlerdeki hava yağlamanın, mevcut hava yağlama teknikleri ile direnç azaltımında etkin bir yöntem olamayacağını ortaya koymuştur. Yatay düzlemlerde hava yağlama deneyleri için

gemi model deney havuzunda bulunan düz dipli bir tanker modeli seçilerek model, silikon bazlı gemi boyasıyla kaplanmıştır. Model dibine delinen deliklerden tek delik ve çok delikten hava enjeksiyonuyla hava filmi oluşturulmuş, ayrıca model dibine özel olarak tasarlanan bir aparatla yerleştirilen poroz yapıdaki metalden mikro kabarcık üretimiyle modelin sınır tabakası değiştirilmiştir. Bu deneyler kapsamında hava yağlamasız kontrol deneyleri ve farklı 3 teknikle hava yağlama deneyleri hem sirkülasyon kanalında hem de model deney havuzunda model dirençleri ölçülerek gerçekleştirilmiştir. Hava yağlamasının hidrostatik basınçla değişiminin incelenmesi için farklı su çekimlerinde ölçümler alınmış ayrıca yağlamanın dalga direncine etkisinin incelenmesi için de model dalga dirençleri ölçülmüştür. Bu deneyler sonucunda yatay düzlemlerdeki hava yağlama tekniği ile önemli direnç azaltımlarının mümkün olduğu ortaya çıkmıştır. Mikro kabarcık yönteminde, verilen havanın akışın ileri kısmında basınç gradyeni dolayısıyla sınır tabaka dışına itilmesi ve poroz metal plakaların kısa bir zamanda tıkanarak kabarcık üretilememesi gibi pratik zorluklarla karşılaşmıştır. Bunun yanında tek delikten hava enjeksiyonu yönteminin, hem kolay uygulanabilirliği hem de direnç azaltımı potansiyeli dolayısıyla daha avantajlı bir yöntem olduğu sonucuna varılmıştır.

Tek noktadan hava enjeksiyonu kavramının tanker modelinin dibine uygulanması sonrasında elde edilen umut verici sonuçlar, tek noktadan hava yağlamasının daha iyi anlaşılması için geniş kapsamlı araştırmalara ön ayak olarak bu çalışmanın da ana kapsamını oluşturmuştur. Bu nedenle çalışma, sirkülasyon kanalında düzlemsel bir levha üzerinde tek delikten verilen bir hava jeti ile sınır tabakanın değiştirildiği hava filmi uygulaması üzerinde yoğunlaşmıştır. Deneyler İstanbul Teknik Üniversitesi Ata Nutku Gemi Model Deney Laboratuvarında bulunan kapalı devre sirkülasyon kanalında yapılmıştır. Deneylerde boyu 580mm, genişliği 480mm ve kalınlığı 15mm olan rijit düz levha kullanılmıştır. Levha su içerisinde yatay olarak konumlandırılmış ve hem hidrodinamik pürüzsüzlüğün sağlanması hem de yukarıdan gözlemin yapılabilmesi amacıyla plexiglass'dan yapılmıştır. Modele hava enjeksiyonu ve yerel duvar kayma gerilmeleri ölçümleri için 5 adet bağlantı parçası, yüzeye sıfır olacak şekilde yerleştirilmiştir. Bunlardan biri hava enjeksiyonunu sağlarken diğerleri de duvar kayma gerilmeleri ölçümleri için ayrılmıştır.

Genel olarak sınır tabaka modifikasyonuna yönelik deneyler, amaçlanan değişikliğin sınır tabaka yapısındaki etkilerinin incelenmesi için ilgili cisim üzerindeki hız alanının incelenmesini gerektirir. Bu bağlamda, türbülans şiddeti ve diğer karakteristik parametreler, incelenen hız alanından türetilir. Bu çalışmada yatay düz levha sınır tabakası hava enjeksiyonuyla değişime uğratılmıştır. Böyle bir olayın incelenmesi için sınır tabaka boyunca hava faz oranları profillerinin ve su fazına ait ikinci momentleri de içeren hız bilgilerinin türetilmesi gerekmektedir. Bu amaç doğrultusunda PIV ya da LDA gibi ölçüm sistemlerinin kullanılması da seçenekler arasındadır; ancak bu sistemlerin çok fazlı akış ölçümlerinde karşılaşılan birçok kısıtları bulunmaktadır. Bu nedenle, deneysel çalışmada detaylandırılan tek ve iki fazlı akışa ait sınır tabaka hız alanlarının ölçümünde birçok türbülanslı hava-gaz akış çalışmalarında temel araç olarak kullanılan sabit sıcaklık anemometresi (CTA) kullanılmıştır. Hız ve hava oranlarının ölçümlerinde kalın quartz kaplanmış sınır tabaka nikel fiber film probundan faydalanılmıştır. Bu prob, bilgisayar destekli konumlandırma mekanizmasına tutturularak levha altında istenen konumdaki hız profillerinin ve hava faz oranlarının elde edilmesinde kullanılmıştır. Böylece, sıvı faz akım hızları, yerel hava oranı ve türbülans şiddeti 6 ayrı konumda (istasyonda) ve her istasyonda 24 duvar normali doğrultusundaki noktalarda sıcak film sınır tabaka probu ile toplanan voltaj verilerinden türetilmiştir.

Yerel duvar kayma gerilmeleri ölçümünde ise kalın quartz kaplanmış ve yüzeye sıfır monte edilen sıcak film probu kullanılmıştır. Bu algılayıcı, pleksiglas levha alt yüzeyine sıfır yerleştirilmesi için özel bir bağlantı elemanına monte edildikten sonra levhaya özel bir düzenele tutturulmuştur. Levha altına yerleştirilen 4 farklı konumda alınan sinyallerle yerel duvar kayma gerilmeleri ölçülmüştür. Hem sınır tabaka hız ve hava fazı oranları ölçümlerinde hem de duvar kayma gerilmeleri ölçümlerinde tek kanallı sabit sıcaklık anemometresi kullanılmıştır. Bu anemometre içerisinde yüksek ve düşük geçirgenlikli filtrelemenin yapılabildiği sinyal koşullandırıcısı ve aynı zamanda sinyal amplifikatörü de bulunmaktadır.

Hava enjeksiyonuyla değiştirilmiş sınır tabakada yapılan hız ve yüzey kayma gerilmeleri ölçümlerinde tabaka içinde hareket eden hava kütleleri ve kabarcıkların her iki probdan geçmesi, problemlerde ani voltaj düşüşlerine neden olarak U şeklindeki voltaj sinyallerinin gözlenmesine neden olmuştur. Gerek bu sinyallerin daha iyi incelenmesi gerekse hava fazının ayrıklaştırılmasını sağlayan bir algoritmanın kurulabilmesi için yüksek hızlı kamera kayıtları alınmıştır. Yüksek hızlı kamera kayıtlarıyla eş zamanlı toplanan sıcak film anemometre sinyallerinin senkronizasyonu bu konuyla ilgili detaylı bir analiz yapma olanağı sağlamış ve faz ayrıklaştırılması için gerekli yazılım, bu konuda literatürde belirtilen yöntemlerin de kullanılmasıyla geliştirilmiştir. MATLAB tabanlı bu yazılım, her toplanan voltaj sinyalleri için faz eşik voltaj değerlerini, dolayısıyla faz belirleme fonksiyonlarını hesaplamakta ve faz belirleme fonksiyonlarının ortalamasını alarak yerel hava fazı oranını hesaplamaktadır. Böylece her bir sinyal için hava-sıvı fazları ayrıklaştırılmakta ve sonrasında da sıvı fazı için de hız ve türbülans şiddetleri aynı yazılım vasıtasıyla hesaplanabilmektedir.

Sıcak film problemlerinden alınan sinyallerin hızların bulunması için işlenmesi ve analizi, kalibrasyon teknikleri ve sıvı hız değişimlerinin ve yerel hava oranlarının analizleri amacı ile teknikler geliştirilmiştir. Düz levha altındaki akım yan ve dip pencelerden gözlemlenmiştir. Akım görüntüleme deneyleri video kamerası ile kaydedilmiş, ve ölçüm noktalarındaki değişimler incelenmiştir. Havanın verildiği deliğin arkasında V şeklini aldığı, ve V'nin kollarının hava sınırını belirlediği görülmüştür. V'nin açısı verilen hava debisi ile orantılıdır. Buna karşın aynı açının akım hızı ile ters orantılı olduğu gözlemlenmiştir.

Düşük hızlarda ve artan hava debilerinde, V açısının artmasıyla beraber kollar arasındaki bölümün su ile temasta olduğu ve havanın V nin kolları etrafında yoğunlaştığı görülmüştür. Orta hız ve düşük hava debilerinde, V nin kolları arasındaki bölümün hava ile kaplı olduğu, ve akımda hava kabarcıkları görüldüğü tespit edilmiştir. Yüksek hızlarda ve artan hava debi miktarlarında ise V açısının daralmasıyla beraber, havanın V kolları arasında daraldığı görülmektedir.

Yan pencereden yapılan akım görüntülemelerinde havanın eliptik esnek bir cisim gibi davrandığı ve arkasında bir kavite oluşturduğu görülmektedir. Dağılan hava kabarcıklarıyla tekrar birleşim hattının da görülmesi, hava kavitesine benzer bir akımı ortaya koymaktadır. Yüksek hava akım oranlarında, daha dik hava kavitesi gözlemlenmektedir. Hava jeti bir kaynak gibi davranarak eliptik bir cismin arkasındaki akımı oluşturmaktadır. Kaynağın arkasındaki akım hızlarının artması, V kolları oluşturmakta ve sınır tabaka içinde hızlanmalar görülmektedir. Hava jetinin arkasındaki akımın anlaşılabilmesi için, sınır tabakası hız profilleri, hava oranının belirlenmesi ve duvar gerilmelerinin ölçümü yapılarak analiz edilmiştir.

Sonuç olarak, sürtünme direncinin lokal hava oranına bağlı olduğu ve bu orandaki ani düşüşlerin türbülans şiddetlerindeki artışla birlikte lokal direnç artışına neden olduğu gözlenmiştir. En iyi lokal direnç düşüşlerinin elde edildiği akım hızlarında,

enjeksiyon hava debi artışlarının neden olduđu çok fazlı akım rejimindeki deęişimler nedeniyle yüksek lokal direnç artışlarının da olabileceđi görölmüştür. Bu olay, hem lokal yüzey kayma gerilmelerinin hava oranı düşüşü ile artışı, hem de sınır tabakada meydana getirilen süreksizliklerin neden olduđu form direnci artışıyla sonuçlanmaktadır.

## 1. INTRODUCTION

According to the June 2011 BP Statistical Review of World Energy, the majority of the energy currently consumed in the world is supplied by oil, coal, natural gas, hydroelectricity and nuclear. Oil was the world's largest source for energy consumed in 2010 (36%) with coal (31.8%) and natural gas (25.6%) being the second and third largest sources, respectively (BP, 2011). The main advantages of using these energy sources are easy usage, storage and transportation comparing with other sources. On the other hand, they have the disadvantage of having a negative impact on the environment due to particulation and greenhouse gas emissions which plays an important role on climate change and being limited in quantity (they require extremely long time for renewal) which induces the cost and sustainability issues.

Climate Change is a general term referring to changes in the statistical properties of the weather over long periods of time, such as millennia, and a topic of vital importance to all of us. It includes several distinct phenomena, including acid rain, ozone layer depletion, global warming and greenhouse gas production. In many cases these phenomena may be interconnected in a complex way, for example ozone depleting substances may also be greenhouse gasses. As greenhouses, isolate warm air inside a glass structure so that heat is not lost by convection, whereas the greenhouse effect concerns heat radiation. The greenhouse effect is caused by the absorption and emission of thermal radiation by greenhouse gases, principally water vapor, carbondioxide, methane and ozone. Water vapour is the largest contributor but there is little that can be done to vary this natural process. Carbon Dioxide represents the great majority of man made greenhouse gas (Solomon et al., 2007). That is why the united nations efforts have been primarily concerned with reductions in CO<sub>2</sub> emmissions.

Antartic ice samples have been shown that carbon dioxide levels in the athmosphere have risen dramatically in the past 200 years (Armstrong, 2011). There are arguments that this increase in carbon dioxide levels could be a natural phenomenon, and there is little evidence that it is man-made. Nevertheless, the overwhelming

scientific evidence is that high-levels of carbon dioxide are result of human activity. The great majority of CO<sub>2</sub> emissions are of course natural and not man-made. According to data from the United Nations Environment Programme UNEP (2005), natural sources of CO<sub>2</sub> are approximately 20 times greater than man-made sources, but for hundreds of thousands of years these natural sources have been balanced by natural sinks, such as the oceans and forests. It is only in recent years that man-made emissions have created an imbalance between sources and sinks (Armstrong, 2011).

In 1988, an Intergovernmental Panel on Climate Change (IPCC) was created by the World Meteorological Organization and the United Nations Environment Programme (UNEP). This group issued a first assessment report in 1990 which reflected the views of more than 400 scientists. The report stated that global warming was real and urged that something be done about it and the report referred burning of fossil fuels as a primer contributor of man made CO<sub>2</sub> emissions. Therefore UN has set a target to reduce global warming resulting from imbalances to the greenhouse effect, which is 70% reduction in man-made CO<sub>2</sub> emissions by the year 2050, achieved through a mix of operational and logistical measures, application of existing technology, and new technology that is not yet identified (IMO Secretariat, 2010). For these reasons numerous research attempts around the world is searching for alternative energy sources that are renewable and environmentally friendly such as wind, solar and geothermal. In addition, much effort has been focused on the efficient use of the oil, coal and natural gas sources, with the purpose of reduction in wasted energy and air pollution, hence lower particulation and reduced greenhouse gasses.

The use of energy in the world can be typically divided into three categories as; transportation, industrial and residential & service. Almost 30% of the total energy consumption in the world is for transportation, which is primarily provided from oil (IEA, 2011). According to United Nations Conference on Trade and Development (UNCTAD), about 80% of world trade by volume is transported by ships (UNCTAD Secretariat, 2009). Due to the fact that shipping is the most energy efficient mode of transport, only 3.3% of overall carbon dioxide emissions were accounted from shipping in 2007(Buhaug et al., 2009). However, global approach to further improve its energy efficiency and effective emission control is needed as sea transport will continue growing apace with world trade.



Over a decade ago, most countries joined an international treaty: The United Nations Framework Convention on Climate Change (UNFCCC) the objective was to begin to consider what can be done to reduce global warming and to cope with whatever temperature increases are inevitable. More recently, a number of nations approved an addition to the treaty: the Kyoto Protocol, which has more powerful measures. (The target agreed upon was an average reduction of 5.2% from 1990 levels by the year 2012.) The major feature of the protocol is that it sets binding targets for 37 industrialized countries and the European community for reducing greenhouse gas (GHG) emissions. The detailed rules for the implementation of the Protocol were adopted at COP 7 in Marrakesh in 2001, and are called the “Marrakesh Accords”. The Protocol entered into force in 2005 and contains provisions for reducing GHG emissions from international aviation and shipping and treats these sectors in a different way to other sources due to their global activities that is, pursuing through the International Civil Aviation Organization (ICAO) and the International Maritime Organization (IMO) respectively.

In September 1997, an International Conference of Parties to the MARPOL Convention, which adopted the Protocol of 1997 to amend the MARPOL Convention (MARPOL Annex VI), adopted resolution 8 on CO<sub>2</sub> emissions from ships. The resolution invited the Marine Environment Protection Committee (MEPC) to consider what CO<sub>2</sub> reduction strategies might be feasible in light of the relationship between CO<sub>2</sub> and other atmospheric and marine pollutants. The resolution also invited, in cooperation with the UNFCCC, to undertake a study of CO<sub>2</sub> emissions from ships for the purpose of establishing the amount and relative percentage of CO<sub>2</sub> emissions from ships as part of the global inventory of CO<sub>2</sub> emissions.

In 2000, the first IMO GHG Study on greenhouse gas emissions from ships was published, which estimated that ships engaged in international trade in 1996 contributed about 1.8 per cent of the world total anthropogenic CO<sub>2</sub> emissions. Following to that study, the IMO Assembly adopted resolution A.963(23), IMO Policies and practices related to the reduction of greenhouse gas emissions from ships in 2003, which urged the MEPC to identify and develop the mechanism or mechanisms needed to achieve the limitation or reduction of GHG emissions from

international shipping. In the ensuing years, MEPC has since been energetically pursuing measures to limit and reduce GHG emissions from international shipping.

In 2006, MEPC agreed to update the “IMO Study of Greenhouse Gas Emissions from Ships” from 2000 to provide a better foundation for future decisions and to assist in the follow-up to resolution A.963(23). An updated study was completed in 2009, with the title “Second IMO GHG Study 2009” and the main objectives of the study were to assess; present and future emissions from international shipping, the possibilities for reduction of these emissions through technology and policy and impacts on climate from these emissions. It is concluded that:

- Exhaust gases are the primary source of emissions from ships. Carbon dioxide is the most important GHG emitted by ships. Both in terms of quantity and of global warming potential, other GHG emissions from ships are less important.

- If a climate is to be stabilized at no more than 2°C warming over pre-industrial levels by 2100 and emissions from shipping continue as projected in the scenarios that are given in this report, then they would constitute between 12% and 18% of the global total CO<sub>2</sub> emissions in 2050 that would be required to achieve stabilization (by 2100) with a 50% probability of success.

- Mid-range emissions scenarios show that by 2050, in the absence of policies, carbon dioxide emissions from international shipping may grow by a factor of 2 to 3 (compared to the emissions in 2007) as a result of the growth in shipping.

- A significant potential for reduction of GHG through technical and operational measures has been identified. Together, if implemented, these measures could increase efficiency and reduce the emissions rate by 25% to 75% below the current levels (Buhaug et al., 2009).

The study has identified the emission policies of IMO in more detail and has provided detail of the proposed measures to reduce emissions. Within IMO, emission policies were grouped in three categories as Technical policy options, aimed at improving the design efficiency of the fleet. Operational policy options, aimed at improving the operational efficiency of the fleet and market-based policy options, instruments addressing CO<sub>2</sub> emissions directly with the purposes such as: climate change mitigation and adaptation activities, research and development, offsetting of emissions and serving as an incentive for the industry to invest in more fuel-efficient

technologies. The GHG working group has defined an index for new ships named as EEDI (Energy Efficiency Design Index) to stimulate innovation and the technical development of all the elements influencing the energy efficiency of a ship, thus making possible to build more energy-efficient ships in the future. To enable ship operators to measure the energy efficiency of their ships, EEOI (Energy Efficiency Operational Index) has been defined which translates the efficiency of specific ship, thus enabling comparisons between similar ships. This index was focused on the ships in operation. For both indexes, the agreed fundamental principle is that the value expresses the ratio between the cost (in terms of GHG emissions) and the benefit that is generated, which is expressed as transport work capacity. Moreover, to incorporate the best practices into the operation of each ship, including speed and power optimisation, improved fleet management, voyage planning, optimised ship handling and energy management, Ship Energy Management Plan (SEMP) was also defined by the working group.

Through out the study, a comprehensive overview of policy options like: a mandatory limit on the Energy Efficiency Design Index (EEDI) for new ships, mandatory or voluntary reporting of the EEDI, mandatory or voluntary reporting of the Energy Efficiency Operational Indicator (EEOI), mandatory or voluntary use of a Ship Efficiency Management Plan (SEMP), mandatory limit on the EEOI value combined with a penalty for non-compliance, a Maritime Emissions Trading Scheme (METS) and International Compensation Fund (ICF) to be financed by a levy on marine bunkers were discussed in detail.

Further studies on ship energy efficiency regulations were extended by the MEPC's sessions from 2008 to 2011. The majority of the committee meetings were focused on the setting of the thresholds named as baselines (finalised as reference lines) in order to establish "Required EEDI" values which is currently set for seven types of ships (bulk carriers, gas tankers, tankers (oil, chemical, NLS), container ships, general cargo ships, refrigerated cargo carriers, and combination carriers) for a range of deadweights. With parallel to threshold studies, technical and operational developments for the compliance of new regulations were also discussed in detail.

As a conclusion of the committee meetings, in July 2011 (MEPC 62<sup>nd</sup> session) a new chapter to MARPOL Annex VI (Chapter 4) was adopted and scheduled to enter into force on 1 January 2013, which calls for all new ships of 400 gt and above to be

certified with an International Energy Efficiency Certificate and have an “Attained EEDI”. Attained EEDI can be calculated from the formula based on environmental impact / benefit (transport) principle. (Ships which have diesel-electric propulsion, turbine propulsion or hybrid propulsion systems are exempt until such time as the method of calculation of attained EEDI for these categories of ships is established. Also, specialized dry cargo ships (e.g., barge or heavy lift ships) are exempted at this time.) According to new chapter in Annex VI, an attained EEDI value does not exceed a maximum allowable “Required EEDI” which is set by reference lines. Ships which undergo major conversions are also subject to the EEDI requirement, to varying degrees. All ships are required to be provided with a Ship Energy Efficiency Management Plan (SEEMP) containing procedures to improve the energy efficiency of a ship's operation. The allowable EEDI (required) values will be reduced in three 10 percent increments for new ships built over a period of 12 years. That means the allowable EEDI for a ship contracted for construction on or after 1 January 2025 will be 30 percent lower than for the same ship had it been contracted for construction on 1 January 2013. Assuming entry into force in 2013, with the implementation of the EEDI for all new ships, it is expected that between 45 and 50 million tonnes of CO<sub>2</sub> will be removed from the atmosphere annually by 2020, compared with “business as usual” and depending on the growth in world trade. For 2030, it is calculated that, the reduction will be between 180 and 240 million tonnes of CO<sub>2</sub> annually just from the introduction of the EEDI (IMO, 2011).

Since the EEDI formula takes into consideration special design features and needs, including the use of energy recovery, the use of low-carbon fuels, performance of ships in waves and so, the value will only be changed if the design is altered. Therefore it is obvious that this new regulation will be a great challenge for ship designers to comply with their new designs.

With the ship owners' point of view, the ship owner will be stressed by three factors. At first, by regulations on GHG emission reductions. Secondly, by the fuel cost which is now accounted for up to 50% of a ship operating costs in some sectors and trades due to the fast increase in oil price. Finally by a number of mechanisms such as MBI's (Market Based Instruments) based on Emission Trading Schemes (a carbon tax system). So a ship owner who achieves a better use of fuel consumption will be more competitive on his trade.

Due to reasons given above, shipping industry is now emerging to find out feasible solutions in order to gather more efficient ships which means lower GHG emissions, lower fuel costs as well as lower taxes in the future. Roughly, more energy efficient ships (in terms of cost and emissions) can be obtained in two ways, by minimising the potential energy losses (improving energy efficiency) or by utilising alternative energy sources which can supply additional energy such as solar or wind power, rather than fuel.

Regarding the use of wind power on ships, there are various ways such as traditional sails, fletner-type rotors and solid wing sails which require rigging in order to fix the system on the ship. This necessity is coming up with a negative impact on cargo handling. As an alternative, kites are found to be the most feasible solution having a small footprint during installation and retrofit. Applications of this concept can be seen on some merchant ships. Even, up to 30% fuel consumption (2 tons of fuel a day) was reported by Ship&Offshore (2011) in the trials., drawbacks with the kite systems including the complex launch, recovery and control systems that are needed, prevents the concept to be a primary means of alternative energy. (Above all, the renewable energy sources like wind and sun is not always available)

Speed reduction seems to be the easiest way through the aim of energy efficiency hence the reduction of emissions. That is why this option was discussed in detail during the regulatory meetings. The power consumption is commonly assumed to vary with the cube of the speed, reducing the cruising speed of a ship reduces its power demand. (This relation is based on the frictional resistance of a ship in calm water.) However, a special attention has to be paid when calling for speed reduction generally named as “slow steaming”. Considerations should include the aspects like safety, fleet size, finances and how the market works: it was deeply discussed that, if ship speeds are reduced, and in turn the installed power gets lower, at some point attention must be paid to guaranteeing the safe manoeuvrability of ships in adverse conditions. (Number of papers has been submitted by IACS concerning this subject) If ships were to go much slower on a large scale, this would necessitate a larger fleet to serve the market, incurring investment costs and increasing the upstream share of life cycle emissions. Long cargo delivery times are associated with the cost of capital (in form of the cargo) being tied up. Furthermore, a number of different types of actors involved means that bringing about a change in the currently typical range of

speeds is complicated (Traut et al., 2011). As a conclusion, slow steaming alone, can not be an option to reduce the power demand hence the energy losses reduction. But a simultaneous application of this method with other technologies reviewed below can be an effective combination.

In order to improve the energy efficiency of a ship, energy losses on board ship have to be minimised. For better understanding of the components of ship board energy losses, an example given in Buhaug et al., 2009 was visited and summarised as shown in Figure A.1. In this example a small well maintained cargo ship moving at about 15 knots in Beaufort 6 head weather condition was taken as a case study and breakdown of the total fuel energy usage was figured out. The bottom bar in this figure represents the energy input to the main engine from the fuel. In this case, 43% of the fuel energy is converted into shaft power while the remaining energy is lost in the exhaust or as heat losses. Due to further losses in the propeller and transmission, only 28% of the energy from the fuel that is fed to the main engine generates propulsion thrust in this example. The rest of the energy ends up as heat, as exhaust, and as transmission and propeller losses. The majority of these remaining 28% (as about 16%) are spent overcoming hull friction, while the remaining energy is spent in overcoming weather resistance and air resistance, as residual losses and for generating waves (about 5%). Additional to this is the fuel energy for operation of auxiliary engines. Ships other than the case shown will have the same types of losses; however, the relative sizes will differ.

It is surprising that only a fraction of the fuel energy going into the ship's main engines actually ends up generating propulsion thrust. Therefore engine manufacturers have continuously made an effort to optimize their engines specific fuel oil consumption, e.g., through the implementation of concepts such as variable valve timing, pulsed injection, new material metallurgies resulting in higher thermal efficiencies. However, despite the extraordinary engine technology advances more than 50% of the ship energy input is wasted so approximately 50% of the energy input is available, but only a percentage of it, the one with high quality is recovered today for auxiliary ship services, or by using "power take in systems" may be recovered a maximum of 10% that may be used for propulsion purposes.

As a naval architectural point of view, the most interesting component given in the diagram is ofcourse the propulsion of the hull rather than engine related

components. Obviously, energy losses from hull friction (viscous drag) and the wave generation are dominating components. Also reduction of energy losses regarding ships hull is a focal point of interest originated more than a century ago. Majority of the researchers and naval architects have involved in the topic of wave generation losses. Therefore there were many extensive research performed on the optimisation of hull forms by streamlining the shape of the hull in order to reduce radiated waves and avoiding flow separation and in this way omitting the associated losses. As a conclusion, many numerical tools regarding wave resistance reduction such as potential flow as well as RANSE based codes have been developed, by this way perfect hull forms in terms of wave resistance had been created. However this potential is reaching its limits resulting in viscous component to become the focal point of interest.

A number of techniques to reduce the viscous resistance have been proposed by boundary layer modification with the utilisation of both active and passive methods. Patterned surfaces such as riblets, shark fins and dimplets as well as state of the art anti fouling coatings can be given as an example to passive methods. Polymer injection and air lubrication methods are promising applications that can be given as an example to active methods. Both methods have received some accelerated interest specially for past five years due to its potential on viscous resistance reduction.

Globally, several projects were started up to investigate the subject in detail. As an example EU/national funded projects were completed with success such as PELS, aimed to study the capabilities on theoretical and numerical grounds and by extensive model tests, PELS 2; focused on air cavity method and SMOOTH aimed to investigate the effect of air lubrication and state of the art coatings on resistance and propulsion, seakeeping and maneuverability using both model scale and full scale experiments. A good example of currently started project can be given like TARGETS, aims to provide substantial improvements to ship energy efficiency by adopting a holistic approach to energy generation, transmission and utilisation with a focus on life-cycle issues. (both active and passive methods of BL modification will be investigated)

Experiments on hull friction resistance reduction has shown that, air lubrication is one of the most profitable technique in boundary layer modification hence the frictional drag reduction. The underlying principle of air lubrication is to separate the

surface of the hull from the water flow around the hull with a layer of air. Reduced wetted surface area is leading considerable amount of reduction in skin friction. Micro bubbles, air film or air cavity concepts are widely utilised techniques in order to achieve an effective lubrication. However, the utilisation of these techniques effectively requires the key parameters of the concept to be carefully optimised. Otherwise the practical problems in larger scales prevent to achieve expected frictional resistance, sometimes with the adverse effect, resistance increase in some cases is experienced. That is why there are several examples of unsuccessful application to larger scale, due to this challenge. This challenge has stimulated the author's interest on the air lubrication concept. Throughout this study, air lubrication by injecting air from an orifice to the cross water flow was investigated with the help of experiments and computer simulations.

The main objectives of the work presented in this thesis are:

- 1) To conduct a review of the state of art resistance reduction methods, particularly air lubrication.
- 2) To improve the understanding of the effects of air injection on boundary layer modification.
- 3) To obtain experimental data for boundary layer modification by air injection through a single hole to cross-waterflow.
- 4) To improve a method of obtaining void fraction profiles as well as a method of decomposition of the water phase velocity data from the air-water mixture.

The remainder of this work is divided into four chapters. Chapter II presents a general review of air lubrication concept, Chapter III is presented with experiments performed on model scale tests in ITU towing tank basin. Chapter IV presents the flat plate experiments on boundary layer modification by utilising air jet, injected through a single hole to cross water flow, within this chapter a method of single phase velocity decomposition by processed signals from CTA data is also discussed. The dissertation then concludes with Chapter V that provides a summary of the conclusions drawn from the entire work.



## **2. GENERAL REVIEW OF VISCOUS DRAG REDUCTION BY BOUNDARY LAYER MODIFICATION**

### **2.1 Introduction**

Resistance reduction of ships is a focal point of interest that was originated more than a century ago. Ship's hull resistance decomposition can be generalized as viscous and wave making resistance components. Majority of the researchers and naval architects have involved in the topic of wave resistance. Therefore there were many extensive research performed on the optimization of hull forms by streamlining the shape of the hull in order to reduce radiated waves and avoiding flow separation and in this way omitting the associated losses. Consequently, many experiments on the subject had been conducted which lead to the development of numerical tools regarding wave resistance reduction, by this way number of perfect hull forms in terms of wave resistance had been created, however this potential is reaching its limits. Furthermore increase in oil price and upcoming regulatory issues have forced the maritime industry to revisit the use of additional resistance reduction techniques focused particularly on viscous component.

Since the viscous drag is the dominating component especially for conventional displacement ships (ships that have relatively low Froude number), reduction in that component leads to a substantial decrease in total reduction, hence results in lower fuel consumption as well as lower GHG emissions. Viscous drag reduction can be achieved via modification of boundary layer by means of passive or active techniques. Over the decades, both techniques were investigated in detail.

This chapter gives a general review on boundary layer modification techniques that have potential on frictional drag reduction of ships. Since the scope of the thesis is on the air lubrication method, which is an active type of modification, further details on air lubrication such as mechanisms, pros and cons of the techniques were also discussed while review of others (passive methods) were given just for brief information intended to gain better understanding of the whole picture.

## 2.2 Active Methods

### 2.2.1 Bubble Induced Drag Reduction

Bubble-modified boundary layer and associated skin friction reduction have been an active area of research for hydrodynamics (i.e. ship hull drag reduction) in recent years due to its energy saving potential. The drag reduction in a turbulent boundary layer can be realized by reducing the skin friction under suitable conditions when small gas bubbles are injected into the flow from an upstream position. Bubbles are generally introduced into the boundary layer by injection through a porous surface or by electrolysis. The injection of gas into a liquid turbulent boundary layer to form bubbles reduces skin friction drag locally by up to 80 % (Merkle and Deutsch, 1992 and Truong, 2001).

The concept of the microbubble-modified boundary layer came into existence in its present form from the pioneering experimental work conducted by (McCormick and Bhattacharyya, 1973). They used a copper wire wound around a fully submerged axisymmetric body. With varying electrical current given to the wire, different rates of hydrogen bubbles on micro scale were created by electrolysis. The drag force acting on the body 0.91m in length was measured and the net drag reduction approaching 40% at Reynolds numbers ranging between 0.3 and 1.8 million was reported. It was realised that, hydrogen bubbles were playing an important role particularly at lower Reynolds number and drag reduction was increased by increasing electrical current hence, gas generation rate.

A few years later, three experimental studies were reported in a series of articles from the Soviet Union. An experiment of Migirenko and Evseev (1974) and Dubnischev et. al. (1975) was conducted in a fully developed pipe flow facility of rectangular cross-section. Another experiment of Bogdevich and Evseev (1976) was conducted on a flat plate in a water tunnel like the one performed by Bogdevich and Malyuga (1976) (the lower wall of a rectangular water tunnel was used for microbubble injection). In these experiments, microbubbles were supplied from a porous media and zero pressure gradient turbulent boundary layer was observed. The series of experimental data include local skin friction measurements from floating element balances and surface mounted hot film probes and near wall velocity profiles. Additionally surface pressure fluctuations as well as concentration

profiles measured by capacitance probes were also reported. The local skin friction measurements showed reductions as high as 80%. Another important finding of Bogdevich & Evseev (1976) was, drag reduction decreases with increased distance from the injection location until the original drag levels are achieved which can be named later as “poor air layer persistence”. It is worth noting here that all three experimental works were reported for the condition in which the boundary layer is above the plate. Results presented later show that the buoyancy forces play an important role on the efficiency of the micro bubble BL modification especially at lower speeds.

Following to the Soviet Union experiments, as the method seemed to be a promising one a number of questions raised regarding the crucial parameters acting on the air induced BL modification such as;

What should be the best air flow rate needed to obtain a required level of skin friction reduction?

Is the type of gas injected to BL, an important factor?

What is the effect of injector geometry?

Is bubble size supplied to BL an important factor?

What about the role of surface roughness as well as surface tension?

How can the air lubricated downstream distance be maximized?

Which condition is better in terms of effective skin friction reduction? BL at top, BL at bottom or at side?

Merkle & Deutsch (1992) and Zalek et al. (2004) provide an elaborated review on questions listed above. However, even today some of these questions are still in discussions and still not yet clearly understood. That is the reason why today, a considerable amount of experiments in both model and full scale are conducted to find out the right recipe of optimum air lubrication mechanism.

After the questions were raised in the Soviet Union, an extensive research on the subject was launched by Pennsylvania State University in the United States. There are three remarkable studies in open literature. Firstly, Madavan (1984) used the tunnel wall boundary layer in the rectangular test section. In the second one, in order to investigate effect of pressure gradient Deutsch and Castano (1986) tried an

axisymmetric body mounted in the circular test section, and final study was by Pal et al. (1988) who had performed experiments on flat plate mounted on circular test section. For all of three experiments, drag reduction on small flat plate turbulent boundary layer were measured. (The length of plates were on the order of one meter) Following to those studies, findings of experiments were supported with articles by Madavan et al. (1985a), Clark and Deutsch (1991), Fontaine and Deutsch (1992), Merkle and Deutsch (1992) and Deutsch et al. (2003). Findings reported can be summarized as: the type of gas has minimal impact on bubble induced reduction, according to experiments with varying pore sizes ranging from 0.5 to 100  $\mu\text{m}$ , injector pore size does not affect the drag reduction, bubble size is most sensitive to free-stream velocity and gas injection rates, buoyancy forces affect the performance of bubble induced reduction, it was found that: plate on top performed better than plate on bottom orientation which was also agreed later by Kato et al. (1994) and finally Clark and Deutsch (1991) reported that: a weak favorable pressure gradient significantly reduces the efficiency of bubble induced drag reduction, whereas a weak adverse pressure gradient leads, separation and large reductions in the skin friction drag at low gas injection rates. Later, about the effect of pressure gradients, similar results have been agreed by (Kawakita and Takano, 2000).

An extensive research was started in Japan by the end of 90's Guin et al. (1996), Kato et al. (1998) and Moriguchi and Kato (2002) has examined the subject deeply by injecting bubbles to the top and bottom flow boundaries of a turbulent boundary layer formed by a channel flow. Length Reynolds numbers around  $10^6$  was examined. Findings of Guin et al. (1996) and Kato et al. (1998) were similar to those of Madavan et al. (1984, 1985a) in terms of frictional drag reduction.

Local skin friction measurements of the above mentioned experiments were shown that the bubble induced drag reduction effect decreases with the increasing streamwise distance to air injection point (Downstream). This reality leads an improper scaling up estimates for full scale practical applications. Therefore, a series of experiments have been performed by a group of Japanese researchers at larger scales (12 to 50 m in length) in a 400 m long towing basin. The streamwise distribution of local skin friction was measured by Watanabe et al. (1998) and by Kodama et al. (1999a). Watanabe et al. tested two plate models (20m and 40m long) with 0.6m wide and 0.2m deep at the speed of 7m/sec, whereas Kodama et al. tested a

little longer (50m long) and wider (1m wide) model at 5m/sec. The test models were very slender and the air was injected over the center 50% of the plate span. It should be noted that there was no skeg or a similar arrangement to keep the air underneath the models, so air may have escaped from the sides of the vessel. Kodama et al., (2002) reports that drag reduction measurements made in the span-wise direction showed poor uniformity, decreasing from a maximum at the model centerline to nearly zero at the outer edges. Fortunately, in spite of the problem overall skin-friction reduction about 20% has been reported on the 50 m long model, though drag reduction decreased along the model until only a few percent was observed at its end. Similarly, the reports of the experiments by Takahashi et al. (2001, 2003) with 50-m-long flat bottom of a towed model was reported the maximum total drag reduction of 13%. The experiments were conducted with achieved maximum speed of 7m/s which corresponds the length Reynolds number of  $Re_L=10^8$ . The resulting reduction in friction was addressed to a significant drag reduction under the hull.

Those results were motivated the group for the application of the concept to a full scale vessel which was a significant step towards a practical application of air bubble injection. The group has selected a training ship with a length of 116 meters. (Seiun-Maru) Air was injected near the bow of a ship through horizontal arrays of holes at flow-rates, up to 43 m<sup>3</sup>/sec. The first sea trial was reported by Kodama et al. (2000) and there was no net power savings achieved. It was believed that skin friction reduction hence the power saving was achieved by utilizing the lubrication, however air entrainment into the propeller caused the lack of net power saving. Further experiments on full scale models were reported by (Kato and Kodama, 2003), (Kodama et al., 2002), (Nagamatsu et al., 2002) and (Kodama et al., 2006). The common conclusion was agreed that only few percent of power saving were achieved by injecting air beneath the hull. It is worth noting here that there are some full scale trials which reported no appreciable effects of air bubble lubrication (Foeth et al., 2009) and there are some others referring energy loss (when considering the power consumed by air supply systems) rather than saving (Foeth et al., 2010).

Obvious discrepancies between model scale and full scale experiments have directed the researchers to investigate the subject deeply, in order to understand the mechanisms governing the bubble modified boundary layers. Due to the practical difficulties encountered during sea trials (such as sea conditions, surface curvature

and roughness parameters low repeatability of trials etc.) there was not enough information gathered to understand the physics of the subject. That is why a group of researchers from the University of Michigan has started high-Reynolds number testing with specially designed 12.9 meters test model “HIPLATE” which was intended to bridge the gap between the small scale laboratory experiments and the full scale ship studies (Details of the setup is given in Sanders et al. 2002). Sanders et al. (2006) conducted the first experiments, in which the drag reduction was measured directly on near-zero pressure-gradient turbulent boundary layer. The free-stream speed was ranging between 6 m/s to 20 m/s, yielding Reynolds numbers over  $10^8$  based on downstream distance. It was concluded that, peak levels of local friction drag reduction of 80% were achieved near the injector where local void fraction was ranging between 0 to 0.4. Those levels of void fraction were only present within the first couple meters of injection and that negligible drag reduction persisted downstream except for a few conditions such as low speed and higher injection rates. Within the same study, a scaling relationship was proposed for smooth plates but it was noted that the poor downstream persistence of the bubble induced drag reduction prevents the concept to be implemented in real world applications. Therefore, further investigation by Winkel (2007) and Elbing et al. (2008) were performed on the same model aiming to understand the governing mechanisms of downstream persistence. Although additional insights were produced; significant improvements to downstream persistence have not been achieved.

Experiments as well as numerical studies on bubble induced drag reduction spanning a wide range of scales and flow conditions have been conducted. However, the underlying physical mechanisms of bubble induced drag reduction remain unclear due to the fact that the concept continues to be an active topic of study. It is well understood that several processes are at work simultaneously. A common agreed principle is; the level of drag reduction is strongly dependent on the near-wall void fraction (Elbing et al., 2008, Guin et al., 1996, Madavan et al., 1985a, Sanders et al., 2006). The governing mechanism of bubble induced drag reduction can be discussed under those aspects generally:

Injection of lower density fluid such as air modifies the average density hence the viscosity of the water-air mixture. Legner (1984) performed the first theoretical study based on a simple mixing length model used for the turbulence and concluded that

combination of density reduction and turbulence modification were the reasons for drag reduction. Marie (1987) has conducted additional work proposing viscous sublayer was increased by the existence of the microbubbles. In both study, drag reduction mechanism were simply explained by reference to such aspects as the reduction in density of the mixture and modification of the effective viscosity inside the boundary layer. Madavan et al. (1985b) presented a similar result by calculating the skin friction reduction assuming that Einstein's formula on the viscosity of a mixture was valid in the case of water with microbubbles. All analyses demonstrate how the presence of finite void fraction near the wall can lead to a thickening of the sublayer and reduced friction drag, concluding that the bubbles are most effective when they are located in the buffer layer of the turbulent boundary layer. It is worth noting here that significant portion of turbulent transport process which is important for the production of friction drag take place within a few tens of wall units of the surface (Pope, 2000). Kunz et al. (2007) employ an Eulerian multiphase calculation for bubble induced drag reduction that captures the evolution of the near-wall bubble populations that are coupled to the development and loss of drag reduction ( Ceccio, 2010).

Modification of turbulence structure by interaction of bubbles with the flow: The reduction in bulk density would result in decreased Reynolds shear stresses,  $-\overline{\rho u'v'}$  in the near-wall region. If the drag reduction is the product of a reduction in bulk density then the drag reduction should scale with the near-wall void fraction. Lumley (1973, 1977) hypothesized that bubbles locally increased viscosity and turbulent fluctuation levels and increased the thickness of the sub-layer and buffer region. This theory has been supported by the work of Pal et al. (1989) which observed that not only did mean skin-friction levels decrease, fluctuations in skin-friction were suppressed as well in both polymer and gas injection flow. Madavan et al. (1985a) reported a reduced high-frequency component of flush mounted hot film signals. In contrast to proposed reduction in turbulence levels, experiment of Nagaya et al. (2001) utilizing PIV, concluded with an increase in turbulent fluctuations with gas injection. Although increases in both  $u'$  and  $v'$  fluctuation components were observed during drag reduction, decoupling of fluctuations were resulted in decreased Reynolds shear stresses. Bubble flow interactions were also investigated through numerical computations of multiphase flow. Utilizing DNS, Druzhini and Elghobashi

(1998) showed that turbulent fluctuations were reduced during bubble migration to the vortex cores in a turbulent shear flow. Eulerian-Lagrangian models were employed by Xu et al. (2002) and Ferrante & Elghobashi (2004, 2005) in which, detailed interactions between bubbles and turbulent flow in the near-wall region were simulated with bubble sizes on the order of viscous wall unit and  $We \ll 1$ . It was realised that even at relatively small void fractions, bubbles or bubble clusters can modify near-wall streamwise vortices yielding amount of reduction in friction drag. Further investigation (DNS) particularly for larger ( $dB/lv \sim 50$ ) and deformable bubbles ( $We \sim 0.5$ ) was performed by Lu et al. (2005). It was found that larger bubbles can also interact with streamwise vortices provided that they are present in the buffer region. Particularly for flows at relatively low Reynolds number and void fractions, experimental evidence for such drag-reducing bubble-flow interactions has been reported by Murai et al. (2006) and Gutierrez-Torres et al. (2008). Other investigations on drag reducing bubble-vortex interactions were performed by Murai et al. (2008) and Sugiyama et al. (2008) show that at low Reynolds number flows, coherent vortices can be damped by the buoyant motions of microbubbles. However, with the increasing Reynolds and Weber number, the coherence of the vortical flow is reduced and the effect of the bubbles on the friction drag becomes smaller. In this case other mechanisms such as bubble splitting, deformation, and compressibility are governing.

Dynamics and interactions of the bubbles lead to changes in the flow: Meng & Uhlman (1998) proposed that “bubble-splitting” could be responsible for the observed reduction in drag by arguing that energy is extracted as larger bubbles split into two or more smaller bubbles. More small bubbles yield larger surface area hence higher surface energy. (The surface area,  $A_s$ , increases resulting in a higher "surface energy",  $a.A_s$ , where  $a$  is the surface tension.) They suggested that energy required for bubble splitting could serve as a significant energy sink for turbulence.

The bubbles introduce compressibility to the flow (Lo et al., 2006)

A major issue that has persisted in the study of bubble induced drag reduction is the influence of bubble size. Although there are many experimental investigations on the subject, the issue is still in discussion today. Experiment of Moriguchi and Kato (2002) was conducted in two dimensional channel which has different water inlets. The diameters of the bubbles were modified by channel speed. By changing the



water inlets three flow velocities were tested. A high speed camera with image processing software was utilized in order to measure the mean void fraction. It was reported that frictional resistance reduction increased with the increasing mean void fraction and there was no effect of microbubble diameter. Experiment of Takahashi, et al. (2001) on a towed body was concluded similarly. Surfactants were employed in order to reduce the bubble sizes and no apparent difference was detected. Another comparison of the effect of bubbles on drag reduction was performed by Winkel, et al. (2004). They used saltwater rather than fresh water in the experiments and they observed that saltwater is capable of reducing bubble diameters by approximately a factor of four. If bubble size does play a role in BDR, experimental results obtained in freshwater may not directly apply to sea-water applications. However, direct skin-friction measurements made by Shen, et al. (2006) with gas injection into both fresh and salt-water, produced no measurable difference in drag reduction (Winkel, 2007). Further research of Shen, et al. with very small lipid stabilized bubbles injected to the boundary layer was concluded with no measurable improvement in drag reduction for equivalent void fractions. Sanders et al. (2006) reported that the flow will reshape the injected air into bubbles due to interactions with the turbulent boundary layer when size of the bubbles compared to the viscous length is about in the order of  $10^2$  and  $We$  is around 1. This result was also in good agreement with the observed insensitivity of the bubble formation to the method of gas injection and the resulting drag reduction (Madavan et al., 1985a and Pal et al., 1988). In contrast with others, Kawamura et al. (2003) produced bubbles with two different methods. Firstly they have injected air through a slot and finally through a porous media so that an order of magnitude larger diameter bubbles were obtained. They concluded that the smaller bubbles are nearly twice as effective at reducing skin friction at equivalent void fractions. However, experiments were performed while the plate was located at the bottom of boundary layer so result of the increase in rise velocity of the larger bubbles, causing them to migrate from the plate surface much more quickly might be responsible for that. It is worth noting here that when the size of the bubbles appeared in above experiments were compared to the viscous length, the sizes of bubbles are apparently large. Furthermore, assuming that a basic mechanism of drag reduction is density reduction near the wall as well as bubble interactions with the near wall vortical flow, the drag reduction is directly proportional to near wall void fraction. Near wall void fraction is also directly oriented by liquid entrainment,

buoyancy as well as turbulent mixing as going downstream of the air supply. At high shear rates where the viscous length is about in the order of  $10^2$  and  $We$  is around 1, bubble lift forces are sufficient to overcome buoyancy and move bubbles away from the wall a distance on the order of the bubble diameter concluding with lower void fraction near the wall. In these cases bubble induced drag reduction reduces significantly (Ceccio, 2010).

### **2.2.2 Air Film**

When a continuous air flow with sufficient volume flux is supplied to the bottom of a horizontal flat flow field, a low viscous stable film between solid boundary and liquid flow (i.e. water) may be formed. Obtained “air film” can lead to a favorable skin friction drag reductions up to 80% in case of a proper film formation. During the experiments intended to investigate bubble induced drag reductions, air film formations have been also observed and reported without naming it as air film formation. Bubbles injected into the turbulent boundary layer can coalesce to form larger bubbles with size on the order of  $\delta$ . Such large, no spherical bubbles persist when the Weber number of the flow is low, usually because of slow free-stream speeds (Ceccio, 2010). Fortunately, these bubbles can also reduce drag like given in (Murai et al., 2007) Reed (1994) and Fukuda et al. (2000) discussed the use of special arrangements such as special coatings etc. to enhance the formation of larger bubbles. However, it was experienced that even at higher speeds, smaller bubbles can coalesce beneath the flow surface given a sufficiently high gas flux (Ceccio, 2010).

Madavan et al. (1985a), Kodama et al. (2002) and Shimoyama et al. (2002) have tried to establish an air film along a flat plate test model at a free-stream speed around 10 m/s. According to the reports no stable air film was established (Air injection rates were not given in the reports). They could observe an air film which was persisted for 20cm downstream only. The short length film were dispersed into air slugs and it was observed further downstream that the slugs were separated into bubbles. Similar observation was reported by Watanabe et al. (1998) and Kodama et al. (1999b). Insel et al. (2009) focused on the effect of silicon based water repellent paints on the formation of air films. The concept was applied by injecting air through a porous media located at the flat of the bottom of a Tanker model with special coating. That was reported that no favorable effect of the state of the art paint system on air film formation was reported.

Air film concept have been discussed by researchers from University of Michigan with the name of “air layer”. Sanders et al. (2006) observed at low flow speeds and high injection rates drag reduction in more than 80% over the entire model length. This improved performance was attributed to the formation of an air layer on the model surface, but the air layer could only be achieved for a limited number of conditions and further investigation was not possible since it was not the focus of that study. Winkel (2007) and Elbing (2007) conducted specific experiments focused on air layer drag reduction. They reported air layer drag reduction at speeds up to 15.3 m/s on a 12.9 m long “HIPLATE” test model with injection over nearly 90% of the model width, and air trapped below the model by the tunnel walls. Much explanatory results were reported by Elbing et al. (2008) which concludes with three distinct regions categorized in terms of drag reduction. According to this categorization:

Region I was named as “bubble drag reduction zone”. In this region drag reduction has a tendency of linear increase with air flow flux injected into boundary layer. Region II was named as “transition zone” where drag reduction increases linearly but more accelerated which means a much steeper slope than in region I was encountered in the air injection rate versus drag reduction plot. Finally, in region III; increasing injection rate leads little or no improvement in drag reduction but around 90% drag reduction is achieved by the formation of thin stable air film. Figures explaining further details on the concept was taken from (Elbing et al., 2008).Figure 2.1 : Upper sub-figure 2.1 shows the level of local drag reduction at a measurement location 6m downstream of the injector for varying air injection rates while the lower sub-figure 2.1 shows the effect of free stream velocity  $U$  on transitional and critical air fluxes.

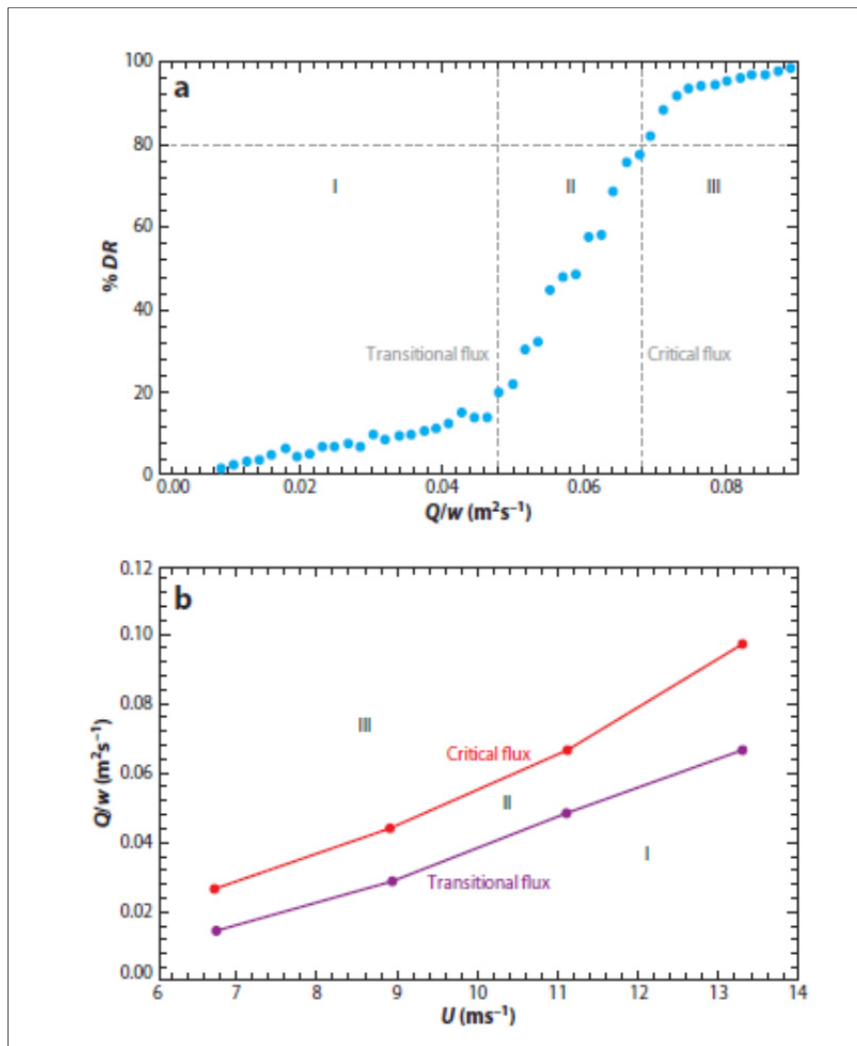


**Figure 2.1** : Transition from bubble drag reduction to air-layer drag reduction (Elbing et al. 2008)

It is worth noting here that in order to obtain a stable air film which yields drag reduction, more air feed is required than other methods i.e. microbubbles. It is also obvious that, implementation of the method in real time applications requires not only drag reduction but also net power reduction which means amount of energy consumed for the air film formation i.e. pumping requirements etc. should be smaller than the amount of energy saved. A study which was called as “Cost – Benefit Analysis” was performed by (Ceccio, 2010). Energy costs associated with the injection of the air compared to the propulsive energy that would be saved by the resulting reduction in friction drag were considered. The experimental results from (Elbing, 2009) were utilized to derive the polynomial relations between air injection rates and velocity of the body. Obtained equations were used to estimate required air injection rates in order to form air film for the velocities interested. On the other

hand power needed to move the fluid across the surface was derived utilizing frictional drag coefficient formula for smooth surfaces given by (White, 2006). Both smooth and rough surfaces were considered propulsive and pumping efficiencies were assumed. In the parametrical study speed ( $U$ ), draft ( $d$ ) and length ( $L$ ) was taken into consideration and those findings were suggested, air injection rate required to form air layers increases by  $U^2$ , while the propulsive power increases by  $U^3$  so after a certain speed the energy gain achieves a constant. For the draft consideration, the required pumping power will increase by  $d^2$ . Finally, the relative benefit will increase with increasing  $L$  assuming the effective air persistence through the overall length of the vessel. In spite of the picture positively drawn by the experimental data, with the light of experiences gained from the full scale trials (i.e. unsteadiness and three-dimensionality of a ship hull and air escapes from the sides) the practical applications would not be so promising.

### **2.2.3 Air Cavity**

Another effective method of air lubrication is air cavity. With comparison to other methods, air cavity has been frequently preferred on ships which have moderate to high Froude numbers due to its higher potential of resistance reduction.

Practically, unlike in air cushion vehicles such as surface effect ships, no flexible skirts are required for retaining air under the hull, and as air is not used for lifting up the ship; a power requirement for the air injection on air cavity concept is an order of magnitude smaller than that on SES. (Matveev et.al, 2009)

Theoretically, unlike in other methods of air lubrication, air cavity is not a method based on the control of multiphase boundary layer because water underneath the hull separates from the hull boundary. The method was established to create an air layer over the hull bottom by using an air cavity behind a sudden hull form discontinuity, i.e. a step. It is within our knowledge that a natural cavity can be established behind a bluff bodies or step at high speeds by use of vapors of the ambient liquid. Underlying principle of air cavity concept is: extension of the cavity zone by feeding air inside the cavity so that, wetted surface of the hull is reduced leading reduction of frictional drag. See Figure 2.2. Figure 2.1 :

The concept has more real world applications than other air lubrication methods. This technique was adapted in flying boats (Bell, 1935). Examples of applications to

full scale vessels followed in 1990's Russia with 30 knot 70 passenger river ferry Linda, 30 knot 105 displacement ton tank landing ship Serna (Ivanov and Kaluzhny, 1996), 38 knot 13 displacement ton patrol boat Sajgak and 50 knot 99 displacement ton Merkurj (Sverchkov, 2005). Up to 35% and 30% resistance reduction were reported for planning and semi-planning hull forms respectively. The penalty of approximately 3% of the main engine power for air supply was indicated. Numerous variations have been suggested in a number of patents such as (Chaban et al., 1993), (Burg, 1993) and (Harley, 1996).

Although the concept is not ideal for lower speed ships, applications of the concept to ships with low Froude number can be seen on several examples like a 5000 ton river ship Volgodon moving at 11 knots reported by Basin et al. (1969) with achievement of reported total drag reduction up to 15%. The river ship described by Foeth (2008) can be shown for another example.

Initial studies of air cavity have shown that the cavity length could not be extended to the whole craft length for low speeds (Partial cavity rather than supercavity). Suggestions were made to utilize a series of steps to extend the partial cavities (Butuzov et al., 1999). Fortunately, with a careful selection of key parameters, cavity length can cover the whole bottom with one step at high speeds.

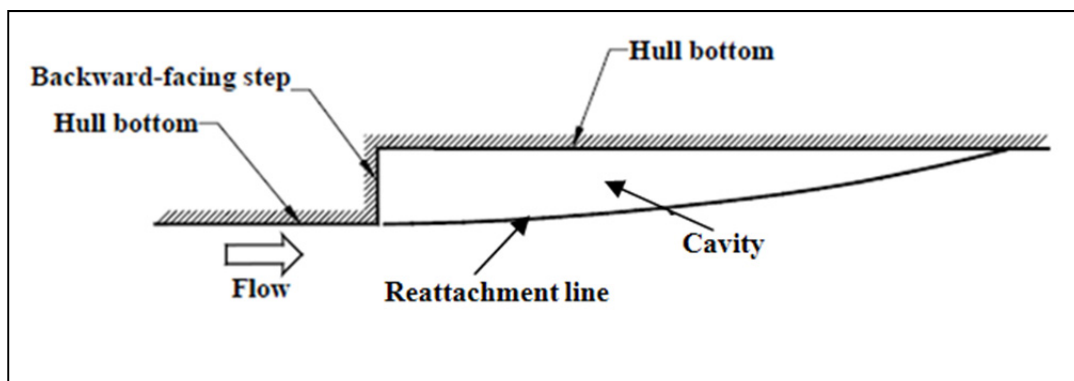


**Figure 2.2 :** Cavity formation on downstream of backward facing step.

### 2.2.3.1 Experiments on air cavity

In order to understand the cavity mechanisms as well as to optimise the above mentioned crucial parameters, various laboratory scale experiments were conducted with combination of numerical studies. A towing tank test of (Gokcay, 2001) and further investigation by Gokcay et al., (2004) offer a clear perspective about the concept. As a starting point, a basic hard chine planning hull form, proposed by

Savitsky and Brown (1976) was selected as a model. The model was built in two parts as the retrofitable parabolic bow form and the aft prismatic body. Two prismatic bodies were built; one of them had the cavity chamber at the bottom while the other one had conventional hard chine bottom without cavity which was used for baseline model. For reference tests, prismatic body without cavity chamber was mounted to bow and for following air cavity tests, the parabolic bow form was fitted to other prismatic body with cavity chamber. Air cavity tests were performed for three different air supply rates including no air injection case. Total resistance, sinkage, running trim as well as wave pattern resistance data were measured in order to extract the viscous component from total resistance. As a result of experiments, mainly two distinct types of flow were observed in the air cavity models in the range of 0.2 to 1.0 Fr.

- 1) At the low speeds, air follows the cavity channel and escapes from the transom stern.
- 2) As the craft is speeded up, air escape from the stern disappears, and air escape from the sides starts to occur (See Figure 2.3). The length of cavity section changes both with air injection rate and with the speed. Air escapes from the sides generates a larger air lubricated area.

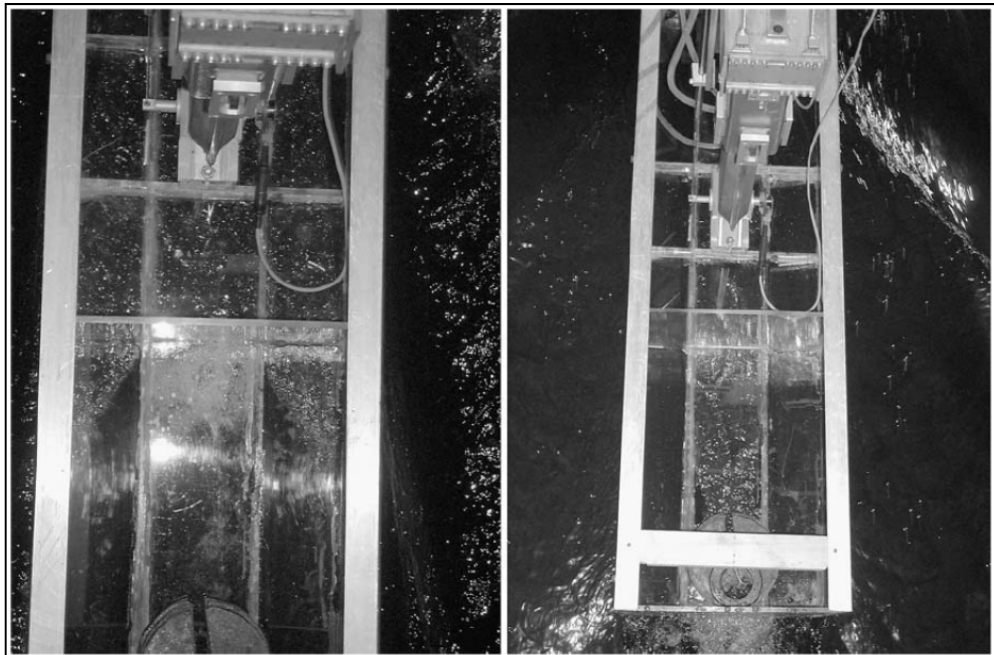


**Figure 2.3** : Escape of air from sidewalls and stern ramp (Gökçay et al., 2004).

Considerable resistance increase, between 2% and 10% was observed from baseline model to air cavity form (with no air supply) in the speed range of  $F_n$ : 0.3 to 0.8 probably due to discontinuity at the form. In contrast, when air was injected into cavity, total resistance decrease was about 10% and 20% up to Froude number 0.6 and 1.0 respectively. The effect of air supply rate on the resistance reduction was found to be small and air supply was required only to sustain the air inside the cavity and replenish the air losses.

Measurements of sinkage, trim and wave pattern resistance enabled the decomposition of total resistance. Accordingly three important findings were figured out regarding resistance decrease in air cavity:

- 1) Resistance decrease by wetted surface area reduction due to aerostatic lift,
- 2) Resistance decrease by wetted surface area reduction due to decreased frictional area in the air cavity,
- 3) Resistance decrease by wave pattern resistance reduction

It was concluded that pressure field around the hull bottom was positively induced by air film so that wave pattern resistance was decreased. However wave pattern resistance reduction was very small in comparison with viscous resistance reduction. Viscous resistance change was summarised in Figure 2.4. In the figure terms HC, AC0, AC1, AC2 correspond to baseline model, air cavity model with no air supply, AC model with air supply rate of  $9.7 \text{ m}^3/\text{h}$  and AC model with air supply rate of  $20.1 \text{ m}^3/\text{h}$  respectively). For further details about experiments, see (Gökçay et al., 2004)



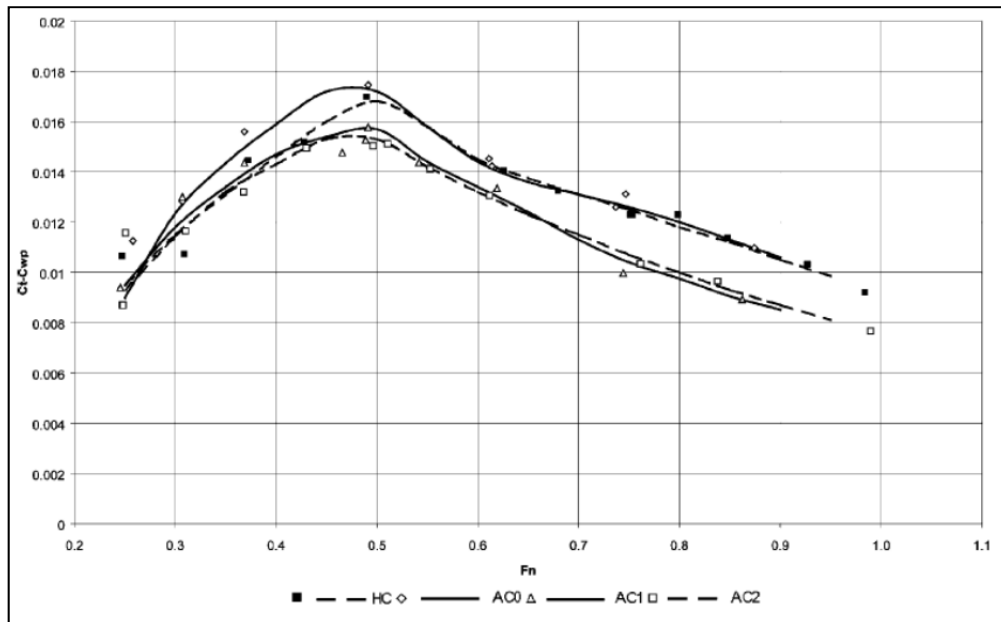


**Figure 2.4 :** Comparison of viscous resistance coefficient ( $C_t-C_{wp}$ ) for HC and AC forms. (Gökçay et al., 2004).

Similar experimental setup was established by Matveev et al. (2009) in an open-surface water channel. With parallel to experiments, computational work validated by experimental data was performed. Characteristics of the air cavity have been studied in a range of water flow velocities and model attitudes. The study pointed out different air cavity regimes particularly for cavity tail. General conclusions can be summarized as:

- The cavity length increases with the water flow velocity, and with increasing velocity the air cavity regime becomes two-dimensional form.
- Test results with different trim angles suggest an optimal trim position with the largest air cavity area.
- Significant scatter in the cavity size and pressure values were reported which is affecting the efficiency of the system and inducing strong sensitivity to design parameters. Detailed investigations of this sensitivity, unsteadiness, air escape and other measurements were suggested for future experimental research.

Another experimental effort was given by Lay et al. (2010) using “HIPLATE” model originally established for microbubble research. The study was launched in order to fill a gap of a systematic investigation of the concept for high Reynolds numbers. Initial design parameters for cavity were accomplished using numerical computation. Linear gravity wave theory and Matveev’s (2003) potential flow solution were used

for the computation. Determined cavity characteristics were also validated by two-dimensional inviscid numerical model. Local measurements such as local friction drag, air flow rates, and cavity pressure were measured over a range of air fluxes and speeds. Findings from the experiments have shown that, simple linear wave theory is useful in obtaining an approximate operating speed range for a particular cavity length, but it is not indicative of the speed sensitivity of the cavity. Stable air cavities were produced, leading more than 95% skin drag reduction over the extent of the cavity, including the cavity closure. Finally, cavities were shown to be stable with respect to large changes in air flux and slow perturbations in tunnel speed and pressure (Lay et al., 2010).

It is worth noting here that majority of the work cited here are outcomes of the experiments conducted in ideal conditions. i.e. calm water conditions. However, it is within our knowledge that air lubrication concept, particularly air cavity, is very sensitive to ship motions. For instance, few degrees of roll due to turning maneuver or due to beam sea causes air escapes beneath the hull yielding dramatical reductions on cavity efficiency. Ivanov and Kaluzhny (1996) has reported 10% speed decrease of SERNA in sea state 3 which means that its 30% power saving in calm sea completely disappeared in sea state 3 (Amromin et al., 2011). Therefore special attention have to be paid during the design stage of such ships. Experiments with a model of 4000 ton ship conducted by Amromin et al. (2011) have shown that: with a special consideration of bottom hull cavity in terms of seakeeping aspects, it is possible to keep the major part of drag reduction by air cavity (at least in sea state 5 for a 90 meter length ship). Within the scope of the work mentioned, numerical tools based on ideal fluid theory for this consideration were also prepared. The work is also a good example of the application of the concept to moderate Froude number range ( $0.35 < Fr < 0.7$ ) and it was stated that up to 25% drag reductions achieved with just 4% penalty paid for air supply energy.

### **2.2.3.2 Numerical computations on air cavity**

As indicated above, there are many promising applications of this concept to ships. On the other hand; it is obvious that designing an effective air cavity ship is a serious challenge. Parameters such as cavity step height, width, stern ramp length and height have great importance. Utilizing trial error methods to find out the optimized geometry is obviously expensive. With the help of modern computing opportunities ,

state of the art numerical codes now enable researchers to perform parametric studies which is essential for optimization. Due to the fact that, with the accelerated development on computing power from the beginning of 2000's, reliable tools such as numerical codes on cavity or CFD (Computational Fluid Dynamics) have been an active area of research.

Due to air cavity concept is based on the principles of cavity, previously developed cavity flow calculation methods have been applied to air cavity flows. Fortunately, it was found that some characteristics of the air cavity behavior has been captured by this way. Details of the cavity flow calculations with the applications to partial ventilated cavities are given by (Ceccio, 2010).

Initial computational efforts are generally focused on two dimensional air cavity profiles using potential flow codes. Callenaere et al. (2001) has investigated basic features of two dimensional cavities at high Froude number with re-entrant jet induced instabilities while a moderate Fr number application was performed by (Matveev, 2003). Bernoulli's theorem was applied at the cavity boundary streamline (Re-attachment line) and equations were written in terms of cavitation number (non-dimensional form). The cavity was simulated with distribution of sources. As a conclusion, the cavity problem was reduced to an integral differential equation. In order to solve the equations a numerical procedure proposed by Butuzov (1967) was utilized. The cavity curvature was approximated by second order polynoms by this way the shape of the cavity profiles were calculated.

Gokcay (2003) performed 2D computations by using computational fluid dynamics (CFD) software Fluent, which is a Reynolds Averaged Navier Stokes Equation based solver. Wedges located beneath the flat plate were simulated by this way parametric study was carried out by trying 3 kinds of wedge shape with different angles yielding various step heights. The flow is considered as two dimensional and fully turbulent (Two equation model was utilized). In order to model air as second phase Volume of Fluid (VOF) model was utilized hence multiphase model was activated. VOF is a surface-tracking technique applied to a fixed Eulerian mesh. It is designed for two or more immiscible fluids where the position of the interface between the fluids is of interest. With parallel to computational work, experimental setup was established in the circulating channel and flow visualization was carried out by utilizing particle tracking methods. Particularly changes in reattachment length was selected as a key

parameter and the length in each set was measured from video records. As a conclusion, measurements taken from the visualization were in a good agreement with findings from the computations.

Matveev et al. (2009) has developed three dimensional linearized potential-flow model, assuming the flow is irrotational, steady and uniform far upstream of modeled hull shape. Similar assumptions were made as in Matveev (2003) regarding the reattachment line and different cavity profiles were calculated within the speed range. Calculations were supported by two dimensional viscous model by using finite volume computer code Fluent. When calculated average length of the cavity compared with the test data, linear three dimensional potential flow model was in good agreement except for the cases where non-linear effects were minimal. As a low-cost approach, it was stated that the potential-flow model may be a convenient tool for preliminary design of air-cavity hulls. Regarding viscous modeling authors stated that macroscopic features of the cavity were predicted well however, unrealistically large air-water mixtures encountered.

Another model established by CFD can be seen in (Lay et al., 2010). Authors utilized two dimensional model assuming an inviscid, unsteady and incompressible flow. Again Fluent was utilized to setup and run the model. As a conclusion, cavity's optimum operational speed for experiment (details given in experimental reviews) was determined and it was indicated by the results that forming of a stable cavity would require significantly more air flux to establish the cavity than to maintain it. Results were in agreement with Matveev's (2003) solution.

Three dimensional computational fluid dynamics study on the air cavity performance of a high speed planning hull was performed by (Gokcay and Insel, 2011). They used the experimental data obtained from (Gokcay et al., 2004). The flow around the hull was considered as three dimensional and fully turbulent. Since the focal point of this study was on viscous part of the resistance, free surface was not taken into account. ANSYS Fluent 12.0 was employed for pre-processing, compiling and post processing. In order to discretize the flow domain, patch conforming method with around 3 millions unstructured tetrahedral elements was utilized. Thanks to pre-processor which enabled the reconstruction of the grid parametrically for each run in order to simulate the running trim and sinkage taken from experimental data. Uniform velocities ranging from 1.21 to 4.05m/s were given at the inlet boundary

which corresponds the same  $Fn$  range of experiments. To model air as second phase Volume of Fluid (VOF) model was utilized hence multiphase model was activated. Results of CFD calculations were pointed out, similar flow regimes occurring around the cavity of the hull. In the results of experiments it was stated that: at the low speeds, air follows the cavity channel and escapes from the transom stern and air escape from the stern disappears while air escape from the sides starts to occur as the craft is speeded up. In order to visualize the flow close to cavity region, velocity streamlines of injected air were figured out which was given in Figure 2.5. It can be easily seen that streamlines spread outside the cavity with the increase of speed while following straight lines at lower speeds and escape from the stern ramp as in experiments. The results from the simulations have shown that macroscopic features of the air cavity was well predicted including the tendency in drag reduction however, the frictional data comparison has given some discrepancies from the measurements probably due to the changes in hull sides wetted surface area effected by free surface waves which was not taken into account.

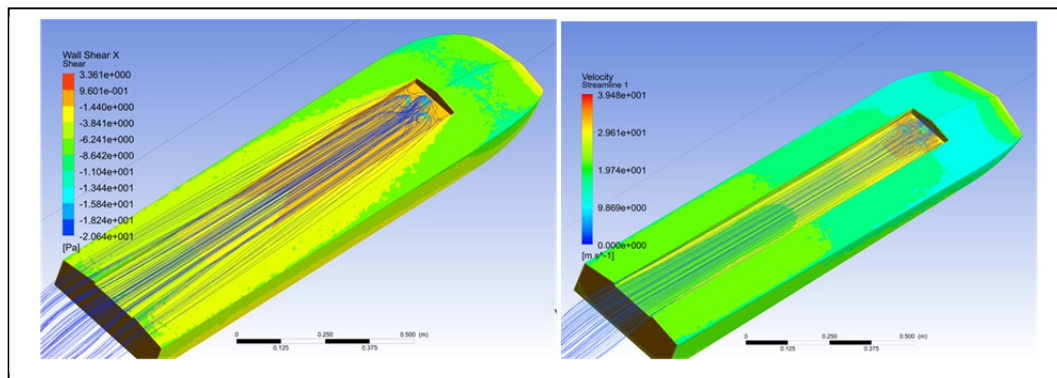


**Figure 2.5 :** Velocity streamlines of air phase combined with wall shear.

A further study was performed by (Amromin et al., 2011). The wave impact on the cavity shape and drag reduction was estimated with an analytical approach which considers the air cavity as a combination of two interacting flows. Pressure fluctuations in the cavity due to wave impact were modeled as perturbed steady cavitating flow. It was stated by the authors that utilizing this method enables to predict the effects of surrounding water like air entrainment from the cavity closure. By this way compressibility of the cavity can be also taken into account.

As a conclusion, performed experiments and following CFD calculations have pointed out that, air lubrication by means of air cavity concept is found to lead

substantial resistance reductions on ships, mainly due to viscous resistance reduction by reducing frictional area. More energy efficient ships can be designed by utilizing air lubrication. Additionally validated CFD models as well as basic numerical tools will be a cost effective choice in the optimization stage of air lubricated ship designs.

#### **2.2.4 Polymer injection**

Injecting polymer additives to boundary layer aiming to reduce drag is one the most widely studied and most often applied drag reducing method particularly for internal flows such as oil pipelines, sewage systems and fire hoses. The presence of high molecular weight polymers injected the near wall region of a turbulent wall bounded flow can lead to reductions of skin friction drag by up to 70% even when the polymer concentration is on the order of a few weight parts per million (wppm).

The idea of injecting dilute polymer solutions to turbulent boundary layer was first proposed by (Toms, 1948). After his first article that reports the drag reduction data (later named as “Toms effect”) various defense applications was initiated by the work of Pruitt and Crawford (1963) and Savins (1964). Hoyt (1972) from U. S. Navy organizations have made significant contributions to the drag reducing potential of the dilute solutions of polymers (Truong, 2001). As an example, full scale testing of a submarine has shown that the power requirement of the submarine was reduced with parallel to reduction of self-noise as well as the radiated noise generated by the propeller. Due to potential of the concept, many research as well as review articles were published and so many others did not due to military secrecy. Since the concept is not in the scope of this thesis no more literature review will be given. However, for further details see White and Mungal (2008) and Elbing (2009) which offer recent updates on the subject.

A number of theories have been proposed to explain the mechanism acting on drag reduction. Generally, it was agreed that similar to bubble induced drag reduction, injected polymers are leading changes in turbulent structure. However, it is understood that complex mechanisms are at work simultaneously which is not understood completely. A common explanation is: polymer chains interact and disrupts the eddies and micro vortices present in turbulent flows. (Changes in the mean profile as well as turbulent statistics of the turbulent boundary layer support this) Researchers have revealed a number of key parameters which effects the level

of polymer drag reductions observed, including: polymer molecular weight, concentration, chemical makeup, extensional viscosity, injection rate, and free-stream speed (Winkel, 2007).

Although polymer injection into turbulent boundary layer offers a considerable amount of drag reduction, the application of the concept to external flows (like surface ships) have some practical problems. First, continuous addition of polymer additives with a constant injection rate is required. Second, obtaining a homogenous distribution of mixture is not possible because, the polymer solution rapidly decreases in concentration due to turbulent mixing with liquid in turbulent boundary layer through the downstream of injection point. Due to the fact that, for a feasible practical application; the cost of carrying, mixing, and injecting the polymer and the benefit of the resulting drag reduction have to be considered carefully which is another challenge.

## **2.3 Passive Methods**

### **2.3.1 Compliant Coatings**

For more than fifty years, compliant coatings has fascinated scientists and engineers searching for methods to delay laminar-to-turbulence transition, to reduce skin-friction drag in turbulent wall-bounded flows.

Compliant coating technique is passive, relatively easy to apply to an existing vehicle or device, and also not too expensive. Unlike other drag reducing techniques such as suction, injection, polymer or particle additives, passive compliant coatings do not require slots, ducts or internal equipment of any kind (Gad-el-Hak, 1989).

First experiment on the concept was carried on by Kramer (1957) who was fascinated by the amazing swimming abilities of the dolphin. Following the experiments on Long Beach Harbor – California, he reported that a compliant coating can reduce drag by up to 60%. Until the analysis of Carpenter and Garrard (1985) and experiments by Gaster (1988), there were many attempts to duplicate his findings which many of them were failed. They were concluded that transition Reynolds numbers, which exceed by an order of magnitude those on rigid surface boundary layers, can be achieved. Additionally, it was reported that the coatings can also suppress noise on marine vehicles which is an attractive aspect of the concept

for military applications.

Theoretical studies have shown that the turbulent-laminar transition can be delayed through the attenuation of so called “Tollmien-Schlichting waves” (TSW) (Benjamin, 1960). The early work of Benjamin (1960) and Landahl (1962) showed that as the compliance characteristics of a coating is increases the growth of the TSW is progressively suppressed. Theoretically, if the coating were to be made sufficiently compliant the TSW would be completely stabilized resulting in the maintenance of laminar flow for indefinitely high Reynolds numbers but, a special attention has to be given while tuning the compliance of the wall otherwise a rapid breakdown may occur through the amplification of wall based instabilities.

Since there are many small scale experiments reporting the potential of this type of coatings, it is indicated by calculations of the drag reduction of Gad-el-Hak (1996) that, there is no significant benefit on a large vehicle such as submarines but the coatings can reduce the drag for smaller objects. So further investigations (both experimental and numerical) have to be made in order to apply the concept to larger objects like ships.

### **2.3.2 Antifouling (Biofouling Control)**

Biofouling control can be considered as an indirect way of boundary layer modification because, majority of the antifouling do not directly contribute the modification of turbulent boundary layer and they just provide a control on the surface roughness of a ship throughout the service. Increase of surface roughness by fouling (roughness of newly built ship can easily increase from 80  $\mu\text{m}$  to 1000  $\mu\text{m}$  ) causes dramatical frictional resistance increases. For instance, measurements in cargo carriers and tankers have been reported as total resistance increases up to 80-90% (Lackenby, 1962). For high-speed craft the resistance increase due to fouling yields almost 50% increase on total resistance (Candries, 2001).

Today, the most widely applied type of antifoulings are Tin free Self-Polishing Copolymers (SPC) and Foul Release systems. The working principle of Tin free SPC systems is killing the organisms that have attached to the hull surface by gradually leaching the toxin. As opposed to SPC systems, Foul Release systems are non-toxic and made of silicone elastomers of low surface energy which reduces the ability of fouling organisms to attach strongly to the surface. Attached organisms are self



cleaned by hydrodynamic shear forces when the ship is sailing in a required speed.

Although there are many sources regarding the effects of antifouling on hull performance, only few of them offer a systematical study on the subject explaining the effects of system on boundary layer structure. A systematic experimental study of the drag, boundary-layer and roughness characteristics of antifouling technology was presented by Candries (2001) and the outcomes of the study have motivated many researchers on the application of state of the art coatings in combination with active methods of boundary layer modification. Further details of this application will be given in the next chapter which provide experimental results on silicon based foul release system applied Tanker model, air lubricated by microbubbles and air film. The synergistic effect of the two applications will be discussed (Joint action of air lubrication and Silicon based foul release coatings)

## **2.4 Conclusions**

Naval Architects have made considerable progress on the application of air lubrication for the ship drag reduction. Technologies such as air cavity, microbubbles and air film are being actively developed in order to implement these concepts on the ships. As our understanding of multiphase flows increases, these techniques may be further optimized. Important practical considerations should be raised when air lubrication is considered for drag reduction on ships.

-First of all, the power required to inject the air under the hull must not be larger than the propulsive power saved. The energy for the air supply becomes large especially when the air is supplied to a region with high static pressure. Higher the draft of the boat, more energy is needed to obtain air lubrication. Therefore, it is necessary to continue the research experimentally as well as theoretically in order to find out more efficient air injection devices.

-The presence of the air beneath the hull must not reduce the propulsion efficiency of the ship. The design of the aft end and the propulsion system is highly affected by the air lubrication.

-The proportion of friction drag that a hull experiences is highest at lower speeds (compared to form and wave drag), which makes friction drag reduction attractive. With increasing speed, the proportion of resistance from the friction drag typically

decreases. Because the power loss due to friction rises with 3rd power of speed, whereas the supply rate of the injected gas usually increases at a slower rate, friction drag reduction with gas injection may become more cost-beneficial at higher speeds.

-Microbubbles represents the widest application potential for ship resistance reduction due to use of surfaces with curvature. However the boundary layer dynamics for the air bubble stability is still not well understood. As the distance from the bubble generation increases, the bubbles are pushed outside the boundary layer, reducing the effectiveness of the microbubble air lubrication. Microbubbles also suffer from practicality of generation system due to use of porous media and clogging due to corrosion, marine growth.

-Air film represents the simplest methods for air lubrication of ships due to air feed system, however stability of the air film is the challenge for the scientists.

-Air cavity is the only method currently applied into ships. The concept is well understood, but the ship design procedure to optimize the number and size of cavities is not developed yet. Cavity shape is also a concern for the further research.

-The lines of the ship are designed to reduce the total resistance, so care must be taken not to increase the other components of drag in an effort to contain the lubricating layers.

-The most significant challenge is the unsteady flows around the hull that result from ship motions and maneuvers while travelling in a seaway that would break up and dissipate cavities or air layers. The loss of a air layer can lead to tremendous increases in drag. In addition, the presence of the cavities cannot degrade the sea keeping of the ship. Given the complex dynamics of the air layers, and the need of ships for maneuvering and sea keeping, it is likely that active monitoring and control of air lubrication process will be required for crafts operating in the open water. Design of such hull forms will rely on a combination of modeling and experiments using the most advanced tools developed.

### **3. AIR LUBRICATION EXPERIMENTS ON FOUL-RELEASE COATED SURFACES**

#### **3.1 Introduction**

In this chapter, the summary of the experimental work, which was intended to understand the governing mechanisms of air-films, is given. Two series of experiments were performed in ITU Circulating channel as well as in large towing tank, located at Istanbul Technical University Ata Nutku Ship Model Testing Laboratory.

First series contain numerous set of experiments performed with a custom built vertical composite flat plate which was coated with state of the art foul release antifouling (silicon based Intersleek 900 manufactured by AkzoNobel). Resistance measurements as well as flow visualization studies were also performed in order to understand the efficiency of air lubrication in a vertical surface.

Following to the vertical flat plate experiments, the focus has been given to apply the air film concept on horizontal surfaces by injecting air to the bottom of a water repellent surface. One of the models of ITU towing tank has been selected and painted with water repellent paint. The paint used was the same one employed in the first series. In order to investigate the air film created by porous media, the model was fitted with porous media units which was custom manufactured. The units were flushly mounted to the bottom and to the parallel sides of the tanker model. Air film, formed by a single hole was also investigated through the project as a second set of the series. Generally, the effect of water velocity, airflow rate, draught and finally coatings on the formation of air film and micro bubble concepts was investigated.

The purpose of this chapter is to provide experimental evidence (in model scale) about the drag reduction potential of air lubrication for low speed ships. As stated in the previous chapter, the proposed synergetic effect of active and passive methods of frictional drag reduction was also analyzed (Mechanism governed by joint action of air lubrication and foul release coatings). Furthermore, the effect of air lubrication on the

wave resistance component of total resistance was investigated through performed wave cut analysis as well.

### **3.2 Motivation and Background**

With the light of statistics regarding the global transport, it is well known that, almost 80% of the world trade by volume is transported by ships and it is obvious that the major portion of the sea transport is realized by low speed ships. Therefore, a little effort that leads a considerable amount of drag reduction on those ships will create an enormous global benefit in terms of drag reduction thus fuel consumption, which is a key parameter for green house gas emissions and operating costs. As explained in detail in Chapter 1, both operational and environmental aspects of the subject, forces ship owners as well as ship designers to create ships that are more efficient.

Since low speed ships are dominating the global trade, launching an extensive research focused on that kind of ships would be a good starting point in terms of priority. When the resistance characteristics of low speed ships are visited, it can be easily recognized that skin friction drag is a major contributor to the total drag and yields up to 60% of a ship's total resistance (in case of very low speed range). Therefore, the frictional resistance of that kind of ships should be reduced by utilizing active and passive frictional drag reduction techniques that elaborately reviewed in Chapter 2. Fortunately, hull shape of those ships involves parallel bodies that require two vertical surfaces (flat of side) and a horizontal bottom (flat of bottom). From the gained experiences agreed with the reviewed literature, that is for sure that flat horizontal surfaces offer an ideal condition for air lubricated boundaries so the efficiency of the lubrication is favorably affected by the hull geometry in this case. On the other hand, it is also known that due to buoyancy forces are dominating the air lubrication mechanism and reducing the efficiency when the method is applied on vertical surfaces such as ship sides, drag reduction is adversely affected by hull geometry. When the contributions of the side and flat of bottom to the wetted surface area of a ship compared, ship sides cover more than 1.5 times bigger area than flat of bottom.

By considering the above, it can be derived that in order to achieve higher drag reductions, air lubrication should be applied to vertical surfaces in addition to

horizontal ones. Therefore, some additional techniques have to be applied with air lubrication simultaneously not only for providing lubrication in vertical surfaces but also improving the efficiency of air lubrication on horizontal surfaces.

Thinking in the similar direction, Fukuda et al. (2000) recognized that super water-repellent coatings may play a critical role in the ability to hold an air film underwater thus the efficiency of lubrication system can be increased by coating the hull with this type of paints. This work has sparked further research efforts on the issue over a decade. For example, European Union sixth framework project **Sustainable Methods for Optimal Design and Operation of Ships with Air Lubricated Hulls (SMOOTH)** was initiated to investigate the synergetic effects of state of the art coatings on air lubrication performance. Research institutes like MARIN, SSPA and ITU (Istanbul Technical University) were participated in the consortium and conducted experiments especially on air lubricated and specially coated surfaces, which were coated by Akzo Nobel.

The current chapter includes the experimental work conducted by ITU within the scope of the SMOOTH project. In order to investigate the air lubrication formation with vertical surfaces, a vertically inclined flat plate was utilized, while a tanker model with a flat bottom was employed to investigate the effects on horizontal surfaces. Details of the work was also published as Insel et al. (2009) and further study which was extended with CFD computations was published as Insel et al. (2010)

### **3.3 Experiments on vertical surfaces**

#### **3.3.1 Experimental Setup**

An experimental setup was established on the circulating water channel located in Istanbul Technical University Ata Nutku Ship Model Testing Laboratory. The setup contains four main components: a six-component force balance, a plate, a frame and air supply system. The frame, which carries the whole setup, was fixed between the circulating channel's two side walls. The six component force balance that has capability of measuring force components in x, y and z directions was located at the middle of the frame and fixed through a stainless steel plate which was specially manufactured for the balance and attached to the frame by steel bolts. The

connection of force balance with the plate was provided by an apparatus. The apparatus includes a rod with a custom manufactured flange welded (suitable for the balance's flange) in one end and a welded small plate (which is sandwiched between two plates) at the other.

The plate with dimensions of 2100mm x 600mm x 20mm was manufactured from plywood with sandwich method. Two 10mm thick plywood were prepared, the slots for two inner sides of the plywoods were machined in order to fit the steel plate as well as four air injection pipes while the outer sides of plywood plates were machined in order to obtain a tapered end (The thickness of the plate was reduced from 20mm to 8mm gradually in 100mm length). The fixing apparatus and the pipes were sandwiched by two plywood plate by using epoxy. Finally in order to provide the strength and water tightness, the plate was covered by a carbon textile with epoxy. Fortunately, wrapping the carbon textile around the edges provided a well elliptical leading and trailing edge. After surface preparations, the plate was coated with Intesleek 900 silicon based foul release coating. Two sets of fifteen holes, each has 4mm diameter had been drilled on the plate where the air pipe was sandwiched inside the plate. First set of holes was located 300mm downstream of leading edge while second set was at the trailing edge. After first trials, in order to investigate the air injection through leading edge, the plate was flipped so that the trailing edge became the leading edge.

The air supply system was consisted of a compressor, two sets of air filters and an airflow rate controller. The system components were connected by pneumatic pipes with flow directing valves and fittings. A compressor with air supply capacity of 25 l/h was utilized as the air source. In order to control the intensity of airflow injected through the fittings, an electro-pneumatic regulator was utilized. This regulator is a pressure reducing device with two solenoid valves, a pressure sensor, a set of pressure membrane and a control circuit inside. It can reduce 1MPa. input pressure to 0.005 - 0.9 MPa range of output range. The device needs 24V of DC as a supply voltage. The adjustment of the reduction rate was provided by connecting the excitation voltage port of the device circuit to a transformer, which can give 0 - 10V range of DC. The potentiometer of the transformer was set to a requested pressure. Output pressure, which would be the pressure at injection nozzle, could be monitored by the display of the device. Since the device had a limited display resolution, output

signal port of the device has been connected to a multimeter. Output signal was also recorded in terms of voltage. Supplied air from the compressor was filtered in order to prevent a potential damage on flow rate controller. Further details of the air filters are given in Chapter 4. The air supply system (except the compressor) was located on the frame. The whole setup is explained in Figure 3.1.

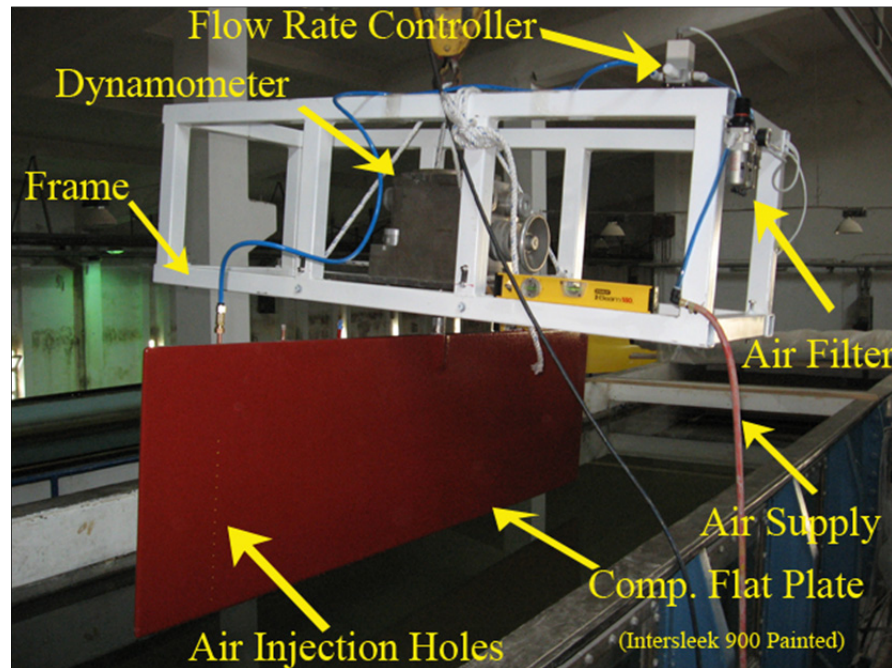


**Figure 3.1 :** Experimental Setup (Composite Vertical Flat Plate).

Flat plate experiments require an accurate adjustment of stream wise alignment, which is usually a challenging process. A minor misalignment in the stream wise adjustment may cause an angle of attack with the upcoming flow which forms a boundary layer flow with pressure gradients (favorable at one side and adverse at the other). In this study, an iterative process of plate adjustment was carried on. Thanks to force balance which can measure the resistance components in x,y and z direction. Here the x component corresponds the resistance of the plate in stream wise direction while the y component gives the resistance along span wise direction hence the lateral force acting on the plate. Since any misalignment would lead a lift in the plate, it was enough to obtain a well-adjusted plate by just searching for minimum lateral force in an iterative manner. The plate angle could be adjusted by just turning the lever located at the side of the force balance. In addition, another method of plate alignment was performed by measuring the lateral distance between the edges of the plate and channel sidewall. It was found that direct alignment by distance

measurement gives inconsistent results with the iterative method probably due to sidewall misalignment or lack of span wise uniformity of the upcoming flow.

### **3.3.2 Test Matrix**

The flat plate experiments were conducted for fourteen different free stream channel speeds (free stream velocity) ranging between 0.31m/s to 1.85m/s, corresponding Froude numbers of 0.07 and 0.407 respectively. The draft of the plate was about 425mm and remained constant, however for higher speeds due to the presence of free surface waves, difference between fore and aft drafts were observed. Both drafts were measured during the experiments, which was taken into account in the wetted surface area calculations (for calculating the frictional resistance coefficients). According to general conditions given above, three sets of experiments were carried on and in each set three different airflow rates were tried; no air injection condition for reference tests, airflow rates of 0.5 m<sup>3</sup>/h for lower air supply and 1.50 m<sup>3</sup>/h for higher air supply rates.

In the first set, air was injected through the pipe, which was located 300mm downstream of the leading edge. The holes of this pipe were drilled in the direction of plate's normal (90 degrees to the incoming flow)

In the second set, air was injected through the same air pipe as in the first set but with the drilled holes of 22.5 degrees of inclination with the plate rather than 90 degrees.

In the third set, a leading edge air pipe was drilled with 22.5 degrees of inclination with the plate.

Finally, in the fourth set, the effect of leeway and heel angle was investigated to simulate realistic hull surface conditions (5 degrees of heel and 10 degrees of leeway).

### **3.3.3 Results and Analysis**

The results of the vertical flat plate experiments have generally indicated that: In spite of the water repellent coating, an air film could not be formed. During the first set, due to the domination of buoyant forces especially for lower speeds and air supply rates, created bubbles has followed a nearly vertical streamline and quickly reached the free surface as shown in Figure 3.2 to the air injection can be easily seen in the photos taken from the windows of the circulating channel's side wall and



given in the Figure 3.2 and Figure 3.3. Since, air was injected through a manifold (an air pipe with drilled 14 holes in a vertical line), it was recognized that the hydrostatic pressure was governing the injection mechanism. In lower air supply case, eleven of fourteen holes were injecting air while three of them at the bottom were inactive due to hydrostatic pressure (Figure 3.2). The same phenomenon was observed in higher water speeds. So the pressure in the air pipe was equal to the water head (measured from the lower hole to the waterline) times the water density, this was also agreed well with the monitored pressure values acquired from the electro pneumatic regulator.

In general, bubble coalescence was observed. Injected air caused bubble formation and the bubbles were merging to bubble clusters while tracking a vertical direction, for lower water speeds a mass of water-air mixture was appeared close to waterline and the mass was released with a kind of explosion, which creates free surface waves (Figure 3.6). The explosion takes place near the wall for lower air supply rate while for the higher rates, wave occurs far away from the wall. For the higher air injection rates, bubble merging caused bubble coalescence at the middle rather than near free surface. Therefore, steepness (wave height to length ratio) of the waves was reduced with compared to waves created by lower air injection rates.

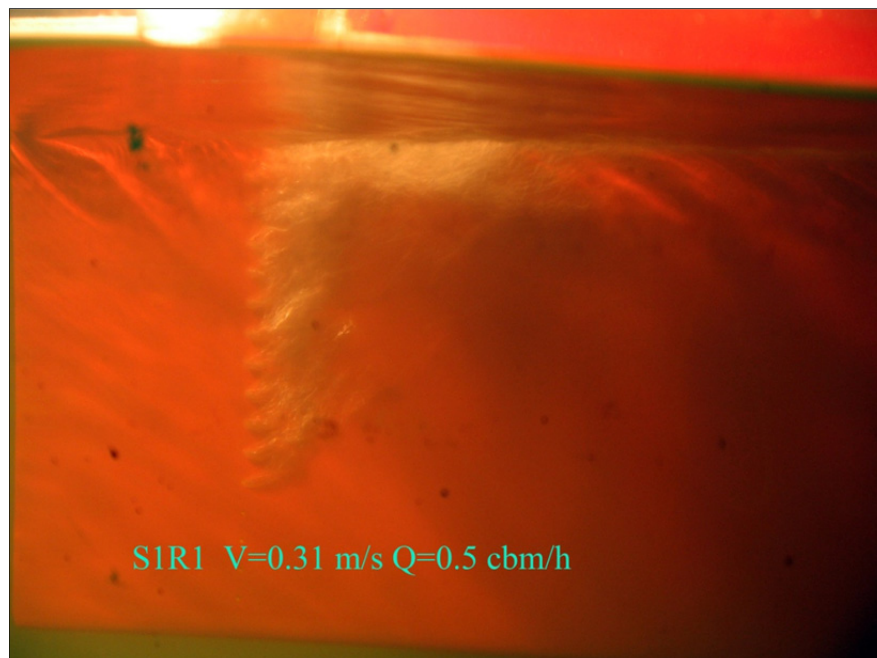


**Figure 3.2 :** Vertical flat plate test for  $V=0.31$  m/s and  $Q=0.5$  m<sup>3</sup>/h.

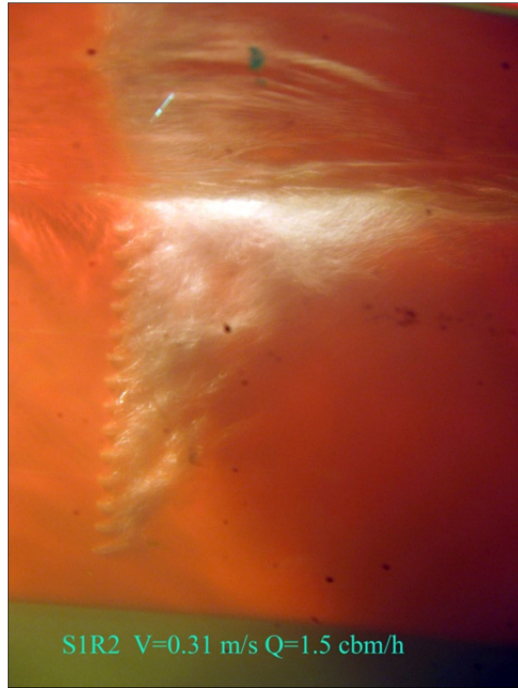


**Figure 3.3 :** Vertical flat plate test for  $V=0.31$  m/s and  $Q=1.5$  m<sup>3</sup>/h.

Regarding the effect of airflow rates in higher speeds, there was not so much to note. Comparison of Figure 3.4 with Figure 3.5 gives; the length of the air film obtained in the higher supply rates was longer than the lower one. Additionally, higher airflow rates enable higher air covered areas due to the advantage of additional three bottom injectors.



**Figure 3.4 :** Vertical flat plate test for  $V=1.75$  m/s and  $Q=0.5$  m<sup>3</sup>/h.

Comparison of Figure 3.3 with Figure 3.5 can explain the effect of water speeds on air film formation. As higher water speeds achieved, bubbles were tracking horizontal lines curving upwards while going downstream of injector (rather than tracking vertical streamlines which was the case for lower speeds). More homogenous air-water mixtures obtained probably due to higher rates of dispersion.

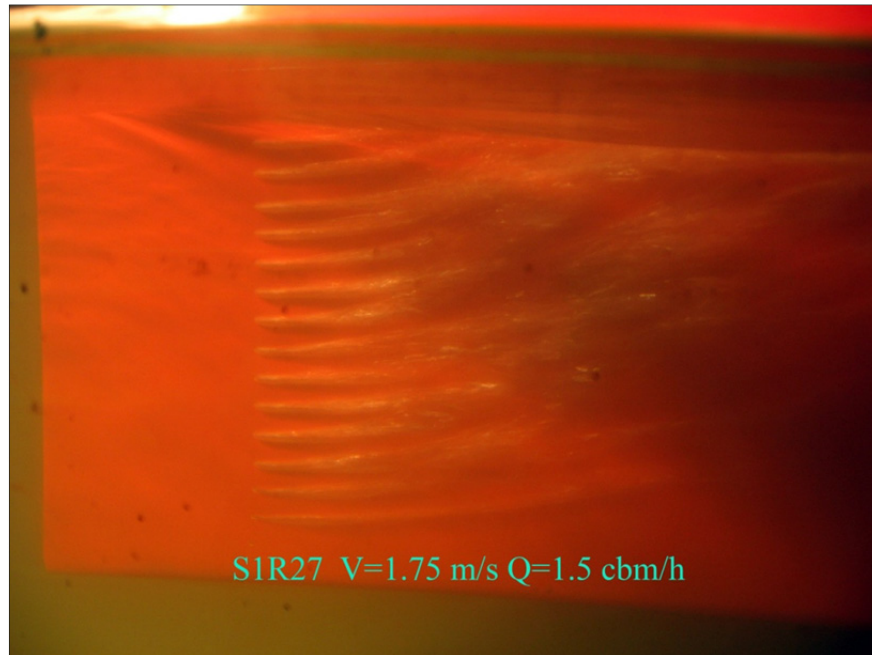


**Figure 3.5 :** Vertical flat plate test for  $V=1.75$  m/s and  $Q=1.5$  m<sup>3</sup>/h.

The area covered by air film was obviously an order of magnitude greater than in lower speed case, so the same of amount of air was extended to bigger area. This was also concluded with less steeper waves with higher wavelengths at free surface. In addition, air excited wave appeared at the middle of the plate which was at the fore part in the lower water speed case.

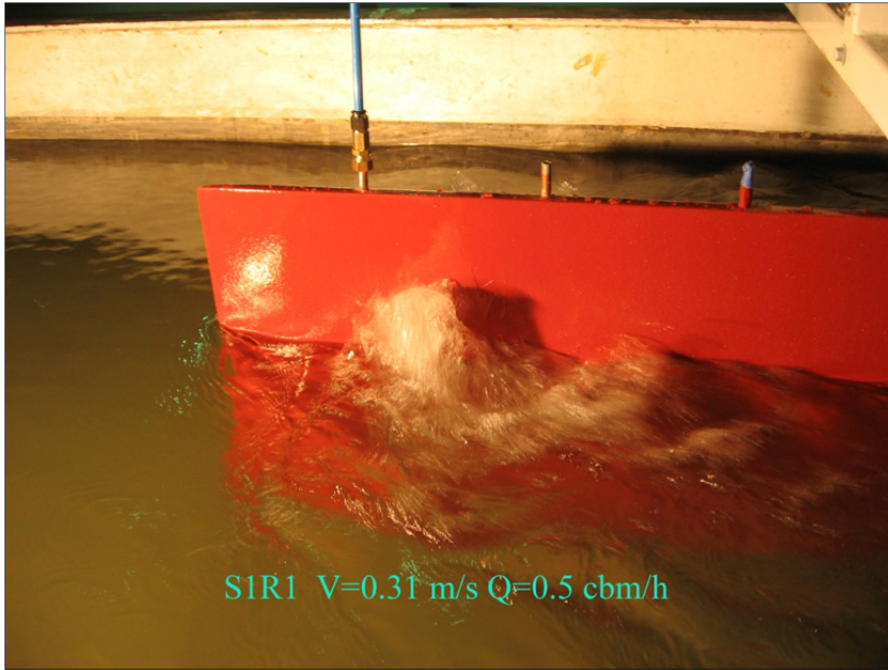


**Figure 3.6 :** Free surface waves created by the explosion of bubble coalescence.

Following the flow visualization studies, acquired resistance data was analyzed. The x direction component of the resistance was taken into account for the calculation of friction coefficients for each case. The coefficients were calculated via equation (3.1).

$$C_F = \frac{R_F}{\frac{1}{2} \cdot \rho \cdot S \cdot V^2} \quad (3.1)$$

Where,  $R_F$  is the frictional resistance which can be taken as total resistance in x direction for a well aligned flat plate (the wave resistance is neglected).  $S$ , is the wetted surface of the plate,  $V$  is the free stream velocity and  $\rho$  is the density of the channel water. The frictional coefficient comparison is given in Figure 3.7 plot has shown that, air lubrication has no favorable effect on the frictional resistance. In the lowest speed, it was interesting to see the adverse effect of lubrication and it was commented that forces created by the disturbance of the boundary layer due to air injection were bigger than the plate's resistance.

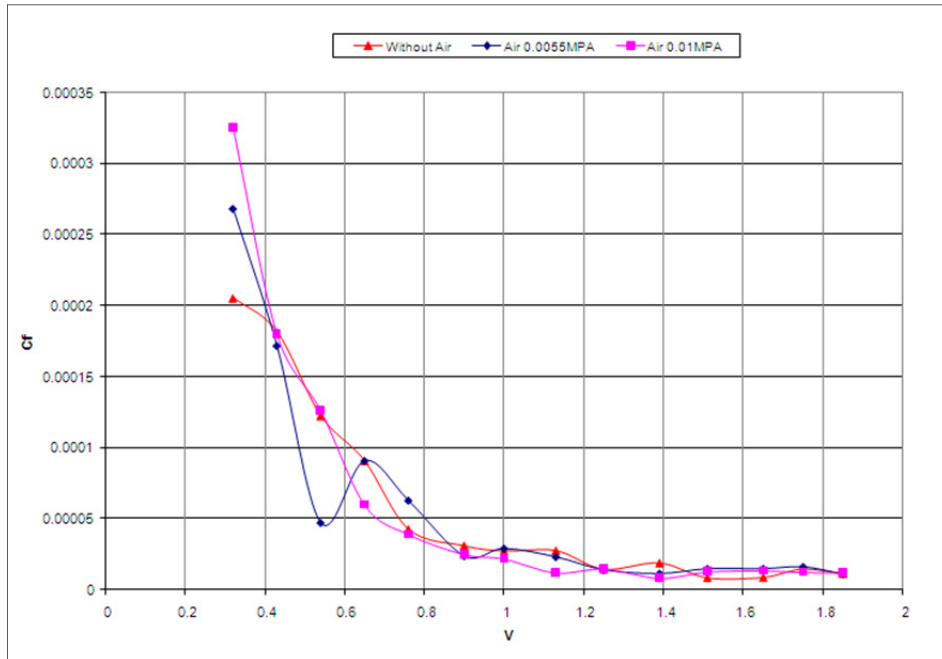


**Figure 3.7 :** Comparison of frictional coefficients for vertical flat plate experiment.

Following the frictional resistance comparison, the method of air injection and then the place of injection were changed. As mentioned in “test matrix” section, second set was carried on by air injection through the same air pipe as in the first set but with the drilled holes of 22.5 degrees of inclination and there was no difference between the first set in terms of flow visualization as well as resistance values.



**Figure 3.8 :** Vertical flat plate experiment (air was injected from leading edge)

The third set was carried on with a leading edge air pipe, that was drilled with 22.5 degrees of inclination with the plate. No difference was observed as in second set.

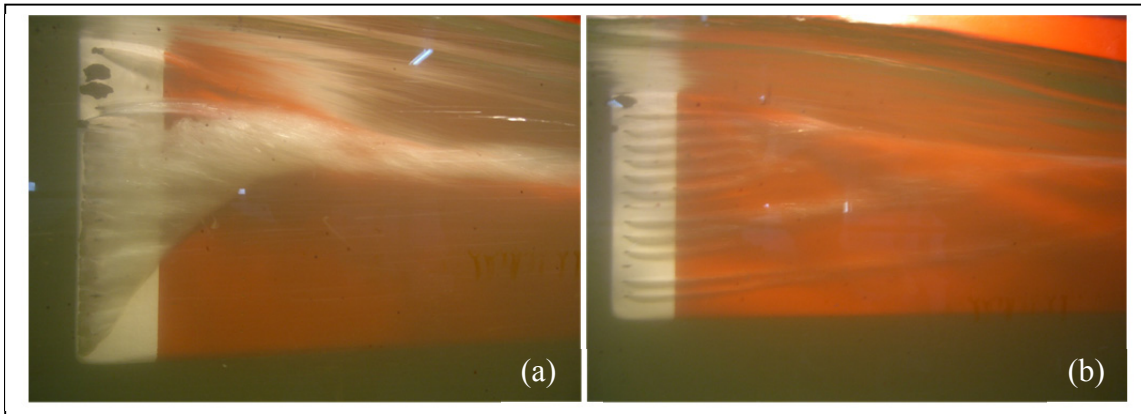


**Figure 3.9 :** Vertical flat plate exp.: (a) 10 degrees of leeway. (b) 5 degrees of heel.

Finally, the fourth set was carried on to see the effect of leeway and heel angle. When the plate was aligned with 10 degrees of leeway, the leading edge behaved like a cavity step. Therefore, a cavity was obtained as given in Figure 3.9(a). Hydrostatic pressure has shaped the cavity in a triangular form as per vertical distribution of static pressure. When the plate was aligned with 5 degrees of heel, it was observed that lines of air film lasted longer than no heel case. However, there was no favorable effect of lubrication encountered in terms of resistance.

As a conclusion, it was agreed that air film formation in vertical surfaces was dramatically inhibited by buoyancy forces therefore resistance reduction could not be achieved that means there was energy loss in terms of net energy. Furthermore, when considering the effect of silicon based foul release coating, which was the main scope of the study, it was clarified that the coating could not improve the efficiency of the air lubrication process in vertical surfaces.

### **3.4 Experiments on horizontal surfaces (Tanker Model flat of bottom)**

Following to unpromising results of experiments on vertical composite flat plate it was understood that, in order to improve the efficiency of air lubrication in tankers further research is needed on horizontal surfaces. i.e. flat of the bottom of a tanker. Therefore, proposed hybrid application of active and passive methods appealed an interest. Studies on the subject were concluded with the decision of two series of

tests. The first one includes flow visualization studies conducted in the circulating channel while the last one covers the resistance tests conducted in the towing tank.

### 3.4.1 Flow Visualizations in Circulating Channel

All flow visualization tests were conducted in a circulating water channel with a testing section of 6 m long, 1.5 m wide and 0.75 m deep, which is located in Istanbul Technical University, Ata Nutku Ship Model Testing Laboratory. The flow underneath the hull of a tanker model was observed through the windows located at sidewall as well as located at the bottom of the channel. Visualization data was obtained utilizing a high-speed camera, so that acquired visual data could be converted to quantitative type with the help of image processing based on particle tracking method.

#### 3.4.1.1 Experimental Setup

A stock model with large horizontal flat bottom has been selected for flow visualization and resistance measurements. The model hull form denoted as M266B has been selected due to its reasonable geometry for air lubrication applications. The hull has a block coefficient of 0.772 which has a flat of bottom, connected to parallel side walls. The principle characteristics of the tanker form are given in Table B.1, the body plan is given in Figure A.2. The stock coating of Akzo Nobel (Intersleek 900) was applied to the model in order to see the effect of water repellence on air lubrication (Figure 3.10).



**Figure 3.10 :** Reference model and painted model.

Following the reference resistance tests in the towing tank, small modifications at the model bottom was made. For single hole air injection experiments, a hole was drilled perpendicularly to the bottom of the hull. Considering the waterline at flat of the bottom, the location of hole was chosen at the centerline and 400mm downstream of

fore perpendicular for transverse and longitudinal positions respectively. Air injector was obtained by mounting the copper pipe (has a diameter of 8mm) inside the drilled hole vertically and the pipe was fixed utilizing SIKA filler. In order to provide a connection between pneumatic hose of air supply system to the air injector, special pneumatic quick-connect fitting were fixed to the upper end of the pipe. To prevent a potential leakage from the air pipe fitting, the length of the pipe was selected provided that the pneumatic quick-connect fitting was located above the waterline. Similarly, in order to prepare the model for multiple hole air injection experiments, bottom modification was made by following the same procedure given above.

Additionally, in order to conduct air film experiments in which, air was injected through porous media units rather than holes, bottom of the model was modified to fit the porous media units flushly. The units were custom manufactured in order to obtain high efficient injection. Aluminum block with dimensions of 500x40x15mm were machined to obtain air slots with the beam of 20mm, length of 500mm and the depth of 10mm. At the middle of the aluminum block, a pneumatic quick-connect fitting was fitted so that the connection of the air supply system was provided to the unit. Brass sinter metal filter plates with the dimensions of 125x40x2.3mm were utilized as porous media. The plates were flushly fitted via screws to the aluminum unit and air tightness was provided by sika as a sealer. Four plates were fitted to obtain a unit. In order to flushly fit the compact prous media air injector unit to the flat of the bottom, a slot suitable for the unit was machined on wooden bottom. The position of the slot was selected as forward as possible where maximum beam of the hull reached considering maximum area coverage by air lubrication. The corresponding position was 1000mm downstream of forward perpendicular. The mounted unit can be seen in the Figure 3.19 for further experiments focusing the effect of bubble size on air lubrication, the sinter metal was changed with pvc based filter which has lower porosity. The picture of the pvc porous media is given in the Figure 3.20.

Finally, the bottom of the model was marked with permanent marker to enable measurements on visual data. Marking was also utilized as reference of particle tracking studies. The intervals of marking was 50mm for transverse direction and 75mm for longitudinal.



To fix the model in the circulating channel the mechanical frame was utilized which is used generally for resistance measurements with Atwood dynamometer. Model has restrained to sway, yaw and heel but free to surge, trim and heave. The ratio of the model length to channel beam was 2.7, in addition the model beam to channel beam ratio was 0.41 so the blockage of the model was considerably high. Therefore, no arrangement for the resistance measurements was done.

The same frame as used in the flat plate experiments was located near the model, by doing so air supply and air flow rate measurement system were utilized. Former experiments showed that more air capacity was needed to try higher flow rates of porous media injection, so instead of using small compressor used in the flat plate experiments, a compressor with higher air feeding capacity was employed by taking a branch from the air supply system of 5 axis CNC milling machine.

High-speed camera was employed for recording the visual data. The camera was produced by Vision Research with the model name of Phantom V.5.1. The camera has the capabilities of sampling 1200 frames per second for smaller areas. In order to capture larger area, sampling rate was limited with 120 frames per second. Both side and bottom video records were taken however; it was not possible to take synchronized videos of both views simultaneously due to having only one camera. For an efficient high-speed recording, a setup including two tripods and a special illumination was established.

#### **3.4.1.2 Test Matrix**

As mentioned before three type of air feed system has been tested. Air film obtained by all means of air injection were investigated through the free stream velocity range between 0.42m/s and 1.52m/s corresponding to  $Fn$ ., 0.066 and 0.24 respectively. To understand the effect of velocity, circulating velocities of 0.42, 0.76, 1, 1.4 and 1.52m/s were achieved. In order to understand the flow rate effect, per each velocity three levels of airflow injection rates were tested. The varying levels for airflow rate were; 0.5m<sup>3</sup>/h for lower air supply, 0.75m<sup>3</sup>/h for moderate air supply and 1m<sup>3</sup>/h for higher air supply. For multiple hole injection, the flow rate was evenly distributed to the holes with the help of a manifold. As a conclusion, varied velocities with the combination of varied flow rates were required more than 45 runs.

### 3.4.1.3 Results and Analysis

General conclusions about single hole injection can be drawn by analyzing the visual data. Figure 3.11 to Figure 3.13 are given for the effect of airflow rate while Figure 3.11, Figure 3.14 and Figure 3.15 are given to understand the effect of free stream velocity. Generally, injected air separates into V shaped arm just behind the hole and it is obvious that the arms were created by the edge of air film. The angle of the V shape is directly proportional with airflow rate. In contrast, the angle is inversely proportional with free stream velocity.

A basic type of image processing performed on the pictures and the angle between one arm and the centerline was calculated. The plot of the angle versus velocity gives a simple relation about the effect of velocity and the flow rate on the arm angle. Also with the help of third order polynomial approximation, it can be seen that the angle is reducing by the order of  $U^3$  (At third order, the curve fit results with a satisfactory correlation coefficient). The plot is given in Figure 3.21.

For slower speeds and increasing airflow rates, while the angle is getting larger, the area between the V arms contacts with only water and air is concentrated near the V arms and escapes from the hull sides. Hence, the increase in angle results in air escape at a short distance from the hole meanwhile it does not cause any increase in the area covered by the air film.

For faster speeds and increasing flow rates, while the angle is getting smaller, air is dispersing through the area between V shape arms and generates air slugs. At this condition, more increase in the speed leads separation of air slugs to smaller bubbles.

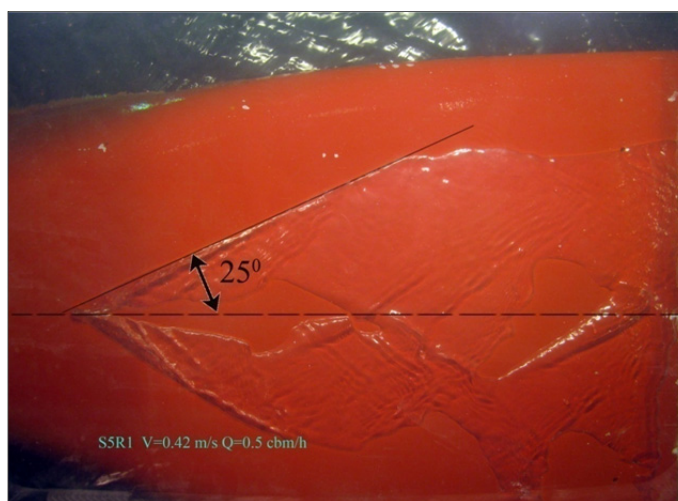


**Figure 3.11** : Angle of air film edge. S5R1,  $Fn=0.06$ ,  $Q=0.5\text{m}^3/\text{h}$ .

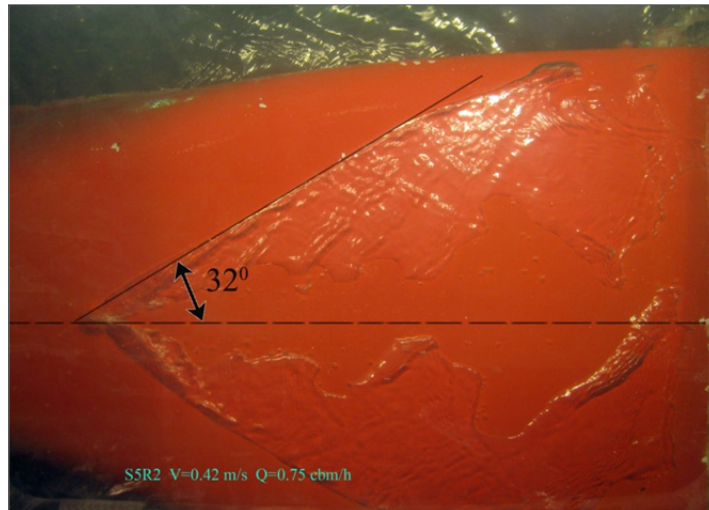


**Figure 3.12** : Angle of air film edge. S5R2,  $F_n=0.06$ ,  $Q=0.75\text{m}^3/\text{h}$ .

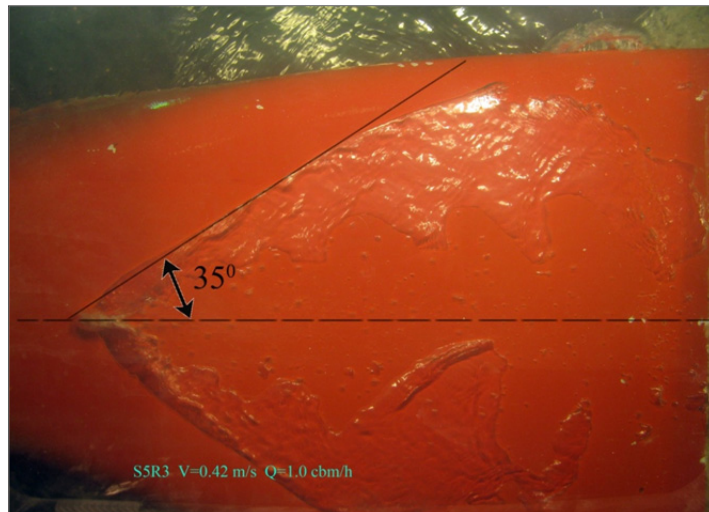


**Figure 3.13** : Angle of air film edge. S5R3,  $F_n=0.06$ ,  $Q=1.0\text{ m}^3/\text{h}$ .

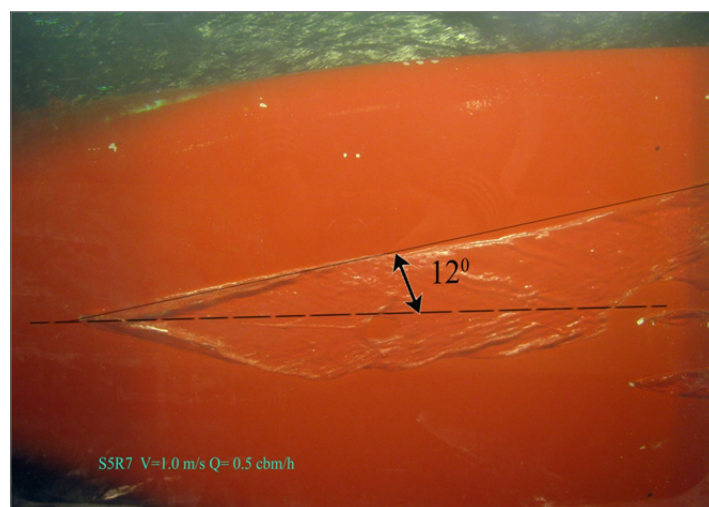


**Figure 3.14** : Angle of air film edge. S5R7,  $F_n=0.158$ ,  $Q=0.5\text{ m}^3/\text{h}$ .

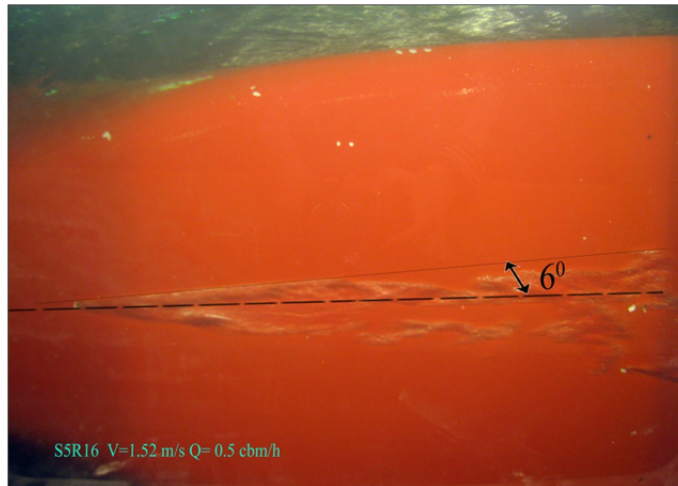


**Figure 3.15 :** Angle of air film edge. S5R16,  $Fn=0.24$ ,  $Q=0.5 \text{ m}^3/\text{h}$ .

For moderate speeds and lower air flow rates, air escapes from the sides of the hull at a larger distance and the area is mostly covered with air film resulting in larger frictional resistance decrease.

However, if the angle gets very small like in the Figure 3.15, the air covered area also becomes very small and air film stability cannot be sustained. Hence there is an optimum speed and it depends on air flow rate. The flow visualization results for single hole air supply have shown that forming an effective air layer between hull and surrounding water is so sensitive to water speed and injected air flow rate. In addition, the instability of air film was observed when the hull was heeled for few degrees. In that case air film becomes asymmetric and injected air escapes earlier than in the case of even keel position.

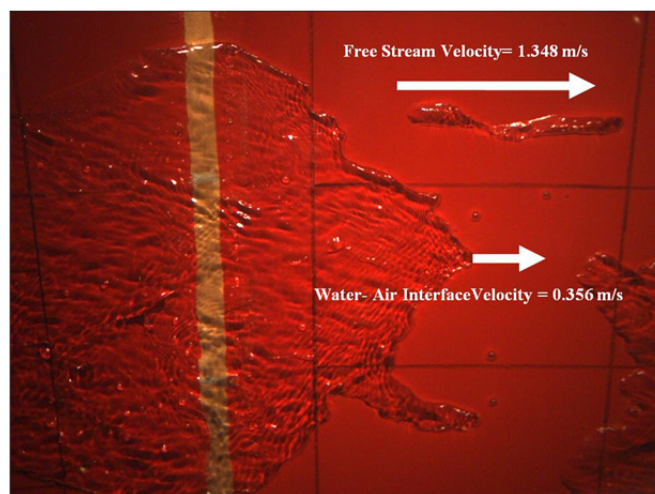


**Figure 3.16 :** Advection velocity of the water-air interface estimated by HSC particle tracking method.

In order to further understand the mechanism of boundary layer modification by air, water-air interface of air slugs was investigated by using particle tracking method. The interface was followed by a camera software. With the help of reference distance marked on the hull and the recorded sampling time, advection velocity of the water-air interface was calculated (See Figure 3.16). It was found that the advection velocities of the interface were 20% of the free stream velocity ( $0.2U_\infty$ ). It is worth here to note that, this rate means the interface propagates with the velocity of a particle streaming in the inner layer of turbulent boundary layer. Capillary wave system was also observed like shown in Figure 3.16 which may lead a boundary layer instability.

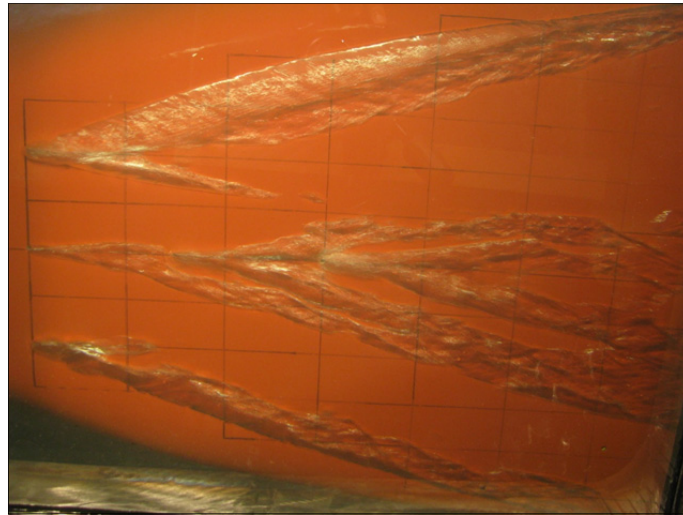


**Figure 3.17 :** Multiple hole injection at high speed.

After the experience gained with the single hole air injection, the effect of the longitudinal and transverse position of the hole has been investigated by using multiple hole configurations. The tested variations are: Three holes at the same longitudinal position by varying transverse position like given in the Figure 3.18 three holes at the centerline by varying longitudinal position like given in the Figure 3.18(b) and finally five holes by varying both longitudinal and transverse position which is showned in the Figure 3.17.

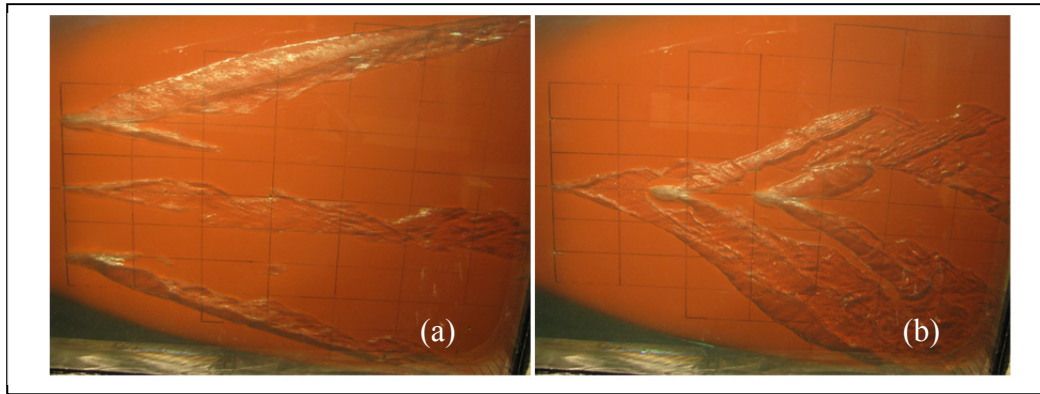


**Figure 3.18 :** Multiple hole injection (a) transverse holes (b) longitudinal.

It is very clear from the flow visualization results that the air feed from each hole interacts with others strongly. It was expected that the air from different holes would form a common air film before the tests. However air from different holes were separated very clearly due to pressure differences as shown in Figure 3.18. As a conclusion, it can be assumed that each air injector behaved like a point source.

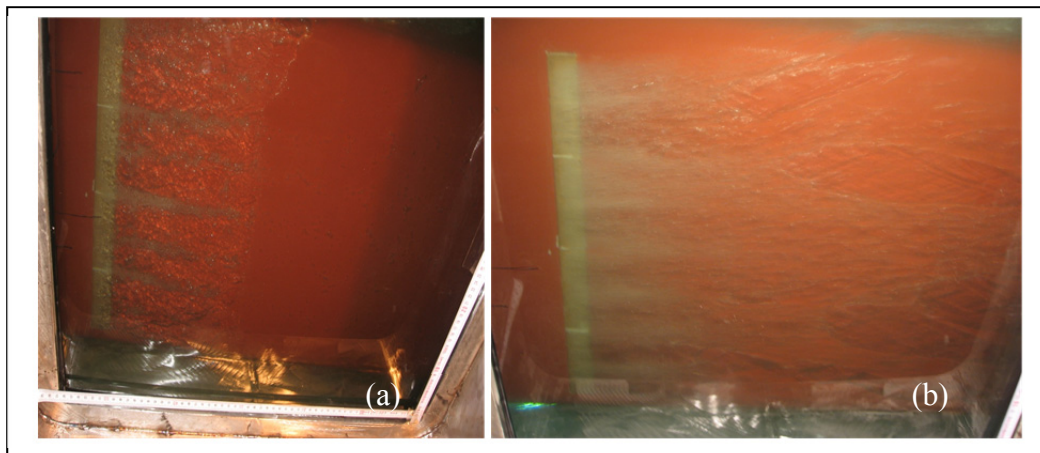


**Figure 3.19 :** Air flow from porous media (a) low speed (b) high speed.

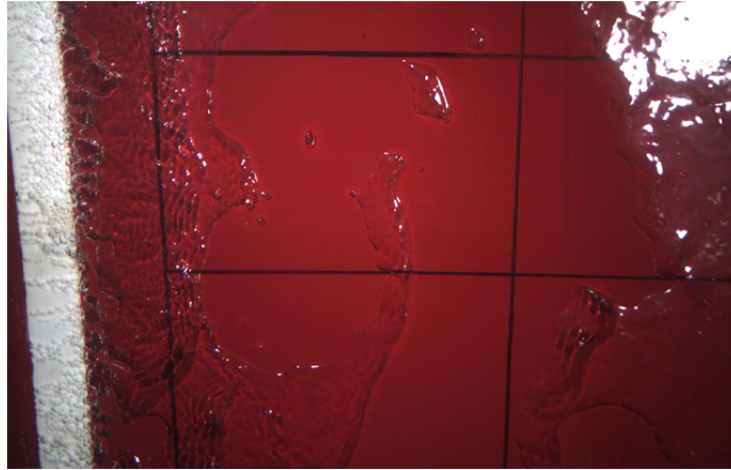


**Figure 3.20 :** Bubbles from the plastic porous media

Regarding the air lubrication experiments on porous media, it was concluded that; Porous media is an effective way of bubble generation. At low speeds, air film was formed just for about  $10B$  downstream of porous unit, where  $B$  is the beam of the unit. The air film-water interface can be easily recognized. It was also observed that from the interface, small bubbles are detaching to the downstream of the flow periodically as given in Figure 3.19(a). As the speed of the water increased, the interface was slipped further downstream and bigger air film was observed. See Figure 3.19 for larger air film. The change in air flow rate was concluded with a thicker air film therefore more air slugs detaching to downstream.

During the porous media experiments, an interesting problem was observed. Sinter metal filter elements which were used as a porous media, was corroded after a short period of usage (even they were made of Brass). Due to the fact that after two sets of experiments air feeding mechanism became out of order.

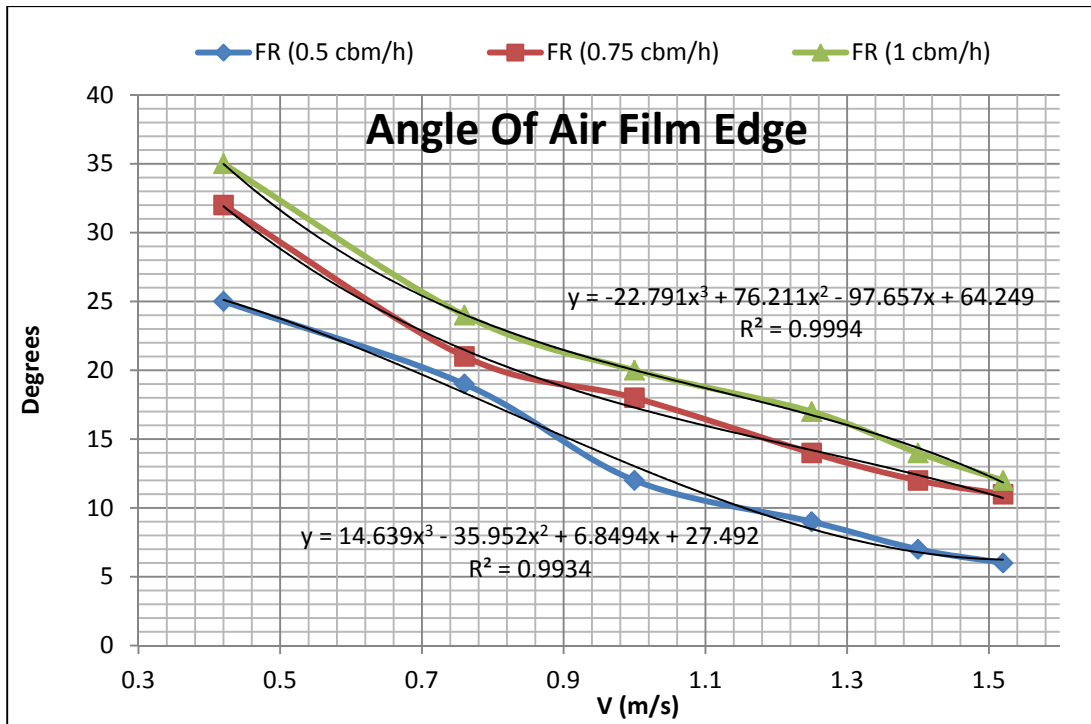


**Figure 3.21** : Angle variation of air film edge with speed and air flow rate.

### 3.4.2 Experiments in Towing Tank

Flow visualization studies have provided a general understanding of the air lubrication by means of air film applied to a tanker model. The main characteristics of the phenomena were investigated and general conclusions were drawn about the key parameters such as water speed and air flow rate. However, at the end of the tests there was not much findings in hand in terms of quantitative measurements. In this respect, to provide further understanding on the cases in quantitative manner, resistance measurements have been conducted with the tanker model. Total resistance tests as well as wave pattern measurements were conducted in the large towing tank of ITU Ata Nutku Ship Model Testing Laboratory towing tank with 160 m length, 6 m width and 3.4 m depth.

#### 3.4.2.1 Total Resistance Measurements

Total resistance measurements were conducted with Atwood dynamometer. So the model has been restrained to sway, yaw and heel but free to surge, trim and heave. Firstly the model without air lubrication has been tested to create a comparison base for both draught. Since it was experienced that there was no need to use multiple holes as an injection style, tests with multiple hole air injection were omitted from the test matrix. So two types of air injection have been utilized, air injection through



a single hole located at the centre of the model close to the model bow, and air injection through a porous media located near bow and covering almost all model width. Both air injection techniques have been tested in two air feed quantity: 0.5 m<sup>3</sup>/hour as low air supply and 1.0 m<sup>3</sup>/hour as high air supply. The model has been tested in two draughts to observe the hydrostatic pressure effects. In order to understand the results better, coding of test matrix for tanker model experiments are given in Table 3.1:. For each testing condition, the model was tested for the same water velocities as in the flow visualizations.

**Table 3.1:** Coding of test matrix for tanker model experiments.

Tested Condition	Full Draught	Low Draught
Without Air Injection	FDN00	HDN00
Single Hole Air Injection at 0.5 m <sup>3</sup> /hour rate	FDH05	HDH05
Single Hole Air Injection at 1.0 m <sup>3</sup> /hour rate	FDH10	HDH10
Porous Media Air Injection at 0.5 m <sup>3</sup> /hour rate	FDP05	HDP05
Porous Media Air Injection at 1.0 m <sup>3</sup> /hour rate	FDP10	HDP10

#### 3.4.2.2 Wave Pattern Resistance Measurements

As our understanding, air lubrication particularly reduces the frictional drag and generally towing tank tests on air lubrication focus on total drag measurements. Therefore, amount of reduction in total resistance is accounted to frictional component without suspecting about the effect of other component, which is wave pattern resistance. With remembering the experiments on air cavity by Gökçay et al.(2004) it is also possible that, pressure field around the hull bottom may positively induce the air film so that wave pattern resistance may decrease. Within the scope of this study, this possibility was considered and the effect of air lubrication on wave resistance was investigated by conducting wave pattern measurements. The measurements were conducted for all test conditions given in Table 3.1: with the exception of low draught experiments.

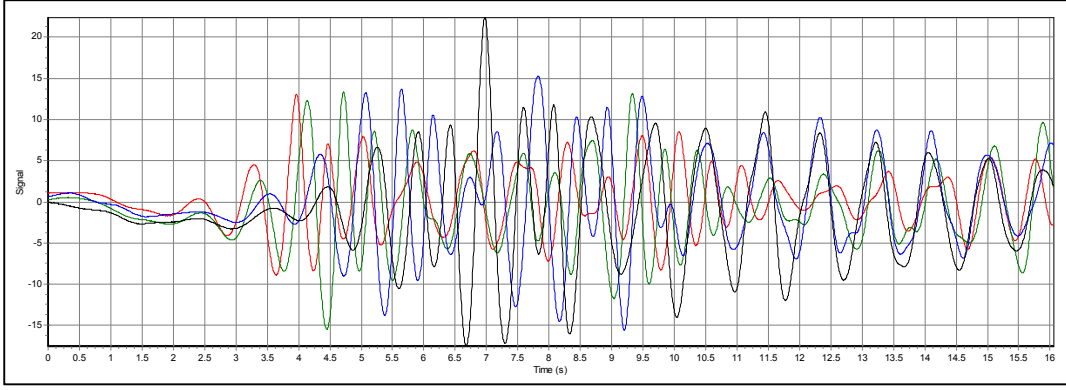


**Figure 3.22 :** Recorded wave cuts for model without air injection,  $Fn=0.225$ .

The waves generated by the models were acquired through four resistance type wave probes and a computer aided data acquisition system. An example of acquired wave cut data is given in Figure 3.22.

The wave pattern of a model in a towing tank can be mathematically expressed as;

$$\zeta = \sum_{n=0}^N [\xi_n \cos(\omega_n x) + \eta_n \sin(\omega_n x)] \cos\left(\frac{2\pi y n}{W}\right) \quad (3.2)$$

Where,

$$\omega_n = K_n \cos(\theta_n) \quad (3.3)$$

$$K_n \sin(\theta_n) = \frac{2\pi n}{W} \quad (3.4)$$

$$K_n - \frac{g}{V^2} \sec^2(\theta_n) = 0 \quad (3.5)$$

Where  $W$  is the width of the tank,  $n$  is the wave harmonic number,  $K_n$  is the wave number, and  $\theta_n$  is the angle of the harmonic wave. The wave pattern resistance can be written from the law of the conservation of momentum (Insel, 1990) as follows:

$$R_{WP} = \frac{\rho g W}{2} \left[ (\xi_0^2 + \eta_0^2) + \sum_{n=0}^N (\xi_n^2 + \eta_n^2) (1 - 0.5 \cos^2(\theta_n)) \right] \quad (3.6)$$

An example of the analysis is given in the Figure 3.23. By conducting comparisons not only on the basis of wave pattern resistance but also on the harmonic basis, the change in the wavemaking can also be investigated.

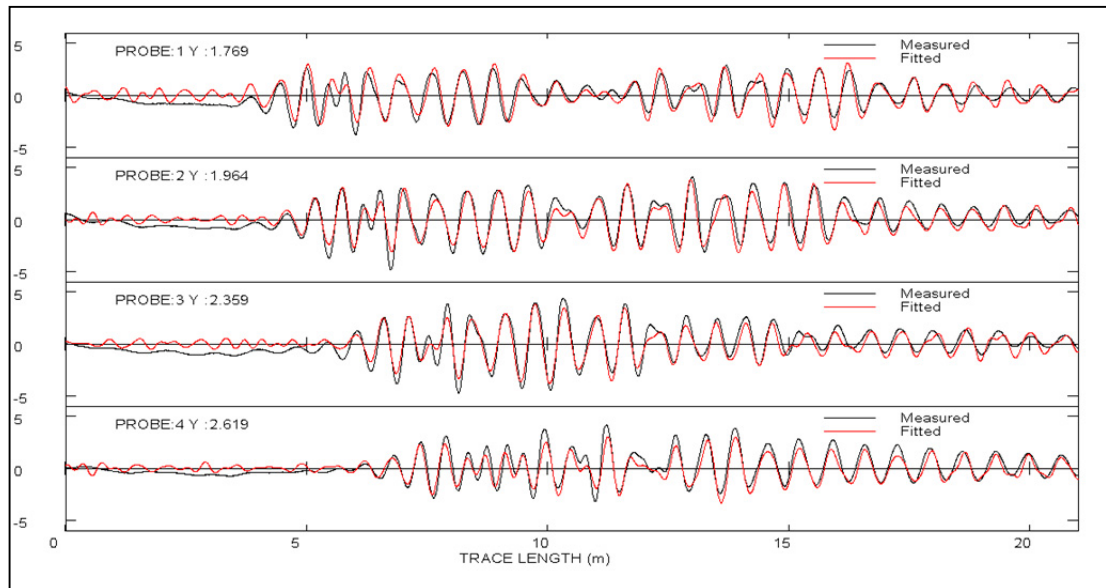


**Figure 3.23 :** Recorded wave cuts and wave cuts produced from wave pattern analysis for model without air injection,  $F_n=0.225$ .

### 3.4.2.3 Results and Analysis

As given in the Figure 3.25 and Figure 3.26, both porous media and single hole air lubrication has resulted in resistance reduction for speeds up to 1.4 m/s, i.e. Froude number of 0.22. The resistance reduction due to air feed is about 11-20 % for Froude numbers of 0.11 or 8 knots of ship speed. For ship design speed of 14 knots the resistance reduction is about 4-5 %. Similar conclusions can be drawn from the half load draught tests, about 6-8% resistance reductions were observed for the design speed. The plot regarding half draught tests is given in Figure 3.27.

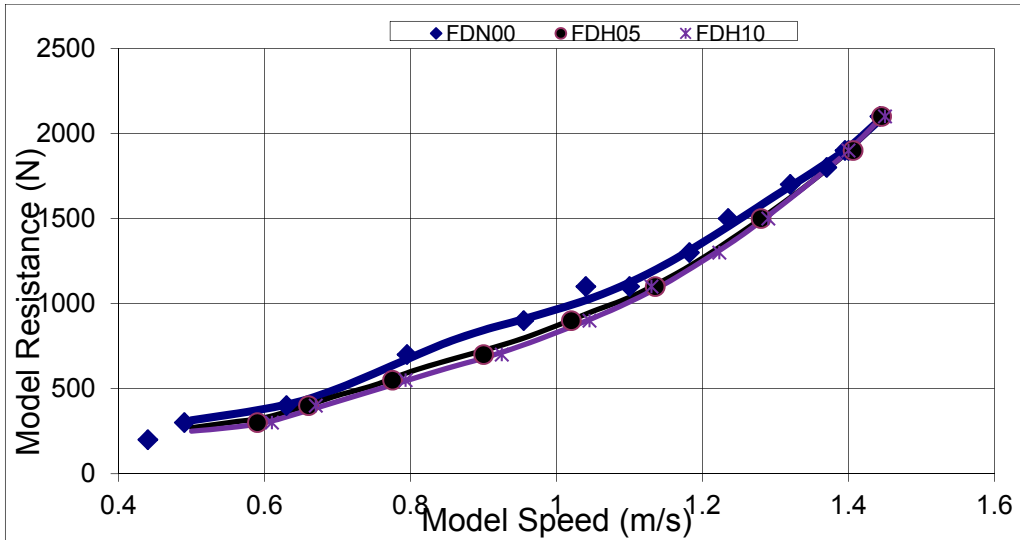


**Figure 3.24 :** Full Load Draught base model and single hole air lubrication comparison.

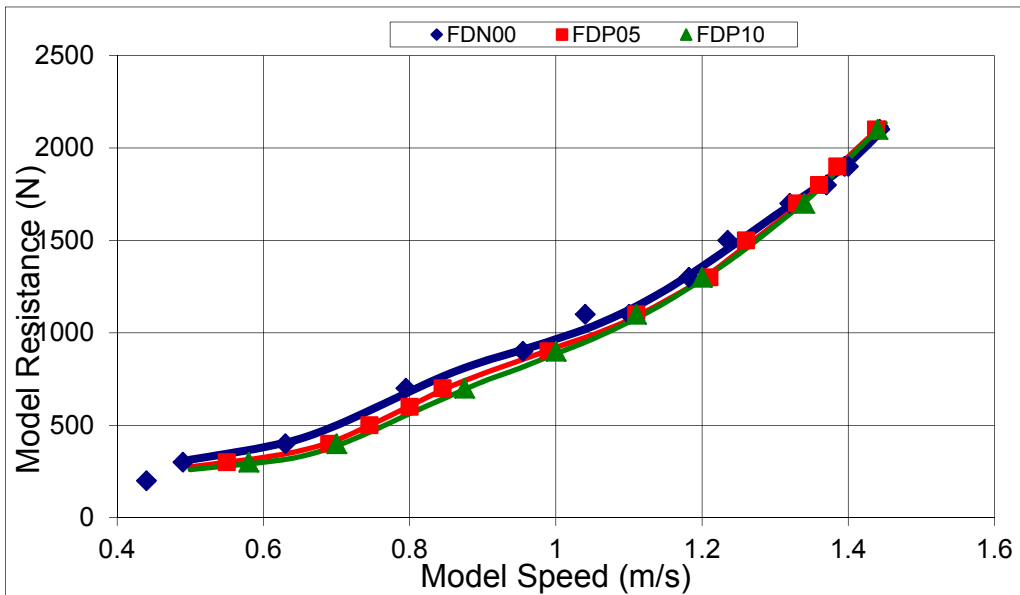


**Figure 3.25 :** Full Load Draught base model and porous media air lubrication comparison.

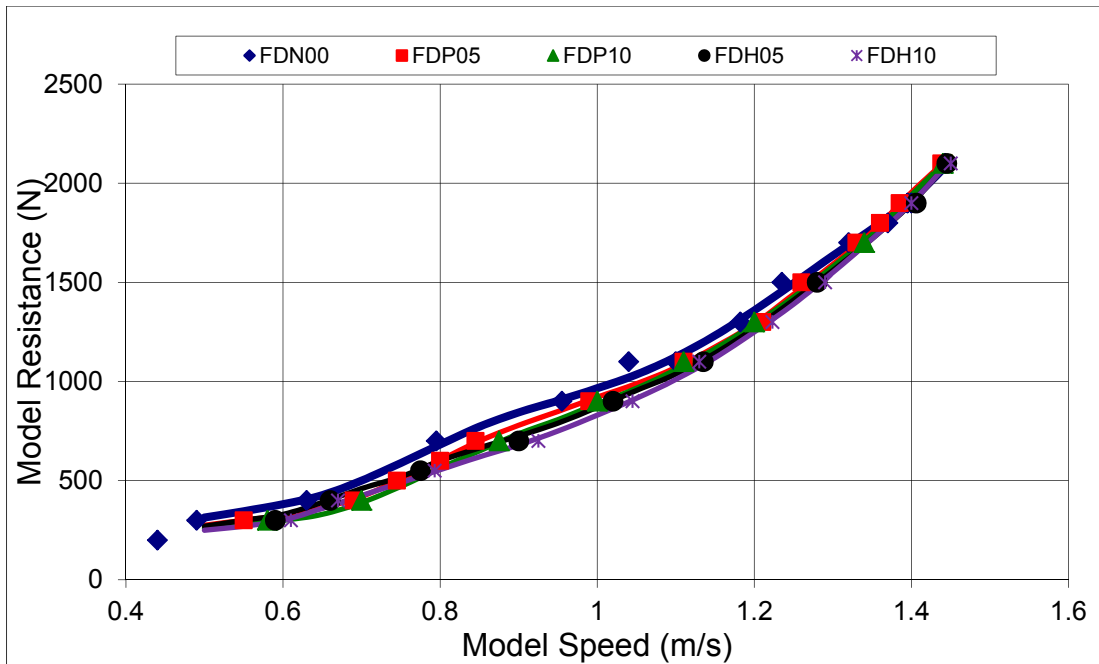


**Figure 3.26 :** Full Load Draught base model and air lubrication comparison.

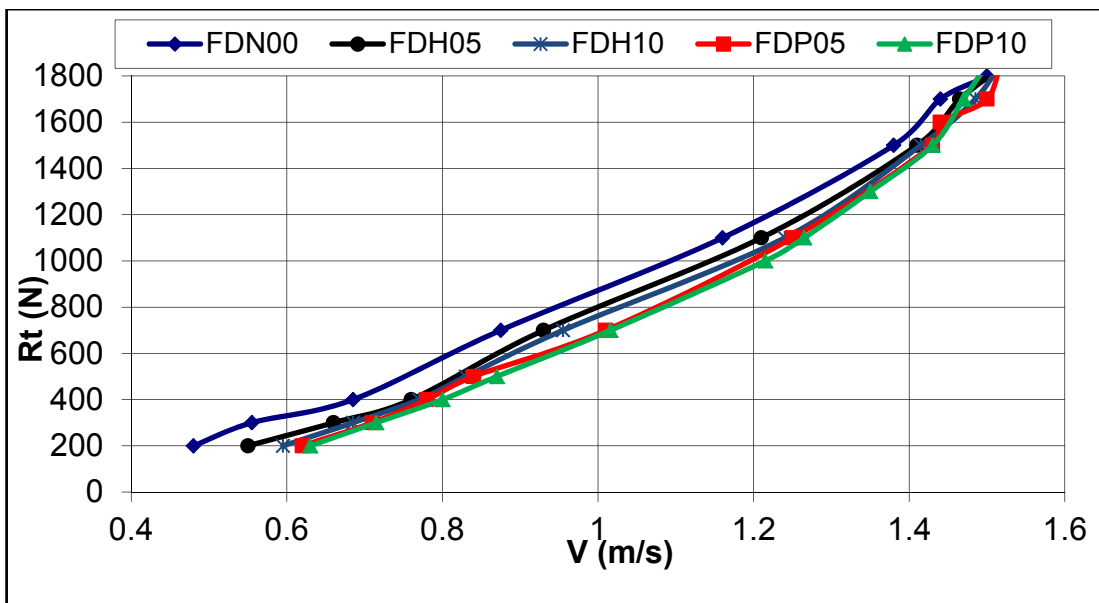


**Figure 3.27 :** Half Load Draught base model and air lubrication comparison.

Results from the wave pattern analysis are shown in the Figure 3.28. Wave pattern resistance results indicate that there is no noticeable difference among the hulls. Wave pattern resistance obtained is very low comparing to the total resistance within the tested speed range.

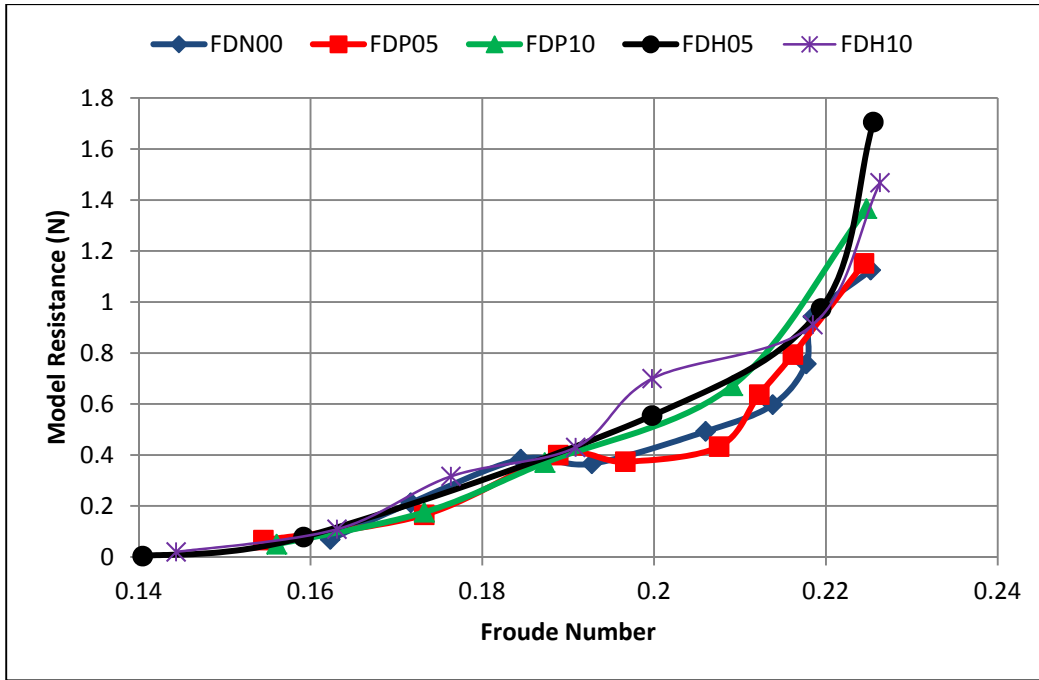


**Figure 3.28 :** Wave pattern resistance comparison between original and air lubricated forms.

It was expected that the escaping air would cause a distinct peak at higher frequencies, however, except for porous medium ventilation of 0.5 m<sup>3</sup>/h and at 1.44m/s, see Figure 3.28, no such peak was found. Low frequencies, however, were reduced at high speeds but amplified at lower speeds (See Figure 3.29). Possibly, this can be explained by the interference with the bow wave crest with the position of the ventilation strip. Though an effect of the waves was traced, its contribution to the total resistance was in the order of a few percent. As wave pattern resistance usually underestimates the residual resistance, this could be seen as a reasonable result.

Summarizing the wave pattern analysis, the escaping air at model scale is able to affect the wave pattern, its contribution, however, is relatively small.

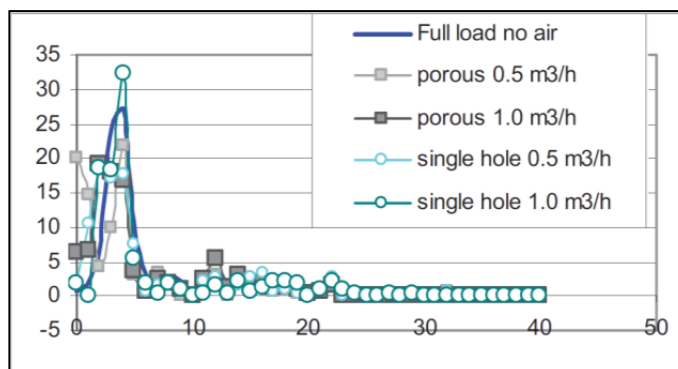


**Figure 3.29 :** Wave pattern analysis at 1.0 m/s.

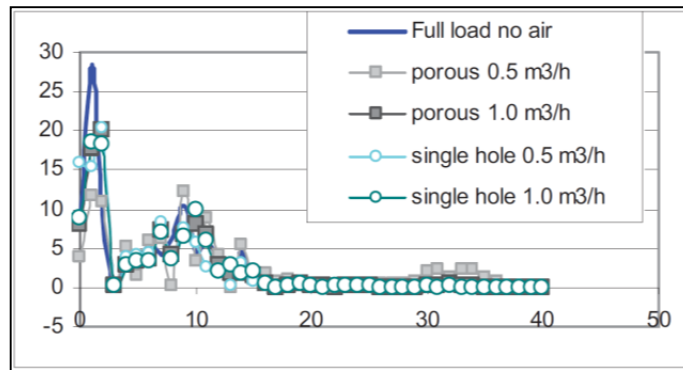


**Figure 3.30 :** Wave pattern analysis at 1.44 m/s.

### 3.5 Conclusions

The case study approach in this work indicates that resistance reduction in the range of 5% to 10% of the total resistance can be obtained in the model scale for lower speeds, even though resistance reduction at the service speed could not be achieved. However, it is too early to speculate the engineering benefits of the concept, because the power required to supply air was not calculated. Therefore, full scale results are needed to confirm such gains as scaling of air film shall differ from conventional ships.

Location and air supply rate of air feed has the prime importance for the optimum performance of air lubrication technique. Single hole air feed system is simpler but optimization of location air supply rate is very critical. Porous media air injection is possible to utilize for the creation of air film. The pore size and injection rates are also in need of further research for the best air film lubrication. Moreover, the difficulties encountered during the porous media air supply (corrosion of the sinter metal and negative changes in the filter performance) have shown that, it would lead many other practical problems while applying the technique in real world applications like fouling of the porous injectors etc.

This extensive research also appealed the attention of this thesis on single hole air lubrication. It was recognized that single hole injection gives almost same contribution to resistance reduction as porous media does. Additionally, application of the concept not only for new building ships but also for existing ships is practically more easier than other concepts such as air cavity or porous media. Due to the fact that, in order to gain further understanding on the mechanism of single hole

lubrication flat plate boundary layer experiments were scheduled. Next chapter will discuss deeper of the work done on this concept.



## **4. EXPERIMENTS ON BOUNDARY LAYER MODIFICATION BY SINGLE HOLE AIR INJECTION TO CROSS WATER FLOW**

### **4.1 Introduction**

Following the promising results of single hole air injection concept applied to a tanker's flat of bottom, an extensive research was initiated in order to gain further understanding on the mechanism of single hole air lubrication. Therefore, a simple model of a flat plate was selected and a test setup was established in order to conduct the experiments focusing on the boundary layer modification by air jet, injected through a single hole to cross water flow.

The experiments were performed in a circulating water channel; flow visualization studies as well as boundary layer measurements were also conducted. The analysis of the acquired data was performed by utilizing in house developed MATLAB code. Key factors of modification such as velocity of liquid phase, local void fraction, turbulence intensity profiles as well as wall shear were extracted from the acquired signals by utilizing a developed signal processing method.

Finally, modified boundary layer measurements were compared with the undisturbed boundary layer characteristics in order to understand the influence of the air injection on boundary layer modification. The results were also supported by the flow visualizations. The purpose of this chapter is to present an experimental method which was developed for a detailed investigation on air lubrication via single hole air injection.

### **4.2 Experimental Facility**

The experiments were conducted at the circulating water channel located at Istanbul Technical University Ata Nutku Ship Model Testing Laboratory. The photograph of the tunnel is shown in Figure A.4. This closed-circuit water channel has a 6m long test section with 1.5 m wide and 0.7 m depth. Water in the channel is accelerated by a potentiometer controlled electrical motor with a power of 35kW and maximum

revolutions is 1500rpm. The channel may be operated at steady empty test section flow speeds from 0.2 m/s to 2.5 m/s. However, due to bubbly flow formation and increase in free surface waves generated at low speeds higher than 1.2 m/s, high scatter in the velocity calibration of the channel was observed. Accordingly, highest velocity in the tests was limited by 1.1 m/s. At the flow speeds included in the test matrix, the channel's centerline turbulence level was measured between 2% to 3%. Additional channel facility details can be found in Gökçay, 2003 and Cussons Product Sheet. Circulating water velocity was set by the help of a potentiometer lever, which has an indicator located at the control panel, however there was no enough information (i.e. velocity calibration curve) supplied by the system manufacturer that corresponds the real water velocity to the lever indicator value. This velocity setting lever was calibrated by a special pitot tube before each set of experiments. Also possible shifts in the channel velocity calibration were checked at the end of each experiment set. Calibration of the circulating water speed with respect to potentiometer indicator lever is detailed in Section 4.3.2

Widely experienced problem encountered in such kind of open top type circulating channels is low transparency which leads to a dramatic decrease of the quality of flow visualization studies. In addition to that, this issue is crucial for the accuracy of the velocity measurements conducted by constant temperature anemometry in this study. Because low transparency means more particles are travelling with the flow (the higher ppm values of water) as a consequence, contamination of the measuring probe occurs which affects the voltage output of CTA hence the accuracy of the velocity measurements. Since the channel is located close to the model manufacturing area and other towing tank facilities, contamination of the water was observed in a short period of time due to open top channel configuration. In order to minimize the contamination of the circulating water, a filtration system which consists of a sand filtration tank, a circulating pump and a special 6-way valve were fitted. Additional chemical cleaning were provided by adding a few amount of Chlorine to the channel water against the gradual build up of fouling, scale, algae and minerals which is another important factor for transparency.

During the preliminary flat plate tests, free surface wave generation at upstream of measuring section was observed particularly for water speeds above 0.9 m/s which may lead an angle of attack with subjected plate. It was found that the height of the

water at the test section was dominating the wave generation characteristics. After some trials 700mm water level was determined as the best level and for the same application in each experimental setup, water level was marked at the side channel wall. It was also experienced that (also known common practice) putting a well adjusted flap has a damping effect on the generated waves. In order to ensure a stream wise parallel flat plate, an adjustable hinged flap is fitted with the purpose of reducing the amplitude of the generated free surface waves. The optimum position of the flap was found by CTA experiments by figuring out the minimum velocity fluctuations (root mean square of velocity records calculated) at the measuring section.

The channel measuring section has 4 side windows, enabling the observation of the model to be tested. The scope of the study was focused on the boundary layer modification of horizontal surfaces (i.e. flat of bottom of a tanker and a flat plate) so the bottom view of the experiment was also essential for the observation of the physical phenomena. Due to the fact that, additional 4 bottom windows were fitted. Underneath the bottom windows, a setup, including two tripods and a special illumination system was established, enabling the use of the high speed camera system. Details of the facility can be seen in Figure A.4.

### **4.3 Experimental Setup**

The test model was a rigid, flat-plate that measured 580mm long, 480mm wide and 15mm thick. In contrast with the experiments reported in Gökçay (2011) , flat plate was located in the test section horizontally. The plate was made of plexiglass to provide an hydrodynamically smooth surface and also processing of this material such as trimming, cutting and drilling is easier than others. Also the transparency of the plexiglass enables to perform a flow visualization by utilizing backlight method, considered as future work. Since the aim of this setup was measuring the boundary layer modification below the flat plate, the upper side of the leading edge was tapered by  $25^{\circ}$  to obtain triangular-wedge shaped leading edge, so the disturbance of the flow was minimized at the upstream of the measured flow field. Due to limitations of the test facility expressed in 4.2, in low Reynolds number flows, the negative effect of sharp trailing and side edges were not expected, therefore other sides of the plate were not machined and kept rectangular. The lower surface of the

plate was marked by a permanent marker with the grid interval of 25mm which was considered as reference lines to enable the distance measurements of regions that are focused on during flow visualizations.

Two types of fitting have been designed and manufactured in order to attach the plate. One was for air injection connections (4.5mm inner diameter), while the other was designed to fix the flush mounted boundary layer hot film probe (DANTEC 55R46) which was essential for measuring the local wall shear stress. See Figure 4.3. Air jet was injected through the lower side of the plate at one location with the help of those fittings. The fittings were manufactured from a brass tube. The upper part of the tube has a screwed section to provide fix attachment to the plate, the lower side of the fitting which is flush to the wall was smoothed by machining to ensure that no disturbance on the boundary layer was induced by fitting's surface. (Roughness was minimized) Both types have the same external diameter so the location of the fittings could be changed easily between the holes particularly drilled for fixing. The inner diameters differ from one type to another, because of the geometry of the flush mounted hot film probe. Due to the fact that the flush mounted hot film probes are direction sensitive, the fittings of the flush mounted probe has additional two set screws which prevents the movement of the cylindrical probe inside the fitting tube. Considering the risk of the fitting movement with the probe, lower flush surfaces of the probe fittings were marked such a way that the plate grids were matched. By this way the direction of the probe could be observed during the experiments. Bottom views of the fittings can be seen in Figure 4.15.

Both for air injection and local wall shear stress measurements, 5 holes were drilled in order to mount the fittings. One of them was drilled for air injection while the others were reserved for wall shear stress measurements. The air injection fitting named as AI, was located at the centre line of the plate. Three of the flush mounted fittings were located at the centerline and named as FM1, FM2 and FM3. Due to V shape form reported at Chapter 3.2, in order to understand the effect of the film edge on shear stress, FM4 was located 70mm away from the centerline transversely. Photograph of the flat plate, showing the air injection and flush mounted holes are given in Figure 4.15. Further details about stream wise and span wise locations of the fittings as well as measurement stations were given in Table 4.1:

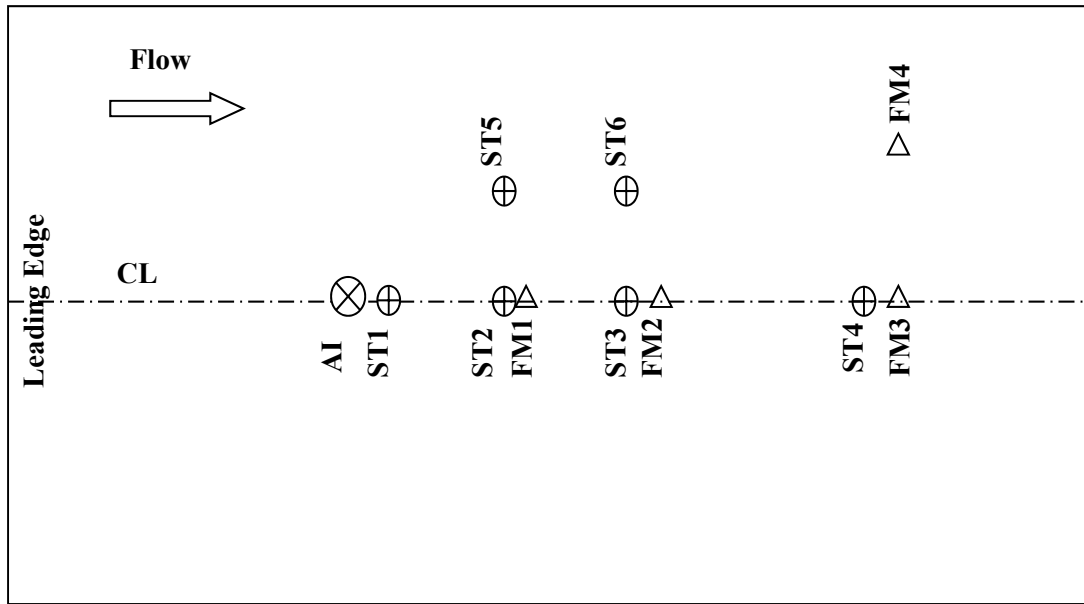


**Figure 4.1** : Schematic of the flat plate showing the air injection and measurement points.

For the reference tests conducted without air injection, smooth undisturbed flat surface was needed to gather reliable information about the boundary layer below the model. Therefore special kestamid pins were manufactured in order to close the holes of both air injection and the flush mounted probe. After pins were mounted inside the fittings a further check was performed to be sure that plate-fitting and the tip of pins was all flush thus the smooth flat plate condition was provided. Those pins were also used while conducting the air injection experiments in order to prevent the air escape from the holes which are not probe fitted or air injected.

**Table 4.1** : Positions of the air injection fitting and measurement stations.

Type	Dist. Fr. LE. (mm)	Dist. Fr. CL. Z (mm)
AI	150	0
FM1	230	0
FM2	305	0
FM3	380	0
FM4	380	70
ST1	165	0
ST2	215	0
ST3	265	0
ST4	365	0
ST5	215	50
ST6	265	50

The coordinate system used throughout the chapter has the X coordinate starting at the leading edge of the plate and extending downstream in the flow direction, Y is

zero at the flat plate bottom surface and vertical increases perpendicular to the flow and Z extends in the span-wise direction.

In flat plate experiments the various reports have stated the importance of the plate rigidity. That is why the thickness of the plate was chosen as 15mm plexiglass. Even low amplitude vibrations in the flat plate may cause a modification at boundary layer. In order to prevent vibration induced boundary layer modification, the plate was mounted to a stainless steel apparatus and suspended through a frame which carries the whole measurement instruments. See Figure A.5. The connection of the apparatus was manufactured from stainless steel plate which has 6mm thickness and consists of four stainless steel extrusion struts (each has 500mm length) that were welded on a steel plate. Welding of the struts to the plate enables the apparatus to be planar hence the stream wise and span wise leveling of the connected plate was provided. The plate of the apparatus were fitted with bolts at the corners in order to set the incidence of the plate for both stream and span wise direction.

When a blunt body is exposed to a cross flow, it is oblivious that flow separation induced fluctuating forces shall excite the body and depending on the mass, vibration of the body may occur. With the same analogy, in our case, additional free surface waves exposed struts at cross flow have more risk of vibration. That is why, the cross sectional area of the struts has crucial importance in terms of vibration. Therefore, struts were extruded from a stainless steel pipe in such a way that, the cross section was formed in elliptical shape. Moreover, elliptical shape struts have an advantage of lower drag, acting on the system, which enables the easier handling of the experimental setup.

Due to the fact that experimental facility used for other purposes like laboratory demonstrations for lectures as well as commercial experiments, it was needed to carry the system out of the facility frequently which increased the total set up time of the experiment. That's why majority of the experimental setup components such as flat plate, the struts and connection apparatus, air supply hoses, air filters as well as measuring instruments like air flow meter, flow rate controllers with their power supplies have been compacted on one frame in order to handle the setup easily. So totally complex measurement system was converted into all in one system (10 in 1), giving the opportunity to just position the frame, plug and measure.

### **4.3.1 Air injection system**

#### **4.3.1.1 Air supply system**

Air supply system consisted of a compressor, two sets of air filters and an air flow meter. The system components were connected by pneumatic pipes with flow directing valves and fittings.

In the previous study of air lubrication, a portable compressor was utilized as a mean of air supply. The air feeding capacity was only 25 l/h, which was not enough for continuous and stable air feeding. Sudden pressure drops due to low capacity were encountered when the motor of the compressor starts to work which reduces the air flow rate hence the instable air supply at the time of data acquisition. Those runs were cancelled and repeated. Frequent repeating was experienced particularly for higher flow rates. Therefore, another alternative for the air supply were required. The problem of the stable air feeding was solved after the use of air supply system of CNC milling machine. Ekomak DMD 75 type compressor was used which has the air feeding capacity of 49.2 m<sup>3</sup>/h, by consuming 5.5kW. This system is essential for cleaning of the sawdust created due to milling of a wooden ship model. The air feeding capacity was found satisfactory in terms of stable air supply for the flat plate air lubrication.

In order to control the intensity of airflow injected through the fittings, SMC-ITV2050 series electro-pneumatic regulator was utilized. This regulator is a pressure reducing device with two solenoid valves, a pressure sensor, a set of pressure membrane and a control circuit inside. It can reduce 1MPa. input pressure to 0.005 - 0.9 MPa range of output range. The device needs 24V of DC as a supply voltage. The adjustment of the reduction rate was provided by connecting the excitation voltage port of the device circuit to a transformer which can give 0 - 10V range of DC. The potentiometer of the transformer was set to a requested pressure. Output pressure, which would be the pressure at injection nozzle, could be monitored by the display of the device. Since the device had a limited display resolution, output signal port of the device has been connected to a multimeter. Output signal was also recorded in terms of voltage.

Supplied air from the compressor was filtered in order to prevent a potential damage on flow rate controller as well as on air flow meter. Two sets of filtration were

applied. The first one was located after compressor and had the capability to eliminate the particles of 10 $\mu$ m size while the second one was positioned before the flow rate controller. The purpose of the second one was the filtration of the particles as well as separating the mist due to condensation of pressurized air. SMC-AFM30-F03 series mist separator with the nominal filtration rating of 0.3 $\mu$ m were mounted with the SMC- AW30-F03H type mist separator regulator. During the experiments, regular drainage of the water stored in the separator was needed. Therefore, drain valve located at the bottom of the separator was switched on frequently. A pressure gauge, measuring the air pressure of 0 - 0.7 MPa range, was fitted to the separator regulator. (SMC-G36-10) When the main valve of the air supply system was switched on, firstly the mist separator regulator was set to a required pressure by the help of pressure adjustment screw located on separator. Pressure gauge was utilized while mechanical adjustment of air pressure. A sensitive pressure adjustment was performed electronically by electro-pneumatic regulator. Until the required flow rate value was adjusted on the flow rate meter's display, the potentiometer of the DC transformer which supplies power to flow rate controller was turned.

#### **4.3.1.2 Air flow metering**

One of the most important parameter that is forming the shape of the air jet, injected through the hole is surely airflow rate. Similar to experiments reported by Shen et al. (2006), Elbing et al. (2008) and Elbing (2009), air injection rate was monitored with thermal mass flow meter. IFM Effector 300, SD6000 type flow meter was fitted before the air injection fitting. The diameter of both inlet and outlet piping diameter was 21.3mm. An attention was paid to the potential turbulence effects on the flow rate measurements. Therefore, the piping of the device inlet was kept as 50D (1065mm) while the outlet was kept as 10D. Pipes used as inlet and outlet of the device were made of stainless steel. (316L)

This device had an air flow rate measuring range of 0.25m<sup>3</sup>/h to 75m<sup>3</sup>/h with the measuring error of 0.3% which was satisfactory. The flow meter could give an analogue output between 4-20mA enabling the acquisition on computer. However, due to achievement of a stable air supply system, there was no need to acquire the flow rate data in PC. Even the response time of the device was just 0.1s, the flow rate



value at the device's display was constant so the air flow rate was read from the display and noted for each run.

#### **4.4 Velocity Calibration of Circulating Channel**

##### **4.4.1 Instrumentation**

Velocity calibration of the circulating channel as well as the constant temperature anemometer were carried out by utilizing Wake Survey Device P300q, which is a measurement system designed for determination of three dimensional velocity field behind the ship model in propeller location. The device consists of two mechanical subsystems such as positioning and measurement subsystems schematically showed in Figure A.7. Power source of 1kW (230V,50Hz) is required in order to supply energy for both systems.

##### **4.4.1.1 Probe traversing**

Measuring probe was positioned by a traverse system, manufactured by Ship Design And Research Centre S.A. Structural rigidity is achieved by application of linear rolling bearings on each axis. Drive transmission from the stepping motors is carried out by use of ball screw in Z axis and trigger belt drive in X and Y axis ensuring slackless. Each axis has working envelope of 320mm. Linear bearings of each axis is secured with limit switches. Control of the system is provided using PC based controller according to ISO standard codes. Position detection is integrated in this subsystem. The subsystem has programmable resolution of 0.01mm, with the positioning accuracy of 0.2mm for each axis. (Repeatability of the positioning is 0.1mm for each axis)

##### **4.4.1.2 Five hole pitot tube**

Circulating channel calibration data were acquired by measurement subsystem that is based on the probe, pressure sensors and conditioning system. Spherical 5-hole pitot tube probe is utilized as seen on Figure A.3 in order to determine the pressure distribution in five positions in the sphere which enables to gather the flow velocity components. Measurements up to 6.5m/s water flow speeds can be carried out by this system. Pressure sensors and conditioning system is manufactured by KELLER. Pressure sensors have capable of measuring in the range of 0 to 0.2 Bar with the

resolution of 0.1mbar and have the resonant frequency more than 30kHz. The measurement probe had been calibrated by the device manufacturer for the velocity range of 0.6 through 6.5m/s and the measuring uncertainty of 5% had been reported in (Gökçay, 2011).

Five hole spherical pitot tube is an ideal tool to determine the velocity components of the flow being investigated. The flow direction is expressed in terms of pressure difference of holes. The pressure difference of holes can be expressed as a function of angle between flow and probe centerline. The constants in the subjected function can be determined by calibrating the probe in the calibration rig. Further theory and calibration details were given by (Pien et al., 1958). Velocity derivation from measured pressure values were carried out by an application supplied by the manufacturer.

#### **4.4.2 Circulating channel calibration procedure**

Circulating water velocity values, indicated by the potentiometer lever was calibrated by utilizing the spherical 5 hole pitot tube probe, mounted on a pod, which was fixed in the traversing mechanism. See Figure 4.5. Preliminary velocity measurements were conducted in order to find out the optimum flow regime obtained in the channel's test section.

The traverse mechanism was mounted on two aluminum extruded profiles (with a length of 1500 mm) so that the mechanism could be located easily by just sliding through the longitudinal direction of the test section. The ends of the profiles could be fixed to channel walls by a portable arrangement which was eliminated the risk of slack movement of the measuring system.

The probe was positioned at the centerline of the test section in span wise direction and three different locations were tested in stream wise direction to find out the best flow regime obtained in the test section within the velocity range. Also bottom windows of the test section were considered, while selecting the measuring section.

The traversing of the pressure probe during calibration was performed by the positioning subsystem of Wake Survey Device, which was controlled by PC based software. (NetMCP software) "G" codes for the intended positioning were created by notepad and the positioning codes were called from the subjected software.

In order to get a reference pressure values, zero speed measurements were performed while there is no circulation at the channel. Following the reference pressure measurements, pressure values were read across the range of potentiometer values from 10 to 180 which corresponds the water circulating speeds of 0.2 m/s to 2 m/s.

Three stream wise locations such as 1.38 meter, 2.38meters and 3.38meters downstream of forward end of the channel test section were scanned while the vertical position of the pressure probe was selected as 294mm below the still water level. Vertical position of the probe was determined considering the negative effects of free surface waves generated by the channel as well as the limitation of the pod which has pressure sensors at the top. At higher channel speeds, due to free surface waves, observed water levels were so close to pressure sensors which were crucial for the reliable pressure measurements.

Equally spaced 35 points in each stream wise location were scanned as 7 stations in the span wise direction and 5 stations in the vertical. This allowed the measurement of an area by 300X100mm, span wise and vertical direction respectively. In each point, pressure data was acquired by 10Hz. Velocity derivation from measured pressure values were carried out by software supplied by the manufacturer. (Wake 3D)

Finally, measurement section of 3.38meters downstream of forward end of the channel, was found to be the most satisfactory one. The RMS value of the velocity at this section was found as 1.7% of the measured velocity which was higher up to 3% at other sections. ( $V=1.182$  m/s) So this location of the probe was also marked for CTA measurements of flat plate tests.

Before and after each experiment set, speed calibration of the circulating water was conducted at the measurement section determined as above. The run procedure used for the calibration was as follows. Still water measurements were taken in order to get the reference pressures. The reference pressure values were used to derive the velocity data. The channel velocity was increased gradually for 20 potentiometer indicator values which corresponds twenty speed levels. Following to each increment, the data acquisition were delayed for 60 sec. which was required for a developed steady flow regime at the test section. The data acquisition was triggered for 10sec. During the acquisition the probe was traversed to 3 different points as one

at centerline position, one to the span wise direction and one point to the vertical. Following to acquisition the potentiometer lever was moved to achieve the next circulating speed. While waiting for the next speed level, the pressure values were converted into velocities by utilizing supplied software and the mean of the velocities calculated from three points were calculated. Finally those values were plotted in the calibration curve. This procedure was applied to all calibrations conducted for experiments.

A calibration curve of potentiometer indicator values versus circulating water speeds (m/s) is shown in Figure A.6. Generally speaking, it was found that the calibration curve was almost linear up to circulating speed of 1.25 m/s. Simultaneous free surface wave observations was also supported this finding. The waves generated by the channel up to that speed was almost negligible.(Max. of 15mm) In addition, above the circulating speed of 1.25 m/s the amplitude of the generated waves was dramatically increased up to amplitudes of 200mm which causes an angle of attack between flat plate and the flow. That is why the maximum achieved velocity at CTA flat plate measurements were limited by 1.1m/s.

In the channel calibration plot, two outlier curves could be seen. The curve CAL\_2003 belongs to the calibration conducted in 2003, with the measurements taken by a chronometer. The particles were feeded on to the free surface of the channel and circulating water speed was derived from the elapsed time measured between two points marked along the stream wise direction. The outlier curve CAL\_060411 was the plot of the calibration conducted with lower still water level about 600mm.

## **4.5 Measurements of velocity and volume of fraction profiles**

### **4.5.1 Instrumentation**

Boundary-layer modification experiments generally require the researcher to investigate the velocity field over the body of interest in order to gain an understanding of the mechanism acting on the boundary layer structure. Accordingly, parameters such as turbulence intensity and other characteristics can be derived from the velocity field. In our case, boundary layer of the flat plate had been modified by air injection. So, in such a case characteristic parameters required to be derived are

local void fraction profiles through wall normal direction as well as stream wise direction and the velocity information including second moments of the water phase.

If a technique such as Particle Image Velocimetry was employed, the duration of the experiment could be shorter because the global flow field could be observed almost instantly. However, there are certain limitations for these techniques, especially when the problem of interest is a boundary-layer flow. These methods cannot guarantee that a sufficient number of seeding particles will enter the boundary layer to provide well-resolved (in time or space) velocity measurements. Additionally, reflection of the laser due to the presence of wall, dramatically increases the uncertainty of the near wall measurements. Finally, in multiphase applications, bubbles or air slugs, behaves like a mirror and this phenomenon requires sophisticated software algorithms as well as special lighting techniques to be applied for a reliable image processing.

If an LDV technique was applied to a bubbly flow, then a low void fraction must be used due to the requirement for a clear optical path as in PIV case. It was reported by Migirenko and Evseev (1974), that the LDA signals become too weak for use at bubble concentrations exceeding local void fractions of 3%. It was also stated by Farrar and Bruun (1996) that LDA measurements in bubbly flow is restricted to low void fractions not more than 5%.

Hot film probes generally offer best opportunity to conduct measurements in flows containing a continuous turbulent primary phase such as water and distributed second phase in our case air bubbles and slugs; let's say in multiphase flows (liquid/gas or liquid/liquid flow). As the heat transfer is much bigger in liquids than in gases, a hot wire (or hot-film) can clearly distinguish between liquid and gas phase. For instance, when a bubble hits the sensor, an interaction will take place between the probe and the interface between the bubble and continuous phase. This interaction process can be used for signal-analysis purposes which will be discussed later in the thesis. In applying this technique, there is no significant restriction on the local void fraction (gas phase concentration) in contrast with LDV or PIV techniques.

Hotwires (the general term hotwire also covers hot films used in the study) have an excellent flat frequency response from 0 to 50kHz, therefore measurements up to several hundred kilohertz can be performed and can be positioned anywhere.

Additionally, the nature of the analogue voltage signals produced by constant temperature anemometers makes it possible to perform amplification and filtering processes that provide excellent sensitivity to small fluctuations.

Velocity field of boundary layer and free stream velocity measurements for single as well as two phase flow detailed in this experimental work were conducted by utilizing constant temperature anemometry (CTA) which is the principal research tool for most turbulent air/gas flow studies.

Due to the fact that, hotwires provide only single point measurements, using hotwires leads to long-duration experiments because the probe has to visit a tremendous number of locations in order to scan the domain of interest. This necessitates repeatability and consistency of the experimental conditions that, in turn, demands a completely automated system which means the probe traversing, data acquisition triggering as well as synchronized recording of the data with respect to the scanned point coordinates has to be controlled by one system simultaneously. This ability also enables a real-time analysis of the measurements which is essential for a carefully controlled experiment. Unfortunately, it was not possible to automate a basic type one channel constant temperature anemometer (Dantec MiniCTA) as a measurement system with the traverse adopted from a ship wake measurement device. So the data acquisition was triggered manually for each measurement station. That was the reason why the experiments took longer than expected.

All the experiments described in this work were controlled by a Dell Latitude E6400 personal computer with an Intel Core 2 Duo P8600 processor running the Microsoft XP operating system. This system is responsible for probe traversing as well as acquiring, storing and processing data. The data acquisition system includes a National Instruments 38A0261 USB A/D Unit data acquisition card, featuring a 16-bit resolution analog-to-digital converter. The card has an input range  $\pm 10V$  and provides a maximum sampling rate of 100 kHz.

#### **4.5.1.1 Principles of constant temperature anemometry**

The hot-wire anemometer was introduced in its original form in the first half of the 20<sup>th</sup> century. A major breakthrough was made in the fifties, where it became commercially available in the presently used constant temperature operational mode (CTA). Since then it has been a fundamental tool for turbulence studies. The constant

temperature anemometer is designed with the purpose of eliminating the influence of the thermal inertia of the wire in fluctuating flows, so that the frequency limit of the instrument is mainly determined by the electronic circuitry. This is achieved by supplying electrical energy to the wire at exactly the same rate as heat is lost to the surrounding fluid medium simultaneously. Since the wire temperature is thus kept constant irrespective of the flow velocity, the importance of the heat capacitance of the wire is greatly diminished (Jørgensen, 2002).

The working principle of the hotwire anemometer is based simply on an energy balance: the heat generated in the wire due to electrical resistance is dissipated by the forced convection cooling by air/water moving across the wire. The wire is placed in one arm of a Wheatstone bridge opposite a variable resistor, which defines the operating resistance, and hence the operating temperature of the wire. In the case the bridge is in balance, no voltage difference exists across its diagonal. Now, if the flow velocity increases, the wire resistance will tend to decrease and an error voltage will be present at the input of the current regulating amplifier. This will cause the probe current to increase. The wire will heat and increase in resistance until the balance is restored. Because of the high gain of the current regulating amplifier, a condition of bridge balance exists, which is practically independent of the flow velocity past the wire. The wire time constant is thus reduced by a factor of several hundred times from fractions of a millisecond to some few microseconds. The probe current is represented by the voltage drop across the bridge. As all resistances in the bridge are constant, the squared output voltage  $E^2$  directly represents the heat loss from the wire and can replace  $Q$  in the heat transfer equation for the wire. Ohm's Law and the convective heat loss are related by the heat flux  $Q$  can be written as:

$$Q = \frac{E^2}{R} = hA(T_w - T_a) \quad (4.1)$$

Where  $T_a$  is the ambient fluid temperature,  $T_w$  is the wire temperature,  $A$  is the surface area of the wire which the heat transfer occurs while,  $R$  and  $E$  is the resistance and the potential difference between the wire ends respectively. An increase in the fluid velocity increases the convective heat transfer coefficient  $h$ , hence the heat flux  $Q$  from the wire. This results in an instantaneous drop in the wire's temperature and an instantaneous decrease in the wire's resistance. The

resistance, and therefore the temperature of the wire, is held constant by monitoring  $R$  using a feedback-controlled Wheatstone Bridge circuit that varies the wire's voltage,  $E$ . As a result, any change in the fluid velocity is matched by an appropriate input voltage that maintains a constant wire temperature. The voltage is therefore directly related to the velocity as long as  $(T_w - T_a)$  remains constant. The temperature difference between the wire and the fluid can be adjusted by the overheat ratio, which is defined as the resistance ratio,  $R_w/R_o$ , where  $R_w$  is the resistance of the heated wire at its operating temperature, and  $R_o$  is the resistance of the sensor at ambient fluid temperature. During the experiments overheat ratios for water ranging from 0.1 to 0.8 was tried and it was observed that in higher water velocities like 1.2m/s the MiniCTA could not feed the bridge in order to provide the heat balance. Therefore in the velocity calibration curve, points of voltages stayed constant above 1m/s. Generally in hot film anemometry, higher values of overheat ratio is selected due to its potential of increasing the system's bandwidth hence the probe becomes more sensitive to changes in fluid velocity. On the other hand, large overheat ratios create thermal fatigue, decreasing the effective life of the probe. Also, wire cooling by natural convection can become significant at low velocities as the temperature difference  $(T_w - T_a)$  increases. As a result, the measured voltage may overestimate the actual fluid velocity. For the measurements performed in this work, an overheat ratio of 0.1 (The sensor operating temperature was about 45 °C) which was seemed to be the upper limit for water flow defined within our velocity range.

All the variables in Eq. 4.1 except the heat transfer coefficient  $h$ , can be measured directly. The heat transfer coefficient depends on the flow velocity vector, which can be characterized by the magnitude and the wire's angular orientation with respect to the incoming flow. These two parameters can be collected in a single variable by defining an effective cooling velocity,  $V_{eff}$  of the wire. The relationship between  $h$  and  $V_{eff}$  is determined experimentally through dimensionless parameters given by such as, Nusselt number ( $Nu$ ):

$$Nu = \frac{hd}{k} \quad (4.2)$$

Reynolds number ( $Re$ );



$$Re = \frac{\rho U d}{\mu} \quad (4.3)$$

Prandtl number (Pr);

$$Pr = \frac{C_p \mu}{k} \quad (4.4)$$

As well as Grashof (Gr) and Mach (M) number (Bruun,1995). Where, h is the heat transfer coefficient, k is the thermal conductivity,  $\mu$  is the molecular viscosity and  $\rho$  is the density while  $C_p$  is the specific heat of the fluid at a constant pressure. Obviously, U is used to refer the incoming flow velocity acting on the cylindrical wire element.

Inserting these dimensionless parameters in the energy balance given by Eq. 4.1, and collecting all the constants, the governing equation for convective heat transfer can be expressed in the form obtained by law of King (1914):

$$Nu = A + B Re_D^{0.5} \quad (4.5)$$

Where A and B are empirical calibration constants for each fluid. Another expression for convective heat transfer had been proposed by Kramers (1946), with the dependence of Re number as well as Prandtl number with below given formula particularly for  $0.01 < Re < 10000$  and  $0.71 < Pr < 1000$  range:

$$Nu = 0.42 Pr^{0.2} + 0.57 Pr^{0.33} Re_D^{0.5} \quad (4.6)$$

At assumed constant temperature, this relation can be rewritten in terms of potential difference applied to two ends of wire and the effective cooling velocity, which gives the final form of King's Law used in this work as in equation X. The exponent 0.5 from equation 4.5 is replaced by the variable  $1/n$ , so that better functional relationships can be obtained. Equation 4.7 directly links the effective cooling velocity to the hotwire voltage, and the constants in this expression are provided by proper calibration (Ergin, 2005). Detailed calibration procedure were given in 4.5.2.

$$V_{\text{eff}} = (A + BE^2)^n \quad (4.7)$$

During the experiments constant temperature anemometer of Dantec 54T30 one channel CTA (commercial name is MiniCTA) system was utilized. The system has built-in signal conditioner for high-pass, low-pass filtering as well as for amplification of the CTA signal. The signal conditioner of the system was used to apply low-pass filtering to each acquired signal. Cut-off frequency was selected as 300Hz so that electronic noise from the signal was eliminated. By this way, folding back of spectra (aliasing) was also prevented.

The anemometer has one power adapter input in order to gain 24V DC supply to the electronic circuits. The sensing probe is connected to the system with the help of 4 meter calibrated BNC coaxial cable.(calibrated in terms of resistance) Analog signals produced by the system was transferred through a BNC coaxial cable to National Instruments 38A0261 USB A/D analog digital converter (no calibrated wire needed). For the grounding of the probe, which will be detailed later, a 4 meter copper cable (1 x 2.5mm) was connected from the grounding electrode to the probe BNC connection located on the anemometer. MiniCTA anemometer measurement chain setup is also given in the Figure A.9.

#### **4.5.1.2 Single normal boundary layer probe**

Using hot wire anemometry in the area of fluid research is a bit complicated when compared with the gas studies. In the early hot wire investigations it was realized that, using hot-wire probes in a conducting liquid such as water caused electrolysis which is a major problem for an unprotected wire element. The potential drop across the wire causes electrolysis of the water and this was thought to be the cause of the formation of bubbles on the wire element. More crucially, it resulted slight but continuous reduction in diameter of the wire hence its cold resistance. Continuously shifting calibration makes an unprotected hot-wire probe useless for measurements in conducting liquids. To overcome the electrolysis, insulation material coated probes had been tried but it was difficult to make an homogenous thin coatings at that time. Thicker coatings had been tried but it was found that the probe becomes insensitive to velocity fluctuations. As a result it was not possible to study in conducting flows until the work of (Ling and Hubbard, 1956). Measurements in conducting liquids by hot wire first became a practical option with the development of thin (1-2 $\mu$ m) quartz coating on hot film probes. By this way, the electrolysis problem solved with the

negligible effect on the frequency response while, as an additional benefit, the coating protects the film material from abrasive particles present in the liquid. However, due to the presence of coating on the film, frequencies above 50kHz cannot be achieved in terms of frequency response.

In this experimental work, during the boundary layer and free stream velocity measurements, a nickel hot-film sensor manufactured by Dantec (55R15- Heavy Coating Boundary Layer Fiber Film Probe) was utilized. Fiber-Film probe has the cross section diameter of 70  $\mu\text{m}$  with the overall fiber film length of 3 mm. The sensitive length of the sensor is 1.25mm. The cylindrical film has gold plating at the ends and the film is protected by heavy quartz coating which has 2  $\mu\text{m}$  in thickness. Due to heavy quartz coating, the probe has lower upper frequency limit, therefore it is suggested by the manufacturer that, the use of this probe is better in liquids covering velocities up to 10m/s which fits well to our velocity range. The Characteristics of the probe were also given in Figure A.10.

The probe is specially designed for the use in boundary layer flows so that, the prongs of the probe is offset 3 mm from the probe axis to allow better access to the bounded wall. In order to fix the probe to the traverse mechanism in fluid, water proof probe supports were needed. Those supports also provide electrical connection to the coaxial cables. In the current study, two types of probe supports were tried. Former two sets of experiments were carried on with Dantec 55H20 short support (the overall length is 21mm) and final experiments were conducted with 55H21 long support (the overall length is 235mm).

The supports need to be attached to the traverse arm probe, which has a fine streamlined shape to prevent potential vibrations induced by vortex shedding originated from underwater structure. The traverse arm probe was manufactured as two parts, which are connecting part to the traverse pod and the conically tipped longer part, holding the support. As wake traverse device was used for the traversing, the original probe of the system a 5-hole pitot tube mentioned in 4.4.1.2 was utilized. The connecting part of the new probe to the traverse pod was manufactured as same as the pitot tube connection (there was 5 hole and one extra key hole to prevent slack movement) and from 316L stainless steel while the conically tipped longer part (3 types) was manufactured from stainless steel at the first one, and from 7000 series aluminum bar for the others. The overall length of the parts were 378mm and the

diameter was 30mm. The length was selected in order to provide an access closer to the air injection point which is close to the leading edge of the flat plate. Three types of traverse arm probe was tried. First and the second one was fitted with short support while the last one was fitted with the longer one.



**Figure 4.2 :** Probe types used in the experiments.

The first combination includes, the connecting part, a stainless steel conically tipped longer part and a stainless steel 8mm diameter tube. The longer part was machined in order to create a slot with the depth of 4mm and the tube was fixed on the slot by spot welding. The tube's leading tip was specially machined for support mounting. In order to provide a slackless attachment of the support to the tube, mini o-rings were utilized. Firstly, O-rings were mounted on the aft end of the support and then, the support together with o-rings, placed slightly into the stainless steel tube. The cable of the support which provides BNC connection was passed through the tube. The practical problem encountered with this combination was; due to an elastic material such as o-ring, axial direction of the probe was not fixed well. The other problem was, the minimum suitable stainless tube could be found had the outer diameter of 8mm, which means the center of the tube axis can get closer to the wall with the maximum distance of 4mm. Considering the offset of 3mm by the prongs, designed especially for BL measurements we had only 1mm gap, just in case of the tube had a contact with the flat plate wall, which means you have to go a bit further away and resulted with 1.5mm distance between the probe and a wall at least for the initial BL

scan point. Obviously it is not small enough distance for near wall investigation, for instance in current experiment the velocity measurement at 1.5mm from the wall corresponds 66 % of  $U_{0.99}$  at 1.1m/s.

The second combination includes, the connecting part and an aluminum bar tapered at leading edge. In contrast with other two combination there was no tube neither a long support attached on it. The attachment of the short support was provided by a slot, machined at leading edge tip. The short support was fixed directly on the slot with the help of thin wires and duct tape. In this combination, the BL probe was perfectly approached to the wall. However, during the air injection experiments it was realised that the multiphase flow regime was dramatically affected by the blunt geometry event the tip of the bar was below the flow regime and the tip was tapered. Due to the fact that, a longer support DANTEC 55H21 was ordered with parallel to manufacturing of the new traverse arm probe.

The last combination includes, again the same connecting part and an aluminum conical longer part with long support attached on the machined slot. The length of the traverse arm probe was optimized by the experience gained from previous experiment sets. DANTEC 55H21 long support was used in order to fix the boundary layer hot film and the support was fixed into the slot of traverse arm probe by using just duct tapes.

Common challenge, in the area of boundary layer measurements with hot wires is; the accurate distance measurement between the wire and the wall. The common practice used for the subject is using capacitive or inductive proximity sensors. Unfortunately, those sensors are usually designed for use in air therefore it is more expensive to find a waterproof one. Additionally, using plexiglass as a flat plate (non metal wall) makes inductive sensors impossible to use. The capacitive sensors was not the option either since in fluid flow the capacitance is changing with distance as well as the velocity of the surrounding liquid.

Another way of closest distance measurement between wall and the probe is calibrating the distance by the help of set screws. By doing this, a careful experimentalist can calibrate the initial (closest) distance of the probe and get the other distance information from traverse system. In our case, second option was selected. The traverse arm probe was fitted with four set screws, two of them were

located close to the hot film probe as close as possible and aligned so that a calipper can easily measure the distance between the tip of set screws and upper tangent of the probe support tube. Geometrically, distance between the tangent and the tip of prongs was known and calculated as 1mm. So it was enough to fix the set screws by covering duct tape in calibrated position (1.1mm) and touch the tip of screws to the wall by slow traversing. At the time of contact, recording of traverse wall normal coordinates concludes the distance calibration. Additionally, set screws were used as a securing device which prevents the probe crashing to the wall, because the tips of the screws arranged with the calibration so that, before the prongs of the sensor, screws have already contacted to the wall. This process requires some patience, because four set screws has to be aligned in same manner respectively. After the alignment, final check has to be done by putting the traverse arm probe reversely on an exactly flat table.(i.e. CNC milling table) By this way, distance between the prongs and the surface can be easily measured with the help of caliper. See Figure 4.3.

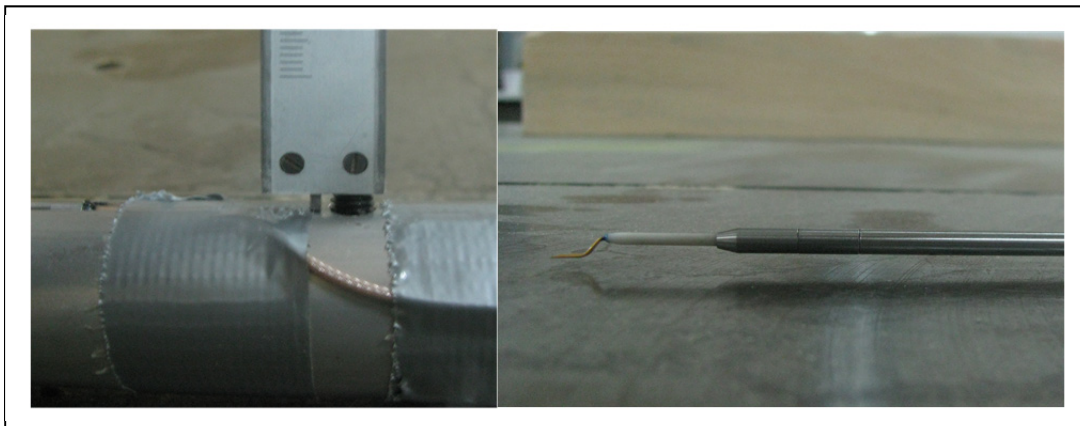


**Figure 4.3 :** Distance calibration of BL probe to the wall.

Before putting in the water, the film probe has to be grounded according to the instructions given with the CTA system. In case of a voltage difference between the sensor film and the liquid builds up by electric charges in water, the insulating quartz coating may break down and the thin-film will be etched away due to electrolysis. The liquid must therefore be grounded to the anemometer's signal ground as close to the probe as possible. Therefore, a copper plate of 30 x 100mm was shaped according to traverse arm probe and fixed on the side by waterproof tape. Four meter copper wire was connected to the plate from one end, and to the CTA grounding from other.

#### **4.5.2 Probe Calibration Procedure**

In contrast with the LDV systems, hot wire anemometry requires velocity calibration experiments which need to be carefully controlled. Another important aspect of hot wire is, due to temperature changes or contamination the sensor response changes by time. This reality necessitates the frequent calibration experiments which are essential for an expected measurement uncertainty.

Since the direct output from the hot-film anemometer is a voltage, the purpose of the calibration experiments is to obtain enough relationship between the voltage given by the anemometer and the corresponding velocity of the liquid phase where the probe is placed in. The voltage measured from the anemometer can be expressed as a function of dominating parameters such as:

$$E = f(U, T) \quad (4.8)$$

Where,  $U$  is the velocity component in the mean flow direction, while  $T$  is the temperature of the surrounding liquid. Assuming the experiments is conducted in constant temperature for both calibration and measurement phase; temperature dependency can be eliminated. So the calibration of the probe involves, obtaining a set of calibration points for reference velocities versus corresponding voltages. It is suggested by Bruun (1995) that, at least 10 calibration points, spaced evenly over the selected velocity range is needed for a satisfactory calibration. Accordingly, the equation of fitted curve of  $(E,U)$  plot gives the relationship(transfer function) which is used for the data reduction. The question rises here is how can be accurate reference velocities obtained? This can be achieved by calibration using specially designed facilities or in-situ calibration.

##### **4.5.2.1 Calibration using specially designed facilities**

The most satisfactory arrangement is to calibrate the hot-wire probe in the facility in which the measurements are to be taken, since the disturbance caused by the probe and its holder and the influence of the geometry of the test facility will be the same during the calibration and experiment. However, in practice it may not always possible to carry out such a calibration. For instance, in our former experiments there was no opportunity of using the spherical pitot tube in circulating channel and also stated before there was no reliable velocity information given for the channel. Due to

these restrictions, it was necessary to calibrate the probe in either a small circulating channel designed for this purpose (suggested by DANTEC) or in a separate, special, calibration facility. That is why; a calibrator for our velocity range was designed and manufactured.

The set up includes a flexible hose (24mm diameter) which drains the circulating channel by the help of a valve located at the bottom of the channel, a filter, flow meter and a Plexiglas pipe (22mm inner diameter). By connecting all of these components in the serial form a calibrator for the hot-film were provided. For the calibrator setup see Figure 4.4. Before the calibration starts, the probe is located at the center of the Plexiglas pipe. The traverse arm probe was fixed by clamps in order to prevent the movement while water is flowing out of the pipe. The velocity of the flow was arranged by the adjustment of the draining valve, with a small adjustment in valve yields the different reading in the flow meter. To relate the flow rate  $Q$  to the centerline velocity  $U_c$  at the axial position chosen in the pipe, as described in Samways et al. (1994). Based on mean velocity profile measurements at the selected axial position it was founded that:

$$U_c = 1.202U_a - 0.012 \quad (4.9)$$

Where  $U_a$  is the area-averaged velocity and can be calculated from flow rate  $Q$ , measured from the flow meter as given in the equation:

$$Q = U_a \pi R^2 \quad (4.10)$$

where  $R$ , is the radius of the pipe. Knowing the functional form of equation (4.9) enables a complete computer based calibration of the probe placed on the pipe centerline to be carried out. Selecting 10 points covering the required velocity range (typically 0.1 – 1.4m/s), the values of ( $E$ ,  $Q$ ) at each point were acquired digitally. As the flow is turbulent (turbulence intensity was about 2%), recordings at each point were taken over a period of about 10s and the corresponding mean time values (ensemble averages) were used for the calibration process. The initial data obtained in the form ( $E$ , $Q$ ) where then converted into ( $E$ , $U_c$ ) data using equation (4.10). These data were fitted to curves by using a power-law relationship by King (1914). Also given in the detail by equation (4.7).



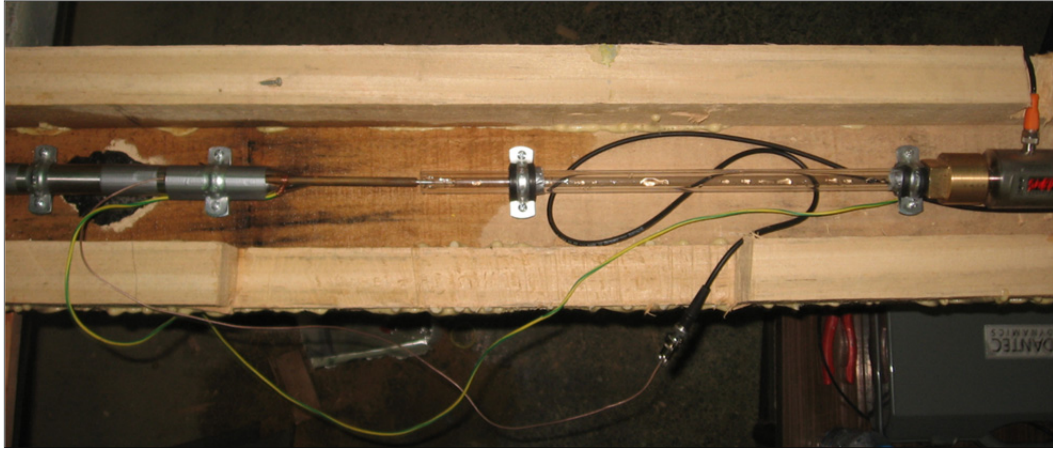


**Figure 4.4 :** BL probe calibrator.

However, this method was found to be an exhaustive one and had several disadvantages. The calibration has to be located at the bottom of the channel, because hydrostatic pressure was utilized while supplying the water to the calibrator but in order to conduct the experiments following calibration, the system had to be moved close to the test section. Such a movement requires the anemometer to be switched off and in many cases the disconnection and reconnection of probe and cables. Furthermore, the risk of probe failure is severe during the movement. This was a highly undesirable process since a large number of uncertainties may be introduced between the calibration and the experiment. Additionally, this type of calibration has extended the duration of the experiments from hours to days, when considering the need for frequent calibration of the probe. That is the reason why, ways of in-situ calibration was investigated and that method of calibration performed for the following experiments.

#### **4.5.2.2 In-situ calibration of the single normal boundary layer probe**

Experiences gained from the calibration by using custom built calibrator, have led to find out the way for in-situ calibration. Fortunately, a traverse system that was adopted from wake survey device had a measurement sub system which includes a 5-hole spherical pitot tube connected to pressure transducers. By using this probe two types of calibration were conducted.

First calibration setup involves the traverse system with the pitot tube mounted on the traverse pod and the probe mounted on the thin steel plate. With the knowledge of span wise flow uniformity of the channel which was determined by former

pressure measurements, the probe and the pitot tube were positioned at the same longitudinal section close to the measurement position. The velocity values gathered from the pressure transducers were utilized as input of probe reference velocities. By this way the probe was calibrated. The setup is shown in the Figure 4.5. Since the probe traverse arm have to be connected to the traverse pod during experiments, after each calibration the pitot tube had to be removed from the traverse pod and the calibrated probe had to be placed instead of the tube which requires again a movement of the calibrated probe as well as switching the anemometer on and off. The process turned out to be out of in-situ calibration.

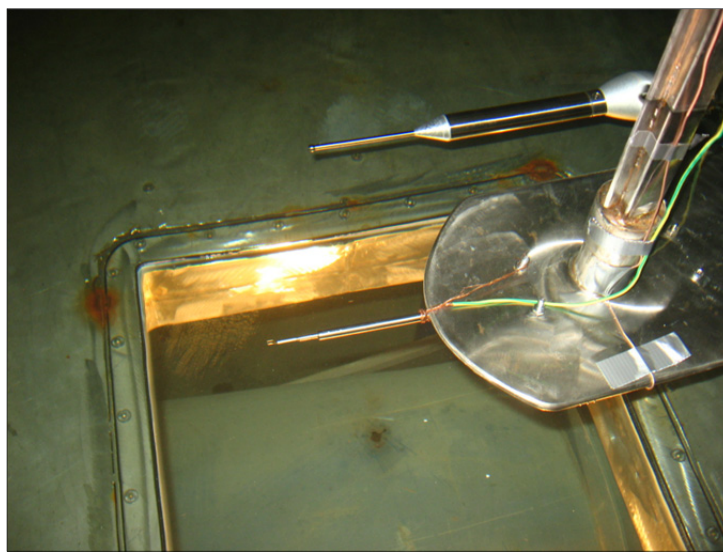


**Figure 4.5 :** Calibration of the hot film probe by pitot tube.

Therefore, calibration of the probe was conducted by calibrating first, the circulating channel and than the probe. Circulating channel calibration was assumed to be accurate enough after evaluation of the calibration curves obtained from more than 10 circulating channel calibrations. This procedure was given in 4.4. Before and after each set of experiment, the channel was calibrated by pitot tube. In case of no shift between two calibrations, velocity values were used as the reference velocities for the calibration.

In order to correctly use the data of channel calibration as a reference, all hot film probe calibrations were conducted in the same conditions as stated in 4.4. Before the calibration, the still water level of the channel was checked with the help of level markers fixed on the observation windows, since the water level was found to be the dominating factor on the circulating water velocity. The probe of the digital thermometer was put into the water to provide a real-time monitoring of the water

temperature. More than 0.5 °C change in the temperature yields a new calibration. The frame which carry the whole setup was rotated 90° clockwise so that the flat plate was put into water. By this way the flat plate was positioned 224mm below the still water level. The traverse system with the hot film probe attached was longitudinally positioned upstream and vertically 70mm below the flat plate (294mm) in order to be sure that the probe is outside the boundary layer, at free stream as shown in Figure 4.6:

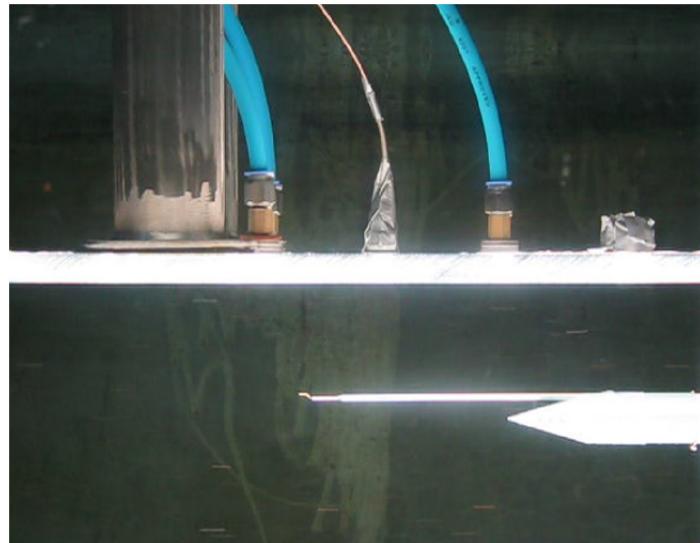


**Figure 4.6 :** In-situ calibration (70mm out of the wall).

The run procedure used for the calibration was as follows:

-The MiniCTA software was started and configured for the current setup. Configurations such as: the type of the probe with support and the length of the coaxial cable were selected from the software's library. Resistance values of the current probe and the overheat ratio was defined in the probe details module. Finally A/D card data acquisition options such as sampling rate and the total number of data samples were given by using hardware setup module. For the calibration, data was acquired with the sampling rate of 1kHz and with the total of 10.000 samples which makes elapsed time of 10seconds for each calibration point.

-The calibration module of the software was configured for 12 evenly spaced calibration points starting from 0.16m/s to 1.25m/s corresponding for the potentiometer indicator values from 10 to 120 with the increment steps of 10.

-For each speed level, data acquisition was manually triggered from the software for 10seconds.

-After the data acquisition for that point, the corresponding voltage was recorded to the system and could be observed from the calibration plot, given by the software. In case of a big scatter, data could be acquired again to obtain better calibration fit.

-Following to acquisition the potentiometer lever was moved to achieve the next circulating speed and the acquisition for the new point was delayed for 60 seconds, which was required for a developed steady flow regime at the test section.

- Once data has been obtained across the velocity range of interest, the software uses the power law algorithm to estimate best fit values for the calibration constants A, B and n. Typical calibration plot is given in the Figure 4.7:

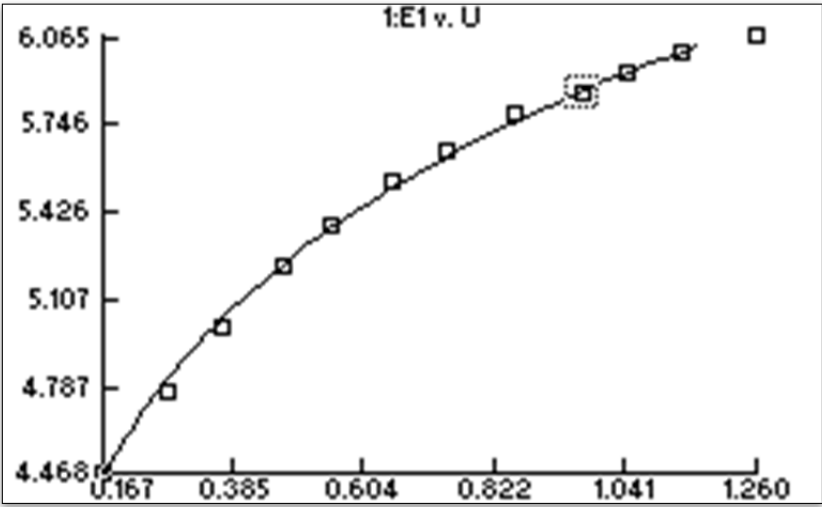


**Figure 4.7 :** Typical calibration plot with curve fitting.

There are some difficulties associated with hotwire velocity measurements. As explained by Bruun(1995) the application of hot-film probes in water can be severely affected by drift of the calibration due to the accumulation of contamination on the surface of the sensor. In order to minimize this problem a relatively coarse sand filter was fitted to the circulating channel. Unfortunately, the filter used could not completely eliminate the water contamination problem. An experiment was performed for ten minutes period, in order to understand the effect of contamination on voltage drift of the CTA. Data were taken with an interval of 1 minute, with a sampling time of 10 seconds and that was found that 6% of velocity reduction was observed, see Figure A.8. Consequently, frequent probe calibrations were crucial for the accuracy of the velocity measurements. Compensation of calibration drifts were proposed by Jørgensen (2002) in case of linear drifts with respect to time by using transfer function based on the averages of velocities calculated from identical voltage

values inserted into the transfer functions from the first and the second calibrations which can be summarized with equation (4.11).

$$U_{av}=(U_1+U_2)/2=(f_{cal1}(E_1)+f_{cal2}(E_1))/2 \quad (4.11)$$

However due to observation of random drifts even within a short period of time, calibration of the probe were carried on before changing of each water speed. After each acquired data point, mean voltages and combined velocities from calibration can be monitored in the CTA software, which enables comparing of the actual data with expected values. In case of sudden drift, running experiments were interrupted and recalibration of the probe was performed.

#### **4.5.3 Data Acquisition and Run procedure (Test Matrix)**

During experiments, the signals from the CTA were acquired by Dell Latitude E6400 personal computer. Mini CTA software were utilized for the data acquisition which was triggered manually from the software. National instruments 38A0261 USB, 16 Bit, A/D card was responsible for the digitization of the analogue signals. Since the signal conditioner of the CTA anemometer was set to 300Hz low pass filter for noise reduction, 1kHz of sampling rate was selected in order to satisfy the nyquist criteria. In order to determine the data sampling time, autocorrelation functions as well as power spectra of the signals were utilized. Due to random characteristics of the signal determined from the autocorrelation functions as well as low frequency content of the power spectra, 10 seconds of sampling time was determined for each data point taken during the entire experiment.

The run procedure for the boundary layer measurements with single normal boundary layer probe was as follows. Calibration of the probe was conducted longitudinally in station 1, which is the upstream station at centerline of the plate. After the calibration of the probe, the channel velocity was held constant firstly at the channel velocity of 0.55m/s (potentiometer indicator was set to 50) and the air flow rate was set to zero (no air injection), than the boundary layer scans were performed at six stations respectively where the coordinates of the stations were given in Table 4.1. For each station, 24 data points were acquired. The first and the last data point were taken from the free stream (71mm from the wall) as reference while the other 22 points were taken through the wall normal direction.

Travelling of the probe was controlled by the computer. “G” codes for the traverse were created for each measuring station. Traversing of the each station was triggered manually by calling the corresponding “G” code from the traverse software, but the wall normal movement was automatically performed by the traverse system with time steps of 15 seconds. As soon as the probe was traversed to the next data point, the data acquisition of the CTA system was triggered manually from the MiniCTA software. Since the data sampling time was 10 seconds, for each data point only 5 seconds of delay was arranged for manually triggering of the data acquisition. The distance between data points in wall normal direction was arranged so that, dense acquisition near the wall was provided in order to gather more information close to the wall. As the probe is travelling further away from the wall, distance between the data points was gradually increased. Following the completion of scanning 6 stations for undisturbed boundary layer measurements (no air injection), the pin of the air injection fitting mentioned before was removed and the air injection system was activated. By real-time reading of the air flow meter, air flow was set to the next value which was  $1.4 \text{ m}^3/\text{h}$ .

The same procedure was repeated for the flow rate setting of  $2.8 \text{ m}^3/\text{h}$ . As a result, experiments for the channel water velocity of  $0.55 \text{ m/s}$  was completed. Prior to next flow speed experiments, the hot film probe was calibrated with the procedure given in 4.5.2.2. Above detailed procedure was repeated for the channel flow speeds of 0.88 and 1.08 respectively (corresponding potentiometer indicator values of 80 and 100).

#### **4.6 Local wall shear and wall void fraction measurements**

Reports of various experiments on air lubrication have indicated that, drag reduction achieved by air lubrication was mainly provided by the modification of turbulence transport particularly realized at buffer layer as well as at viscous sub layer of the boundary layer. In addition it was commonly stated in the reports that the major problem encountered in the area of air lubrication is lack of downstream air persistence through near wall region. Moreover, local frictional quantities are also active topic of interest regarding the effectiveness of the air lubrication locally. So in order to gather enough information on these important points, parameters such as

local void fraction at the wall as well as wall shear stress have to be acquired both in terms of amplitude and frequency spectrum.

Utilizing single normal boundary layer probe for those purposes usually do not conclude with successful results due to these reasons. First, physical restrictions (i.e: probe damage in case of wall contact) while approaching the wall, prevent the required positioning of the hot film probe, so the sensing element is positioned at the outer layer. Second, uncertainty of the measurements performed near the wall is increasing due to heat convection to the wall. This causes over estimated velocities due to the influence of wall. The wall influence starts at  $y^+ < yU_\tau/\nu = 3.5$  where  $y$  is distance to the wall,  $U_\tau$  is the frictional velocity and  $\nu$  is the kinematic viscosity. The critical wall distance starts about 0.2mm depending on the free stream velocity (Khoo et al., 2000).

Due to the fact that, particularly for local wall shear stress measurements, there are several techniques available. Techniques such as preston tubes, stanton tubes, sub layer fences, small floating-element balances, electrochemical shear stress meters and flush mounted hot films were developed and tested for a wide range of flow applications (Madavan, 1984). A good review on the subject is provided by Hanratty and Campbell (1982). With the purpose of measuring the local void fraction at the wall, techniques such as high speed camera imaging (by processing binary bubble images) and electrical impedance probes are frequently utilized. Details, regarding the application of those techniques are given by Murai et al. (2007) and Elbing (2009) respectively.

In the present study, flush mounted hot film probe was employed in order to measure both wall shear stress and wall local void fraction. To the author's knowledge it is the first time that, flush mounted hot film probe was utilized as a flushly mounted void fraction probe.

#### **4.6.1 Instrumentation**

In this experimental work, during the wall shear stress and local wall void fraction measurements, a nickel hot-film sensor manufactured by Dantec (55R46- Heavy Coating Flush Mounted Hot Film Probe) was utilized. Hot-film probe has the sensor diameter of 0.75 x 0.2mm. The sensing part is fitted and compacted on the top of a stainless steel cylinder with the diameter of 2.5mm. The sensor is protected by heavy

quartz coating which has 2  $\mu\text{m}$  in thickness. The further characteristics of the probe is given in Figure A.10. The probe was fixed inside a manufactured fitting as mentioned in 4.3 and fitted flushly on the plexiglass flat plate.

Like in the boundary layer velocity profile and void fraction measurements, same type of constant temperature anemometer of Dantec 54T30 one channel CTA (commercial name is MiniCTA) system was utilized. Due to difference in sensor resistance and frequency response, another CTA was employed which was configured particularly for Dantec 55R46.

The anemometer has one power adapter input in order to gain 24V DC supply to the electronic circuits. The sensing probe is connected to the system with the help of 4 meter calibrated BNC coaxial cable.(calibrated in terms of resistance) Analog signals produced by the system was transferred through a BNC coaxial cable to National Instruments 38A0261 USB A/D analog digital converter (no calibrated wire needed). The setup is given in the Figure 4.8. Same MiniCTA software was utilized to acquire the data as used in the boundary layer scans.

Since the operational principle of the flush mounted hot film probe is to relate the heat transfer rate from the film to the shear stress at the wall, in order to calibrate the probe, a flow regime has to be obtained where the shear stress is known. The wall shear stress can be obtained either from theory or an independent measurement. During the flat plate experiments it was experienced that a zero pressure gradient flow could not be obtained, so theoretical calculations could not used for the calibration purposes, so it was necessary to conduct independent measurements. Therefore a special calibrator was manufactured which involves a magnetic inductive flow rate sensor, a Plexiglas module, water supply system and flexible hoses which connect these three components to each other. Details of the setup is given in the Figure 4.8.

Similar to air flow rate measurements reported in the experiments with hot film boundary layer probe, water flow rate was monitored with magnetic inductive flow meter. IFM Effector 300, SM7000 type flow meter was fitted in the line of water feeding hose of the calibrator, so that the flow passes through the calibrator can be acquired in real-time. The diameter of both inlet and outlet piping diameter was 16.6mm. An attention was paid to the potential turbulence effects on the flow rate



measurements. Therefore, the piping of the device inlet was kept more than 5D (100mm) while the outlet was kept more than 2D. Pipes used as inlet and outlet of the device were made of stainless steel. (316L)

This device had an water flow rate measuring range of 0.01m<sup>3</sup>/h to 3m<sup>3</sup>/h with the measuring accuracy of 0.5% and the repeatability of 0.2% which was satisfactory. The flow meter could give an analogue output between 4-20mA enabling the acquisition on computer. However, due to achievement of a stable water supply system by arranging the valve connected to the calibrator line, there was no need to acquire the flow rate data in PC. Even the response time of the device was 30s, the flow rate value at the device's display was set to a constant value after a while, so the air flow rate was read from the display and noted for each run.

Water supply system involves a tap and a flow regulator valve, so that the water flow rate can be arranged in order to obtain various flow rate values for the calibration points.

#### **4.6.2 Probe Calibration Procedure**

In laminar boundary layers, this relationship between the heat transfer and the shear stress is embodied in the Reynolds's analogy. Drawing on basic heat transfer theory it is possible to arrive at a relationship between electrical heat dissipation an the wall shear stress. For constant temperature operation of the film, this relationship between voltage output by the anemometer, E which is directly related to the electrical heat dissipated and the shear stress,  $\tau_w$ , is of the form in (4.12)

$$\tau_w^{1/3} = AE^2 + B \quad (4.12)$$

Where A and B are constants. Sufficient experimental evidence is given by Bellhouse and Schultz (1966) showing that a relationship given in the equation (4.12) above is also valid in turbulent boundary layers where the thermal boundary layer is thinner than the hydrodynamic boundary layer (Madavan, 1984). It is obvious that in the case of turbulent flows, due to the turbulent fluctuations, the output voltage and the shear stress values given in the equations are time dependent.



**Figure 4.8 :** Flush mounted hot film probe calibrator.

The constants A and B given in the above equation must be determined by a calibration procedure in a flow where the shear stress is known. Fortunately there is a simple way of obtaining a laminar flow conditions. By utilizing fluid flow between two parallel plates which have a small gap inside, a laminar flow conditions can be achieved and wall shear stress can be found by driving the equation 4-13 based on velocity gradient of the flow,

$$\tau_w = \mu \frac{du}{dy} \quad (4.13)$$

By integrating the equation given by 4-13, wall shear stress can be achieved in terms of water flow rate of the calibrator as given in 4.14 (Çevik, 1997);

$$\tau_w = \frac{6Q\mu}{a^2b_w} \quad (4.14)$$

Where, Q is the water flow rate of the fluid passing through the calibrator, a is the distance between the parallel plates (height of the gap) while b is the width of the gap and  $\mu$  is the dynamic viscosity of the fluid.

The calibration process is illustrated in the Figure 4.8 and the steps given below were followed during the calibration:

The probe was flushly mounted to the calibrator top plate with the help of manufactured brass fittings, same as used in the flat plate.

Tap water was connected to the calibrator and the flow rate was adjusted to the minimum flow rate value by opening the valve. Since the principle of the flush mounted hot film is heat dissipation, it is important to perform measurements in a constant temperature condition so the changes in the fluid temperature has to be noted carefully in order to apply temperature corrections. Fortunately, the flow rate sensor has the ability of measuring temperature which enables simultaneous temperature measurements with flow rate. Therefore, after waiting for a minute, the fluid temperature was monitored from the flow rate sensor and noted manually.

For each calibration point corresponding to a constant flow rate, flow rate  $Q$  was monitored from the sensor and noted manually while voltage information was acquired via PC with the sampling time of 10s and the frequency of 1kHz.

An Excel program was utilized in order to convert the  $Q$  information to wall shear stress  $\tau_w$  by driving the equation 4-12. Obtained  $\tau_w$  value was used as an input to velocity field given in the Mini CTA calibration window so that change of anemometer voltage  $E$  was defined in terms of  $\tau_w$ .

About ten different water flow rates were achieved by adjusting the valve and for each flow rate, above mentioned procedure was fallowed. As a conclusion, relationship between the shear stress and the anemometer voltage output was established and this information was used to find out the constants  $A$  and  $B$  given in the equation 4.12. A typical calibration curve  $\tau^{1/3}$  versus  $E^2$  is given in the Figure 4.9.

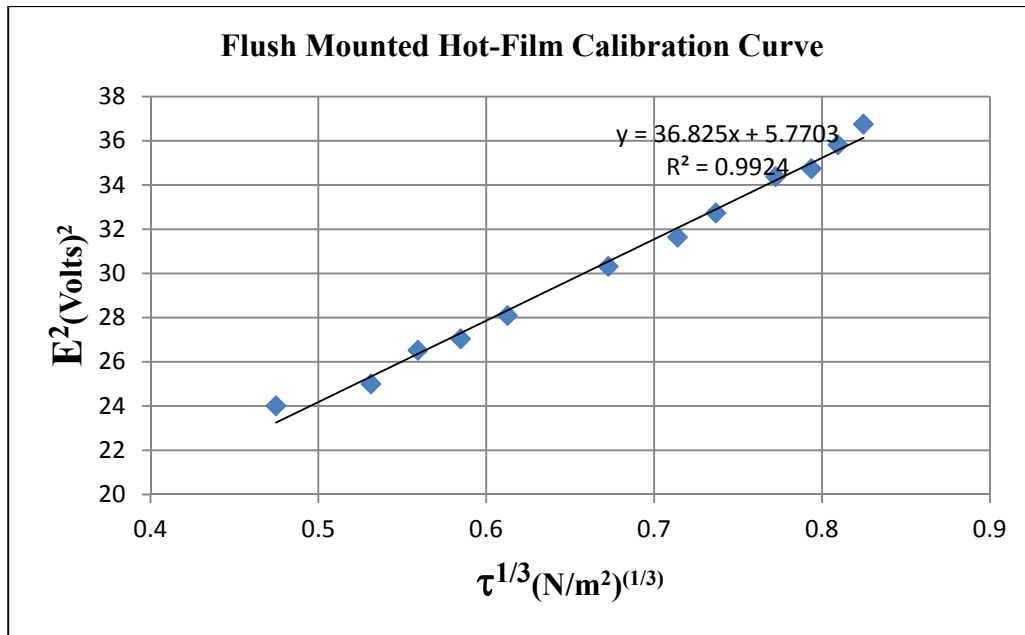


**Figure 4.9 :** Typical calibration plot for flush mounted hot-film probe.

#### 4.6.3 Data Acquisition and Run procedure

During experiments, the signals from the CTA were acquired by Dell Latitude E6400 personal computer. Mini CTA software were utilized for the data acquisition which was triggered manually from the software. National instruments 38A0261 USB, 16 Bit, A/D card was responsible for the digitization of the analogue signals. 1kHz of sampling rate was selected same as used in the boundary layer scans. In order to determine the data sampling time, autocorrelation functions as well as power spectra of the signals were utilized. Due to random characteristics of the signal determined from the autocorrelation functions as well as low frequency content of the power spectra, 10 seconds of sampling time was determined for each data point taken during the local wall void fraction and the shear stress measurements.

The run procedure for the flush mounted hot film probe measurements was as follows. Calibration of the probe was conducted in the calibrator and the probe was removed from the calibrator in order to mount to the flat plate (Unfortunately in-situ calibration was not possible for the flush mounted case). The probe with the fitting was flushly mounted to the position FM1, which is the upstream position at centerline of the plate. See Figure 4.1. Then the plate was immersed into the water by turning the frame to 90 degrees clockwise. After some flat plate alignments performed, data was acquired through the channel speed range without air injection and satisfactory results were obtained like shown in the Figure 4.10.

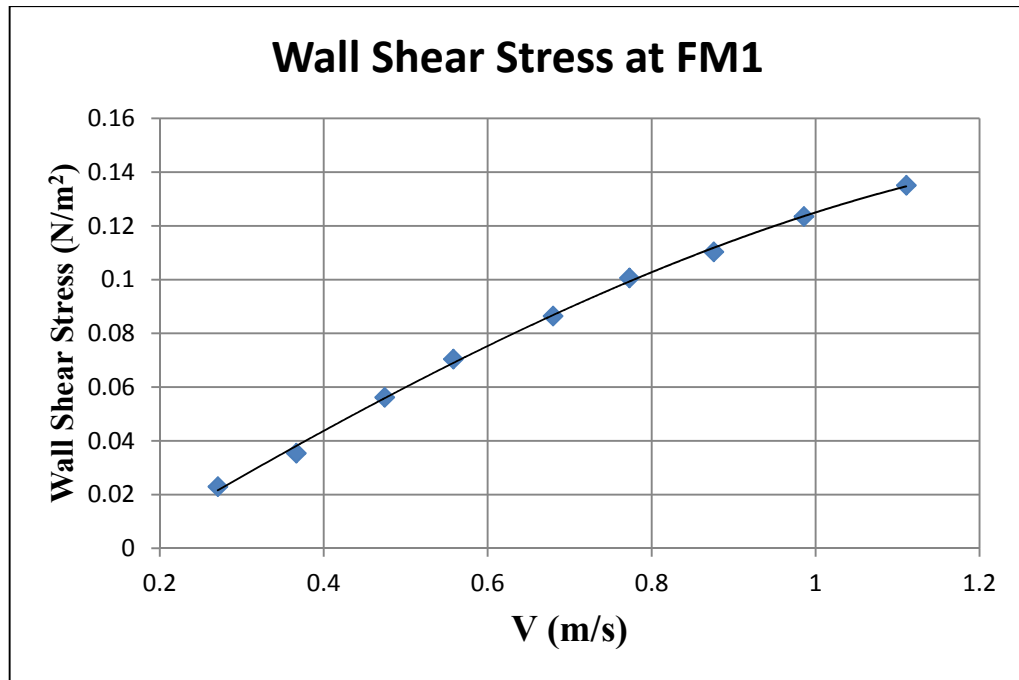


**Figure 4.10 :** Change in wall shear with free stream velocity.

Then the channel velocity was held constant firstly at the channel velocity of 0.55m/s (potentiometer indicator was set to 50) and the air flow rate was set to zero (no air injection), at that condition data was acquired for reference values (without air injection condition) and then air flow rate was set to 1.4m<sup>3</sup>/h, following the voltage data acquisition, next flow rate of 2.8m<sup>3</sup>/h was set by the air supply system and then the data acquisition was performed. Above procedure was repeated for the channel flow speeds of 0.88 and 1.08 respectively (corresponding potentiometer indicator values of 80 and 100).

Same procedure was repeated for the positions FM2, FM3 and FM4. For each measuring position 9 data points were acquired which was concluded with at least 36 measurements. It is worth noting here that the calibration was repeated before each measuring position.

#### 4.6.4 Flow Visualization

The flow underneath the flat plate was observed through the windows located at side wall as well as located at the bottom of the channel. Visualization data was obtained utilizing a camera. For some cases, high speed camera was also employed so that acquired visual data was utilized for the interpretation of the velocity and void fraction profiles of the measurement stations located in modified boundary layer.

Flow visualization studies are represented by the photographs taken from the bottom as well as side windows of the channel as given by Figure A.13 to Figure A.19. Since the air film formation was strongly time dependent especially for the plane of the plate, multiple figures for each case was selected in order to provide a better representation of the phenomena. This instability was dominant for slower speeds and higher flow rates. Therefore, p50 and p80 cases were represented by three figures for each case (Figure A.14 to A.16) while others were represented for just two photographs (Figure A.17 and Figure A.18).

General similarities was observed with the tanker experiments. As in the previous experiments, injected air separates into V shaped arm just behind the hole and it is for sure that the arms were created by the edge of air film. The angle of the V shape is directly proportional with air flow rate. In contrast, the angle is inversely proportional with free stream velocity.

Unlike the tanker experiments, the arms of the air films was not extended so much and the arms were followed a curved lines rather than straight lines encountered in the tanker experiments. Also the structure of the arms was not so clear, dispersion of the gas phase to the liquid phase occurs more frequently through the arms in the flat plate case. It was obvious that, this discrepancy shows the effect of surface energy. As remembered, during the tanker experiments foul release silicon based coating Intersleek 900 was utilized which has a water repellent characteristics. The paint provides better penetration of the injected gas through the boundary layer in span wise direction and forms longer and sharper air film arms.

As agreed with the tanker experiments, for slower speeds and increasing air flow rates, while the angle is getting larger, the area between the V arms gets contact with only water and air is concentrated near the V arms and escapes from the hull sides. The air film edge is following a curved line rather than straight as given in Figure A.14. Hence, the increase in angle results in air escape at a short distance from the hole meanwhile it does not cause any increase in the area covered by the air film. In case of moderate speeds and lower air flow rates, air bubbles are forming at larger distance and the area is mostly covered with air film. See Figure A.15 and Figure A.16. For faster speeds and increasing flow rates, while the angle is getting smaller, air is dispersing through the area between V shape arms and generates air bubbles and the length of the arms are getting shorter (see Figure A.18). At the end of the

arms bubbles are also dispersing through downstream. So more increase in the speed leads separation of air slugs to smaller bubbles.

The side view evaluation of the air injection can be performed with the help of Figure A.19. The figure shows the air jet deformation by the cross water flow with varying air injection flow rates ranging from  $1.4\text{m}^3/\text{h}$  to  $7\text{m}^3/\text{h}$ . It is clear that air jet is behaving like a flexible elliptical wedge and creates a cavity behind. The reattachment line visualized by the dispersed air bubbles can be seen clearly in the Figure A.19(d). Higher the air flow rates, more steeper the air cavities are obtained.

General conclusion from the side view evaluation can be drawn by utilizing flow around an elliptical object. Air jet becomes a point source and forms a compressible elliptical obstacle on the surface. Due to the fact that in the line and downstream of the point source, higher velocity field is occurring which probably creates a V shape air film arms. In order to better understand the structure of the flow field behind the air jet, results of boundary layer velocity profiles with void fraction quantities and wall shear stress measurements were analyzed.

#### **4.6.5 Results and analysis of modified boundary layer measurements**

Modification of boundary layer by air injection to cross flow is investigated by acquiring the data from both boundary layer and flush mounted hot film probes. First, signals acquired from the anemometers are represented and a method of signal processing the data is explained. Second, a software which was developed for extracting the velocity and void fraction data from the processed signal is explained in detail. Finally, modified boundary layer measurement results are analyzed with the non disturbed boundary layer measurements in order to provide a better understanding about the effectiveness of the modification in terms of local drag reduction.

##### **4.6.5.1 Signal processing of acquired data from air injected flow**

In order to understand the governing mechanisms of air modified boundary layer, single normal boundary layer probe as well as flush mounted hot film probes were employed in this study. The expectations from the measurements were to gather enough information about the air modified flow field. The key parameters of air lubrication such as local void fractions, turbulence characteristics of the velocity

profiles of the continuous phase and wall shear stress (local friction resistance) were in the focus of interests. As a starting point, interaction of bubbles with single normal boundary layer hot film probe was investigated by utilizing a basic test setup. With the help of high speed camera and simultaneous hot film measurement, the effect of air slug on anemometer signal was analyzed. Generally, due to air slug or bubble passages, U shaped voltage signals were observed as reported by (Weng et al., 1990), (Hamad and Bruun, 2000), (Farrar and Bruun, 1988), (Wang and Ching, 2001). A typical boundary layer hot film probe signal is given in Figure 4.11:

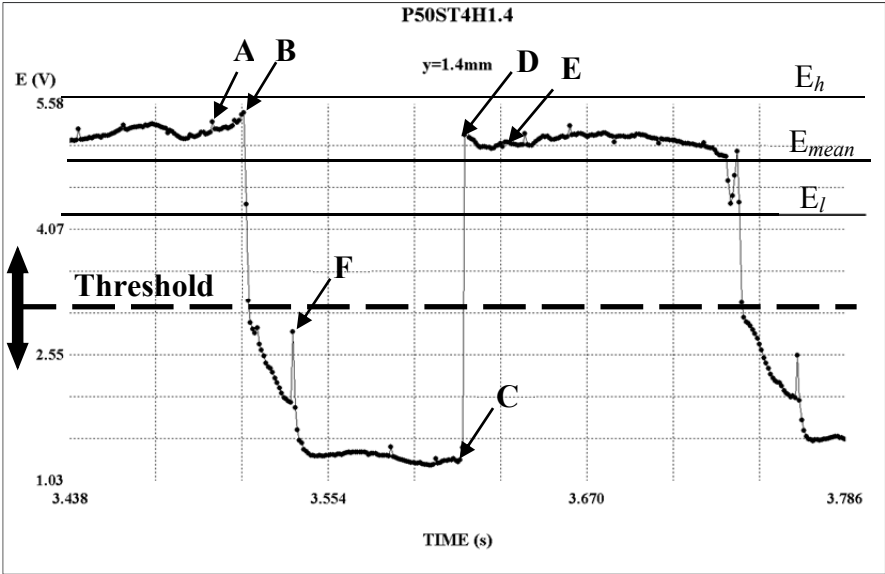


**Figure 4.11 :** Typical boundary layer hot film probe signal in multiphase flow.

Simultaneous high speed camera recordings with hot film measurements have shown that: At time A, an air slug (or bubble) interface reaches the cylindrical sensing element of the probe. Probably due to surface tension, the interface deforms around the probe and penetration does not occur until time B. As the penetration occurs, the voltage suddenly drops. At time C, the rear interface of air slug contacts with the sensing element. At time D, due to influence of the thermal inertia of the sensor’s substrate voltage overshoots Wang et al. (1990) which was named as dynamic meniscus effect (Farrar and Bruun, 1989). Finally at time E, the anemometer voltage achieves it’s stabilized level. In case of breaking the water film between the prongs of the probe while the sensing element is in the air slug, voltage peaks like in time F was also observed. As a conclusion of the probe air slug interaction analysis, it is clear that the air phase starts from A and ends at C. This experience, was utilized to develop a phase discrimination algorithm by this way detecting B-C part of the



acquired signal can give an information about the air void fraction. In other words, time difference between point C and B basically gives the air slug passing time. The ratio of total air slug passing time to data sampling time gives the void fraction of air which is given in the form as in equation (4.15).

$$\alpha = \frac{\Sigma \Delta t_{CB}}{T} \quad (4.15)$$

Where T is the total sampling time of the data. It is worth here noting that, the fraction of time the probe detects the gas can be interpreted as the local void fraction in case of sufficiently long observation (Serizawa, 1974).

Eliminating the same part (C-B) and processing the rest of the signal carefully, gives the information about the velocity and the turbulence characteristics of the continuous phase, which is in water phase so detecting the C-B part is the focus of interest during volume of fraction calculations.

There are several methods to discriminate the C-B part of the signal suggested by Resch et al. (1974) and Jones and Zuber (1978). Common principle of the detection technique is based on an amplitude threshold method. Any data points below the threshold illustrated in the Figure 4.11 are deemed to be associated with the gas phase, and those points which are above are assumed to represent the continuous phase. However, it is sometimes not so easy to apply this method for specific events occurring especially for probe bubble interactions such as partial hit and glancing hit cases which was studied in detail by (Farrar and Bruun, 1989) and (Farrar et al., 1995). The method is useful while determining the volume of fraction values, but for calculating the velocity characteristics, additional detection techniques are needed, since the artificial velocity components coming from point D reduces the accuracy of the turbulence spectra and velocity information for the continuous phase. Due to the fact that more complicated detection techniques like slope threshold method given by Serizawa et. al, 1983 which was based on the first time derivative of the signal. Another method named as combined threshold with slope method was proposed by (Liu and Bankoff, 1990). In this study in order to eliminate the effect of point D, method used by Wang et al. (1990) was utilized. In this study, D-E region of the signal was assumed to be 2ms and while eliminating the signal. Point D and further forward of 2ms acquired points were avoided.

Since the signal processing of the acquired data involves the phase discrimination, velocity decomposition of the continuous phase velocities as well as void fraction calculations, a software has to be developed in order to process the boundary layer scan data determined in the test matrix which yields more than 450 measurement points each has 10000 samples.

#### **4.6.5.2 Developed software for processing the signal**

A signal processing code based on MATLAB(R2010a), was developed to post process the voltage signal. The software uses the exported data points obtained from the Mini CTA software as an input in “.txt” format. For each boundary layer scan station (totally six stations), the Matlab code reads the data automatically for 24 measuring points acquired through the wall normal direction. The software enables data reduction of the voltage data to flow velocities (linearization). Data reduction is performed by using the extended power law calibration coefficients given in the configuration file of the code. Additionally, the program calculates the undisturbed boundary layer velocity profiles, velocity profiles of air injected boundary layer (with the help of phase detection algorithm embedded in the code), volume of fraction air as well as turbulence intensity profiles of modified boundary layer. The algorithm of the software can be summarized as follows:

The program reads the data from the signal file generated by anemometer software and generates two arrays, one is for Time and the other is for signal voltage, E (Each vector has a dimension of 10000, Sampling frequency=1kHz and Sampling Time=10s). Time and voltage signals are stored in these two arrays.

#### **Obtaining velocity characteristics of continuous phase**

The code firstly applies a band pass filter to the signal in order to calculate the mean voltage ( $E_{mean}$ ) of continuous phase which is liquid in our case.  $E_h$  and  $E_l$  values were used as higher and lower band limits of the filter respectively (see Figure 4.11). These band limits are obtained from the calibration file and corresponds to the upper and lower voltage values encountered during the calibration of the probe, so voltages between the calibration range are deemed to be liquid phase and the voltage values are stored as they are, while others are eliminated to provide the true velocity information and zero values are padded to those data points and stored in a matrix. The number of data points which belongs to liquid phase is also recorded by a

counter. Ratio of liquid phase voltage sum to the liquid phase counter gives the mean voltage of liquid phase ( $E_{mean}$ ). It is easy to obtain the liquid phase velocity by just linearization of the  $E_{mean}$  with the help of calibration coefficients but if the turbulence intensity is required, additional step has to be applied since the zero padded signal leads overestimated RMS values. Due to the fact that before the linearization of the voltage data to velocity data, the code applies a windowing function to the voltage signal and obtains the function B given in the form of equation 4.16.

$$B(t) = E(t).W(t) \quad (4.16)$$

$$W(t) = \begin{cases} E_{mean}, & E(t) = 0 \\ 1, & \text{otherwise.} \end{cases} \quad (4.17)$$

Here E(t) is the zero padded signal after the band pass filter applied to the original signal. As a conclusion mean voltage values of liquid phase are patched to the signal so that the RMS value of the concluding matrix is not affected by artificial components. Linearization of the B matrix by using power law calibration coefficients gives the corresponding velocity matrix which offers real-time information about the continuous phase velocity. Two key parameters regarding the velocity profile can be obtained by just calculating the mean and the RMS value of the velocity matrix. This gives the ensemble average of the velocity and the turbulence intensity respectively, regarding the point of interest.

### Calculating local void fraction

Local void fraction evaluations require an improved phase detection technique. Accordingly, the liquid and gas phase of the signal is discriminated via mapping the hot film signal into a binary signal which can be named as “phase indicative function (PIF)”. Since, local void fraction is calculated as the fraction of time the probe is in the gas phase (Farrar et al., 1995), ensemble average of the PIF gives directly the local void ratio. By utilizing this principle, the code obtains the phase indicative function of each acquired signal and calculates the local void fraction by applying the equation 4.15 to discrete time signal by the given form of equation 4.18.

$$\alpha = \frac{1}{N} \sum_{i=1}^N X_L(i) \quad (4.18)$$

Where,  $N$  is the total number of samples acquired ( $N=10.000$ ) and  $X_L$  is the phase indicative function for the liquid phase.

### Obtaining phase indicative function

Since the multiphase flow regime observed during the experiments contains air slugs rather than air bubbles, amplitude threshold algorithm was employed to detect the gas phase. The method requires a threshold voltage value ( $E_{threshold}$ ) which should be carefully selected through a developed subprogram. The threshold, at the same time sets the criteria for the PIF which can be expressed by equation 4.19.

$$X_L(t) = \begin{cases} 1, & \text{when } E(t) > E_{threshold} \\ 0, & \text{when } E(t) < E_{threshold} \end{cases} \quad (4.19)$$

Where,  $E_{threshold}$  is the voltage threshold value illustrated in Figure 4.11,  $E(t)$  is the acquired hot film voltage signal. The code calculates the PIF and plots the time series of acquired discrete signal with PIF in synchronized axis so that for each data point in the profile can be checked by zooming the interested region. A typical PIF calculated by the code is given in Figure 4.11 (the plot was zoomed to 0-2.3s range of 10s record).

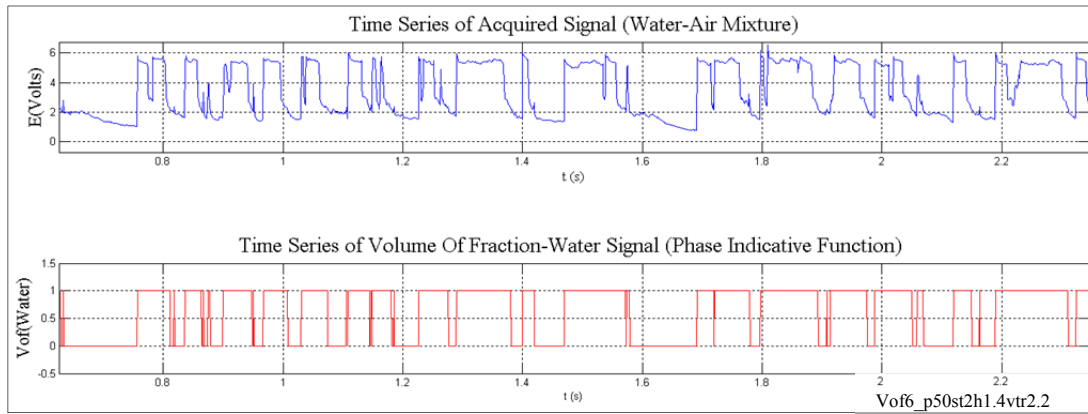


**Figure 4.12 :** Time series of voltage signal and the corresponding PIF.

As stated above PIF includes just binary values 1 or 0 corresponding to just liquid or just gas phase and includes no more information about the sudden drops or increase in the voltage. However, while switching from liquid to gas phase or vice versa the probe interacts with two phase at the same time. Considering those cases, an alternative void fraction calculation method was also taken into account and included in the software so, the code has the capability of calculating void fractions in two methods which is binary PIF and alternative PIF. In the alternative method, to obtain

the PIF; a weighted average of data points between voltage threshold ( $E_{threshold}$ ) and lower calibration voltage ( $E_l$ ) are estimated which offers better representation of the multiphase signal. Alternative PIF can be expressed in the form of equation 4.17.

$$X_L(t) = \begin{cases} 1, & \text{where } E(t) > E_l \\ \frac{(E(t) - V_{threshold})}{(E_l - V_{threshold})}, & \text{where } E_l > E(t) > E_{threshold} \\ 0, & \text{where } E(t) < E_{threshold} \end{cases} \quad (4.20)$$

The difference between the two methods can be explained more clearly by the help of switch-sensor analogy. While the first method is working as a switch, the alternative second method works like a sensor. Due to the fact that the PIF plot of the alternative method gives a smoother function rather than a sharp step function as in the first method. A clear comparison can be made between Figure 4.12 and Figure 4.13. In other words, the time series of the acquired signal is scaled to the 1-0 range with the application of band pass filter while the values one and zero were assigned as upper and lower band limits respectively.

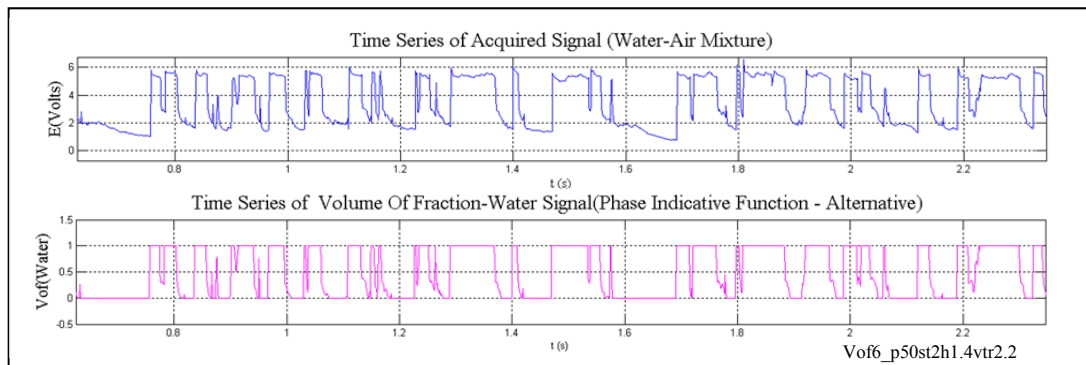


**Figure 4.13 :** Time series of voltage signal and the corresponding PIF-alternative.

The software calculates two types of PIF simultaneously by following two different techniques explained above and reports the both volume of fraction values to provide a comparison. The code also stores obtained data in a listed manner by creating an output file. The output file is utilized as an input of velocity profiles of the modified boundary layer, local void fraction profiles as well as turbulence intensity profiles. A typical output file of the program is given in the Figure A.12.

Up to here, PIF calculation methods are discussed and two techniques are given in order to discriminate the phases. However, an important question rises here about the

most crucial parameter of both methods which is determination of voltage threshold ( $E_{threshold}$ ).

**Threshold determination**

As defined in the previous section, PIF is directly dependent on setted voltage threshold ( $E_{threshold}$ ) so, selection of different threshold values concludes with various number of PIF’s thus local void fractions. Therefore a reliable method is required in order to find out the right threshold voltage value.

A threshold voltage analysis sub program was developed in order to find out the right threshold value. The sub program reads the voltage signal for each point of the scanned boundary layer profile. For each point volume of fractions are calculated by scanning hundred different voltage threshold values and those values are plotted in terms of threshold values versus air volume fractions. A common figure encountered during the threshold voltage analysis is like in the Figure 4.14.

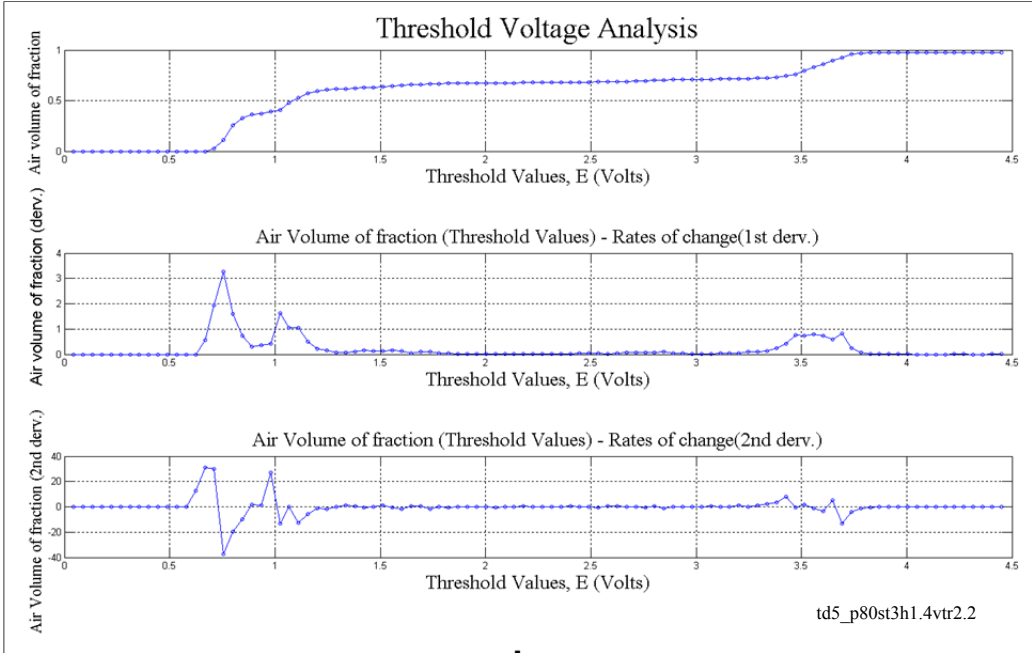


**Figure 4.14 :** The plot of threshold voltage analysis.

The top sub Figure 4.14 shows the air volume of fraction changes by the threshold values. As shown in the figure after a voltage value (here 0.7 Volts) the volume of fraction increases rapidly and sets to a constant value for a while (up to 3.4 volts) and than the value sets to the maximum value which is 1 (all single gas phase after 3.8 volts). The focus of interest here is the moment of achieving the constant value (in this case around 1.5volts). Due to a figure representing a simple case was selected for

a clear explanation, the relationship seems to be so simple. Unfortunately, majority of the figures especially the ones representing the dispersed small bubbly flow are not so clear as illustrated. For those cases, better determination are provided by the help of aided plots based on the first and second derivatives of air volume of fraction function given in the subplots of Figure 4.14 (See subplots at the middle and bottom).

The subprogram also stores the plotted data as an output data file and provides a list of point coordinates, voltage threshold values and corresponding volume of fraction values for further evaluation. A typical output file is given in Figure A.11.

#### **4.6.5.3 Modification in boundary layer parameters**

Velocity, air volume of fraction and turbulence intensity profiles of modified boundary layer are presented in the Figures A.20 to A.28. To the figures, velocity and turbulence intensity profiles of non disturbed boundary layer are also included to provide a comparison. The results of wall shear stress measurements are given in the Figures A.33 to A38 with the values of calculated wall local void fractions. By the help of those figures the effect of free stream velocity as well as air injection rates can be recognized easily.

Since the modification of the boundary layer by single hole injection is a complex phenomena, the analysis of the modification requires the investigation of the multiple parameters simultaneously. Therefore, free stream velocities of p50, p80 and p100 cases (which corresponds slow, moderate and fast velocity levels) are analyzed for each station by utilizing the boundary layer profiles (both with velocity, void fractions and turbulence intensities), wall shear stress results as well as flow visualization outcomes.

Before starting the analysis, giving the positions of the stations in terms of marked lines on the flat plate provides a useful information which is essential for the understanding of the measured quantities. As an example a Figure 4.15 is given below. Considering the first transverse line marked from the air injection point and the centerline (CL) marked longitudinally from the injector, station 1 is at CL and at the middle of the first and the second transverse line. Station 2 is at the CL and at the fourth transverse line. Station 3 is at the CL and at the eighth transverse line. Station 4 is at the CL and at the tenth transverse line. Station 5 and 6 is both located

transversely at the third line (including CL) and longitudinally located at the fourth and eighth line respectively.

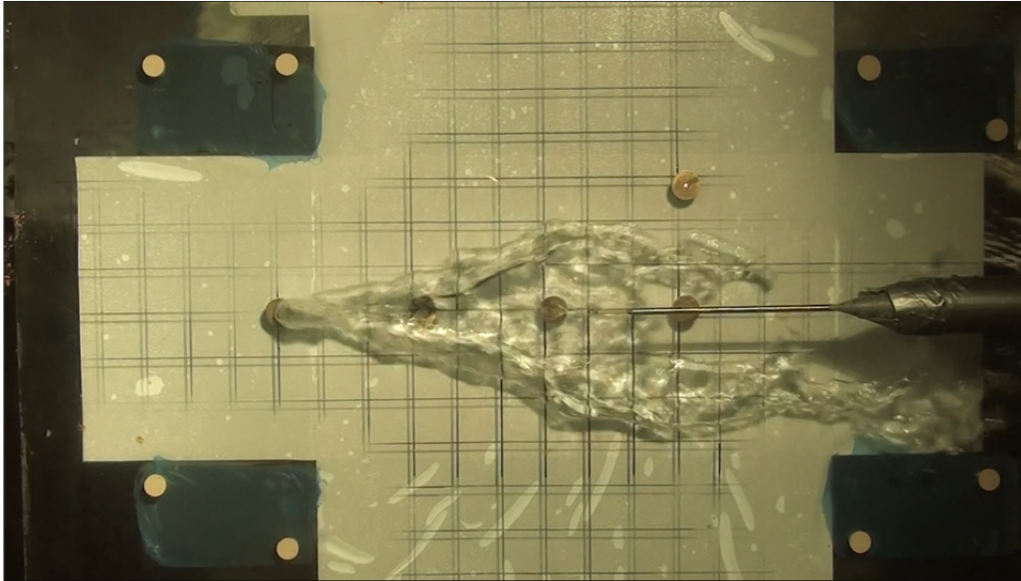


**Figure 4.15 :** Bottom view of air injection.

Since the flush mounted sensors hence the wall shear measuring stations are located so close to boundary layer scan stations of station 2,3 and 4 during the analysis it was assumed that the positions of FM1, FM2 and FM3 stations are same as station 2, 3 and 4 respectively. FM4 is fitted for capturing the effect of V arms with the same longitudinal position with station 4.

As a general note, station 1,2,3 and 4 with wall shear measurement stations FM1,FM2 and FM3 give the information about the air film formation between the V shape arms while station 5 and 6 with FM4 are interested in the edges of the film formation.

The major finding regarding the station 1 (which is the upstream measuring station and located so close to injection point) is the liquid phase velocity with turbulence fluctuation levels were dropped for all free stream velocities under the reference values especially for higher injection rates. See Figure A.20(a), Figure A.23(a) and Figure A.26(a). This conclusion supports the air cavity formation. Behind the backward facing step lower water velocity field obtained while the void fraction values were maximized. While there are different void fraction profiles obtained by increasing the air flow rate for slower and moderate flow velocities (p50 and p80) for the higher flow speed, void fraction profiles are independent of air injection rate. See the air volume of fraction profile for p100 case in Figure A.26(a). For this station,



another important finding is void fraction distribution near wall region. The near wall air volume of fraction for almost all flow speeds are close to zero which means backwards of the air injection point was covered by a thin stable layer of water (turbulent fluctuations were also lower than the reference values).

Regarding the station 2, for the p50 case (lower free stream velocity) the air volume of fraction profiles are almost independent to air injection rate. Looking at the velocity profiles, increase in water phase velocity was observed and for higher air injection rate the water phase velocities were maximized so that the profile deforms up to 30% higher velocities when compared with reference undisturbed boundary layer profiles. See the velocity profiles of Figure A.20(b). It is worth noting here that when the free stream velocity increased to p80 and p100 case, it is recognized that the scatter around the reference profile decreases. For p100 case the profiles are almost following the reference profiles as shown in the Figure A.26(b). As the near wall air volume of fraction maximized (0.45) in moderate speed (p80 case) with lower air injection ratio, local wall shear was reduced by 80%. The Figure A.15 also clearly explains the drag reduction. However, when the air injection rate was increased, the near wall void fraction decreases to zero. The turbulence intensity profiles also support this by showing lower turbulent fluctuations near wall region for lower air injection rate. See Figure A.23(b).

The interesting point here is, the best local frictional drag reduction was achieved by moderate speeds and lower air injection rate. On the other hand, the same case p80, gives the highest drag increase when the air flow rate was increased. With the increase of air flow rate the gas mixture was pushed away from the wall and the liquid phase with higher turbulent fluctuations was penetrated between the wall and the gas phase. See the turbulence intensity profile given in the Figure A.23(b).

Regarding the station 3, in general it was observed that best air layer persistence was observed for all cases p50, p80 and p100 with lower air flow rates. Parallel to that, higher local frictional drag reductions up to 99% was measured (See Figure A.35(b) and Figure A.37(b) for details). Interestingly, when the air injection rate was increased, near wall air volume fraction suddenly dropped more dramatically than encountered at other stations. See Figure A.21(a), Figure A.24(a) and Figure A.27(a).

For station 4, it was found that the air layer persistence was decreased when compared with station 3. See the air volume of fraction profiles given in the Figure A.21(b), Figure A.24(b) and Figure A.27(b). Highest wall shear reduction was measured at higher speed case (p100 case) with the lowest air injection rate.

Up to here, modification of boundary layer was analyzed through a line which is located at the centerline and lays downstream of the air injection point. This line corresponds the symmetry line of the V shaped air film in case of no heel condition. Data acquired from the station 1,2,3 and 4 gives an idea about the air film formation between the arms. In order to investigate the air film edges, the results from station 5 and 6 are presented.

The interesting finding for both stations is the characteristics of the velocity, air volume of fraction and the turbulence intensity profiles. Unlike other stations, particularly for station 5, the velocity profiles of the liquid phase are not deviating from the profiles of the undisturbed boundary layer. See Figure A.22, Figure A.25 and Figure A.28. This is not surprising because, station 5 is located out of the air film region for all free stream velocity cases except the lower velocity case with higher air injection rate. See Figure A.14. Due to the fact that, for the case p50 the only outlier seen in the profiles is in case of higher air injection rate. See Figure A.22(a). But for remaining cases profiles are almost repeating each other. By using the wall shear experience gained from the previous cases it can be concluded that for station 6 and for lower free stream velocity, lower air injection rate is better in terms of reduction in wall shear (Near wall air volume of fraction was about 0.3 while it was zero for higher air injection rate). See Figure A.22(b). Looking at the results of FM4 which is located at the film edge, it can be concluded that moderate speed is better with higher air injection rate. See Figure A.16.

Generally, for all free stream velocities, increasing the flow rates decreases the near wall void fraction and increases the local wall shear through the line of centerline. In contrast, for the sides of air film, with the increasing air injection rates, void fraction increases hence it is possible to achieve considerable amount of drag reductions. See Figure A.34(b), Figure A.36(b) and Figure A.38(b).

#### **4.7 Summary and Conclusions**

The flat plate experiments on boundary layer modification by utilizing air jet, injected through a single hole to cross water flow were conducted in a circulating water channel. Modified boundary layer measurements were compared with the undisturbed boundary layer characteristics in order to understand the influence of the air injection on boundary layer modification.

Profiles of liquid phase velocities, local air volume of fractions as well as turbulence intensities were extracted from the measurements of hot film boundary layer probe in six stations. Local wall shear measurements were also conducted through four measuring points by utilizing flush mounted hot film probes as well. Local wall shear measurements than matched with the boundary layer scan data in order to provide further understanding about the near wall modification. In order to process the acquired data, a software program (based on MATLAB) was developed. The program provides the reduction of the acquired voltage signal to velocity values by using power law calibration coefficients (linearization), the decomposition of the liquid phase velocity magnitudes with fluctuation levels (turbulence intensities) as well as the local air volume of fraction quantities.

The flow underneath the flat plate was observed through the windows located at side wall as well as located at the bottom of the channel. Visualization data was obtained utilizing a camera so that acquired visual data was utilized for the interpretation of the velocity and void fraction profiles of the measurement stations located in modified boundary layer. General similarities was observed with the tanker experiments. As in the previous experiments, injected air separates into V shaped arm just behind the hole and it is for sure that the arms were created by the edge of air film. The angle of the V shape is directly proportional with air flow rate. In contrast, the angle is inversely proportional with free stream velocity.

Unlike the tanker experiments, the arms of the air films was not extended so much and the arms were followed a curved lines rather than straight lines encountered in the tanker experiments. Also the structure of the arms was not so clear, dispersion of the gas phase to the liquid phase occurs more frequently through the arms in the flat plate case. It was obvious that, this discrepancy shows the effect of lower surface energy leaded by the use of water repellant coating in tanker experiments.

As agreed with the tanker experiments, for slower speeds and increasing air flow rates, while the angle is getting larger, the area between the V arms gets contact with only water and air is concentrated near the V arms and escapes from the hull sides. The air film edge is following a curved line rather than straight hence the increase in angle results in air escape at a short distance from the hole meanwhile it does not cause any increase in the area covered by the air film. In case of moderate speeds and lower air flow rates, air bubbles are forming at larger distance and the area is mostly covered with air film. For faster speeds and increasing flow rates, while the angle is getting smaller, air is dispersing through the area between V shaped arms and generates air bubbles and the length of the arms are getting shorter. At the end of the arms bubbles are also dispersing through downstream. So more increase in the speed leads separation of air slugs to smaller bubbles.

The side view evaluation of the air injection shows the air jet deformation by the cross water flow with varying air injection flow rates ranging from  $1.4\text{m}^3/\text{h}$  to  $7\text{m}^3/\text{h}$ . It is clear that air jet is behaving like a flexible elliptical wedge and creates a cavity behind. The reattachment line visualized by the dispersed air bubbles can be seen clearly. Higher the air flow rates, more steeper the air cavities are obtained. General conclusion from the side view evaluation can be drawn by utilizing flow around an elliptical object. Air jet becomes a point source and forms a compressible elliptical obstacle on the surface. Due to the fact that in the line and downstream of the point source, higher velocity field is occurring which probably creates a V shape air film arms. In order to better understand the structure of the flow field behind the air jet, results of boundary layer velocity profiles with void fraction quantities and wall shear stress measurements were analyzed.

As a starting point, interaction of bubbles with hot film probe was investigated by utilizing a basic test setup. Former experiments, focusing on the response of hot film probes to air slug or bubble passages have shown good agreements with the reports of Weng et al. (1990), Hamad and Bruun (2000), Farrar and Bruun (1988), Wang and Ching (2001). In general, U shaped voltage signals were observed. Following the satisfactory results gained from the former experiments, modified boundary layer measurements were performed. According to results of measurements, those general results can be drawn:

As reported by Elbing et al. (2008), Guin et al. (1996), Madavan et al. (1985a) and Sanders et al. (2006), it was also agreed that, the drag reduction is strongly depended on near wall local air volume of fraction. Sudden decreases in void fractions with the increase in turbulent fluctuations lead increases in drag.

For flow velocities which lead best local drag reductions can also lead highest drag increases due to dramatically change in the multiphase flow regime by increasing the air injected flow rates.

For lower speeds air modified velocity profiles of the liquid phase generally deviates from the reference profiles. Especially for higher air injection rates the deviation increases. With increasing free stream velocity, the deviation reduces. This supports the idea of wedge created by the air jet. Like, flow around a foil, the velocity of the liquid flow increases in order to follow the curved streamlines.

Comparison of the turbulence intensity profiles of air modified boundary layer shows a good agreement with the experiments focused on low Reynolds number and larger air bubbles performed by (Murai et al., 2008) and (Sugiyama et al., 2008). It was found that larger bubbles and air slugs can also interact with coherent stream wise vortices which can be damped by the buoyant motions of air phase.

Unlike the air cavity, local drag reduction is strongly depended on air injection rates. Airflow rate increase will conclude both the increase in wall shear due to local void fraction decrease and form drag increases due to more disturbances in boundary layer.



## **5. CONCLUSIONS AND RECOMMENDATIONS**

In the last few years, scientific research and knowledge on climate change have progressed substantially, confirming that the current warming of the Earth's climate is very likely to be due to human activities such as the burning of fossil fuels. Energy efficiency and minimization of greenhouse gas emissions have lately become important topics to reduce global warming. Number of individuals as well as organizations including IMO and IACS has started an extensive research on subject. According to Greenhouse Gas Study, performed in 2009, it was predicted that shipping would account for between 12-18% of global CO<sub>2</sub> emissions by 2050 if no action is taken to reduce emissions from shipping. It was noted that this rate was estimated in 2007 as 3.3%.

IMO has assessed the possibilities for reduction of these emissions through technology and policy. Measures like retrofit hull improvements including superstructures, main engine retrofit, voyage and operations options, hull coating and maintenance, propulsion system upgrades as well as propeller maintenance, power management in auxiliary systems , towing kite, speed reduction and air lubrication were discussed with all aspects.

The global shipping will be stressed by three factors. At first, by regulations on GHG emission reductions. Secondly, by the fuel cost which is now accounted for up to 50% of a ship operating costs in some sectors and trades due to the fast increase in oil price. Finally by a number of mechanisms such as MBI (Market Based Instruments) based on Emission Trading Schemes (a carbon tax system). Due to reasons given above, shipping industry is now emerging to find out feasible solutions in order to gather more efficient ships, which means lower GHG emissions, lower fuel costs as well as lower taxes in the future.

That is why; resistance reduction of ships is appealing more interest than before. When ship's hull resistance can be decomposed into viscous and wave making resistance components, majority of the researchers and naval architects have

involved in the topic of wave resistance. Therefore there were many extensive research performed on the optimization of hull forms by streamlining the shape of the hull in order to reduce radiated waves and avoiding flow separation and in this way omitting the associated losses. Consequently, many experiments on the subject had been conducted which lead the development of numerical tools regarding wave resistance reduction, by this way a huge potential of perfect hull forms in terms of wave resistance had been created, however this potential is reaching its limits.

Since the viscous drag is the dominating component especially for conventional displacement ships (relatively slow ships), reduction in that component leads to a substantial decrease in total reduction, hence results in lower fuel consumption as well as lower GHG emissions. Viscous drag reduction can be achieved via modification of boundary layer by means of passive or active techniques.

Three air lubrication methodologies have distinct characteristics: Microbubble injection has the greatest potential of application due to suitability of the method into curved surfaces, however the effectiveness of the method is degraded with the distance from the injection position as the bubbles are ejected from the boundary layer. As the drag reduction is achieved by the dampening of turbulence energy fluctuations, loss of bubbles from the boundary layer results in cancellation of air injection reduction. Microbubbles also suffer from generation system such as porous media clogging and marine growth.

Air film is the simpler comparing to microbubbles as drag reduction is achieved mainly with reduction of wetted surface and air injection can be via porous media or simple air feeds. However stability of air film on the surface requires careful design of injection hole positions, air feed quantity, surface curvature and surface preparation.

The third method air cavity is only readily available method as technology potential which has been already applied into ships. Optimisation of cavity chamber is still the challenge for the designer.

The current work addressed several issues concerning the implementation air film technique. By using air film technique application on tanker model, it is possible to achieve total resistance reduction in the range of 5% to 10% for lower speeds. Location and air supply rate of air feed mechanism has the prime importance for the



optimum performance of the technique. Porous media air injection is possible to utilize for the creation of air film but the technique have some practical problems caused by the corrosion and fouling of the porous injectors. Single hole air feed system is simpler but optimization of location and air supply rate is very critical. However, it is too early to speculate the engineering benefits of the air film concept, because the power required for supplying air was not calculated so full-scale results are needed to confirm such gains as scaling of air film shall differ from conventional ships. It was concluded that single hole injection gives almost same contribution to resistance reduction as porous media does. Considering the application of the concept not only for new building ships but also for existing ships is practically easier than other concepts such as air cavity or porous media.

Single hole air injection has a coverage area affected by the angle of air film border. The angle obtained from tanker model tests depends on the speed, air feed quantity, and depth of air feed. Analysis of tests with variation of first two parameters indicate angle is proportional to the air feed quantity and inversely proportional to the flow speed. Increase of water depth also reduces the border angle.

By conducting extensive research initiated here, it was possible to gain further understanding on the mechanism of single hole air lubrication of boundary layer modification by air jet, injected through a single hole to cross water flow on a flat plate. Analysis of such multiphase flow requires special techniques to be developed as water and air phases should be separated. Boundary layer evaluation techniques are applied only to the water phase to be able to make comparisons between water only flow and water-air multiphase flow by assuming the energy spend on the air is low comparing to the energy lost in water .

Modified boundary layer measurements were compared with the undisturbed boundary layer characteristics in order to understand the influence of the air injection on boundary layer modification by utilizing the developed signal processing code. It was concluded that the local drag reduction is strongly depended on near wall local air volume of fraction.

The influence of air flow rate is the crucial parameter for local drag changes. At low quantities of air flow rate, void fraction increases leading to reductions in turbulence intensity and local drag reduction. Increasing the air flow rate over a limit results in

less void fraction at the surface as the air pushed outside the boundary layer and higher turbulence intensity than the water only case. Consequently, decreases in void fractions lead to increases in local drag even above the water only case. Accordingly, at any specific position and flow velocity, which lead to the best local drag reduction, may also lead to the highest local drag increase if the air flow rate is not optimised.

For lower flow speeds, air modified velocity profiles of the liquid phase generally deviate from the reference profiles. Especially for higher air injection rates the deviation increases. With increasing free stream velocity, the deviation reduces. This supports the idea of a wedge created by the air jet. Comparison of the turbulence intensity profiles of the air-modified boundary layer shows a good agreement with the experiments reported in the literature. It was found that larger bubbles and air slugs can also interact with coherent streamwise vortices which can be damped by the buoyant motions of the air phase. Unlike the air cavity, local drag reduction is strongly dependent on air injection rates. An increase in air flow rate will result in an increase in wall shear due to local void fraction decrease and form drag should increase due to more disturbance in the boundary layer.

In conclusion, the thesis has shown the ability to achieve local skin friction drag reduction approaching 100% at any point with sufficiently low void fraction and especially at the triangular region obtained downstream of the air injector. The results indicate that a single hole air injection concept is a candidate for implementation on low speed displacement ships. Considering the easy application of the concept not only for new built ships but also for existing ships makes the concept more compatible with other methods of drag reduction. However, it is too early to speculate on the engineering benefits of the concept, without performing further research.

Further investigation is required to determine:

The drag reduction is dependent on the stability of the air film downstream. The air volume fraction at the lower levels of the boundary layer has the main effect on the drag reduction. This feature changes with the Reynolds number and the distance from the air injection point. Further research is required to investigate the further downstream effects.

Ship surfaces have curvature in both vertical and longitudinal direction. The behavior of the air film must be investigated on single curvature and double curvature hull forms. The streamlines due to hull curvature may encourage the air film stability by optimizing air injection point and air feed quantity.

Air feeding systems is a concern for the concept, both from the mechanical/hydrodynamic point of view and from energy concern view. To supply air under the hull, correct air quantity should be determined and air should be collected at the aft end of the ship for recirculation to reduce the energy consumption especially for the high draught ships.

Scaling of air lubrication techniques to the full scale, requires further research as most of the scientific work is limited to the low Reynolds number laboratory work. High Reynolds number investigation in the laboratory scale is either not possible or limited to few facilities in the world. Hence, full-scale results are required to confirm the drag reduction results.

Finally, practical design methodology is required to apply this technique to the ship hull forms. This technique should include structural aspects, safety aspects, and environmental aspects as well as hydrodynamic point of view.



## REFERENCES

- Amromin, E., Karafiath, G., and Metcalf, B.** (2011). Ship Drag Reduction by Air Bottom Ventilated Cavitation in Calm Water and in Waves, *Journal of Ship Research*, Vol. 55, No. 3, pp. 196–207, September 2011.
- Armstrong, N. A.** (2011). On the environmental impact of high speed and lightweight craft, *Conference on High Speed Marine Vessels (RINA)*, Fremantle, Australia, March 2-3.
- Basin, A., Butuzov, A., Ivanov, A., Olenin, Y., Petrov, V., Potapov, O., Ratner, E., Starobinsky, V., and Eller, A.** (1969). Operational tests of a cargo ship “XV VLKSM Congress” with air injection under a bottom, *River Transport*, N5, 52–53.
- Bell, J.W.** (1935). The effect of depth of step on the water performance of a flying-boat hull model, NACA Model 11-0, *NACA Technical Notes* 535.
- Bellhouse, B. J. and Schultz, D. L.** (1966). Determination of Mean and Dynamic Skin Friction, Separation and Transition in Low Speed Flow With a Thin Film Heated Element. *Journal of Fluid Mechanics* 24, pg 379.
- Benjamin, T.B.** (1960). Effects of a Flexible Boundary on Hydrodynamic Stability, *J. Fluid Mech.* Vol. 9, pp. 513-532.
- Bogdevich, V.G., and Evseev, A.R.** (1976). Effect of Gas Saturation on Wall Turbulence, in *Investigations of Boundary Layer Control*, edited by SS Kutateladze and GS Migirenko, Thermophysics Institute, Novosibirsk, Siberia, 1976 (in Russian), 49.
- Bogdevich, V.G., and Malyuga, A.G.** (1976). The Distribution Skin Friction in a Turbulent Boundary Layer of Water Beyond the Location of Gas Injection, in *Investigations of Boundary Layer Control*, edited by SS Kutateladze and GS Migirenko, Thermophysics Institute, Novosibirsk, Siberia, (in Russian), 62.
- BP.** (2011). BP Statistical Review of World Energy, London, June.
- Bruun, H. H.** (1995). *Hot Wire Anemometry: Principles and Signal Analysis*, Oxford University Press, USA.
- Buhaug, Ø., Corbett, J.J., Endresen, Ø., Eyring, V., Faber, J., Hanayama, S., Lee, D.S., Lee, D., Lindstad, H., Markowska, A.Z., Mjelde, A., Nelissen, D., Nilsen, J., Palsson, C., Winebrake, J.J., Wu, W., and Yoshida, K.** (2009). *Second IMO GHG Study 2009*, International Maritime Organization (IMO) London, UK, April.
- Burg, D.F.** (1993). Multiple hull air ride craft, *US Patent*, No: 5415120.

- Butuzov, A., Sverchkov, A., Poustoshny, and A., Chalov, S.,** (1999). State of art in investigations and development for the ship on the air cavities, *International Workshop on Ship Hydrodynamics (IWSH'99)*, China, pp. 1–14.
- Callenaere, M., Franc, J.P., Michel, JM., and Riondet, M.** (2001). The cavitation instability induced by the development of a re-entrant jet, *J. Fluid. Mech.* 444:223–56.
- Candries, M.** (2001). Drag, Boundary-Layer and Roughness Characteristics of Marine Surfaces Coated with Antifouling, *Ph.D. thesis*, Department of Marine Technology, University of Newcastle-upon-Tyne, UK.
- Carpenter, P.W., and Garrad, A.D.** (1985). The Hydrodynamic Stability of Flow over Kramer- Type Compliant Surfaces. Part 1. Tollmien-Schlichting Instabilities, *J. Fluid Mech.* 155, pp. 465-516.
- Ceccio, S. L.** (2010). Friction Drag Reduction of External Flows with Bubble and Gas Injection. *Annual Review of Fluid Mechanics*, 42, 183-203.
- Chaban, Y.Y., Matveev, I.I., Rogojkin, S.Y., Matveev, I.I., Ejov, M.V.** (1993). High speed ships, *Russian Federation Patent*, No: 20411116.
- Clark, H., and Deutsch, S.** (1991). Microbubble skin friction reduction on an axisymmetric body under the influence of applied axial pressure gradients, *Physics of Fluids A3*, 2948-2954.
- Çevik, Özkan, E.** (1997). Modelling of Subsea Pipelines and Sea Base Interaction Under Wave Effects, *Doctoral Thesis*, Yıldız Technical University, Istanbul.
- Deutsch, S., and Castano, J.** (1986). Microbubble Skin Friction Reduction on an Axisymmetric Body, *Phys Fluids* 29(11), 3590-3597.
- Dubnischev, Y., Evseev, A.R., Sobolev, V.S., and Utkin E.N.** (1975). Study of Gas-Saturated Turbulent Streams Using a Laser-Doppler Velocimeter, *J. Appl. Mech. Tech. Phys.* 16(1), 114; translated from *Z Prikt Mech Tekh Fiziki* 1, 147.
- Deutsch, S., Money, M., Fontaine, A., and Petrie, H.** (2003). Microbubble drag reduction in rough walled turbulent boundary layers, *Proceedings of the ASME-Fluids Engineering Division Summer Meeting*, 1-9.
- Druzhini, O.A., and Elghobashi, S.** (1998). Direct numerical simulations of bubble-laden turbulent flows using the two-fluid formulation. *Physics of Fluids*, 10(3):685–697.
- Elbing, B.R., Winkel, E.S., Lay, K.A., Ceccio, S.L., Dowling, D.R., and Perlin, M.** (2008). Bubble-induced skin-friction drag reduction and the abrupt transition to air-layer drag reduction, *Journal of Fluid Mechanics*, 612, 201-236.
- Elbing, B. R.** (2009). Skin-Friction Drag Reduction Within Turbulent Flows, *Doctoral Thesis*, University of Michigan.
- Ergin, G.** (2005). Roughness Induced Transition, *Doctoral Thesis*, Case Western Reserve University.

- Farrar, B., and Bruun, H. H.** (1988). Hot-film Probe Measurements in Kerosene-Water flows. *Second UK National Conference On Heat Transfer*, University of Strathclyde, UK, pp. 1269-1279.
- Farrar, B., and Bruun, H. H.** (1989). Interaction effects between a cylindrical hot-film anemometer probe and bubbles in air/water and oil/water flow, *Journal of Physics E. Scientific Instruments*, Volume 22, Issue 2, 114-123.
- Farrar, B., and Bruun, H. H.** (1996). A computer based hot-film technique used for flow measurements in a vertical kerosene-water pipe flow, *International Journal of Multiphase Flow*, 22(4): 733-751.
- Farrar, B., Samways, A. L., Ali, J. and Bruun, H. H.** (1995). A computer based hot-film technique for two-phase flow measurements, *Measurement Science and Technology*, 6, Number 10, 1528-1537.
- Ferrante, A., and Elghobashi, S.** (2004). On the physical mechanisms of drag reduction in a spatially developing turbulent boundary layer laden with microbubbles. *J. Fluid Mech.* 503:345–55.
- Ferrante, A., Elghobashi, S.** (2005). Reynolds number effect on drag reduction in a microbubble-laden spatially developing turbulent boundary layer. *J. Fluid Mech.* 543:93–106.
- Foeth, E. J.** (2008). Decreasing of frictional resistance by air lubrication, *Proceedings, 20 Int. Hiswa Symposium on Yacht Design and Yacht Construction*, Amsterdam, NL.
- Fontaine, A. A., and Deutsch, S.** (1992). The influence of the type of gas on the reduction of skin friction drag by microbubble injection, *Experiments in Fluids*, 13, 128-136.
- Fukuda, K., Tokunaga, J., Nobunaga, Y., Nakatani, T., Iwasaki, T., and Kunitake, Y.** (2000). Frictional drag reduction with air lubricant over a superwater-repellent surface. *J. Mar. Sci. Technol.*, 5:123–30.
- Gad-el-Hak, M.** (1989). Flow Control, *Appl. Mech. Rev.* 42, pp. 261-293.
- Gad-el-Hak, M.** (1996). Compliant Coatings: A Decade Of Progress, *Applied Mechanics Reviews*, 49, no. 10, part 2, pp. S147–S157.
- Gaster, M.** (1988). Is the Dolphin a Red Herring?, in *Turbulence Management and Relaminarisation*, Springer–Verlag, Berlin, pp. 285–304.
- Guin, M.M., Kato, H., Yamaguchi, H., Maeda, M., and Miyanaga, M.** (1996). Reduction of skin friction by microbubbles and its relation with near-wall bubble concentration in a channel. *J. Mar. Sci. Technol.* 1:241–54.
- Gutierrez-Torres, C.C., Hassan, Y.A., and Jimenez-Bernal, J.A.** (2008). Turbulence structure modification and drag reduction by microbubble injections in a boundary layer channel flow. *J. Fluids Eng.* 130:111304.
- Gökçay, S.** (2001). Research and development of air cavity vessels, *Final Year Project*, Faculty of Naval Architecture and Ocean Engineering, Istanbul Technical University, June 2001.

- Gökçay, S.**, (2003). Investigation of artificial air cavity, *Master of Science Thesis*, Faculty of Naval Architecture and Ocean Engineering, Istanbul Technical University.
- Gökçay, S.**, (2011). PhD Progress Report- January, Istanbul Technical University Graduate School of Science Engineering and Technology.
- Gökçay, S., Insel, M., and Odabaşı A.Y.**, (2004). Revisiting Artificial Air Cavity Concept for High Speed Craft. *Ocean Engineering*, 31: 253-267.
- Gökçay, S. and Insel, M.** (2011). Utilising Air Lubrication For Energy Efficient High Speed Marine Vehicles. *Conference on High Speed Marine Vessels (RINA)*, 2-3 March 2011, Fremantle, Australia.
- Hamad, F. A., Bruun, H. H.**, (2000). Evaluation of bubble/drop velocity by a single normal hot-film placed in a two-phase flow. *Measurement Science and Technology*, Number 11, 11-19.
- Hanratty, T. J. and Campbell, J. A.** (1982). Measurement of Wall Sheer Stress. in *Fluid Mechanics Measurements*, (R. J. Goldstein, Ed.), pp. 575-648, Hemisphere Publishing Corporation, New York.
- Harley, H.D.** (1996). Surface effect vessel hull, *US Patent*, No: 5570650.
- Hoyt, J.W.** (1972). Effect of additives on fluid friction. *Journal of Basic Engineering*, 94(2), 258-285.
- IEA** (2010). Key World Energy Statistics. Date retrieved: 13.05.2011, address: <http://www.iea.org/stats/index.asp>.
- IMO** (2011). EEDI-rational, safe and effective, Date retrieved: 13.05.2011, address: <http://www.imo.org/MediaCentre/HotTopics/GHG/Pages/default.aspx>
- IMO Secretariat** (2010). Assessment of IMO energy efficiency measures for the control of GHG emissions from ships, MEPC60/Inf18, *International Maritime Organisation*, London, UK, March 26.
- Ivanov, A. N., and Kaluhzny, V. G.** (1996). The perspectives of applications of ventilated cavities on naval combat ships. Proceedings, *International Conference on 300<sup>th</sup> Anniversary of Russian Navy*, St. Petersburg, vol. A2, 41-46.
- Insel, M.** (1990). An investigation into the resistance components of high speed displacement catamarans. *Ph.D. Thesis*, Department of Ship Science, University of Southampton.
- Insel, M., Gökçay, S., Helvacioğlu, Ş.** (2009). Air lubrication for low speed ships. *13<sup>th</sup> Congress of Intl. Maritime Assoc. of Mediterranean IMAM 2009*, İstanbul, Turkey, 12-15 Oct.
- Jones, O. C., and Zuber, N.** (1978). Use of a cylindrical hot-film anemometer for measurement of two-phase void and volume flux profiles in a narrow rectangular channel. *American Institute of Chemical Engineers, Symposium Series*, 74, 174, 191-204.
- Jørgensen, F. E.** (2002). *How to measure turbulence with hot-wire anemometers - a practical guide*, Dantec Dynamics, Denmark.



- Kato, H., Miyanaga, M., and Yamaguchi, H. et al.** (1994). Frictional Drag Reduction by Injecting Bubbly Water into a Turbulent Boundary Layer and the Effect of Plate Orientation. *Advances in Multiphase Flow*, Elsevier, Amsterdam, pp. 85-96.
- Kato, H., Miura, K., Yamaguchi, H., and Miyahaga, M.** (1998). Experimental study on microbubble ejection method for frictional drag reduction. *J. Mar. Sci. Technol.* 3:122–29.
- Kato, H., and Kodama, Y.** (2002). Microbubbles as a Skin Friction Reduction Device, A midterm review of the research, *4<sup>th</sup> International Symposium on Smart Control of Boundary Layers*, <http://www.turbulencecontrol.gr.jp/PDF/symposium/FY2002/Kato.pdf>
- Kawakita, C., and Takano, S.** (2000). Microbubble skin friction reduction under the influence of pressure gradients and curved surfaces, *Journal of the Society of Naval Architects of Japan*, 188, 11 – 21.
- Kawamura, T., Moriguchi, Y., Kato, H., Kakugawa, A., and Kodama, Y.** (2003). Effect of bubble size on the microbubble drag reduction of a turbulent boundary layer. *Proc. ASME Fluids Eng. Conf. Summer Meeting 2003*:1–8.
- Khoo, B. C., Chew, Y. T., Teo, C. J.** (2000). On near-wall hot-wire measurements, *Experiments in Fluids*, Volume 29, Issue 5, 448-460
- King, L.V.** (1914). On the convection of heat from small cylinders in a stream of fluid: Determination of the convection constants of small platinum wires with applications to hot-wire anemometry. *Phil. Trans. Roy. Soc. A214*, 373-432.
- Kodama, Y., Kakugawa, A., and Takahashi, T.** (1999a). Preliminary experiments on microbubbles for drag reduction using a long flat plate ship, *ONR Workshop on Gas Based Surface Ship Drag Reduction*, Newport, USA, 1-4.
- Kodama, Y., Kakugawa, A., Takahashi, T., and Kawashina, H.** (1999b). Experimental Study on Microbubbles and Their Applicability to Ships for Skin Friction Reduction, *1<sup>st</sup> Int. Symp. On Turbulent Shear Flow Phenomena*, Santa Barbara, U.S.A., pp.1-6.
- Kodama, Y., Kakugawa, A., Takahashi, T., and Kawashima, H.** (2000). Experimental study on microbubbles and their applicability to ships for skin friction reduction, *Intl J. Heat Fluid Flow*, 21, 582–588.
- Kodama, Y., Kakugawa, A., Takahashi, T., Nagaya, S., and Sugiyama, K.** (2002). Microbubbles: drag reduction mechanism and applicability to ships, *24<sup>th</sup> Symposium on Naval Hydrodynamics*, 1-19.
- Kodama, Y., Hori, T., Kawashima, M. M., and Hinatsu, M.** (2006). A full scale microbubble experiment using a cement carrier, *European Drag Reduction and Flow Control Meeting*, Ischia, Italy, 1-2.
- Kramer, M.O.** (1957). Boundary Layer Stabilization by Distributed Damping, *J. Aeronaut. Sci.*, 24, pp. 459-460.
- Kramers, H.** (1946). Heat transfer from spheres to flowing media, *Physica*, 12, 61-80.

- Kunz, R.F., Gibeling, H.J., Maxey M.R., Tryggvason G., and Fontaine A.A., et al.** (2007). Validation of two-fluid Eulerian CFD modeling for microbubble drag reduction across a wide range of Reynolds numbers. *J. Fluids Eng.*, 129:66–79.
- Lackenby, H.** (1962). Resistance of ships with special reference to skin friction and hull surface condition. The 34<sup>th</sup> Thomas Lowe Gray Lecture. *Proceedings of the Institute of Mechanical Engineers*, Vol. 176, pp. 981-1014.
- Landahl, M.T.** (1962). On the Stability of a Laminar Incompressible Boundary Layer over a Flexible Surface, *J. Fluid Mech.*, 13, pp. 609-632.
- Lay, K., Yakusiji, R., Makiharju, S., Perlin, M., Ceccio, S.** (2010). Partial Cavity Drag Reduction at High Reynolds Numbers, *Journal of Ship Research*, Vol. 54, No. 2, pp. 109–119, June 2010.
- Legner, H.H.** (1984). Simple model for gas bubble drag reduction. *Phys. Fluids*, 27, 2788–2790.
- Ling, S.C., Hubbard, P.G.** (1956). The Hot-Film Anemometer: A New Device for Fluid Mechanics Research. *J. Aero. Sci.*, 23, pp. 890–891.
- Liu, T. J., and Bankoff, S. G.** (1990). Structure of air-water bubbly flow in a vertical pipe, Part I, Liquid mean velocity and turbulence measurements. ASME, *Symposium On Gas-Liquid Two-Phase Flows*, Dallas, 9-17.
- Lo, T.S., L'vov, V.S., Procaccia, I.** (2006). Drag reduction by compressible bubbles. *Phys. Rev. E*, 73:036308.
- Lu, J., Fernandez, A., Tryggvason, G.** (2005). The effect of bubbles on the wall drag of a turbulent channel flow. *Phys. Fluids*, 17:095102.
- Lumley, J. L.** (1973). Drag reduction in turbulent flow by polymer additives, *J Polymer Science, Macromolecular Rev.*, 7, 283–290.
- Lumley, J. L.** (1977). Drag reduction in two phase and polymer flows, *Physics of Fluids*, 20, S64-S70.
- Madavan, N. K.** (1984). The Effects of Microbubbles On Turbulent Boundary Layer Skin Friction, *Doctoral Thesis*, Pennsylvania State University.
- Madavan, N. K., Deutsch, S., and Merkle, C.L.** (1984). Reduction of Turbulent Skin Friction by Microbubbles, *Phys Fluids*, 27(2), 356-363.
- Marie, J.L.** (1987). A simple analytical formulation for microbubble drag reduction. *J. Phys-Chem. Hydro.*, 13, 213–220.
- Madavan, N. K., Deutsch, S., and Merkle, C. L.** (1985a). Measurements of local skin friction in a microbubble modified turbulent boundary layer, *Journal of Fluid Mechanics*, 156, 237-256.
- Madavan, N.K., Deutsch, S., and Merkle, C.L.** (1985b). Numerical investigation into the mechanisms of microbubble drag reduction. *J. Fluids Eng.*, 107:370–77.
- Matveev, K.I.** (2003). On the Limiting Parameters of Artificial Cavitation, *Ocean Engineering*, 30(9), pp. 1179-1190.

- Matveev, K.I., Burnett, T., Ockfen A.E.**, (2009). Study of air-ventilated cavity under model hull on water surface, *Ocean Engineering*, 36,930–940.
- McCormick, M.E., and Bhattacharyya, R.** (1973). Drag Reduction of a Submersible Hull by Electrolysis, *Naval Engineers Journal*, Vol.85, No.2, pp. 11-16.
- Meng, J. C. S., and Uhlman, J. S.** (1998). Microbubble formation and splitting in a turbulent boundary layer for turbulence reduction, *Proceedings of the International Symposium on Seawater Drag Reduction*, 341-355.
- Merkle, C. L., and Deutsch, S.** (1992). Microbubble Drag Reduction in Liquid Turbulent Boundary Layers. *Applied Mechanics Reviews*, 45(3): 103-127.
- Migirenko, G.S., and Evseev, A.R.** (1974). Turbulent Boundary Layer with Gas Saturation, in *Problems of Thermophysics and Physical Hydrodynamics*, Novosibirsk, NaRka, (in Russian)
- Moriguchi, Y., and Kato, H.** (2002). Influence of microbubble diameter and distribution on frictional resistance reduction. *J. Mar. Sci. Technol.* 7:79–85.
- Murai, Y., Oishi, Y., Takeda, Y., and Yamamoto, F.** (2006). Turbulent shear stress profiles in a bubbly channel flow assessed by particle tracking velocimetry. *Exp. Fluids*, 41(2):343–54.
- Murai, Y., Fukuda, H., Oishi, Y., Kodama, Y., and Yamamoto, F.** (2007). Skin friction reduction by large air bubbles in a horizontal channel flow. *Int. J. Multiphase Flow*, 33:147–63.
- Murai, Y., Oiwa, H., and Takeda, Y.** (2008). Frictional drag reduction in bubbly Couette-Taylor flow. *Phys. Fluids*, 20:034101.
- Nagamatsu, T. Kodama, T., Kakugawa, A., Takai, M., Murakami, K., Ishikawa., Kamiirisa, H., Ogiwara, S., Yoshida, Y., Suzuki, T., Toda, Y., Kato, H., Ikemoto, A., Yamatani, S., Imo, S., and Yamashita, K.** (2002). A full-scale experiment on microbubbles for skin friction reduction using SEIUN MARU Part 2: The fullscale experiment, *Journal of the Society of Naval Architects of Japan*, 192, 15-28.
- Nagaya, S., Kakugawa, A., Kodama, Y., and Hishida, K.** (2001). PIV/LIF measurements on 2-D turbulent channel flow with microbubbles, *4<sup>th</sup> International Symposium on PIV*, Goettingen, Germany.
- Pal, S., Deutsch, S., and Merkle, C. L.** (1989). A comparison of shear stress fluctuation statistics between microbubble modified and polymer modified turbulent flow, *Physics of Fluids*, A1, 1360-1362.
- Pal, S., Merkle, C.L., and Deutsch, S.** (1988). Bubble Characteristics and Trajectories in a Microbubble Boundary Layer, *Phys Fluids*, 31(4), 744-751.
- Pien, P.C.** (1958). Five Hole Spherical Pitot Tube, David Taylor Model Basin Report No. 1229.
- Pope, S.B.** (2000). *Turbulent Flows*. Cambridge, UK: Cambridge Univ. Press.

- Pruitt, G.T. and Craw, H.R.** (1963). Westco Research Final Report on Contract 60530-8250 to Naval Ordnance Test Station.
- Reed, J.C.** (1994). Using grooved surfaces to improve the efficiency of air injection drag reduction methods in hydrodynamic flows. *J. Ship Res.*, 38(2):133–36.
- Resch, F.J., Leutheussar, H. J., Alemu, S.** (1974). Bubbly two-phase flow in hydraulic jump. *Journal of Hydraulics Division*, American Society of Civil Engineers, 100, 137-149.
- Samways, A. L., Ali, J., Al-Deen, M. F. N., and Bruun, H. H.** (1994). The calibration and measurements with cylindrical hot-film probes in water flows. *Meas. Sci. Technol.* 5, 1554-1559.
- Sanders, W., Dowling, D.R., Perlin, M., and Ceccio, S.L.** (2002) The university of Michigan HIPLATE Experiment, <http://www.turbulence-control.gr.jp/PDF/symposium/FY2001/Sanders.pdf>
- Sanders, W. C., Winkel, E. S., Dowling, D. R., Perlin, M. , and Ceccio, S. L.** (2006). Bubble friction drag reduction in a high-Reynolds-number flat-plate turbulent boundary layer, *Journal of Fluid Mechanics*, **552**, 353-380.
- Savins, J.G.** (1964). Drag Reduction Characteristics of Solution Macromolecules in Turbulent Pipe Flow, *Soc. Petrol. Eng. J.*, 4, 203.
- Savitsky, D., and Brown, P.W.** (1976). Procedures for hydrodynamic evaluation of planing hulls in smooth and rough water, *Marine Technology*, 13 (4), 381–400.
- Serizawa, A.** (1974). Fluid dynamic characteristics of two phase flow. *Doctoral Thesis*, Kyoto University, Japan.
- Serizawa, A., Tsida, K., and Michiyoshi, I.** (1983). Real-time measurement of two-phase flow turbulence using dual-sensor anemometry. *Proceeding of the Symposium on Measuring Techniques in Gas-Liquid Two-Phase Flows*, Nancy, France, 495-523.
- Ship&Offshore** (2011). Wind power as economical alternative, *Special Greentech edition*, pp 34-35. Date retrieved: 05.10.2011, address: [www.shipandoffshore.net](http://www.shipandoffshore.net)
- Shen, X., Perlin, M. & Ceccio, S. L.** (2006). Influence of bubble size on micro-bubble drag reduction. *Experiments in Fluids*, 41, 415-424.
- Solomon, S., Qin D., Manning M., Chen Z., Marquis M., Averyt K.B., Tignor M. and Miller H.L. (Eds.).** (2007). Couplings Between Changes in the Climate System and Biogeochemistry Climate Change 2007, *The Physical Science Basis. Contribution of Working Group I to the Fourth Assessment Report of the Intergovernmental Panel of Climate Change-Ch 7.*, Cambridge University Press, United Kingdom and USA:. ISBN 978-0-521-88009-1., 2007.
- Sugiyama, K., Calzavarini, E., and Lohse, D.** (2008). Microbubbly drag reduction in Taylor-Couette flow in the wavy vortex regime. *J. Fluid Mech.*, 608:21–41.

- Sverchkov, A.V.** (2005). Prospects of artificial cavities in resistance reduction for planning catamarans with asymmetric demihulls, *Proceedings, International Conference on Fast Sea Transport FAST'2005*, St. Petersburg, Russia.
- Takahashi, T., Kakugawa, A., Nagaya, S., Yanagihara, T., and Kodama, Y.** (2001). Mechanisms and scale effects of skin friction reduction by microbubbles, *Proceedings of the 2nd Symposium on the Smart Control of Turbulence*, University of Tokyo, 1-9.
- Takahashi T, Kakugawa A, Makino M, and Kodama Y.** (2003). Experimental study on scale effect of drag reduction by microbubbles using very large flat plate ships. *J. Kansai Soc. Nav. Archit. Jpn.*, 239:11–20.
- Toms, B.A.** (1948). Some observations on the flow of linear polymer solutions through straight tubes at large Reynolds numbers, *Proceedings of the First International Congress on Rheology*, 2, 135-141.
- Traut, M., Bows, A., Gilbert P., Walsh C. and Wood R.** (2011). Towards Very Low Carbon Shipping, *International Conference on Technologies, Operations, Logistics and Modelling for Low Carbon Shipping*, Glasgow, UK, June 22-24.
- Truong, V. T.** (2001). Drag Reduction Technologies. Maritime Platforms Division Aeronautical and Maritime Research Laboratory, Report No: DSTO-GD-0290, June 2001
- UNEP** (2005). Vital Climate Change Graphics, United Nations Environment Programme, Kenya.
- UNCTAD Secretariat** (2009). Review of Maritime Transport 2009, *United Nations Conference on Trade and Development*, New York and Geneva, June.
- Wang, G. and Ching, C. Y.** (2001). Measurement of multiple gas-bubble velocities in gas-liquid flows using hot-film anemometry, *Experiments in Fluids*, 31(4), 428-439.
- Wang, S. K., Lee, S. J., Jones, O. C., and Lahey, R. T.** (1990). Statistical analysis of turbulent two-phase pipe flow, *Journal of Fluids Engineering*, 112, 89-95.
- Watanabe, O., Masuko, A., and Shirase, Y.** (1999). Measurements of drag reduction by microbubbles using a very long ship models. *J. Soc. of Naval Architects of Japan*, 183, 53-63 (in Japanese).
- White, C.M., and Mungal, M.G.** (2008). Mechanics and prediction of turbulent drag reduction with polymer additives, *Annual Review of Fluid Mechanics*, 40, 235- 256.
- Winkel, E. S., Ceccio, S. L., Dowling, D. R., and Perlin, M.** (2004). Bubble size distributions produced by wall-injection of air into flowing freshwater, saltwater, and surfactant solutions, *Experiments in Fluids*, 37, 802-810.
- Winkel, E. S.** (2007). High Reynolds Number Flat Plate Turbulent Boundary Layer Measurements and Skin Friction Drag Reduction with Gas or Polymer Injection, *Doctoral Thesis*, University of Michigan.

- Xu, J., Maxey, M.R., and Karniadakis, G.E.** (2002). Numerical simulation of turbulent drag reduction using microbubbles. *J. Fluid Mech.* 468:271–81.
- Zalek, S., Beck, R., Ceccio, S.L., and Reed, A.** (2004). Drag reduction for high speed ship design, Report to the Office of Naval Research.

## **APPENDICES**

**APPENDIX A** : Figures

**APPENDIX B** : Tables

**APPENDIX A : Figures**

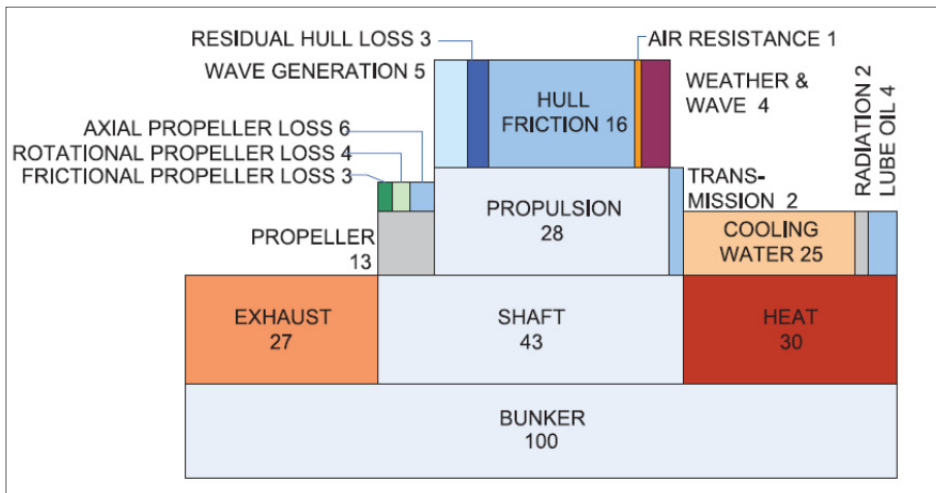


**Figure A.1 :** Use of fuel energy on board for a small cargo ship, head sea, Beaufort 6.

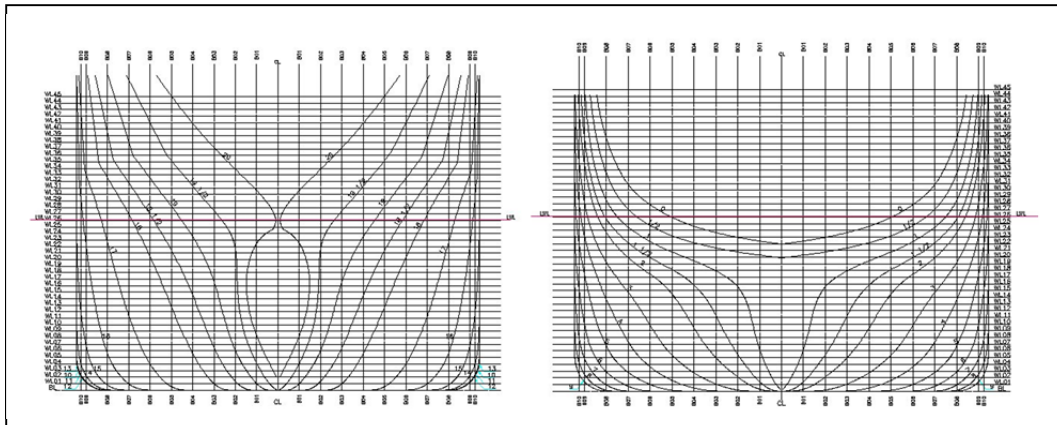


**Figure A.2 :** Body plan of M266.

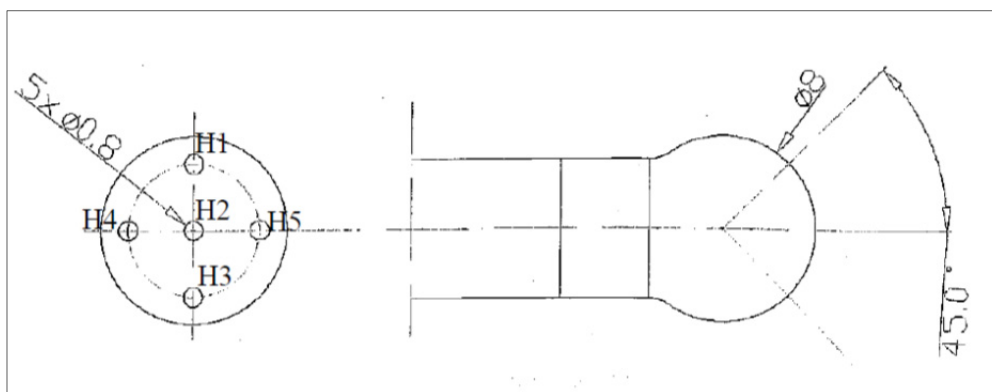


**Figure A.3 :** Sketch of spherical 5-hole pitot tube probe.





**Figure A.4 :** Circulating water channel located at ITU.

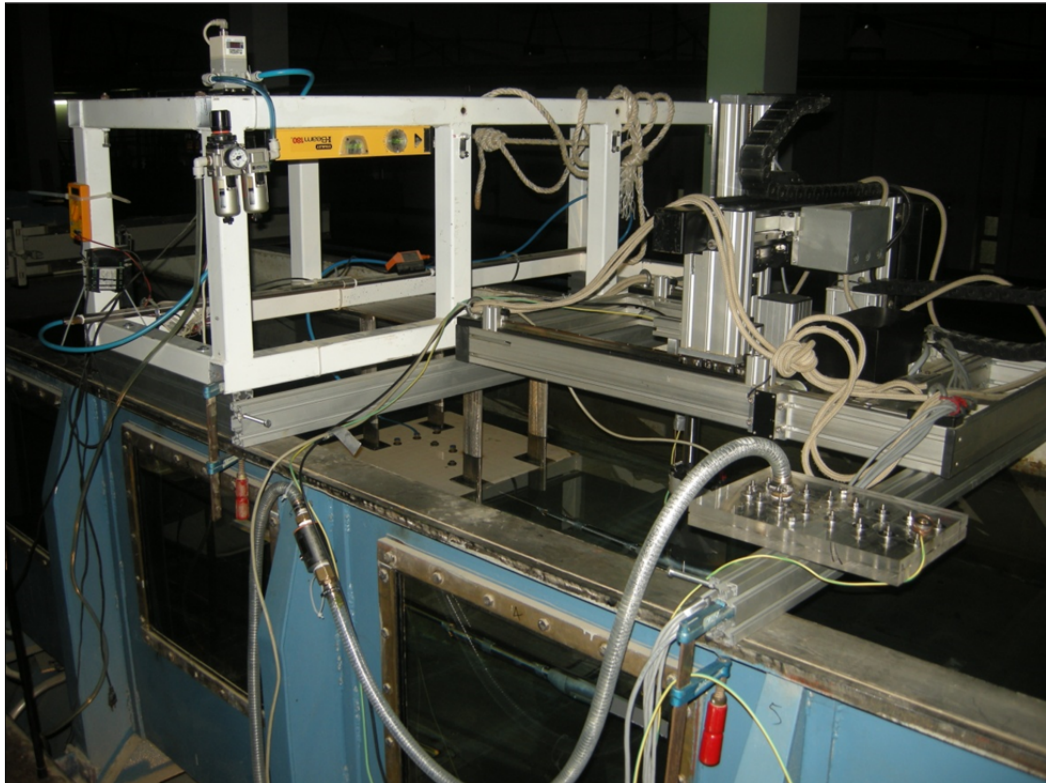


**Figure A.5 :** Experimental setup.

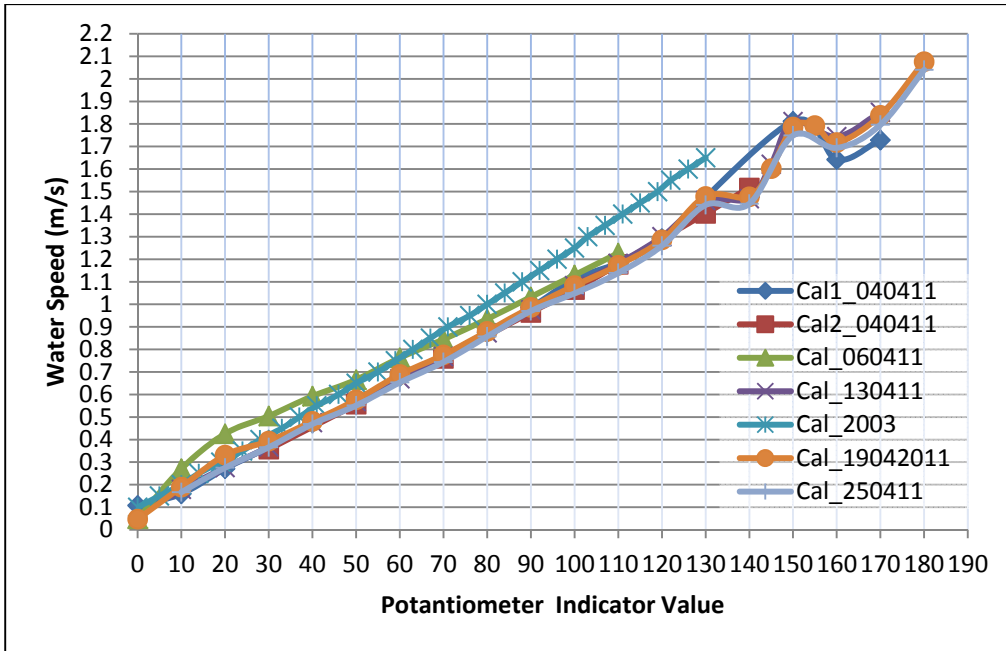


Figure A.6 : Circulating channel calibration plot.

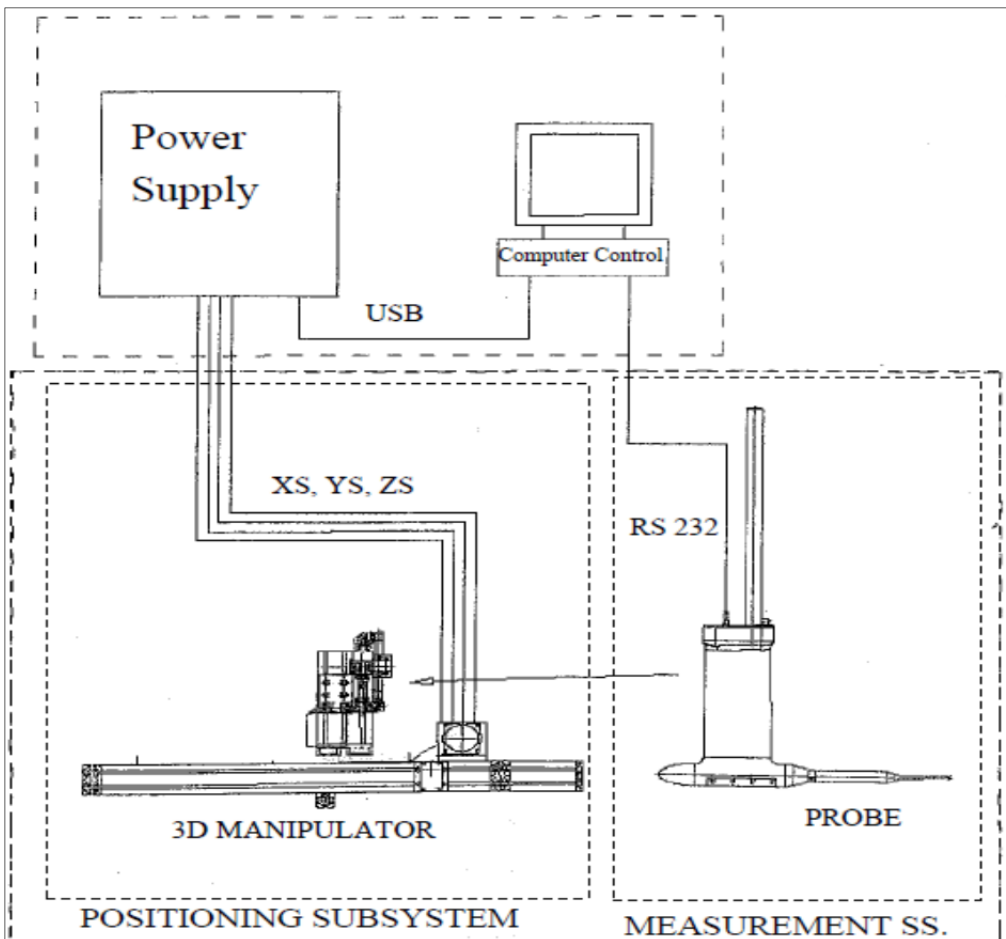
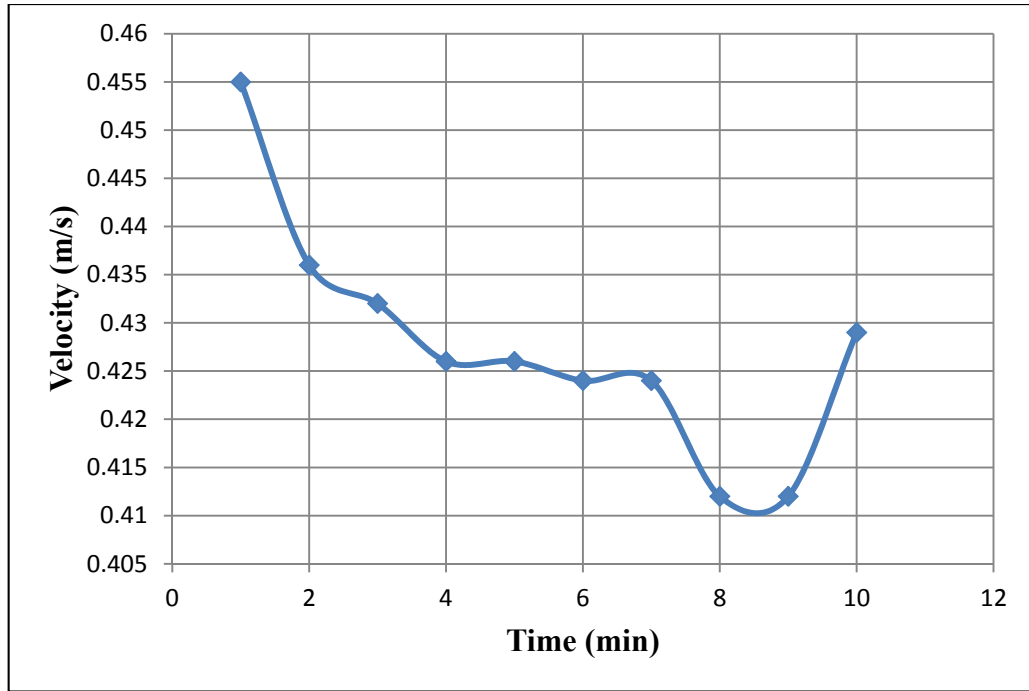
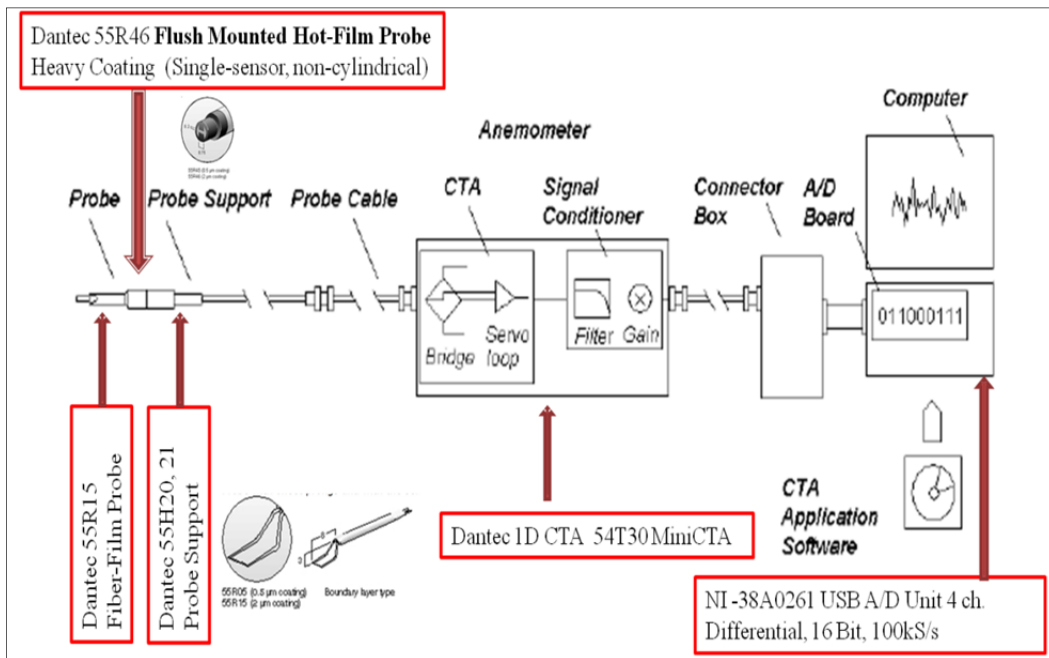


Figure A.7 : Positioning and measurement subsystems of traverse mechanism.



**Figure A.8 :** Effect of contamination on velocity drift.



**Figure A.9 :** Constant temperature anemometer measuring chain.

Dantec 55R15 Fiber-Film Probe			Dantec 55R46 Flush Mounted Hot-Film Probe		
Technical data for fiber-film sensors					
Thickness of quartz coating	0.5 $\mu\text{m}$	2 $\mu\text{m}$			
Medium	Air	Water			
Sensor material	Nickel				
Sensor dimensions	70 $\mu\text{m}$ dia, 1.25 mm long The overall fiber length is 3 mm				
Sensor resistance R20 (approx.)	6 $\Omega$				
Temperature coefficient of resistance (TCR) $\alpha$ 20 (approx.)	0.40%/°C				
Max. sensor temperature	300°C	150°C			
Max. ambient temperature	150°C	100°C			
Min. velocity	0.05 m/s *	0.01 m/s			
Max. velocity	350 m/s	10 m/s			
Frequency limit fmax	175 kHz	30 kHz			
* Influence from natural convection up to approx. 0.20 m/s.					
Technical data for flush-mounting film sensors					
Thickness of quartz coating	0.5 $\mu\text{m}$	2 $\mu\text{m}$			
Medium	Air	Water			
Sensor material	Nickel				
Sensor dimensions	0.75 x 0.2 mm				
Sensor resistance R20 (approx.)	15 $\Omega$				
Temperature coefficient of resistance (TCR) $\alpha$ 20 (approx.)	0.35%/°C				
Max. sensor temperature	200°C	150°C			
Max. ambient temperature	100°C	100°C			
Max. ambient pressure	70 bar	70 bar *			
Frequency limit fcpo (CCA mode, 0 m/s)	0.2 Hz	0.5 Hz			
*At 20°C, decreasing with increasing temperature, 1 bar at 80°C					

**Figure A.10 :** Characteristics of Fiber-Film Probe (Dantec 55R15) and Flush Mounted Hot-Film Probe (Dantec 55R46).

```

p80st3h1.4
-----
Calibration Coefficients:
  A= 1.88423
  B= 33.17133
Power= 0.34993
  E1= 4.44900
  Eh= 6.01300
-----
lower_cutoff= 1.00
higher_cutoff= 3.00
Resolution= 100
-----
Z(position)  No Vtreshold(V)-Int.  Vof-air(Interpolated)  Vtreshold(V)  Vof-air
-----
  2.0    1.0    2.46920                0.000          2.447          0.000
  2.0    2.0    2.51368                0.000          2.491          0.000
  2.0    3.0    2.55818                0.000          2.536          0.000
  2.0    4.0    2.59525                0.000          2.580          0.000
  2.0    5.0    2.92325                0.007          2.892          0.005
  2.0    6.0    2.94693                0.008          2.936          0.007
-----
  3.0    1.0    2.18001                0.000          2.136          0.000
  3.0    2.0    2.22339                0.000          2.180          0.000
  3.0    3.0    2.29123                0.001          2.269          0.001
  3.0    4.0    2.37068                0.001          2.358          0.001
  3.0    5.0    2.43424                0.002          2.402          0.002
  3.0    6.0    2.51368                0.002          2.491          0.002
  3.0    7.0    2.60711                0.003          2.580          0.003
  3.0    8.0    2.63300                0.004          2.625          0.004
  3.0    9.0    2.70944                0.005          2.669          0.004
  3.0   10.0    2.71591                0.005          2.714          0.005
  3.0   11.0    2.88923                0.015          2.847          0.011
  3.0   12.0    2.90297                0.018          2.892          0.015
-----
  4.0    1.0    1.04591                0.030          1.023          0.023
  4.0    2.0    1.28819                0.090          1.246          0.087
  4.0    3.0    1.42638                0.096          1.424          0.096
  4.0    4.0    1.64057                0.113          1.602          0.112
  4.0    5.0    1.80432                0.114          1.780          0.114
  4.0    6.0    1.84027                0.115          1.824          0.115
  4.0    7.0    1.91307                0.116          1.869          0.116
  4.0    8.0    1.91307                0.116          1.913          0.116
  4.0    9.0    1.96969                0.118          1.958          0.118
  4.0   10.0    2.02943                0.120          2.002          0.119
-----

```

**Figure A.11** : Typical output file of voltage threshold analysis sub program.

```

p80st3h1.4vtr2.3
-----
Calibration Coefficients:
  A= 1.88423
  B= 33.17133
Power= 0.34993
  E1= 4.44900
  Eh= 6.01300
-----
Vtres= 2.30000
-----
Z(position) Vof-air Vof-air(alt) Vwater (m/s) Turb.int-Water E-water E-mixture
-----
  1.0 0.00000 0.00000 0.83230 1.80855 5.74385 5.74385
  2.0 0.00000 0.33886 0.53707 6.78245 5.34517 3.77268
  3.0 0.00070 0.37076 0.61294 6.10155 5.46203 3.73920
  4.0 0.13020 0.46479 0.61364 5.64727 5.46304 3.40213
  5.0 0.67820 0.81290 0.68113 2.97731 5.55740 1.82743
  6.0 0.92720 0.93946 0.71265 4.00556 5.59887 1.42994
  7.0 0.96270 0.97066 0.70105 3.52966 5.58378 1.12520
  8.0 0.94280 0.95668 0.72942 3.78512 5.62034 1.35128
  9.0 0.88140 0.91236 0.75201 5.51023 5.64862 1.59486
 10.0 0.26470 0.40942 0.75971 13.21955 5.65811 4.05591
 11.0 0.00120 0.01096 0.81538 9.15852 5.72443 5.67947
 12.0 0.00000 0.00019 0.81224 8.19724 5.72078 5.72012
 13.0 0.00000 0.00000 0.81489 6.71535 5.72386 5.72390
 14.0 0.00000 0.00000 0.80993 6.51868 5.71809 5.71809
 15.0 0.00000 0.00000 0.83085 5.21735 5.74219 5.74225
 16.0 0.00000 0.00000 0.83572 5.77147 5.74774 5.74780
 17.0 0.00000 0.00000 0.83546 5.38777 5.74744 5.74744
 18.0 0.00000 0.00000 0.85021 3.87567 5.76407 5.76407
 19.0 0.00000 0.00000 0.84708 3.52749 5.76055 5.76055
 20.0 0.00000 0.00000 0.85661 3.49967 5.77121 5.77125
 21.0 0.00000 0.00000 0.85537 3.64296 5.76982 5.76982
 22.0 0.00000 0.00000 0.86365 2.26678 5.77900 5.77905
 23.0 0.00000 0.00000 0.86315 1.91350 5.77845 5.77845
 24.0 0.00000 0.00000 0.86617 1.48609 5.78179 5.78182
-----
CPU_Time= 8.53 sec

```

**Figure A.12** : Typical output file of the developed code.

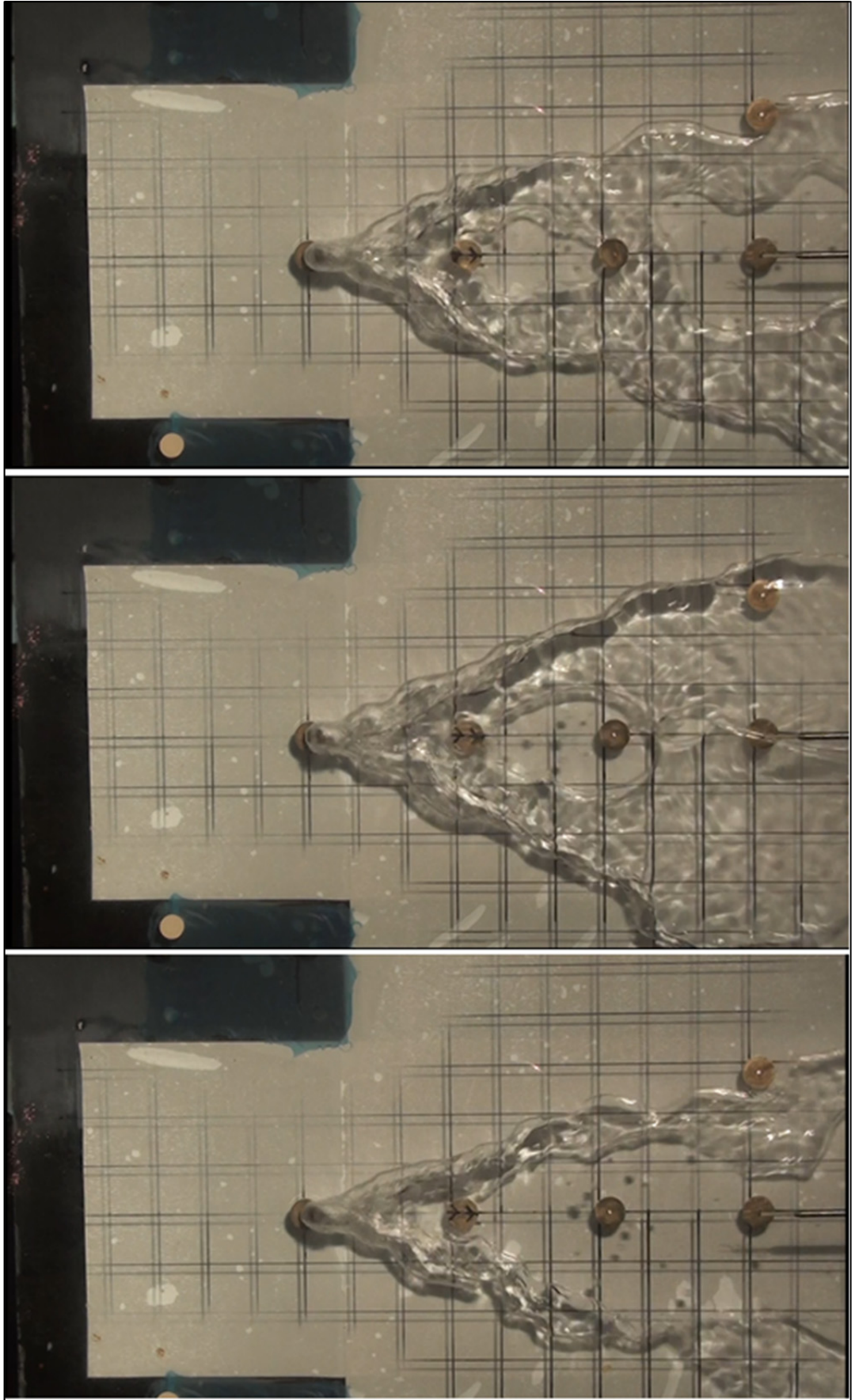


**Figure A.13** : Bottom view of p50 case with air injection of 1.4m<sup>3</sup>/h.

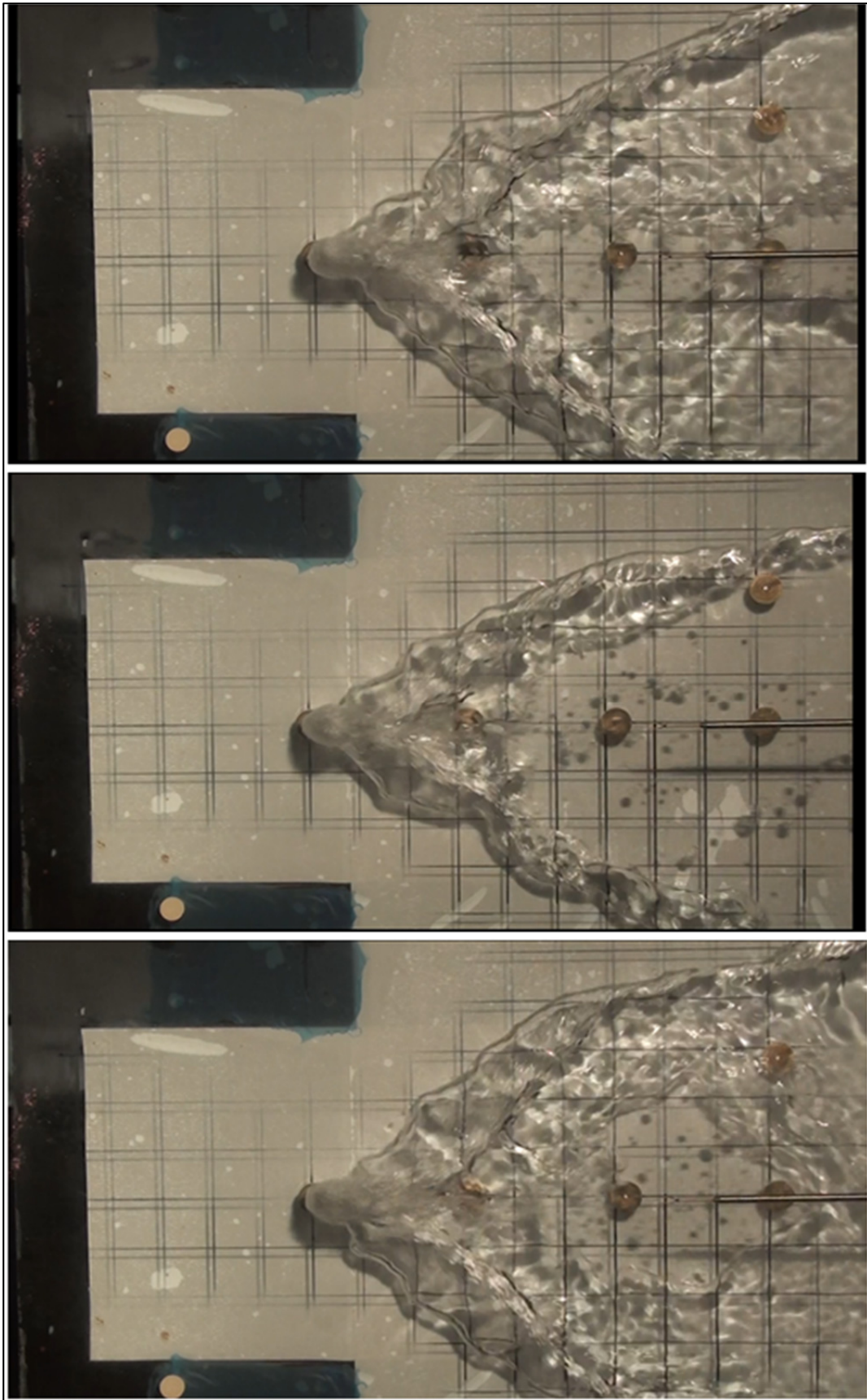


**Figure A.14 :** Bottom view of p50 case with air injection of  $2.8\text{m}^3/\text{h}$ .



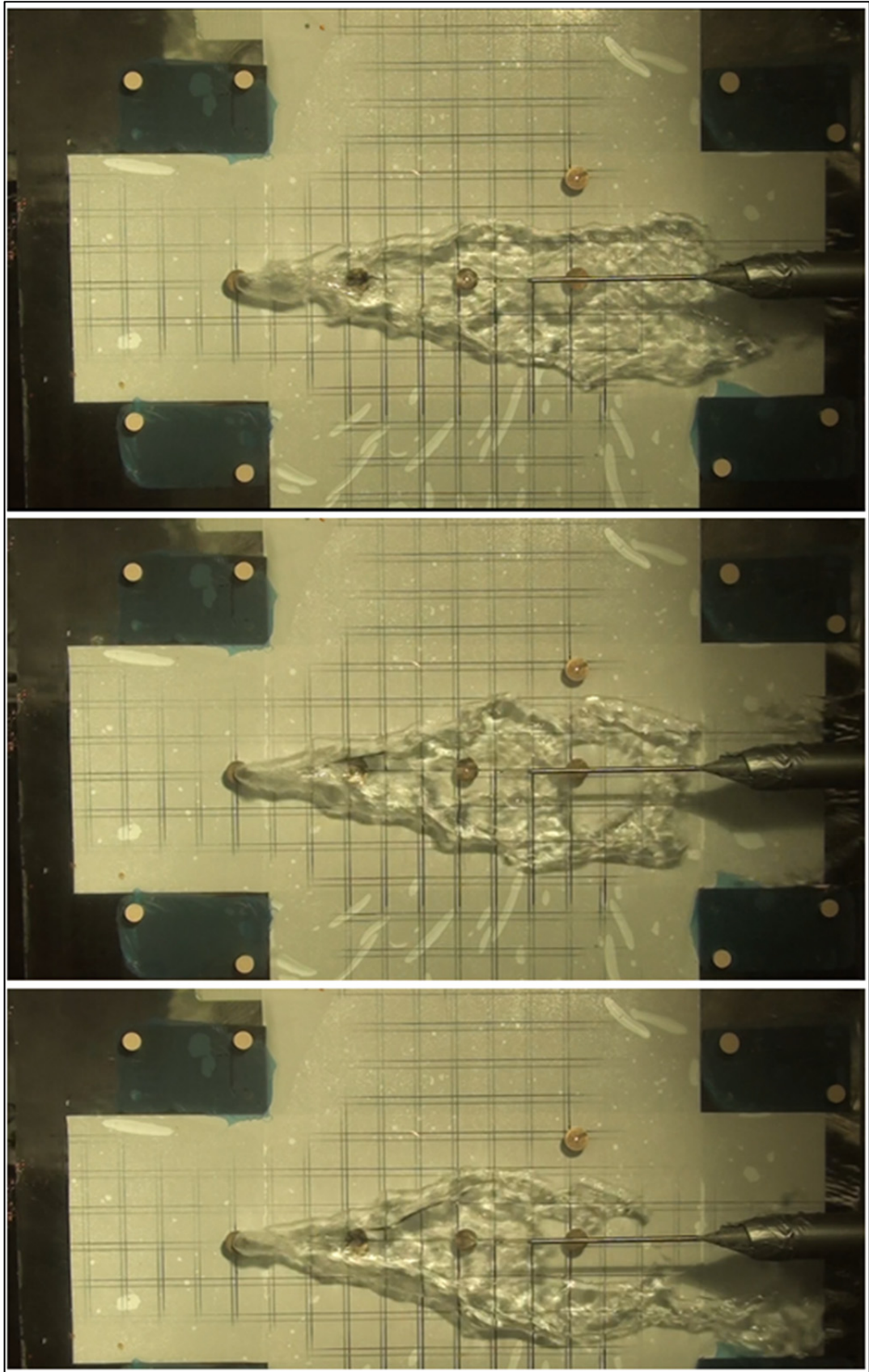


**Figure A.15 :** Bottom view of p80 case with air injection of  $1.4\text{m}^3/\text{h}$ .

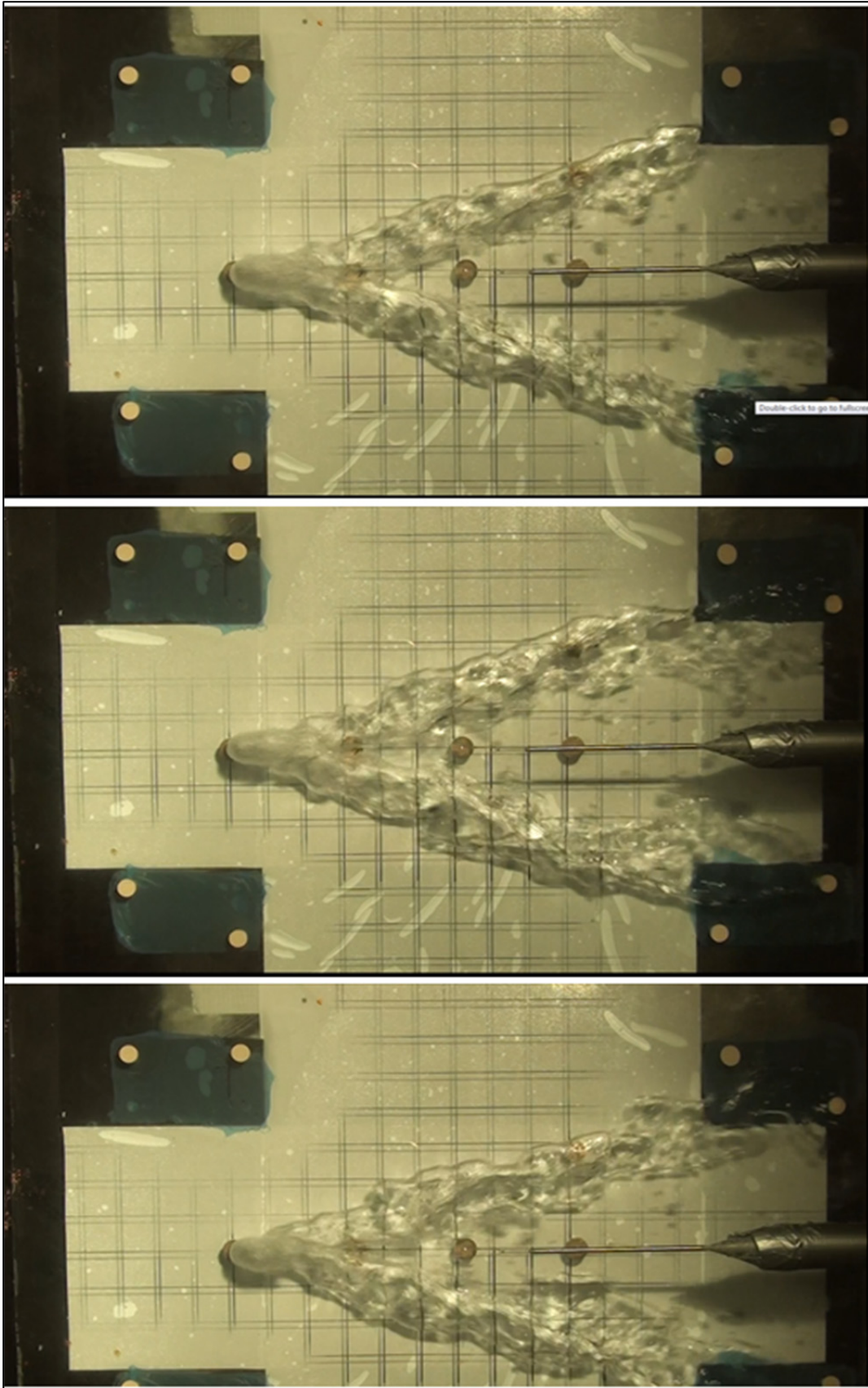


**Figure A.16 :** Bottom view of p80 case with air injection rate of  $2.8\text{m}^3/\text{h}$ .

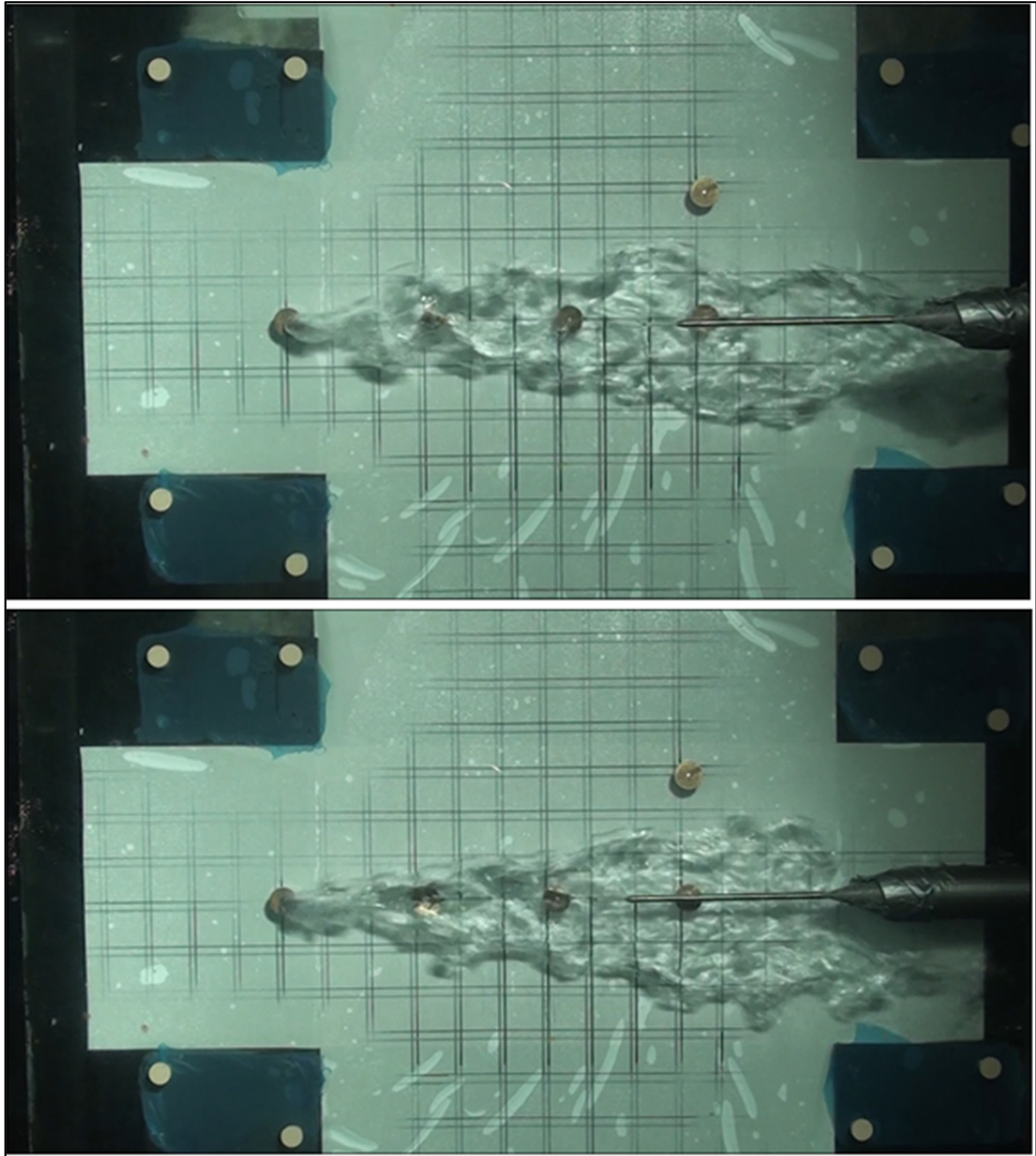


**Figure A.17** : Bottom view of p100 case with air injection of  $1.4\text{m}^3/\text{h}$ .

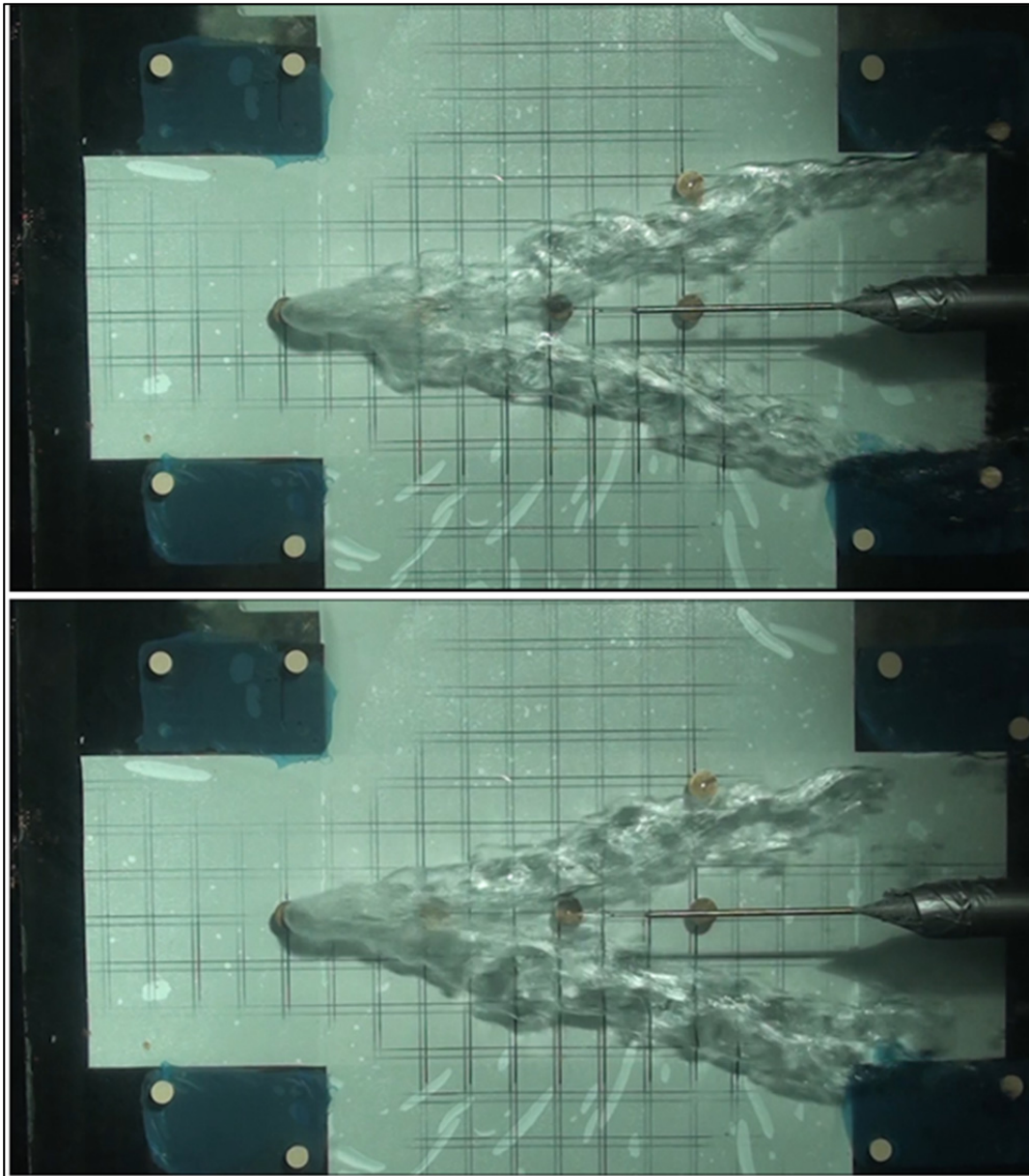


**Figure A.18 :** Bottom view of p100 case with air injection of  $2.8\text{m}^3/\text{h}$ .

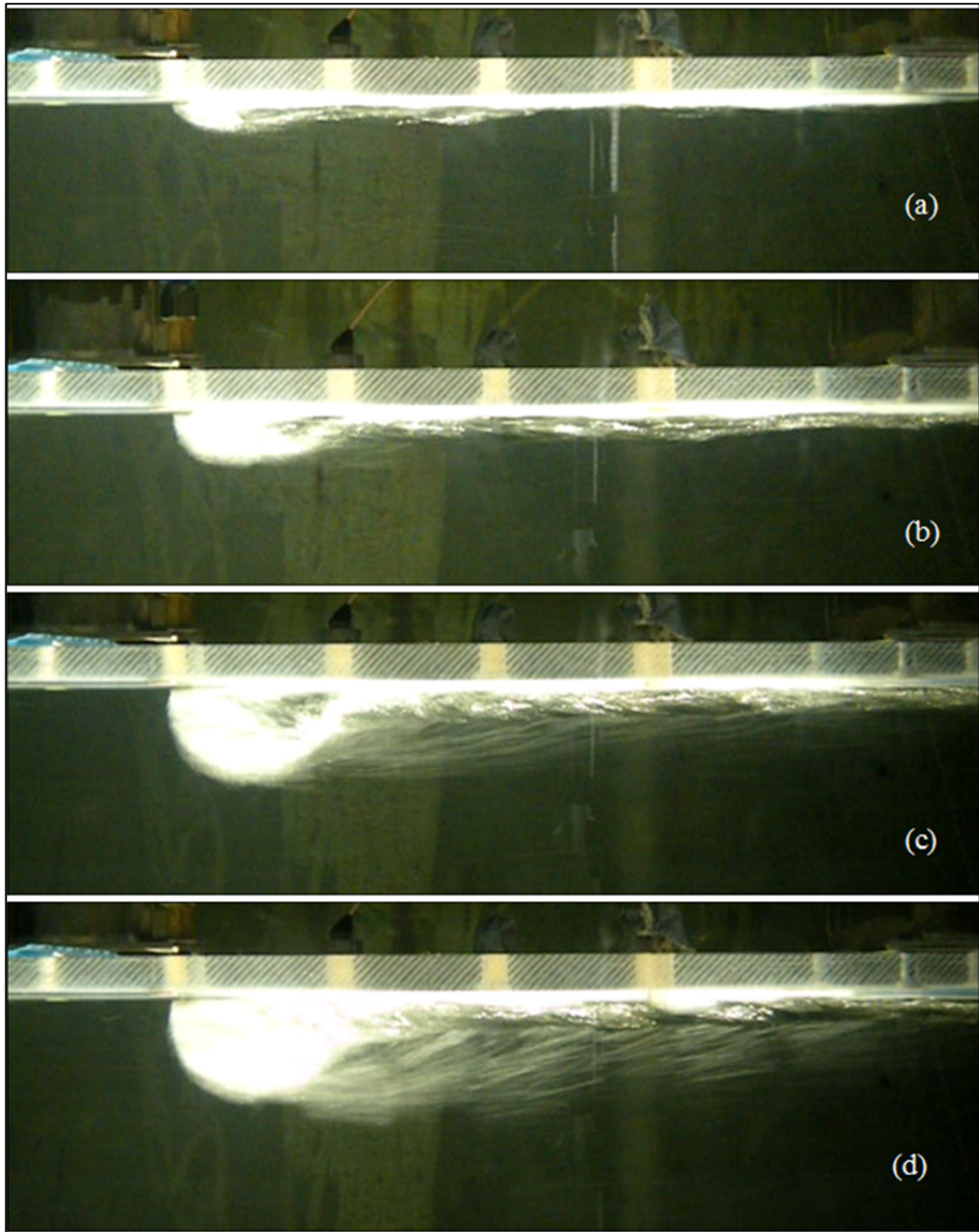


**Figure A.19** : Side view for p100 case for air flow rates: (a)  $1.4\text{m}^3/\text{h}$ . (b)  $2.8\text{m}^3/\text{h}$ . (c)  $5.6\text{m}^3/\text{h}$ . (d)  $7\text{m}^3/\text{h}$ .

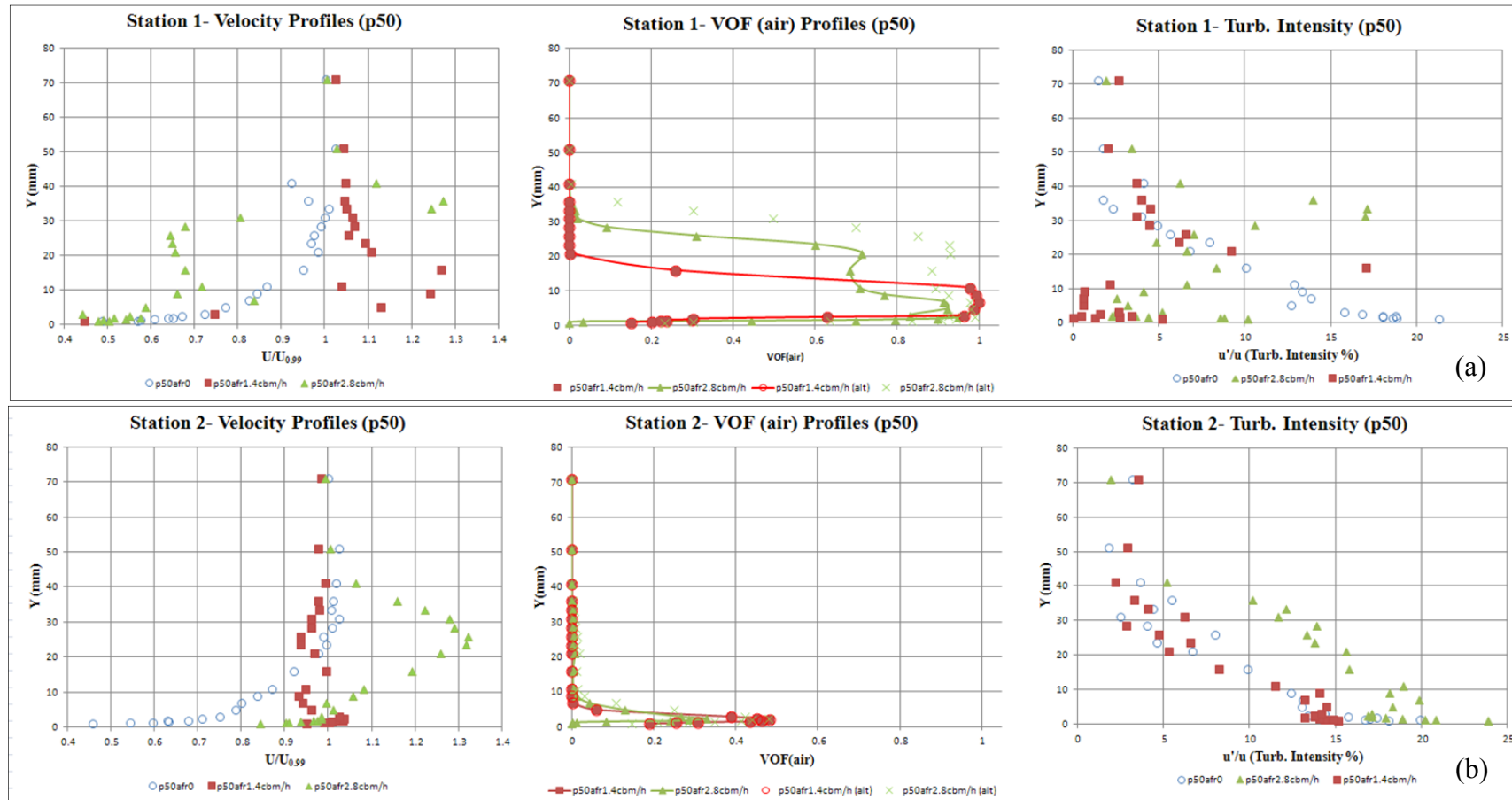


**Figure A.20 :** Velocity, volume of fraction and turbulence intensity profiles for p50 case: (a)Station 1. (b)Station 2.

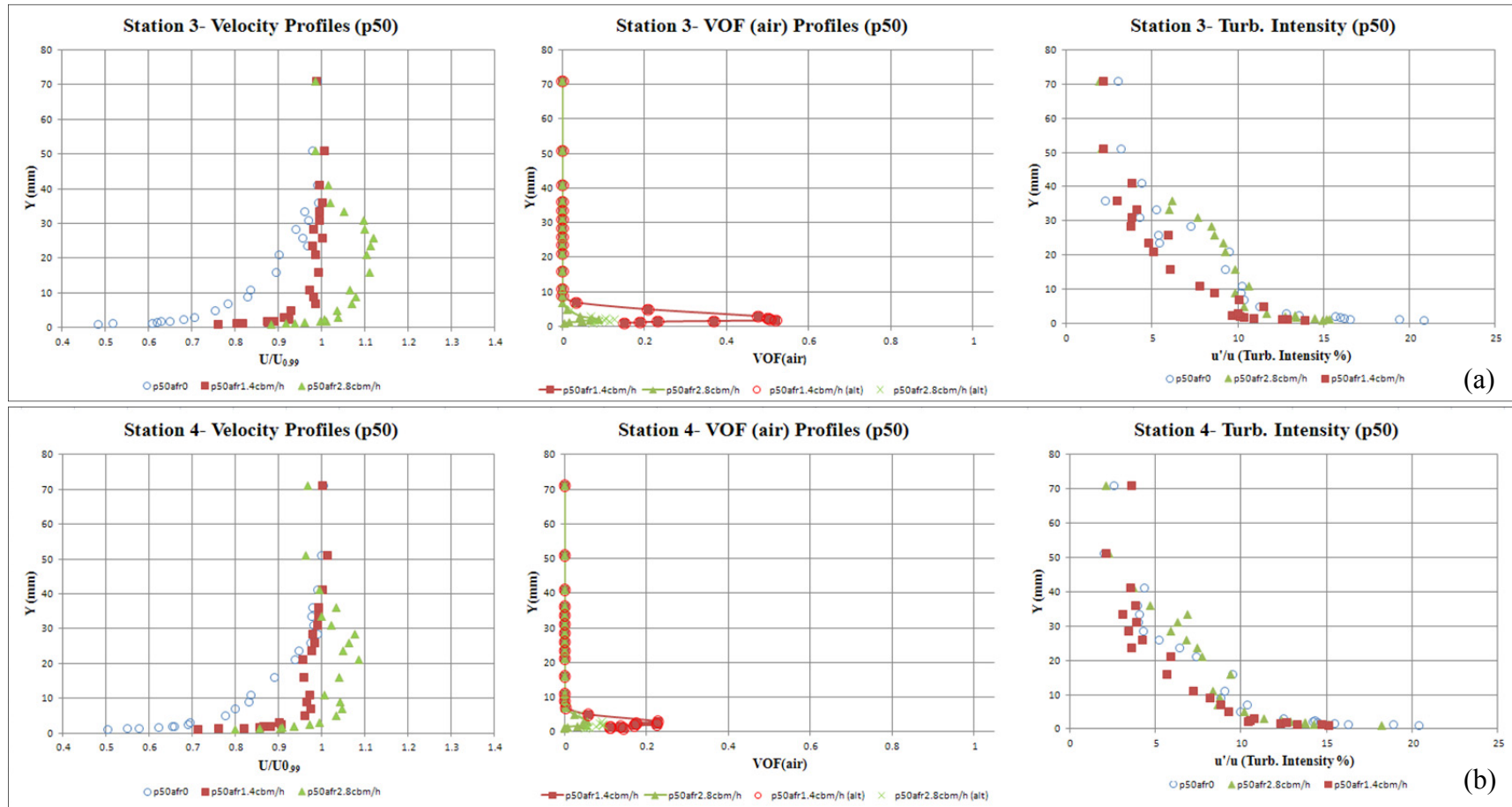


Figure A.21 : Velocity, volume of fraction and turbulence intensity profiles for p50 case: (a)Station 3. (b)Station 4.

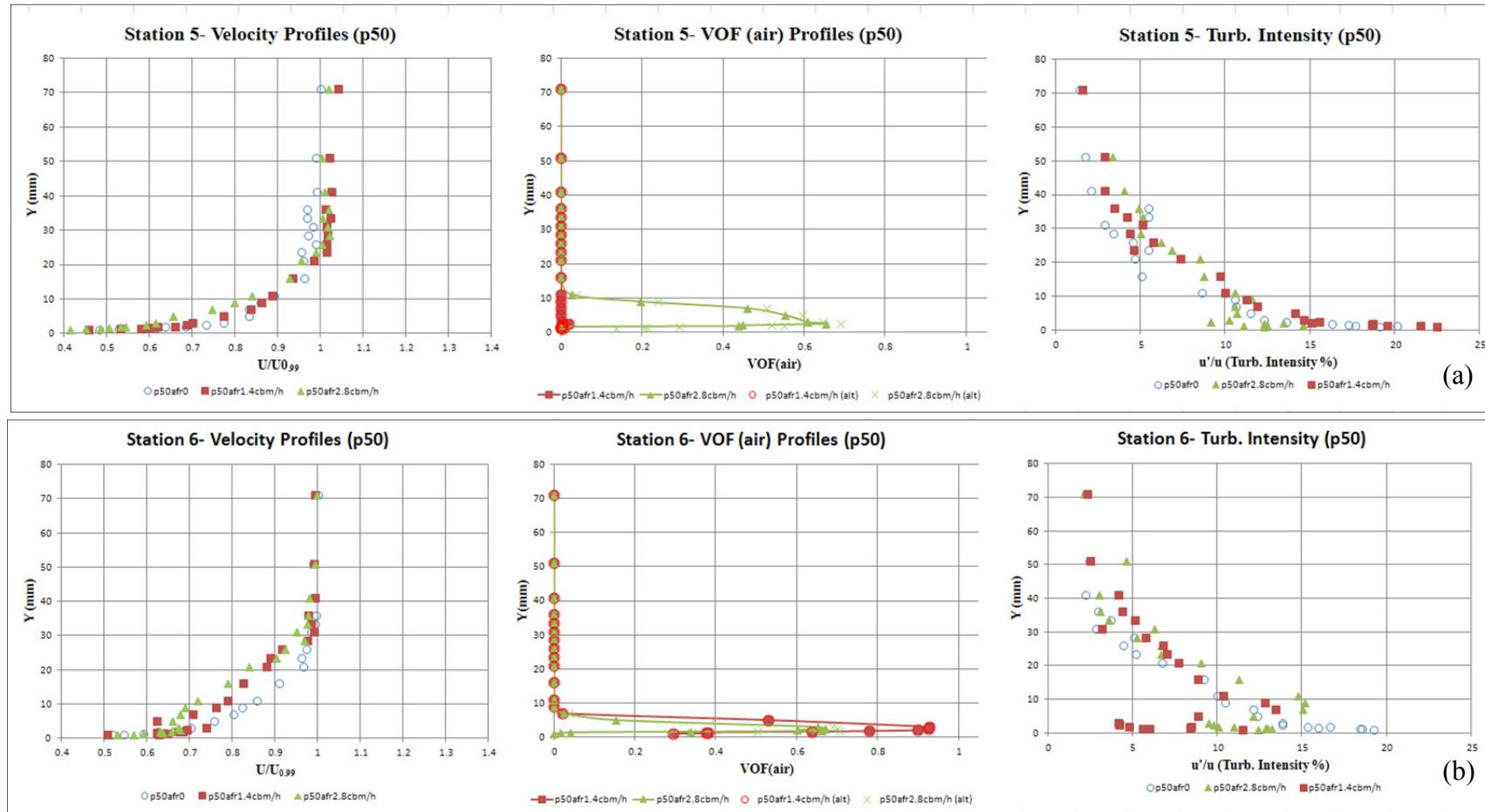
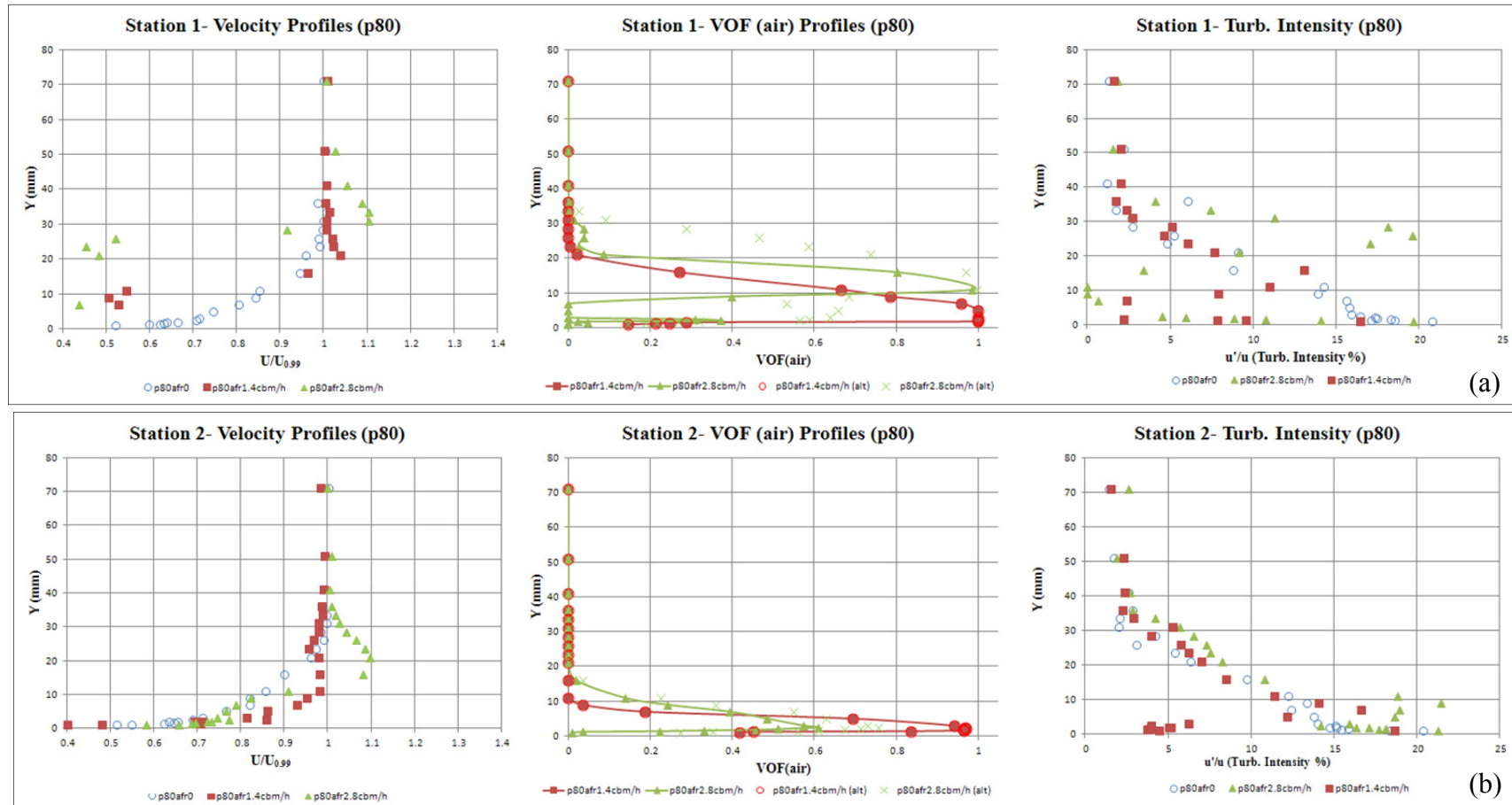
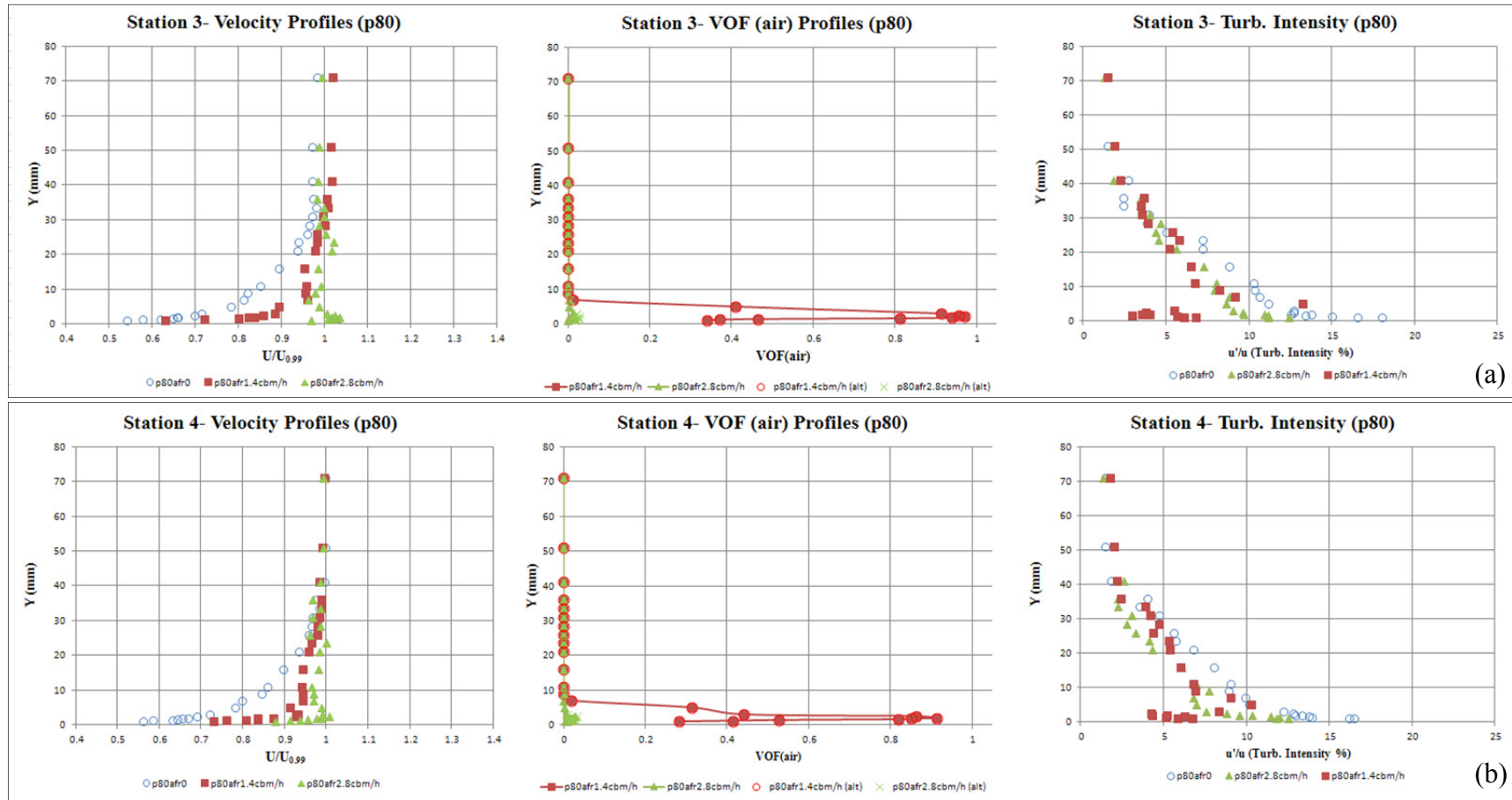


Figure A.22 : Velocity, volume of fraction and turbulence intensity profiles for p50 case: (a)Station 5. (b)Station 6.





**Figure A.23 :** Velocity, volume of fraction and turbulence intensity profiles for p80 case: (a)Station 1. (b)Station 2



**Figure A.24 :** Velocity, volume of fraction and turbulence intensity profiles for p80 case: (a)Station 3. (b)Station 4.

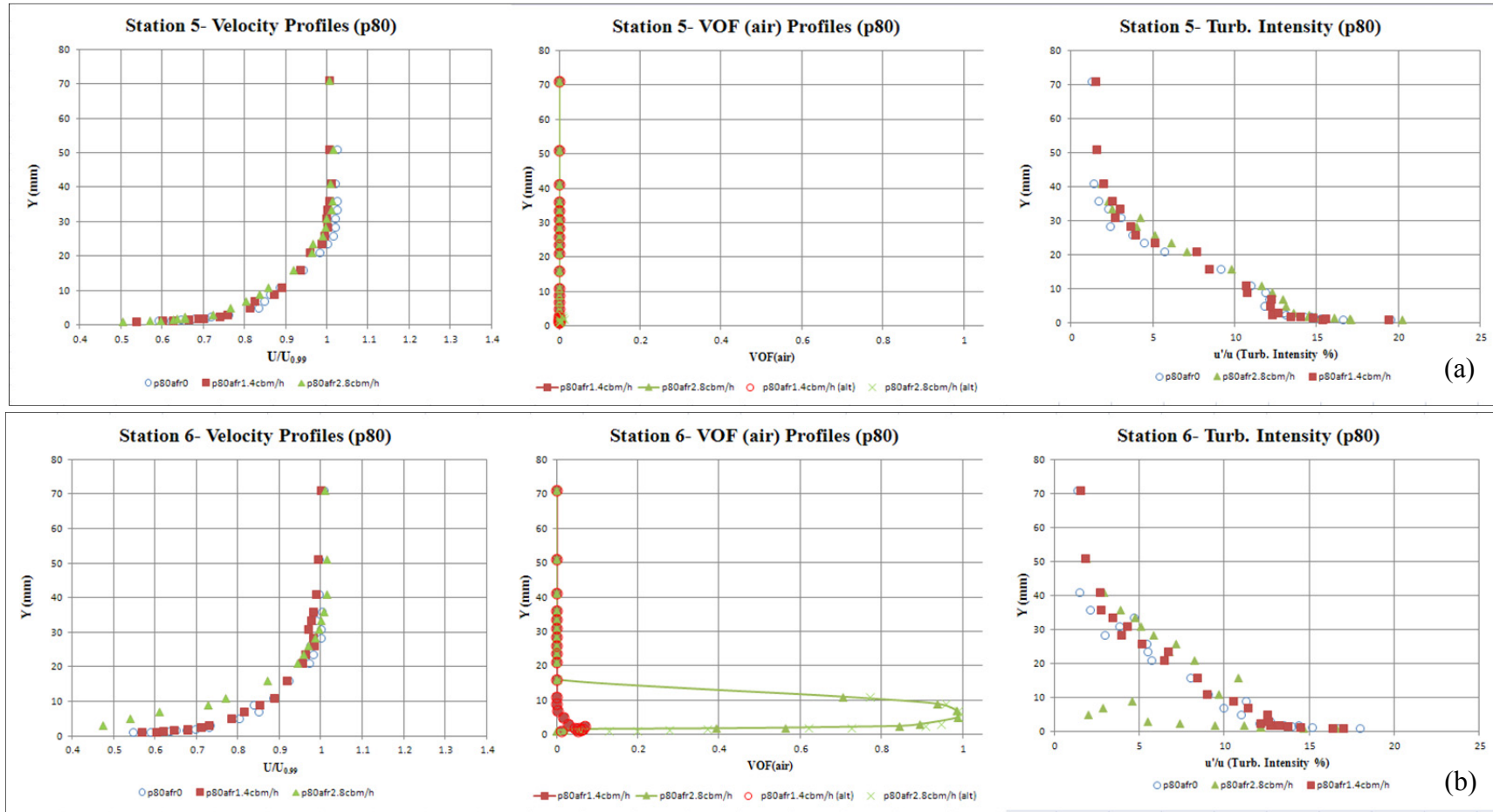


Figure A.25 : Velocity, volume of fraction and turbulence intensity profiles for p80 case: (a)Station 5. (b)Station 6.

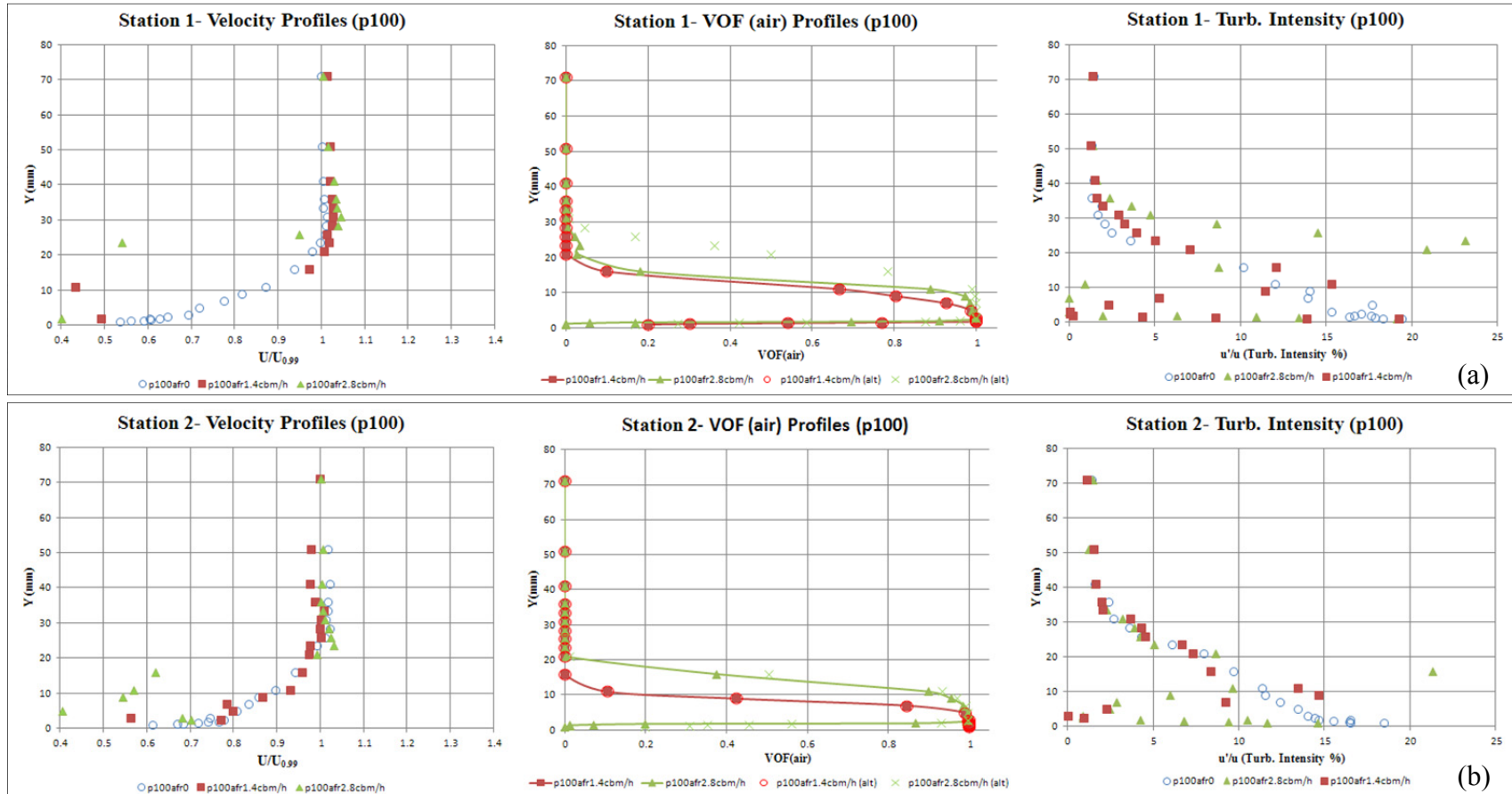


Figure A.26 : Velocity, volume of fraction and turbulence intensity profiles for p100 case: (a)Station 1. (b)Station 2.

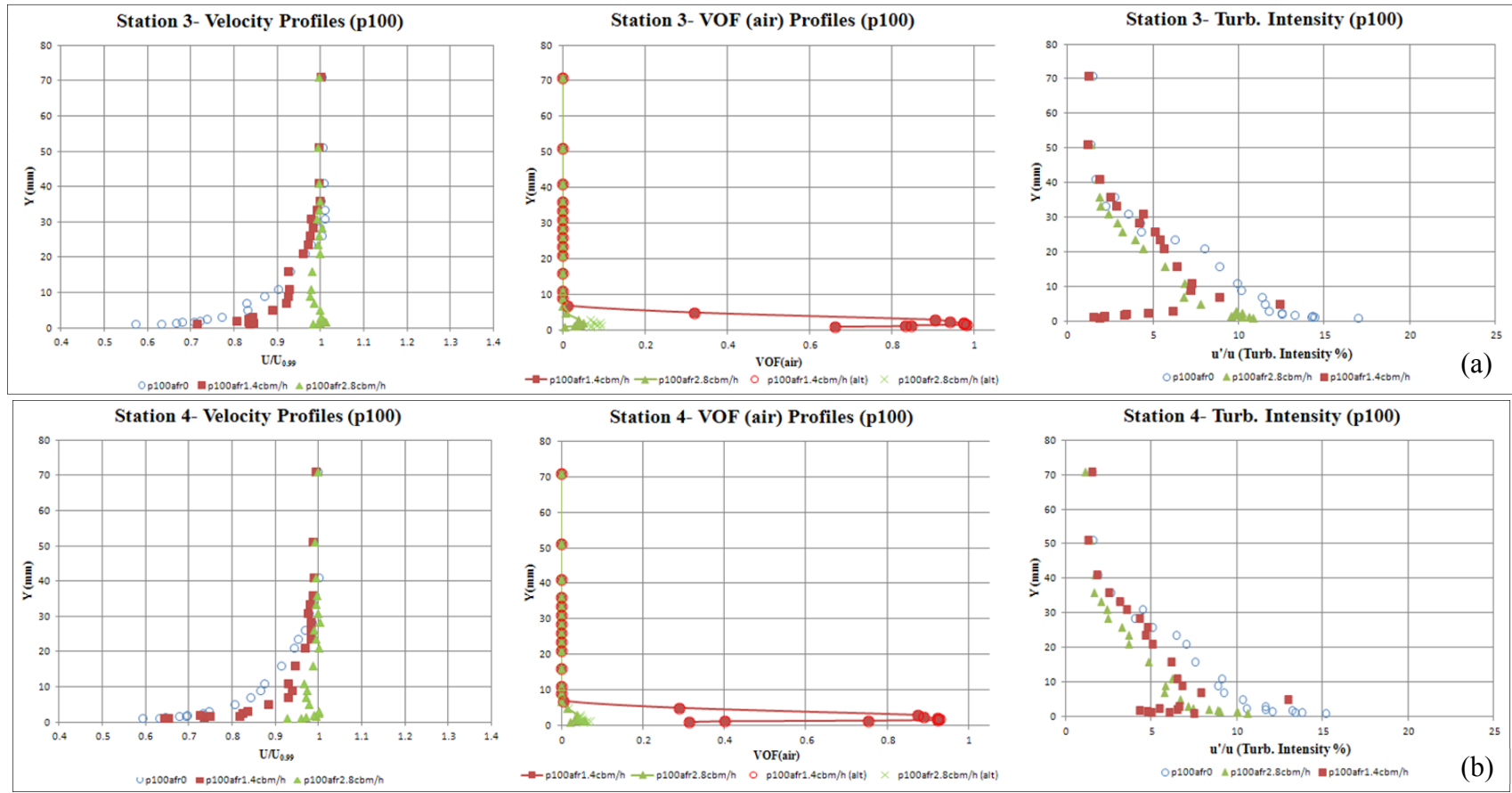


Figure A.27 : Velocity, volume of fraction and turbulence intensity profiles for p100 case: (a)Station 3. (b)Station 4.

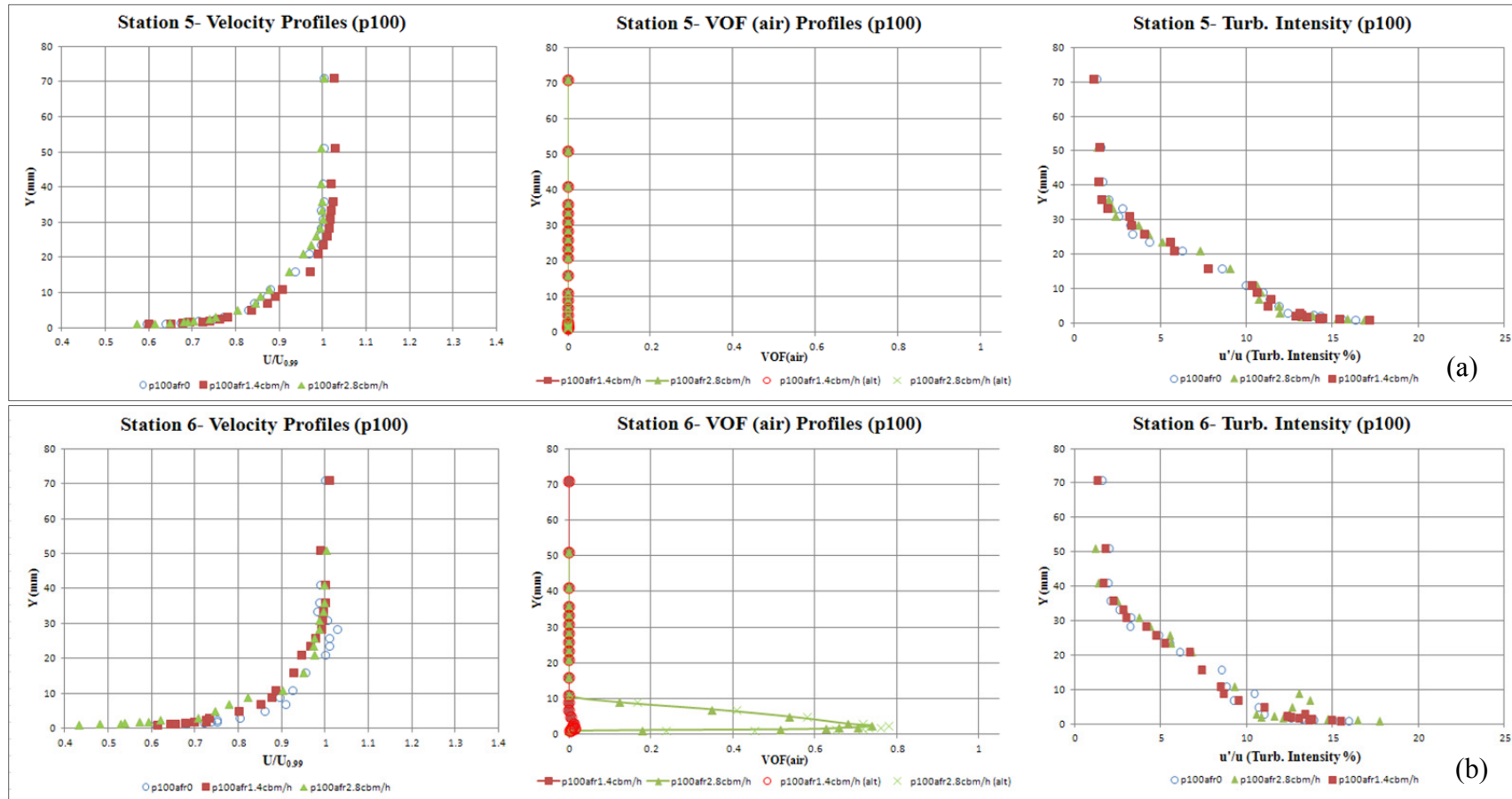
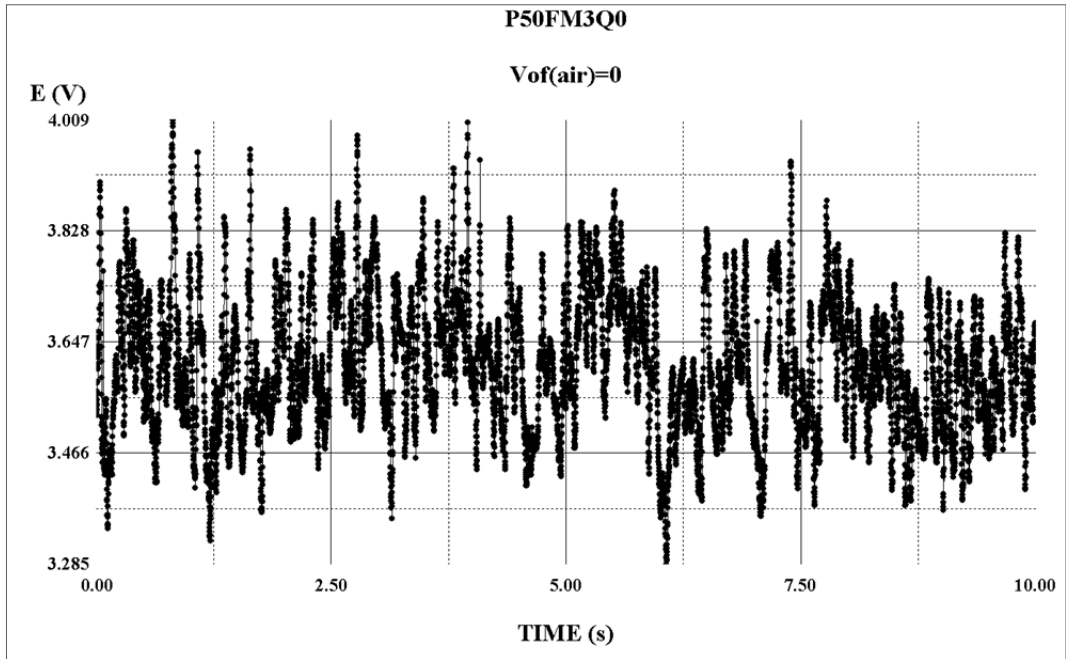
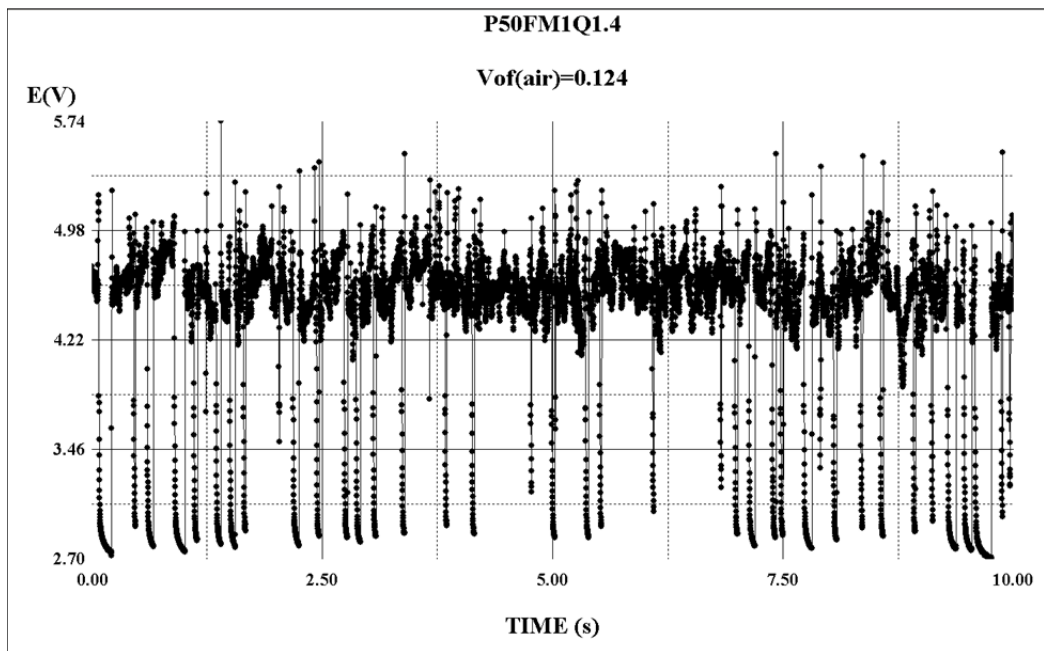


Figure A.28 : Velocity, volume of fraction and turbulence intensity profiles for p100 case: (a)Station 5. (b)Station 6



**Figure A.29** : Flush mounted hot-film signals for p50, FM3 and  $Q=0 \text{ m}^3/\text{h}$ .



**Figure A.30** : Flush mounted hot-film signals for p50, FM1 and  $Q=1.4 \text{ m}^3/\text{h}$ .

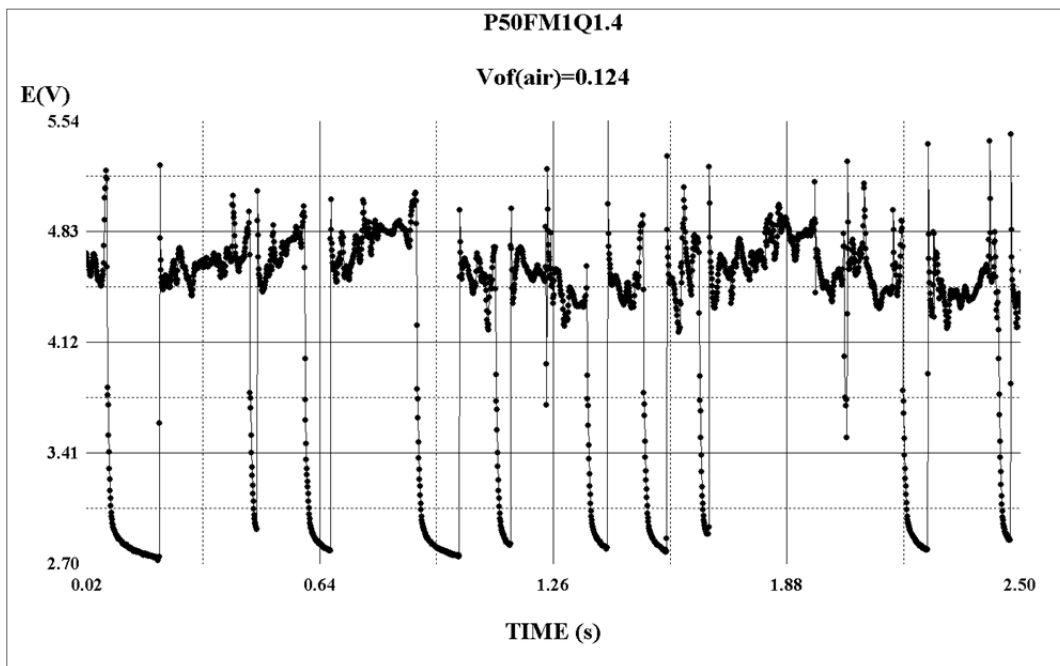


**Figure A.31** : Flush mounted hot-film signals for p50, FM1 and  $Q=1.4 \text{ m}^3/\text{h}$  (zoomed).

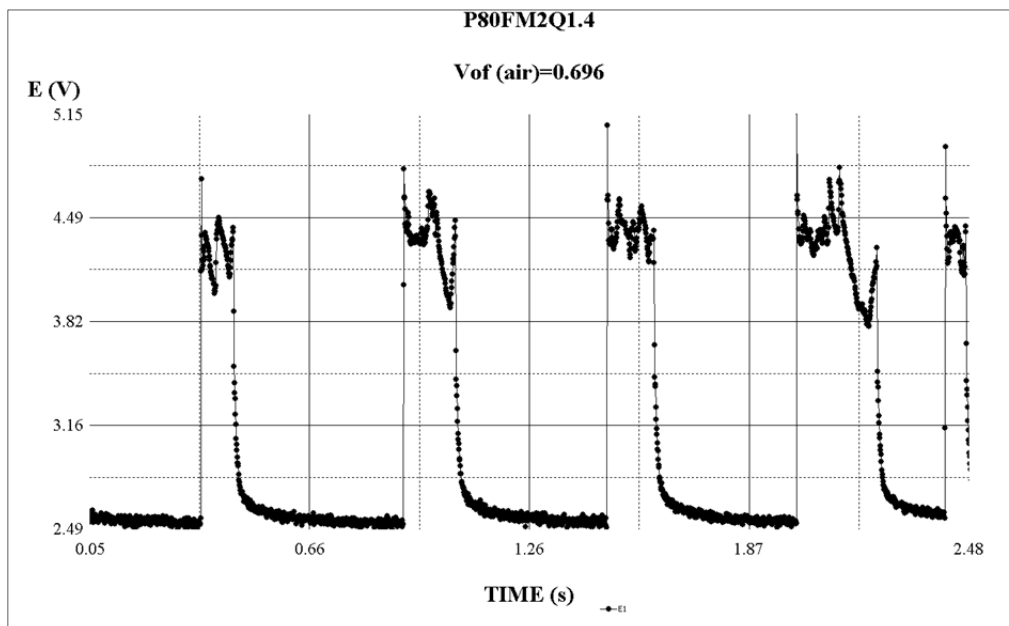


**Figure A.32** : Flush mounted hot-film signals for p80, FM2 and  $Q=1.4 \text{ m}^3/\text{h}$  (zoomed).



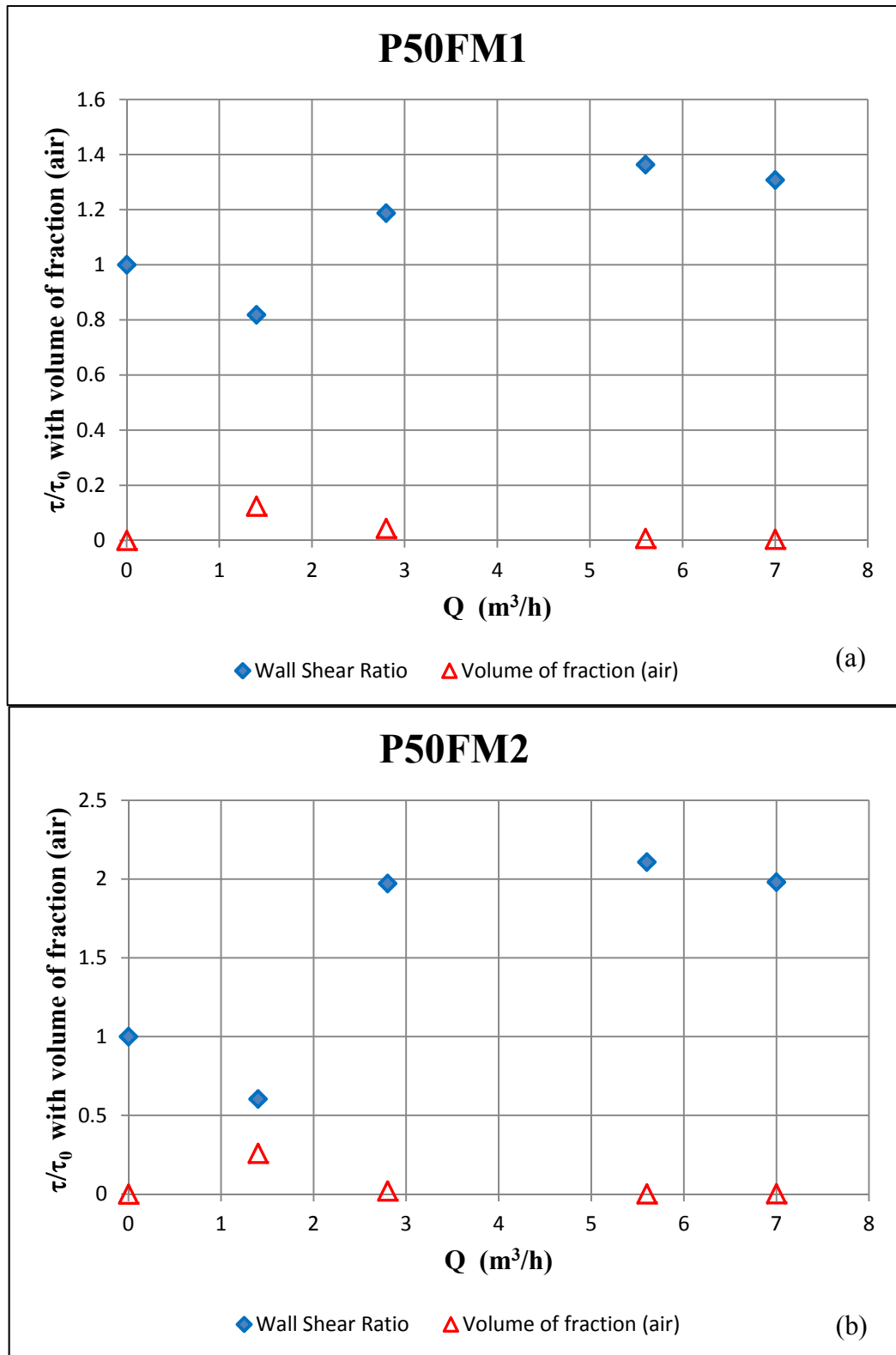


**Figure A.33** : Wall shear stress measurements for p50 case. (a)FM1 position. (b)FM2 position.

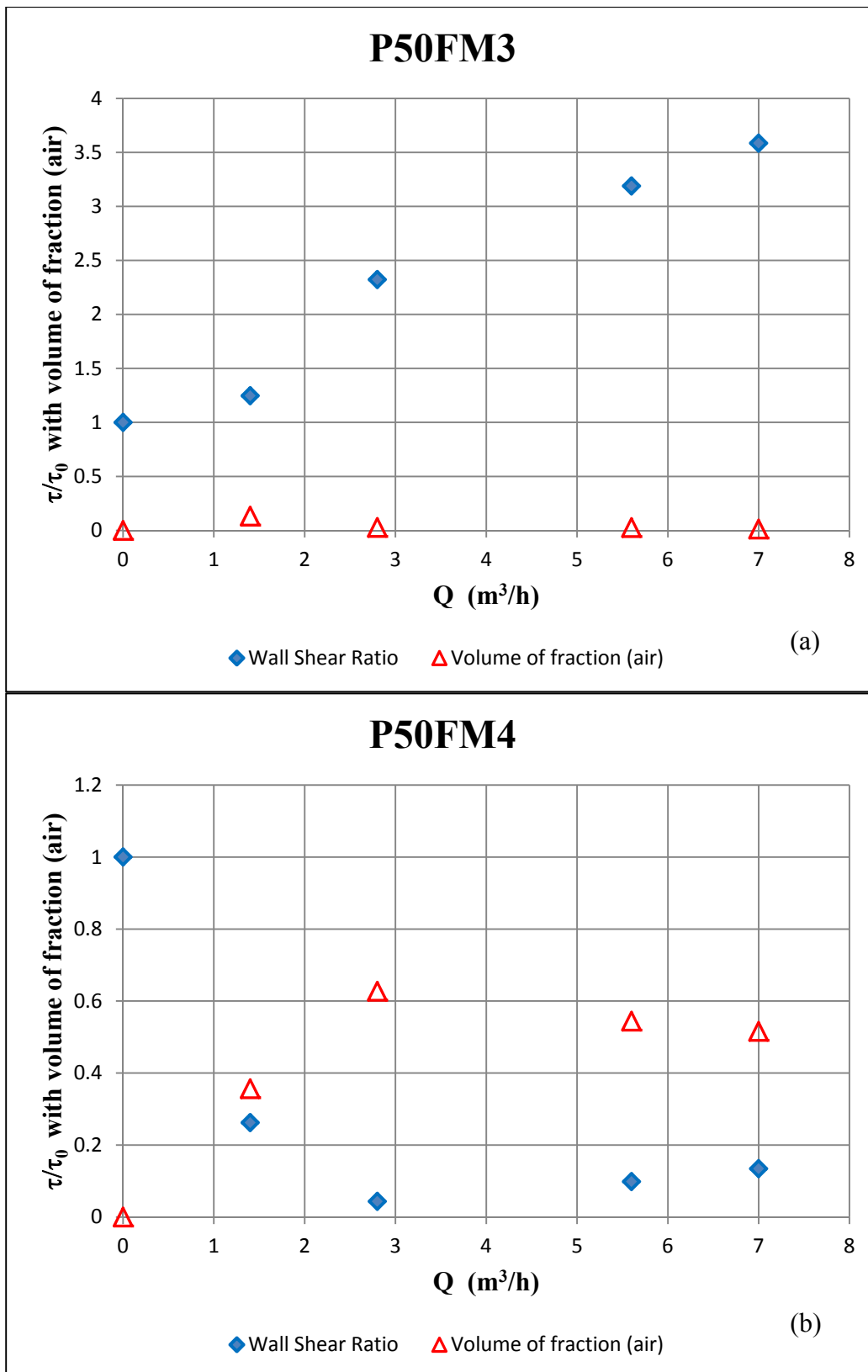


**Figure A.34** : Wall shear stress measurements for p50 case. (a)FM3 position. (b)FM4 position.

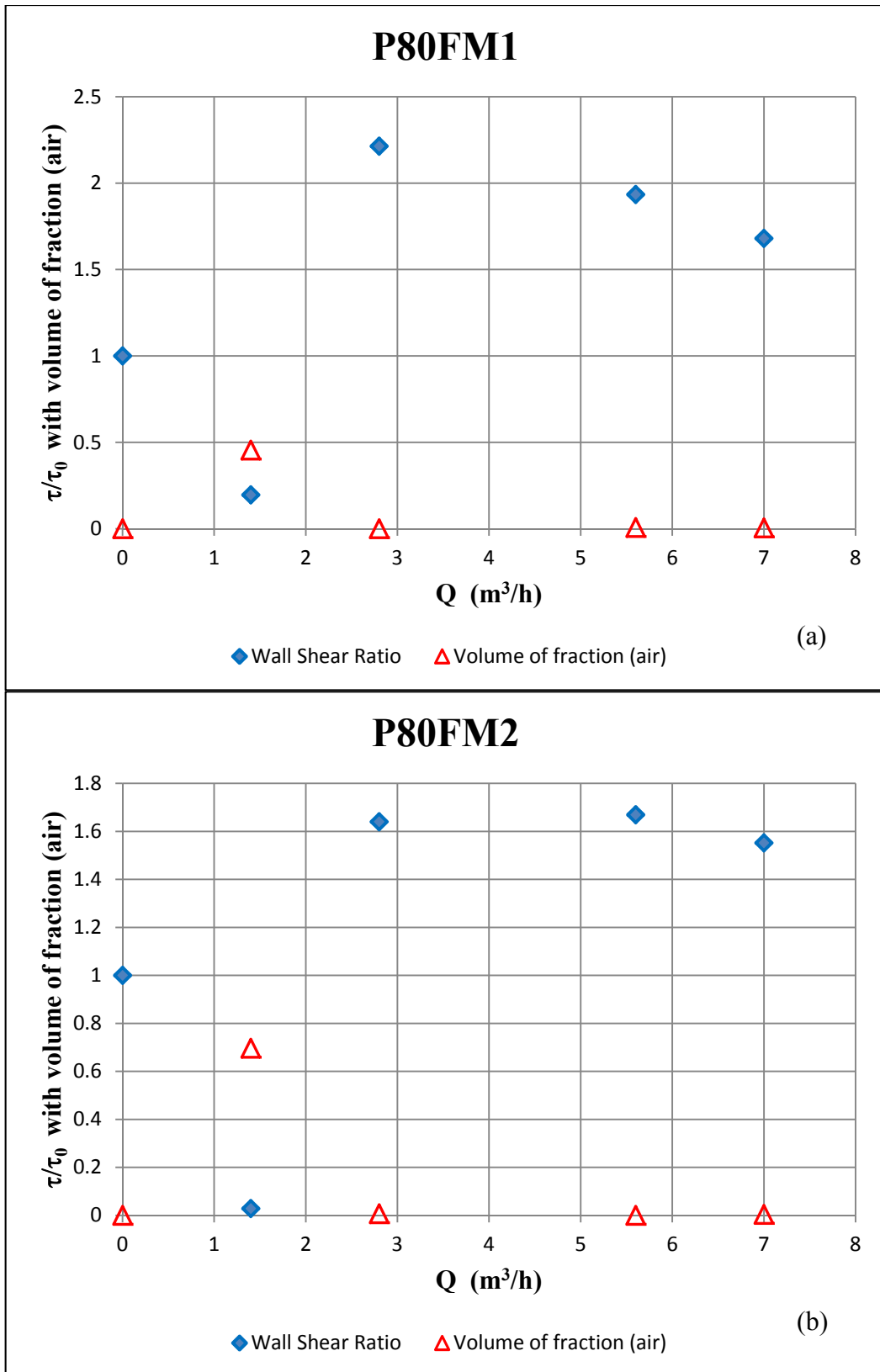


**Figure A.35 :** Wall shear stress measurements for p80 case. (a)FM1 position. (b)FM2 position.

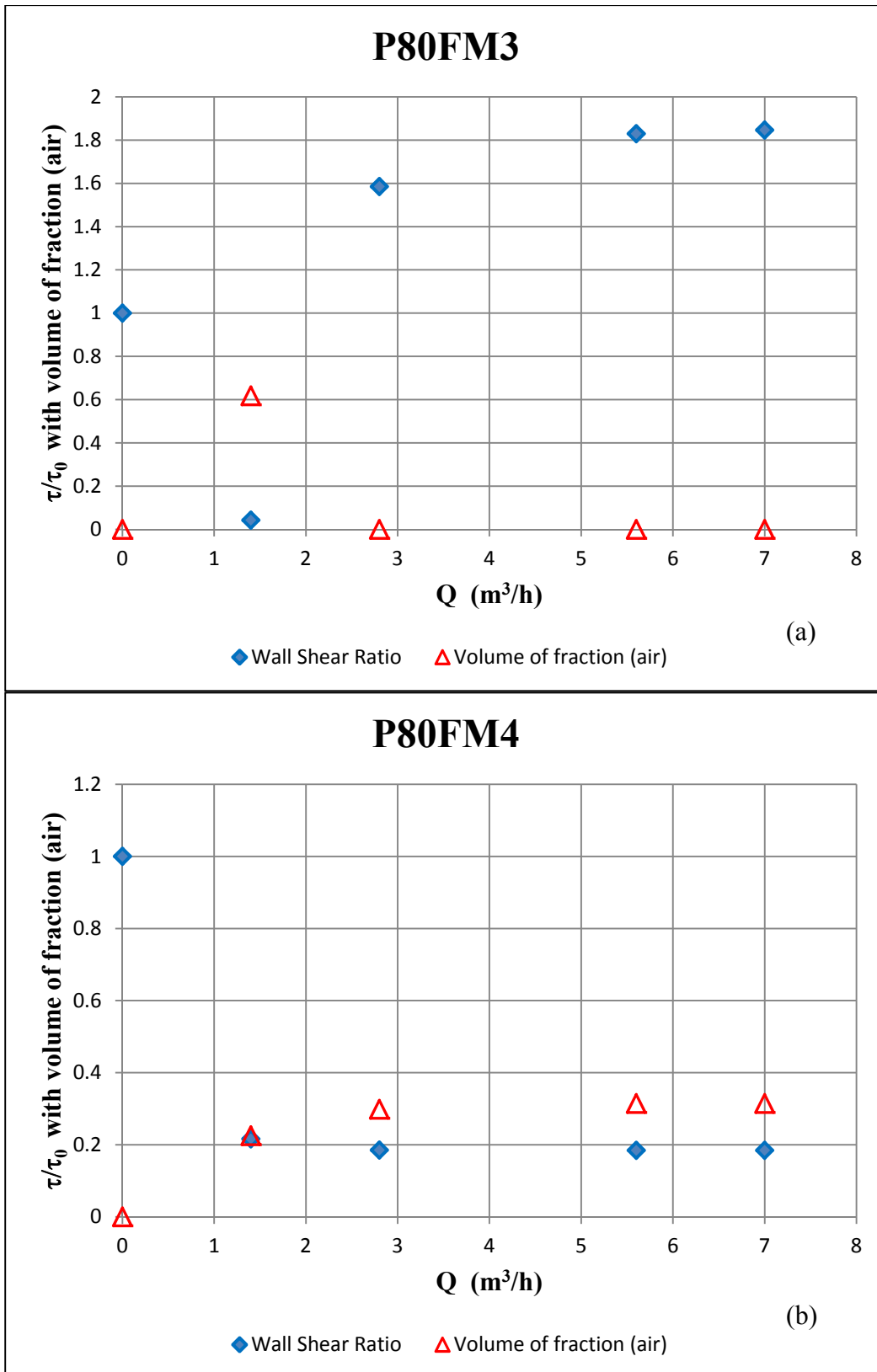


**Figure A.36** : Wall shear stress measurements for p80 case. (a)FM3 position.  
(b)FM4 position.

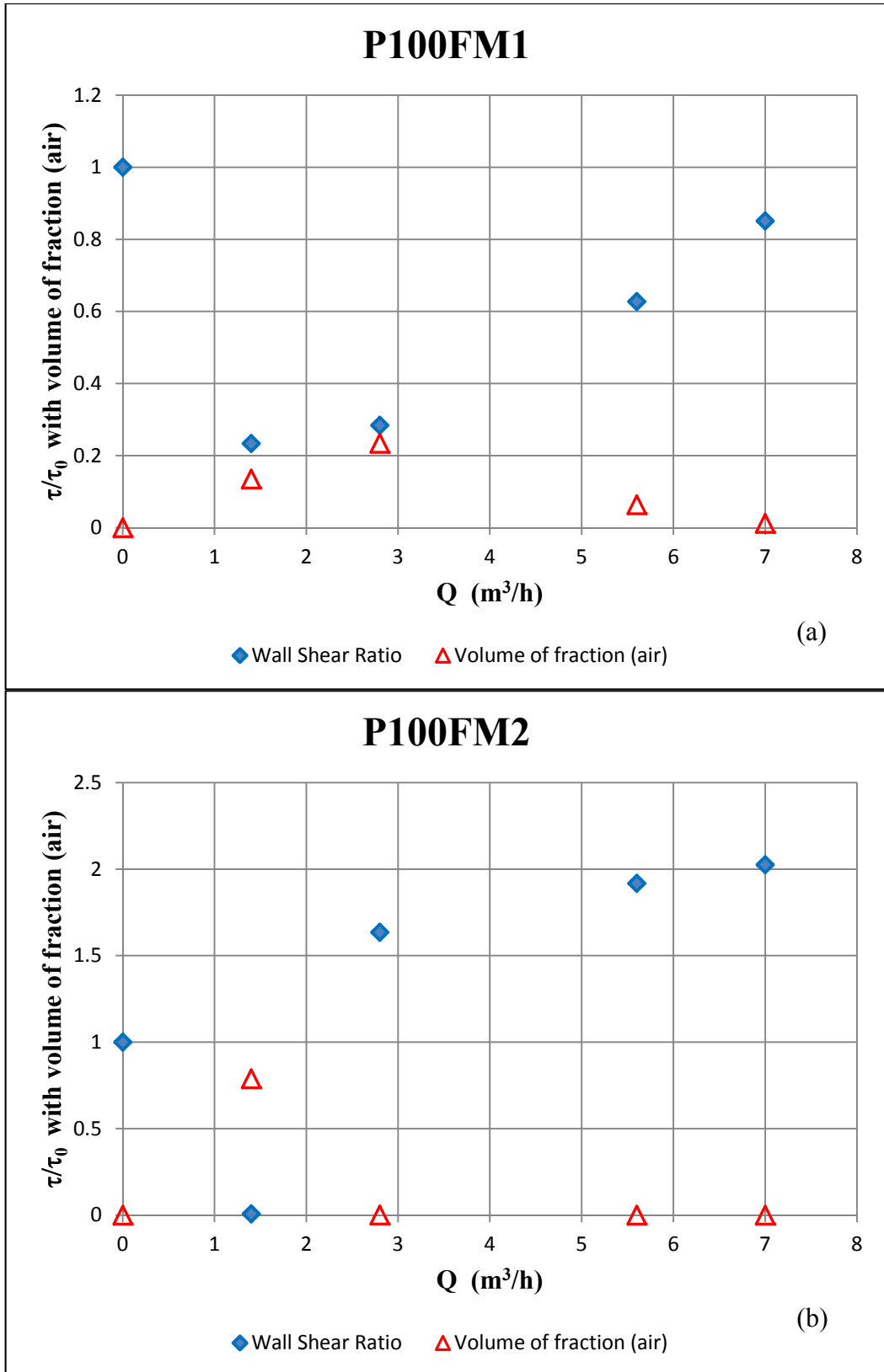


**Figure A.37** : Wall shear stress measurements for p100 case. (a)FM1 position. (b)FM2 position.

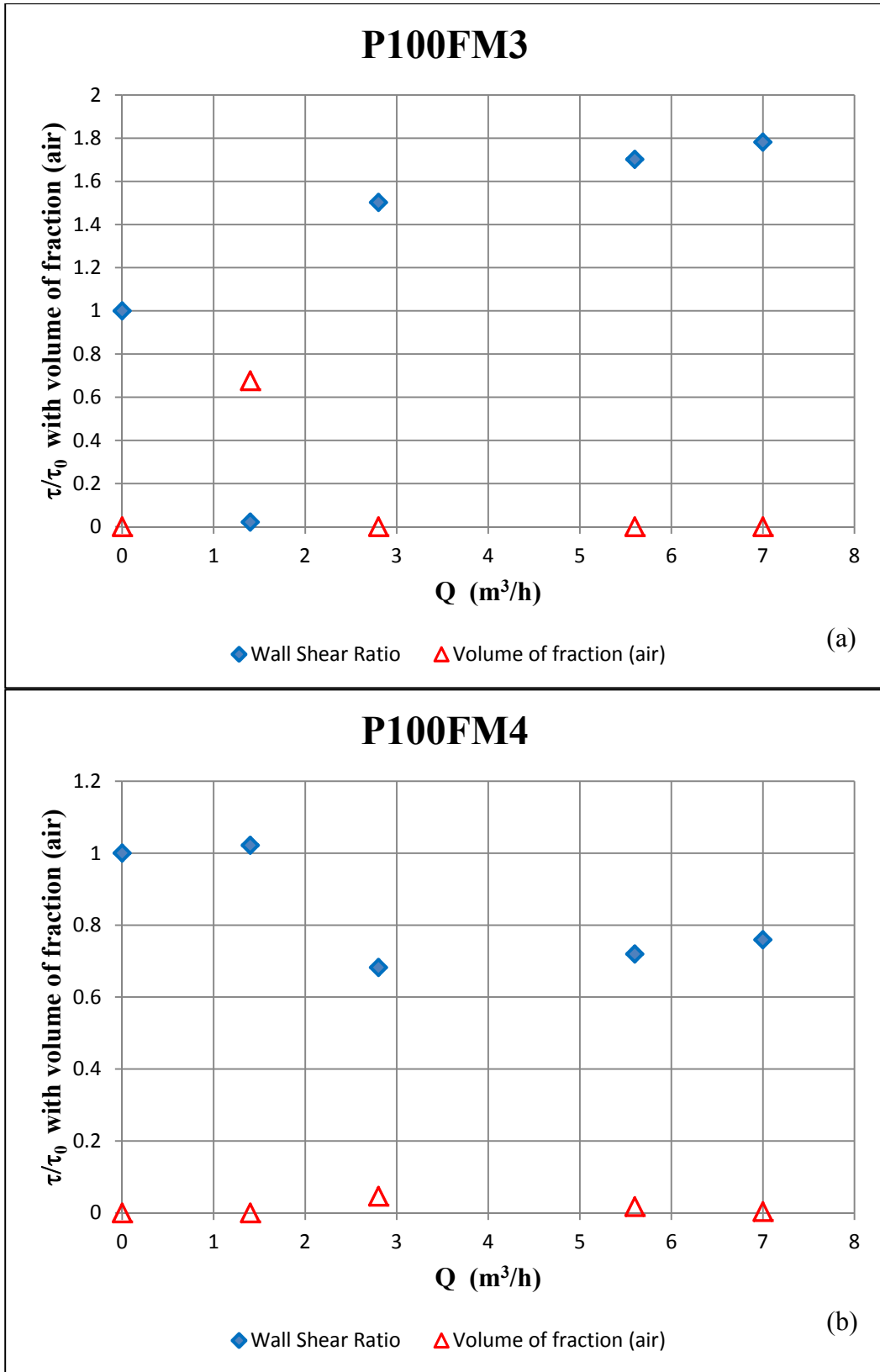


**Figure A.38 :** Wall shear stress measurements for p100 case. (a)FM3 position.  
(b)FM4 position.

**APPENDIX B : Tables**

**Table B.1 : Principle characteristics of the form M266B**

Model	M266B	Scale	30.5
<b>Loading Condition</b>	Full Load	<b>Model</b>	<b>Ship</b>
Length between perpendicular	$L_{BP}$ (m)	4.062	123.90
Length waterline	$L_{WL}$ (m)	4.185	127.63
Length wetted surface	$L_{WS}$ (m)	4.311	131.51
Breadth	$B$ (m)	0.620	18.90
Draught midship	$T$ (m)	0.262	7.98
Draught aft perp.	$T_A$ (m)	0.262	7.98
Draught fore perp.	$T_F$ (m)	0.262	7.98
Displacement Vol.	$\Delta$ (m <sup>3</sup> )	0.509	14431.00
Displacement	$\Delta$ (ton)	0.509	14791.77
Wetted Surface Area	$A_{WS}$ (m <sup>2</sup> )	3.920	3646.63
Rudder Area	$A_R$ (m <sup>2</sup> )	0.053	50.0
Bulbous bow cross section area	$A_B$ (m <sup>2</sup> )	0.016	14.41
Block Coefficient	$C_B$	0.772	0.772
Prismatic Coefficient	$C_P$	0.776	0.776
Midship Section Coefficient	$C_M$	0.995	0.995
Longitudinal Center of Buoyancy	LCB (m) (+fwd)	0.044	1.348
Longitudinal Center of Floatation	LCF (m) (+fwd)	-0.100	-3.039
Service Speed	$V_S$	1.371m/sn.	14.50 kn.

**Table B.2 :** Positions of data points from wall.

Point no	y(mm)-from wall
1	71
2	1
3	1.2
4	1.4
5	1.6
6	1.8
7	2
8	2.5
9	3
10	5
11	7
12	9
13	11
14	16
15	21
16	23.5
17	26
18	28.5
19	31
20	33.5
21	36
22	41
23	51
24	71



## CURRICULUM VITAE

**Name Surname:** Serhan Gökçay  
**Place and Date of Birth:** Ankara - 23.05.1979  
**E-Mail:** serhangokcay@gmail.com  
**B.Sc.:** Research and development of air cavity vessels.  
**M.Sc.:** Investigation of artificial air cavity.

### List of Publications and Patents:

#### PUBLICATIONS/PRESENTATIONS ON THE THESIS

- **Gökçay, S.** (2001). Research and development of air cavity vessels, Final Year Project, Faculty of Naval Architecture and Ocean Engineering, Istanbul Technical University, June 2001.
- **Gökçay, S.,** (2003). Investigation of artificial air cavity', Master of Science Thesis, Faculty of Naval Architecture and Ocean Engineering, Istanbul Technical University, June 2003.
- **Gökçay, S.,** (2011). PhD Progress Report- January, Istanbul Technical University Graduate School of Science Engineering and Technology.
- **Gökçay, S., Insel, M., and Odabaşı A.Y.,** (2004) .Revisiting Artificial Air Cavity Concept for High Speed Craft', Ocean Engineering, 31: 253-267.
- **Gökçay, S. and Insel, M.** (2011). Utilising Air Lubrication For Energy Efficient High Speed Marine Vehicles, Conference on High Speed Marine Vessels (RINA), 2-3 March 2011, Fremantle, Australia
- **İnsel, M., Gökçay, S., Helvacıoğlu, Ş.** (2009). Air lubrication for low speed ships, 13th Congress of Intl. Maritime Assoc. of Mediterranean IMAM 2009, İstanbul, Turkey, 12-15 Oct. 2009

